



A New Modulated Permanent Magnet Twin Stator Machine for High Torque Density and Better Magnet Utilisation

Yasser Abdullah H Alamoudi

School of Electrical and Electronic Engineering

Newcastle University

A thesis submitted for the degree of

Doctor of Philosophy

January, 2015

Abstract

Given the recent interest in the replacement of internal combustion engines with electric machines, the main aim of this research is to design a high torque density permanent magnet machine to an electric vehicle's specification. A new design concept for increasing the torque density of a conventional permanent magnet machine is introduced and described theoretically and mathematically. The proposed method involves splitting the stator teeth in order to introduce a magnetic gear ratio into the torque equation. The introduced machine is also further modified to improve its magnet utilisation.

An investigation is carried out on the impact of different slot to pole combinations on torque density and an optimum combination found.

Thereafter, two optimisation methods are applied. The first method is carried out manually by varying a single parameter and investigating its effect on torque density. The second method is conducted automatically using OptiNet to validate the results achieved with the manual optimisation.

Further analysis is carried out, including mechanical evaluation against centrifugal forces in order to determine the mechanical strength of the rotor.

Finally, a prototype is constructed and tested with detailed discussion on the results achieved and comparison with finite element calculations in order to validate the design and determine its level of performance. The final design is then compared to the Toyota Camry and Prius electrical motors.

Acknowledgements

First and foremost, I would like to thank Glynn Atkinson for his guidance and support throughout these years and for patiently reading and commenting on this thesis. I also appreciate the input of Barrie Mecrow throughout my time at Newcastle University.

I thank Chris Manning for his consistent help with many of the mechanical aspects of this research. Also I will not forget all the good time I spent with everyone in the workshop during the construction of the machine who always stepped in to help, so special thanks go to Jack Noble, Allan Wheatly, Graham Ewart, Luke Coates and Stuart Baker.

I would also like to thank Len Shaw for reading and commenting on some parts of my thesis. I would also like to thank Hala Batooq for her support throughout my PhD period and the time we spent in the library solving problems.

I also wish to acknowledge Min Zhang Andrew Wechsler, Ahmed Althobaiti, Abdulrhman Alfrahan, Chukwuma Ifedi, Osama Abushafa, Muhsien Yazid and Tahani Al-mhana for the discussions we have had and for trying to solve any problems which arose.

To save the best for last, I thank my family for supporting me throughout my PhD. However, words are not enough to express how grateful I am to my father for his care, and support, both emotionally and financially, in order to see me through my education. I cannot imagine being able to go through my education without his support. I am also grateful for having the best mother, who paid me so many visits and supported me in every way.

Also I thank my brothers Bassam, Mohammed and Ibrahim and my sister Yasmeen for their support and multiple visits to Newcastle which I have greatly enjoyed.

*To the memory of my grandfather
who departed at the end of my studies*

Table of Contents

Abstract	i
Acknowledgements	ii
Table of Contents	iv
List of Figures	viii
List of Tables	xv
Acronyms and symbol	xvii
Chapter 1. Introduction	1
1.1 Background	1
1.2 The Research	1
1.3 Contribution to Knowledge	2
1.4 Published Material	3
1.5 Objectives and Overview of this Thesis	3
Chapter 2. An Overview of Electric Vehicles	6
2.1 Introduction	7
2.2 Electric Vehicles	8
2.2.1 Hybrid Electric Vehicles	8
2.2.2 Pure Electric Vehicles	14
2.3 Challenges Facing the Design of EVs	15
2.4 Electric Machines for Electric Vehicles	16
2.5 Electric Motor Performance Requirements for EVs	17
2.6 Challenges of Electric Motors for EVs	19
2.7 Drive Cycle	22
2.8 Conclusion	23
Chapter 3. Electrical Machine Topologies for EVs	25
3.1 Introduction	26
3.2 DC Drives	30
3.3 Induction Machines	30
3.4 Switched Reluctance Machines	31
3.5 Permanent Magnet Machines	33
3.5.1 The Radial Flux Machine (with Magnets on the Rotor)	34
3.5.2 The Radial Flux Machine (Magnets on Stator)	36
3.5.3 Axial Field Machine (AFM)	38
3.5.4 The Transverse Flux Machine (TFM)	40
3.6 FE Analysis Comparison Between a PM Machine Used in an Existing HEV and Other Investigated Alternatives.	41
3.7 Principle of PM Machine Design.	44

3.7.1	Torque Density	46
3.7.2	Efficiency and Machine Loss	48
3.8	Conclusion:	50
Chapter 4.	Introducing the Split Tooth Permanent Magnet Machine	52
4.1	Introduction:	53
4.2	Design Concept	55
4.3	Machine Design	58
4.3.1	Machine Dimensions	63
4.3.2	Winding Arrangements:	63
4.4	No Load Analysis	64
4.4.1	Flux Density Distribution	64
4.5	Load Analysis	65
4.5.1	Static Torque	67
4.6	Conclusion	70
Chapter 5.	Development of the Split Tooth PM Machine	71
5.1	Modified Machine Design	72
5.1.1	Modified Machine Dimensions	74
5.1.2	Modified Machine Mechanical Complexity	76
5.2	No Load Analyses of the Newly Modified Machine Design	77
5.2.1	Flux Density Distribution	77
5.2.2	Flux Linkage	78
5.3	Load Analysis of the Newly Modified Machine Design	79
5.3.1	Static Torque	79
5.4	Evaluation of Flux Concentration Topology over the Conventional Geometry	80
5.5	Comparison between the Four Machine Designs.	80
5.6	Conclusion	82
Chapter 6.	Design Optimisation	85
6.1	Introduction	86
6.2	MagNet™ Software	87
6.3	Slot / Pole Combination	87
6.3.1	Evaluation of the 6 Slot / 20 Pole and 12 Slot / 40 Pole Designs	91
6.3.2	No-Load Back EMF Comparison	91
6.3.3	Cogging Torque Comparison	92
6.3.4	Mean Torque Comparison	94
6.3.5	Torque Ripple Comparison	95
6.4	Design and Optimisation Methods	96
6.4.1	Optimisation Parameters	97
6.4.2	Process of Optimisation:	100

6.5	Conclusion	103
Chapter 7. Investigative Design		104
7.1	Introduction	105
7.2	Investigation Methodology	106
7.3	Outer Stator Dimension Impact on Torque Density	106
7.4.1	Tooth Body Width and Slot Depth	107
7.4.2	Coreback Depth	111
7.4.3	Slot Opening Widths	114
7.4.4	Tooth Split Width	116
7.4.5	Tooth Split Depth	118
7.4.6	Tooth Tip Depth	120
7.4	Rotor Dimension Impact on Torque Density	122
7.4.1	Magnet Height	123
7.4.2	Magnet Thickness	127
7.5	Inner Stator Dimension Impact on Torque Density	129
7.5.1	Tooth Width	130
7.5.2	Inner Slot Depth	132
7.5.1	Coreback Depth	134
7.5.2	With and Without Inner Stator	135
7.6	Conclusion	136
Chapter 8. Further Investigation of the Final STPM Machine		139
8.1	Introduction:	140
8.2	OptiNet Optimisation (Final Optimisation Process)	140
8.3	Rotor Mechanical Strength	143
8.4	Winding Arrangements	147
8.5	Number of Turns	148
8.6	Electromagnetic Torque at Different Operating Currents.	149
8.7	Torque-Speed Characteristics	150
8.8	Magnet Demagnetisation	153
8.9	Conclusion	155
Chapter 9. Design and Construction		156
9.1	Introduction	157
9.2	Stator Design and Construction	157
9.3	Winding Type and Arrangement	160
9.4	Rotor Design and Construction	161
9.5	Permanent Magnets	164
9.6	The Inner Stator	166
9.7	The Shaft Assembly	168

9.8	The Rotor Assembly	172
9.9	Case Design and Construction	173
9.10	Power Connector Design and Construction	176
9.11	Test Rig	178
9.11.1	Static Torque Test Rig	178
9.11.2	High Speed Test Rig	179
9.12	Conclusion	181
Chapter 10.	Experimental Testing and Evaluation	183
10.1.	Introduction	184
10.2.	Coil testing	184
10.3	No Load Test	186
10.3.1	Static No-Load Test	186
10.3.2	Open Circuit Test	187
10.4	Load Tests	192
10.4.1	Static Torque	192
10.4.2	Running Load Test	195
10.5	Thermal Test (No-Load)	197
10.6	Comparing STPM Machine to Existing Machines.	199
10.3.	Conclusion	202
Chapter 11.	Conclusion	203
11.1	An Overview of Electric Vehicles	203
11.2	Electrical Machine Topologies for EVs	203
11.3	Introducing the Split Tooth Permanent Magnet Machine	204
11.4	Development of the Split Tooth PM Machine	204
11.5	Design Optimisation	206
11.6	Investigative Design	207
11.7	Optimisation and Final STPM Machine Design	208
11.8	Design and Construction	208
11.9	Results and analysis	209
References		212
Appendix A		225
Appendix B		233
Appendix C		235
Appendix D		242

List of Figures

Figure 2.1. Four Strokes of the Atkinson Cycle.	9
Figure 2.2. Comparison of the Otto and Atkinson Cycles.	9
Figure 2.3. Series Hybrid EV [21].	10
Figure 2.4. MPG Comparison for Different Types of Vehicles [22].	10
Figure 2.5. Series Hybrid EV [21].	11
Figure 2.6. Parallel Hybrid EV [23].	12
Figure 2.7. Series/Parallel Hybrid EV[25].	12
Figure 2.8. Plug-In Parallel HEV Configuration [21].	13
Figure 2.9. Crankshaft Mounted ISG System Based Hybrid Vehicles [21].	14
Figure 2.10. Pure EV System [32].	14
Figure 2.11. Pure EV Made by Tesla (model X) [32].	15
Figure 2.12. In-Wheel Drive Train[53].	17
Figure 2.13. Ideal Torque and Power-Speed Curves [55].	20
Figure 2.14. Phasor Diagrams at Base Speed and During Field Weakening.	21
Figure 2.15. The New European Driving Cycle [56].	22
Figure 3.1. (a) DC Drive, (b) Induction Machine, (c) Switch Reluctance Machine and (d) PM Machine [24].	26
Figure 3.2. Classifications of the EV Drives [24].	27
Figure 3.3. Segmental Rotor SRM [58].	32
Figure 3.4. Three-Phase, 6/4 SRM. (b) Four-Phase, 8/6 SRM. (c) One-Phase Leg of Inverter [55].	32
Figure 3.5. SRM with Integrated Flywheel and Clutch For HEVs: (a) the Machine's Schematic, (b) the Rotor/Stator Without Windings; and (c) the Assembled Unit [68].	33
Figure 3.6. Schematic Representation of the PM drives.	34
Figure 3.7. (a) Magnets on Rotor, (b, c and d) Magnets Inside the Rotor [55].	35
Figure 3.8. (a) Doubly Salient PM Machine (b) Flux-Reversal PM Machine (c) Flux Switching PM Machine [55].	37
Figure 3.9. (a) Double Stator Single Rotor AFM, (b) Double Rotor Single Stator AFM. [83].	38
Figure 3.10. (a) Assembled View, (b) Disassembled View [84].	39
Figure 3.11. Two Pole Section of a Single Phase of TFM and an Axial View of a the Stator [88].	40
Figure 3.12. Half Cross-Section of (a) PM Machine, (b) SRM and (c) IM [100, 102].	41
Figure 3.13. Performance Comparison at 1500 rpm and 6000 rpm at Maximum Power [102].	43
Figure 3.14. Some Examples of Ways to Reduce Leakage Flux by either Introducing Airspace	

Flux Barriers or by Using an Interpole Magnets [55].	47
Figure 3.15. Some Examples of Ways to Increase the Saliency Ratio [55].	48
Figure 4.1. Cross Section of a High Torque Density PM Machine with Two Rotors [118].	54
Figure 4.2. Parts of a High Torque Density PM Machine with Two Rotors [118].	54
Figure 4.3. TFM Geometry With Flux Concentrated Magnets [120, 121].	56
Figure 4.4. The New Split Tooth PM Machine Structure.	57
Figure 4.5. Optimised 12 Slots/ 4 Poles Brushless PM Machine Using Motor Solve.	59
Figure 4.6. Optimised 12 Slots/ 10 Poles Brushless PM Machine Using Motor Solve.	59
Figure 4.7. FE Cross Section of the Split Tooth PM Machine with 6 Slots and 20 Poles.	60
Figure 4.8. Magnet Required for Each Split Tooth	60
Figure 4.9. Mesh Distribution in a FE Cross Section of the Split Tooth PM Machine with 6 Teeth and 20 Poles.	62
Figure 4.10. The Split Tooth Machine Considering a Frame Size of 200mm.	63
Figure 4.11. Winding Arrangement for the Split Tooth PM Machine.	63
Figure 4.12. No Load Contour Flux Lines Plot of the Split Tooth PM Machine with 6 Teeth and 20 Poles of Surface Mounted PMs.	64
Figure 4.13. No Load Flux Linkage of the Split Tooth PM Machine Over One Full Electrical Cycle.	65
Figure 4.14. Static Simulation Coil Arrangements.	66
Figure 4.15. Shaded Flux Linkage Plots for the 4 Most Appropriate Split Tooth Shapes.	66
Figure 4.16. Static Torques Over a Range of Current Densities of the 4 Most Appropriate Split Tooth Shapes.	67
Figure 4.17. Static Torques Over a Range of Current Densities of Both the Split Tooth PM Machine and the Brushless PM Machine.	68
Figure 5.1. Double Stator and Single Rotor Machines (a) Dual Ring Type (b) Single Ring Type [129].	72
Figure 5.2. The New Modified Split Tooth PM Machine Structure.	73
Figure 5.3. a) STPM Machine With Surface Mounted Magnets b) STPM Machine With Interior V Shaped Magnets.	73
Figure 5.4. FE Cross Section of the Modified Flux Concentrated Split Tooth PM Machine with 6 Teeth and 20 Poles.	74
Figure 5.5. Stator Dimensions of the New Modified Flux Concentrated Split Tooth PM Machine.	75
Figure 5.6. Rotor and Magnet Dimensions of the New Modified Flux Concentrated Split Tooth PM Machine.	75
Figure 5.7. Inner Stator Dimensions of the New Modified Flux Concentrated Split Tooth PM Machine.	76
Figure 5.8. Rotor Lamination with Bridge Pieces Around the Inner and Outer Radii of One	

Magnet.	76
Figure 5.9. No Load Contour Flux Lines Plot of the Modified Split Tooth PM Machine with 6 Teeth and 20 Poles of Flux Concentrated Magnets.	77
Figure 5.10. No Load Flux Linkage of the Modified Split Tooth PM Machine Over One Full Electrical Cycle.	78
Figure 5.11. Peak Flux Linkage Comparison Between Both the Initial and Modified STPM Machines.	78
Figure 5.12. Static Torques Over a Range of Current Densities of the Initial and Modified Split Tooth PM Machine.	79
Figure 5.13. The Torque in Both Air Gaps of The Modified STPM Machine.	79
Figure 5.14. Geometries of Both STPM Machines.	84
Figure 6.1. Flux Contour Plot Lines Obtained from No-Load 2D FE Simulation for the Two Designs.	90
Figure 6.2. Dimensions of the 12 slots/ 40 Poles First Design	90
Figure 6.3. Line Back EMF for 6 Slots/ 20 Poles and 12 Slots/ 40 Poles STPM Machines with Concentrated Magnets.	92
Figure 6.4. Harmonic Spectrum for 6 Slots / 20 Poles and 12 Slots/ 40 Poles STPM Machine with Concentrated Magnets.	92
Figure 6.5. Cogging Torques for 6 Slots / 20 Poles and 12 Slots/ 40 Poles STPM Machine with Concentrated Magnets.	93
Figure 6.6. Peak Torque Versus Current Density for the 6 Slots/ 20Poles and 12 Slots/ 40 Poles Split Tooth PM Machines with Concentrated Magnets.	94
Figure 6.7. Torque Waveform for 6 Slot / 20 Pole and 12 Slots/ 40 Poles Split Tooth PM Machines.	95
Figure 6.8. Outer Stator Dimensions of the STPM Machine.	98
Figure 6.9. Rotor and Magnet Dimensions of STPM Machine with Concentrated Magnets.	99
Figure 6.10. Inner Stator Dimensions of The STPM Machine.	100
Figure 7.1. Outer Stator Dimensions of the STPM Machine.	106
Figure 7.2. Torque Versus Current Density for Various Tooth Body Widths.	110
Figure 7.3. Torque Versus Current Density for Various Slot Depths.	110
Figure 7.4. Torque Density at 15 A/mm ² for Different Tooth Body Widths and Slot Depths.	111
Figure 7.5. Torque Versus Current Density for Various Core Back Depths.	113
Figure 7.6. Torque Density and Ripple Achieved at 15 A/mm ² at Various Coreback Depths.	113
Figure 7.7. Torque Versus Current Density for Varies Slot Opening Widths.	114
Figure 7.8. Torque Density and Torque Ripple at 15 A/mm ² Applied Current Density for Various Slot Opening Widths.	116
Figure 7.9. Torque Versus Current Density for Various Tooth Split Widths.	116
Figure 7.10. Torque Density and Ripple Achieved at 15 A/mm ² at Various Tooth Split Widths.	

	118
Figure 7.11. Torque Versus Current Density for Various Tooth Split Depths.	118
Figure 7.12. Torque Density and Ripple Achieved at 15 A/mm ² at Various Tooth Split Depths.	119
Figure 7.13. Split Tooth with and without Tooth Tip.	120
Figure 7.14. Torque Versus Current Density for Various Tooth Tip depths.	120
Figure 7.15. Torque Density and Ripple Achieved at 15 A/mm ² at Various Tooth Tip Depths.	122
Figure 7.16. Rotor and Magnet Dimensions of the STPM Machine with Concentrated Magnets.	122
Figure 7.17. A Cross Section of the Rotor of Different Magnet Heights.	123
Figure 7.18. Torque Versus Current Density for Various Magnet Heights.	124
Figure 7.19. Variation of Peak Flux Linkage of the STPM Machine with Changing Magnet Heights.	125
Figure 7.20. Torque Density and Ripple Achieved at 15 A/mm ² at Various Magnet Heights.	125
Figure 7.21. Torque to Magnet Mass Index at 15 A/mm ² Applied Current Density for Various Magnet Heights.	126
Figure 7.22. A Cross Section of the Rotor of Different Magnet Thickness.	127
Figure 7.23. Variation of Peak Flux Linkage of the STPM Machine with Changing Magnet Thickness.	127
Figure 7.24. Torque Versus Current Density for Various Magnet Thicknesses.	128
Figure 7.25. Torque Density and Ripple Achieved at 15 A/mm ² at Various Magnet Thickness.	128
Figure 7.26. Torque to Magnet Mass Index at 15 A/mm ² Applied Current Density for Various Magnet Thickness.	129
Figure 7.27. Inner Stator Dimensions of The New Split Teeth PM Machine.	130
Figure 7.28. Torque Versus Current Density for Various Inner Stator Tooth Widths.	130
Figure 7.29. Torque Density and Ripple Achieved at 15 A/mm ² at Various Inner Stator Tooth Width.	132
Figure 7.30. Torque Versus Current Density for Various Inner Stator Slot Depths.	132
Figure 7.31. Torque Density and Ripple Achieved at 15 A/mm ² at Various Inner Stator Slot Depths.	133
Figure 7.32. Torque Density Achieved by Various Inner Stator Core Back Depths.	134
Figure 7.33. Torque Density Achieved by Various Inner Stator Core Back Depths.	134
Figure 7.34. Flux Linkage Obtained with and without the Inner Stator	135
Figure 7.35. Torque Versus Current Density Obtained with and without the Inner Stator.	135
Figure 8.1. Torque against Current Density for the STPM Machines Resulting from Initial and Final Optimisation Processes	142

Figure 8.2. Final Optimised Stator.	142
Figure 8.3. Final Optimised Rotor.	143
Figure 8.4. Final Optimised Inner Stator.	143
Figure 8.5. Bridges Around the Inner and Outer Radii of the Magnets.	144
Figure 8.6. Torque Against Current Density for the STPM Machines Using Different Sleeves.	146
Figure 8.7. Electrical Degrees between the Slots of the STPM Machine.	147
Figure 8.8. Winding Arrangement in the Slots of the STPM Machine.	147
Figure 8.9. A Cross-Section View of the Coils Inside the Slots.	148
Figure 8.10. Current Ratings on a Torque Against MMF Plot for the Final STPM Machine.	149
Figure 8.11. Current Ratings on a Torque Against Current Density Plot for the Final STPM Machine.	150
Figure 8.12. Phasor Diagram for a Single Phase of the PM Machine in its Direct and Quadratic Axis Planes.	151
Figure 8.13. Torque vs Speed Curve Obtained by FE Calculations.	152
Figure 8.14. Direct and Quadratic Axis Currents Against Speed During Field Weakening.	153
Figure 8.15. Magnet Characterisation B-H Curve[140].	154
Figure 8.16. Flux Density Shaded Plot of the Magnet When a Current in the Direct Axis is Applied.	155
Figure 9.1. Stator Core Back Profiles.	158
Figure 9.2. Lamination Stacked and Bonded Methods.	158
Figure 9.3. Lamination Stack While Inside the Wire Cutting Machine.	159
Figure 9.4. Final Constructed Outer Stator Inside the Case.	159
Figure 9.5. Stator Lamination Stack with the Stator Coils, Slot Wedge, Slot Liner and Thermocouples.	160
Figure 9.6. Constructed Rotor Cross Section Drawing.	162
Figure 9.7. Flux Linkage Contour Plot Comparison between the STPM Machine with and without Pins of Steel.	163
Figure 9.8. Rotor Lamination Stack When Attached to the Rotating Back End Shaft by Steel Pins.	164
Figure 9.9. Magnet Axial Length.	165
Figure 9.10. Magnet Cross Section.	165
Figure 9.11. Rotor Lamination Stack Cross Section with Magnets Inserted.	166
Figure 9.12. Inner Stator Cross Section to Show Core Back Profiles.	167
Figure 9.13. Cross Section of the Inner Stator Laminations Stack with a TUFNOL and Bearing to Lock it.	167
Figure 9.14. Stationary Shaft Dimensions.	169

Figure 9.15. Final Constructed Stationary Shaft.	169
Figure 9.16. Rotating Front End Shaft Dimensions.	170
Figure 9.17. Final Constructed Rotating Front End Shaft.	170
Figure 9.18. Rotating Back End Shaft Dimensions.	171
Figure 9.19. Final Constructed Rotating Back End Shaft.	171
Figure 9.20. Side View of the Rotor Assembly.	172
Figure 9.21. Top View of the Rotor Assembly.	172
Figure 9.22. Front and Back Views of the Assembled Case.	174
Figure 9.23. Case Contents When Separated.	174
Figure 9.24. Case Contents Cross Section.	175
Figure 9.25. Final Case Assembly with the Final Winding Connection Box.	177
Figure 9.26. Top View of the Connections on the Socket Holder.	177
Figure 9.27. The Electric Circuit of the STPM Machine.	178
Figure 9.28. Static Torque Test Rig.	178
Figure 9.29. STPM Machine Connections to the Power Supply While Connected to The Static Torque Test Rig.	179
Figure 9.30. High Speed Test Rig.	180
Figure 9.31. Gear Box and Torque Transducer.	180
Figure 9.32. Overview of the High Speed Test Rig.	181
Figure 10.1. Surge Waveform During a Fault Between Two Turns.	185
Figure 10.2. Surge Waveform Obtained for a Healthy Coil.	185
Figure 10.3. Phase Arrangements in 2D FE.	187
Figure 10.4. Phase Arrangements in Practical	187
Figure 10.5. Three Phase Open Circuit.	188
Figure 10.6. Measured Line Back EMF at 4000 rpm.	188
Figure 10.7. Harmonic Spectrum of the Measured Line Back EMF at 4000 rpm.	189
Figure 10.8. Measured and Calculated Line Back EMF verses Speed.	189
Figure 10.9. Measured and Calculated Line Back EMF Verses Speed.	190
Figure 10.10. Iron Loss at Different Temperatures and a Range of Speed.	191
Figure 10.11. Magnet Loss at Different Temperatures and a Range of Speed.	191
Figure 10.12. Predicted No Load Losses Versus Speed.	191
Figure 10.13. Phase Connections During the Static Torque Test.	192
Figure 10.14. Measured and Calculated Torque Verses Rotor Angle.	193
Figure 10.15. Measured and Calculated Torque Verses Applied Current.	194
Figure 10.16. Measured and Calculated Torque Verses Applied Current.	195

Figure 10.17. Measured Efficiency Against Armature Current Generated.	196
Figure 10.18. Measured Efficiency Against Output Load Generated.	196
Figure 10.19. Thermal Test Bench.	197
Figure 10.20. Temperature Rise with Time at 100Amps	198
Figure 11.1. Geometries of Both STPM Machines	206
Figure 11.2. Introduction of Flux Barriers.	211
Figure A3. Iron Circuit with Magnet.	226
Figure A4. Magnet Operating Point.	227
Figure A5. Pitch Angle (α) and Phasor Diagram of a Short Pitched Coil of Two Sides.	229
Figure A6. Distribution Angle (β) Between Two Coils of the Same Phase.	229
Figure A7. Flow Diagram Representation for the VB Script.	234
Figure A8. Torque Waveforms at 15 A/mm ² Applied Current Density for Various Coreback Depths.	235
Figure A9. Torque Waveforms at 15 A/mm ² Applied Current Density for Various Slot Opening Widths.	236
Figure A10. Torque Waveforms at 15 A/mm ² Applied Current Density for Various Tooth Split Widths.	237
Figure A11. Torque Waveforms at 10 A/mm ² Applied Current Density for Various Tooth Split Depths.	237
Figure A12. Torque Ripple at 15 A/mm ² Applied Current Density for Various Tooth Tip Depths.	238
Figure A13. Torque Ripple at 10 A/mm ² Applied Current Density for Various Magnet Height.	239
Figure A14. Torque Ripple at 15 A/mm ² Applied Current Density for Various Magnet Thickness.	239
Figure A15. Torque Ripple at 15 A/mm ² Applied Current Density for Various Inner Stator Tooth Widths.	240
Figure A16. Flux Linkage Comparison Between the STPM Machine with Inner Stator and Without the Inner Stator.	241

List of Tables

Table 2.1. Energy Density Comparison of Different Materials.	15
Table 3.1. Drives Used by Different Manufactures Until Present [18, 24].	27
Table 3.2. Parameter Comparison of PM Machine, SRM and IM [101, 102].	42
Table 4.1. Fixed Dimensions and Specifications for Both Brushless PM Machine and Split Tooth PM Machine.	58
Table 4.2. Comparison between the STPM Machine and the Brushless PM Machine.	69
Table 5.1. The Important Features of All Four Machines.	81
Table 5.2. Comparison between All Three Machines.	83
Table 6.1. STPM Machine Different Slot to Pole Combinations.	88
Table 6.2 Cogging Torque Frequency for Different Slot/Pole Combinations.	93
Table 6.3. A Comparison between 6 Slots/ 20 Poles and a 12 Slots/ 40 Poles STPM Machines.	96
Table 6.4. The Range of Fixed and Variable Parameters.	97
Table 6.5. Outer Stator Dimensions Descriptions and Symbols.	99
Table 6.6. Rotor and Magnet Dimensions Descriptions and Symbols.	99
Table 6.7. Inner Stator Dimensions Descriptions and Symbols.	100
Table 7.1. Outer Stator Dimensions Description.	107
Table 7.2. No Load Shaded Flux Density Distribution of Various Tooth Body Widths.	108
Table 7.3. No Load Shaded Flux Density Distribution of Various Slot Depths.	109
Table 7.4. No Load Shaded Flux Density Distribution of Various Coreback Depths.	112
Table 7.5. No Load Shaded Flux Density Distribution of Various Slot Opening Widths.	115
Table 7.6. No Load Shaded Flux Density Distribution of Various Tooth Split Widths.	117
Table 7.7. No Load Shaded Flux Density Distribution of Various Tooth Split Depths.	119
Table 7.8. No Load Shaded Flux Density Distribution of Various Tooth Tip Depths.	121
Table 7.9. Rotor and Magnet Dimensions Description.	123
Table 7.10. Inner Stator Dimensions Description and Definition.	130
Table 7.11. No Load Shaded Flux Density Distribution of Various Inner Stator Tooth Widths.	131
Table 7.12. No Load Shaded Flux Density Distribution of Various Inner Stator Slot Depths.	133
Table 7.13. Final Investigated STPM Machine Dimensions' Symbol, Descriptions and Values.	137
Table 8.1. Initially Optimised and OptiNet Optimised STPM Machine Dimensions	141
Table 8.2. Properties of Sleeve Types under Consideration.	144

Table 8.3. Sleeve Thickness and Flux Linkage of Various materials	146
Table 8.4. Angle and Reactance of Field Weakening.	152
Table 9.1. Description of Each of the Case Contents.	175
Table 10.1. Maximum and Minimum Measured Inductance.	187
Table 10.2. Comparison between the STPM Machine, Camry and Prius Motors	199
Table 10.3. Cost Comparison Between the STPM Machine, Camry and Prius Motors	201
Table 11.1. Comparison between All Machines.	205
Table A2. Air Gap Flux Density at Different Magnet Locations.	225
Table A3. Torque, Mass and Torque Density for Various Tooth Body Widths and Slot Depths at 15 A/mm ²	235
Table A4. Torque, Mass, Torque Density and Torque Ripple for Various Coreback Depths at 15 A/mm ² .	236
Table A5. Torque, Mass, Torque Density and Torque Ripple for Various Slot Opening Widths at 15 A/mm ² .	236
Table A6. Torque, Mass, Torque Density and Torque Ripple for Various Tooth Split Widths at 15 A/mm ² .	237
Table A7. Torque, Mass, Torque Density and Torque Ripple for Various Tooth Split Depths at 15 A/mm ² .	238
Table A8. Torque, Mass, Torque Density and Torque Ripple for Various Tooth Tip Depths at 15 A/mm ² .	238
Table A9. Torque, Mass, Torque Density and Torque Ripple for Various Magnet	239
Table A10. Torque, Mass, Torque Density and Torque Ripple for Various Magnet Thicknesses.	240
Table A11. Torque, Mass, Torque Density and Torque Ripple for Various Inner Stator Tooth Widths.	240
Table A12. Torque, Mass, Torque Density and Torque Ripple for Various Coreback Depths.	241
Table A13. Torque, Mass, Torque Density Obtained with and without the Inner Stator.	241

Acronyms and symbol

EV	Electric vehicle
PM	Permanent magnet
CAD	Computer-aided-design
MATLAB	Matrix laboratory
FE	Finite element
MMF	Magnetmotive force
kw	Kilowatts
D	Dimensional
ICEVs	Internal combustion engine vehicles
ICE	Internal combustion engine
HEV	Hybrid electric vehicle
PHEV	Plug-in hybrid electric vehicle
FCEV	Fuel cell electric vehicle
ISG	Integrated stator/generator
EMF	Electromotive force
IM	Induction machine
SRM	Switch reluctance machine
SUV	Suburban utility vehicle
RFM	Radial flux machine
AFM	Axial flux machine
TFM	Transverse flux machine
DSPMM	Doubly salient permanent magnet machine
FRPMM	Flux-reversal PM machine
FSPMM	Flux switching PM machine
STPM	Split Tooth PM
SPP	Slot per pole per phase
NEDC	New european driving cycle
rpm	Revolutions per minutes
F_a	Acceleration force
k_m	Compensating factor
m_v	Vehicle Mass
v_T	Vehicle velocity
F_{TR}	Traction force

F_{RL}	Road forces
F_{AD}	Aerodynamic drag force
ρ	Air density in kg/m^3
v_0	Wind's velocity
C_D	Vehicle's drag coefficient (between 0.2 and 0.4)
A	Front area of a vehicle
T_{motor}	Electric motor torque
T	Torque
B	Flux density
l	Conductor length
i	Current carried by a conductor
p	Pole pair number
ψ_m	Flux linkage due to permanent magnets
$I_q,$	Currents in the direct axis
I_d	Currents in the quadrature axis
$L_q,$	Inductances in the direct axis
L_d	Inductances in the quadrature axis
$B_{g\text{max}}$	Magnet loading
B_o	Magnet residual flux density
B_g	Air gap flux density
A	Electric loading
S	Number of slots
N	Number of turns
I	RMS current
D	Centre of air gap diameter
l_m	Magnet length
A_m	Magnet cross sectional area
l_g	Air gap length
A_g	Air gap cross sectional area
$H_m,$	Iron magnetic field strength
$H_g,$	Air magnetic field strength
μ_o	Permeability of free space
B_m	Magnet flux density
μ_m	Permeability of the magnet
$V_1,$	Voltage generated in the first side of a coil

V_2	Voltage generated in the second side of a coil
V_c	Voltage resulted in a coil
α	Pitch angle
β	Distributed angle
m	Harmonic number
f	Supply frequency
N_s	Synchronous speed
SN	Number of slots
PN	Number of phases
TN	Number of teeth
$B_{g \text{ fundamental}}$	Fundamental air gap flux density
α_m	Magnet span
w_{pitch}	Total Pitch that a tooth and slot can fit into
D_r	Outer Diameter of the Rotor
w_t	Tooth width
B_{iron}	Stator iron flux density
w_s	Slot width
d_s	Slot depth
A_s	Slot area
ff	Fill factor
d_{scb}	Core back depth

Chapter 1. Introduction

1.1 Background

Atmospheric carbon dioxide has doubled its levels since pre-industrial times and in order to stabilise it, a serious emission reduction is required globally by all industrial sectors. The electricity sector has played a huge part in this, so its contribution to emission reductions is essential. Electric motors account for a large proportion of electricity consumption [1-3]. The increased use of electric drives in our everyday lives has driven a challenge to produce more economical drives. The incentives of more economical and environmental imperatives have encouraged industries and researchers around the globe to develop better electric drives by introducing different types and contributing new ideas in order to build premium efficiency level motors for cost savings that match the up to date global standards and regulations [3-7]. High efficiency machines play a strong role in saving energy and lower energy consumption decreases operation costs and increases environmental sustainability of drive systems [8, 9]. Designing an energy efficient motor requires consideration of many variables such as performance, frequency, voltage, test methods and costs [10]. Efficiency gains can be increased through the development of different machine constructions and new materials, and considerations must be taken into account to supply machines at their rated voltage [11, 12]. Hence this project explores ways of designing a high performance electric motor which can be used in automotive applications, specifically for electric vehicles (EVs), while overcoming most of the challenges faced by the motor design industries. The search for energy efficient and environmentally friendly vehicles has increased interests worldwide over the past two decades as EVs offer sustainable personal mobility, especially if renewable energy is used [13].

1.2 The Research

This project was carried out within the Power Electronics, Drives & Machines Group at Newcastle University. It explores a novel machine topology to achieve high torque output over a given speed, specifically for automotive applications. The novel machine topology has been designed for torque dense applications such as average passenger EVs, sports cars, industrial vehicles, motorcycles and marine applications. The resulting

machine is designed to be used either as a direct drive traction motor, or coupled to a gearbox (e.g. for transmission) for multiplications, and hence the importance of a more energy efficient and environmentally friendly vehicle [14]. The research is carried out on different machine topologies, and development of these will aim to produce a machine with more torque output. The research will concentrate on permanent magnet (PM) machines that could be implemented in a range of electric, or hybrid electric vehicles, with an emphasis on:

- High power and torque density
- Minimal volume
- Wide speed range
- High starting torque
- High efficiency
- Low noise
- Acceptable cost
- Good voltage regulation
- Relatively low rotor temperatures
- Increased energy efficiency

1.3 Contribution to Knowledge

The work carried out in this thesis has provided new insight into the following:

- A greater torque per unit volume was achieved from a new permanent magnet machine with surface mounted magnets. This machine involved the splitting of the stator teeth in order to introduce a magnetic gear ratio into the torque equation.
- A modified design of the new machine using concentrated magnets and two stators was also designed, optimised, constructed and evaluated.
- An optimisation method was applied using a parameterised model to achieve the maximum torque output for a fixed current density. This method optimises every vertex of the machine to provide the best possible dimensions to give accurate results
- An improved magnet utilisation has been proven using an inner stator to redirect leakage flux to link the coil.

- An improved mechanical structure for the flux concentrated magnet topology was achieved and discussed.
- An improved shaft design for conventional rotors that rotate in between two stators was achieved and discussed.
- An improved fill factor for hand winding was achieved by compressing the coils using a slot shaped tool before placing the coil inside the slot.

1.4 Published Material

1. Alamoudi, Y.A., Atkinson, G. J., Mecrow., “Torque density permanent magnet machine for automotive applications”, ICEM, XXIth International Conference on Electrical Machines, Berlin, Germany, 2-5 September, 2014.
2. Alamoudi, Y.A., Atkinson, G. J., Mecrow., “Torque density permanent magnet machine for automotive applications”, IET, International PEMD on Power Electronics, Machines and Drives, Manchester, UK, April, 2014.
3. Alamoudi, Y.A., Atkinson, G. J., Mecrow., “New high torque density permanent Magnet Machines”, IEEE, IECON 2012, 25-28 October 2012, Montreal, Canada.
4. Alamoudi, Y.A., Atkinson, G. J., Mecrow., “A new design concept for high torque permanent magnet machines”, IET, EFEA 2012, The 2nd International Symposium on Environment-Friendly Energies and Applications, Newcastle upon Tyne, UK, June, 2012.
5. Alamoudi, Y.A., Atkinson, G. J., Mecrow., “High torque density permanent magnet machine for automotive applications”, IET, International PEMD on Power Electronics, Machines and Drives, Bristol, UK, March, 2012.

1.5 Objectives and Overview of this Thesis

This thesis explores the design of a new PM machine topology for automotive application, specifically for EVs, and consists of eleven chapters ranging from a review of existing machines and EVs to the new machine’s construction and test results and finishing with the study conclusion. The thesis starts with an introduction to the research and ends with an appendix. The following gives an outline of each chapter:

- **Chapter 1:** This chapter gives an introduction to the thesis, provides a

background to electrical machines, describes some of the more important points in the research field of electrical machine design, emphasises the importance of this research, also the work published during the research, and the presents study's objectives and gives an overview of this thesis.

- **Chapter 2:** A literature review on various types of electric vehicles is provided in this chapter describing the background and various types of electric vehicles and how their use affects the environment. Also the challenges faced in the development of EVs are highlighted here.
- **Chapter 3:** Different types of electrical machines used in electric vehicles are described along with their advantages and disadvantages. Different rotor and stator topologies in PM machines are discussed for the purpose of designing a novel PM machine topology. Performance comparison between different machines using FE analysis is also reviewed here.
- **Chapter 4:** This chapter describes a novel PM machine design using theoretical and mathematical explanations. The proposed machine is also designed, analysed and evaluated using Two-Dimensional (2D) Finite Element (FE) simulations, and it is then compared to a typical convectional brushless PM machine of the same dimensions in regard to their torque densities.
- **Chapter 5:** A modified design of the new permanent magnet machine shown in chapter 4 is proposed here, which was designed using 2D FE and compared to the pre modified design
- **Chapter 6:** A performance comparison of different slot to pole combinations in the new design topology is given in this chapter. The comparison is carried out by using 2D FE simulations to design and analyse different slot to pole combinations in order to find the optimum combination. Two optimisation methods are described and used to improve the performance of the machine with the chosen combination. The fixed and variable parameters used during the optimisation are also shown here.
- **Chapter 7:** In this chapter, investigations are carried out on the impact of varying the dimensions on torque density using the first optimisation method. This is accomplished in order to find the initial optimum design manually, including the dimensions of the outer stator, inner stator and rotor. The impact of the presence of the inner stator is also observed here.
- **Chapter 8:** The manual optimisation is compared here to the OptiNet

optimisation and the final design is then defined. In addition, the method used to determine the mechanical strength of the rotor is explained, and further investigations on the final design are also assessed here.

- **Chapter 9:** The process of building the novel PM machine prototype is described in this chapter along with the assembly process, which includes the case, windings, shaft and bearings.
- **Chapter 10:** In this chapter an account is given of the test rigs used and the performance results for the novel PM machine prototype. The results are also compared to existing commercially available machines.
- **Chapter 11:** A summary of the research is provided in this chapter along with the conclusions. Possible future research is then discussed.

Chapter 2. An Overview of Electric Vehicles

This chapter discusses the recent increased interest in the replacement of Internal Combustion Engine Vehicles (ICEVs) with in Electric Vehicles (EVs). An overview of current EVs is also provided, examining different types and their effect on the environment. The challenges facing the design and production of EV are then described. This thesis presents research conducted on the design of a motor for EV applications, and hence, the challenges and performance requirements associated with the design of EV motors are detailed.

2.1 Introduction

The concept of EVs is not new. They were first conceived alongside the Internal Combustion Engine (ICE) in the 19th century and were considered a contender to the ICE for some years. And although petrol has a greater energy density than an electrochemical battery, EVs continued to be favored during the late 1800s and early 1900s, especially in urban areas. This was due to their advantages such as a self-starting capability and no requirement for changing gears, which was a most troublesome problem with ICEVs. Furthermore, EVs do not suffer from the noise, vibration and smell associated with ICEVs.

Interest in EVs started to decline by the 1920s due to their limited range thanks to limited battery capability, inferior performance and greater cost, especially after the building of better road systems that linked different cities and which required longer range vehicles. Also, around the same time, cheap petrol became available and an electric starter motor was invented for ICEs which was energy efficient and nonpolluting. Since then, interest focused on ICEs and how to improve their design and make them more efficient, and ICEs subsequently gained in popularity across the world. EVs in the other hand were mainly employed for low speed vehicles for short-range use, such as golf carts.

Interest in EVs never faded completely, and further enthusiasm for EVs was shown whenever specific problems arose with ICEs regarding their operation, especially when concerns over air quality arose in the early 1960s and during the energy crisis in the 1970s. Since then EVs have attracted stronger interest, especially after the turn of the century, for the following main reasons [15, 16]:

- The latest rounds of environmental awareness and energy concerns, as ICEVs have been found to be the main source of urban pollution according to figures released in the U.S. [17, 18].
- The need to reduce dependency on imported foreign crude oil.
- The improvement in motor design and the power electronics associated with EVs.
- The advances in lithium-ion batteries
- The use of regenerative braking rather than friction braking as in ICEVs.

- Although EVs are more expensive than ICEVs, their running costs are very low in comparison.

After years of interest and research in EVs, various different topologies have been invented. For example, Hybrid Electric Vehicles (HEVs) have been very popular recently due to their unique ultralow emissions, high fuel economy, affordable prices and levels of driving performance similar to ICEVs. The Toyota Prius was the first model to implement this technology in 1997 [19, 20].

2.2 Electric Vehicles

The various topologies of EV are described below.

2.2.1 Hybrid Electric Vehicles

This type of vehicle combines an electric motor and an ICE. These are combined in such a way as to gain the most desirable benefits from both at different times in the driving cycle, which has been found to save energy and minimise pollution when compared to ICEVs. This is because the ICE in this system uses the Atkinson cycle, which was invented by James Atkinson, and an example of the behavior of the four strokes of the ICE in this cycle for one position is shown in Figure 2.1. The first stroke is the intake stroke, when the fuel and air mixture is pulled in to the cylinder using the intake valve. This is followed by a compression stroke which differs in the Atkinson cycle when compared to the conventional Otto cycle that is widely used by ICEVs. In this compression stroke, the intake valve does not close until the piston starts to rise up to a specific ratio in the Atkinson cycle. Due to this, some of the air and fuel returns to the intake, unlike in the Otto cycle where the valve closes when the piston reaches the bottom of the piston and hence more fuel is used.

For clarity, it is possible to say that the compression ratio in a normal cycle for a volume of 1.2L inside the piston as seen in Figure 2.1 is 12:1 when the piston is at the bottom of the piston. However, because the intake does not close until the piston starts to rise in the Atkinson cycle, this ratio is reduced to 10:1 in this example.

The third stroke is the power stroke and this is when the piston moves up and

compresses the mixture of air and fuel to 0.1L before combustion takes place. After the power stroke, the piston is pushed to the bottom of the cylinder leaving a volume of 1.2L of exhaust. This results in the exhaustion ratio being more than the compression ratio ($10:1 < 12:1$).

A comparison of the Otto and Atkinson cycles can be seen in Figure 2.2, where the compression strokes in both cycles involve the same amount of pressure ($P_{1O} = P_{1A}$). However, the Atkinson cycle has less volume ($V_{1O} > V_{1A}$), and hence less fuel. In addition, the Atkinson cycle has less pressure inside the cylinder during the power stroke ($P_{2O} > P_{2A}$) and less pressure during the exhaust stroke ($P_{3O} > P_{3A}$). Hence it can be concluded that the Atkinson cycle is more efficient. However, it gives less power and torque, which can be compensated for by using an electric motor as in HEVs.

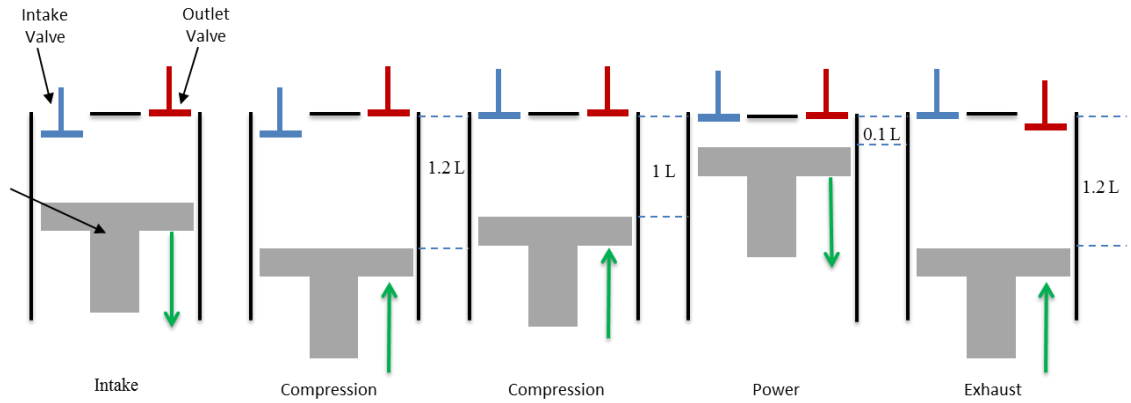


Figure 2.1. Four Strokes of the Atkinson Cycle.

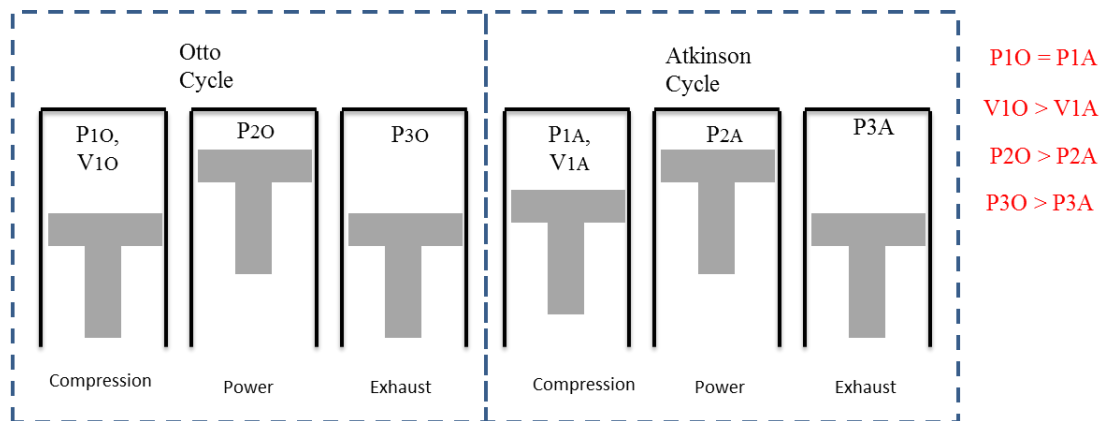


Figure 2.2. Comparison of the Otto and Atkinson Cycles.

Figure 2.3 shows a HEV from BMW (model i8).

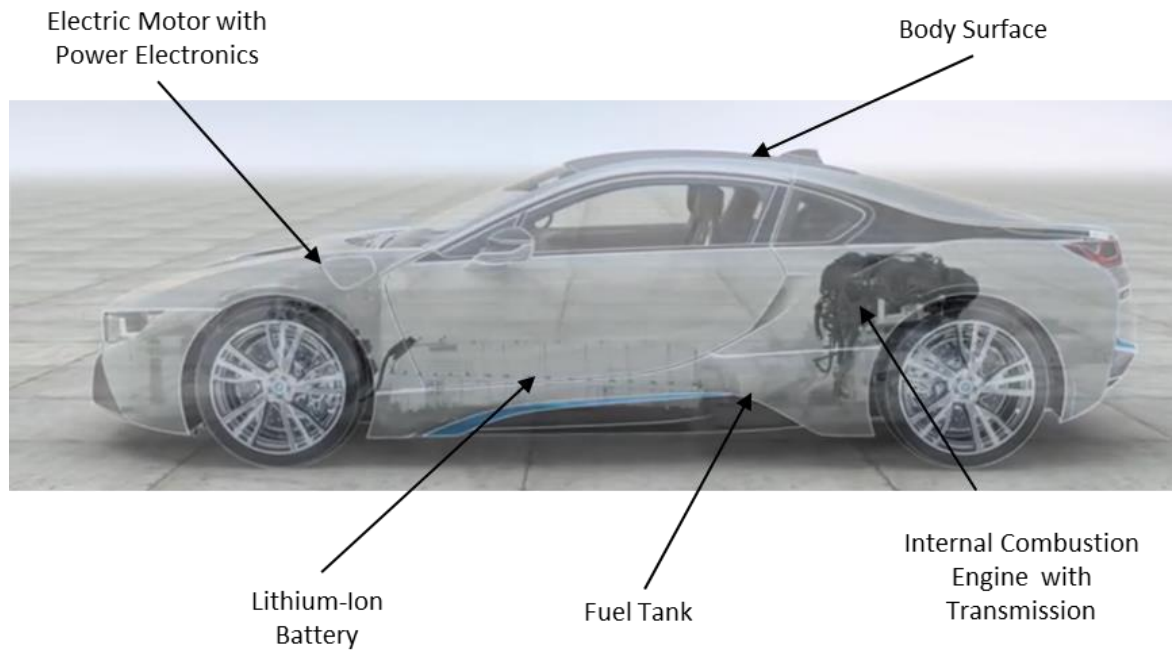


Figure 2.3. Series Hybrid EV [21].

The fuel economy in terms of Miles Per Gallon (MPG) achieved by HEV using petrol or diesel for both city and highway travelling are shown and compared with that of ICEVs in Figure 2.4 [22].

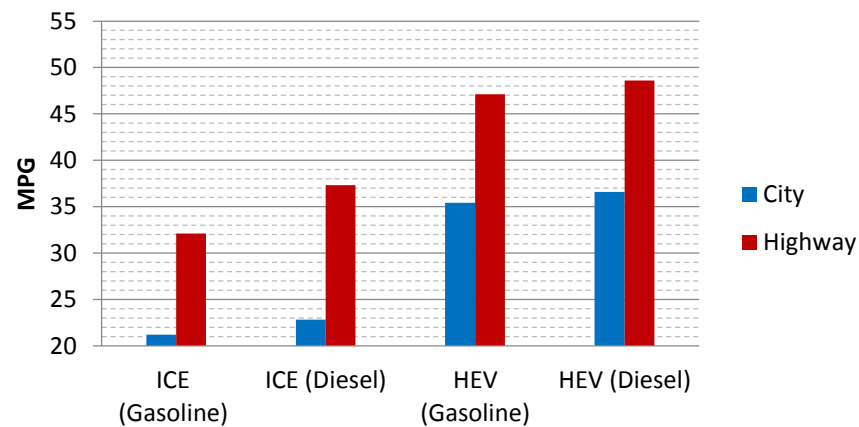


Figure 2.4. MPG Comparison for Different Types of Vehicles [22].

It can be seen from the figure above that HEVs achieve higher fuel economy than ICEVs both in cities and highways.

The sources of power can be connected using different topologies, and therefore, HEVs can be classified as series hybrids and parallel hybrids. However, given the increase in their variety and complexity, HEVs have been further classified as series-parallel hybrids and even complex hybrids [1]. Hybrids have also been categorised as micro-

hybrids, mild hybrids and full hybrids, depending on their operating features and power levels [18, 19, 23].

A. *Series Hybrid Electric Vehicles*

Here an ICE drives a generator which charges the battery, and this in turn powers an electric motor which is directly connected to the wheels. Power can also be supplied directly to the motor through the ICE coupled to the generator. These types of vehicles usually require an inverter in order to charge the battery and drive the electric motor. Figure 2.5 illustrates the arrangement where the ICE is coupled to an alternator, which is connected to a converter to charge the battery and then to the motor controller and inverter in order to drive the electric motor. The motor is then connected directly to the wheels through transmissions and differentials [21, 23].

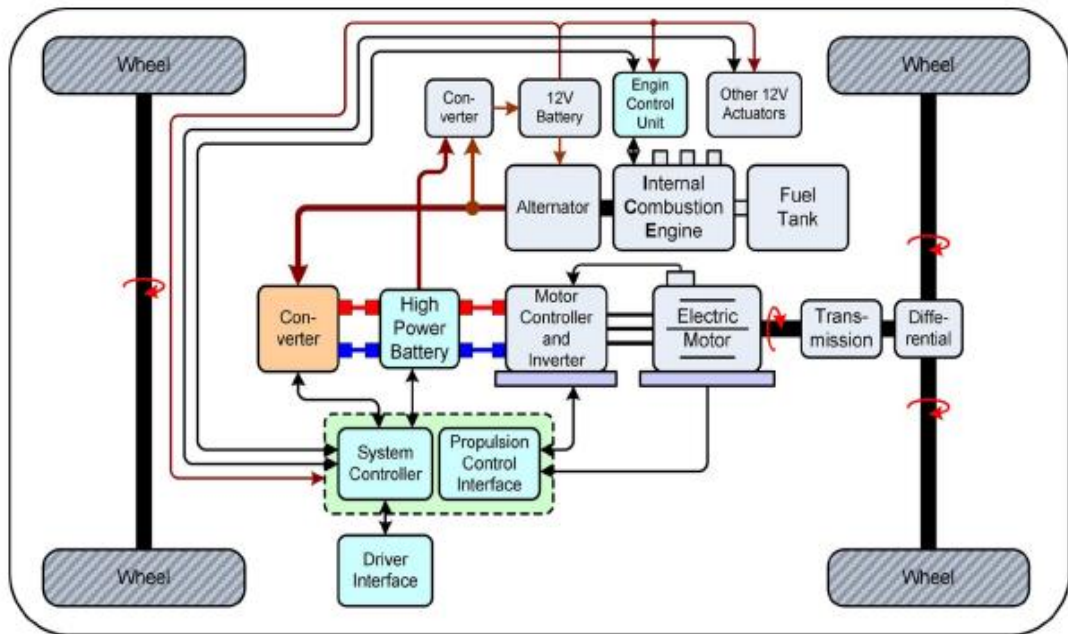


Figure 2.5. Series Hybrid EV [21].

B. *Parallel Hybrid Electric Vehicles*

In this case, the ICE and the electric motor are both coupled directly to the wheels, where they provide mechanical power to drive the vehicle. The electric machine can also act as a generator to charge the battery. This system can offer cheap operating capability but it needs a more complex control system [21, 24]. Figure 2.6 shows this arrangement.

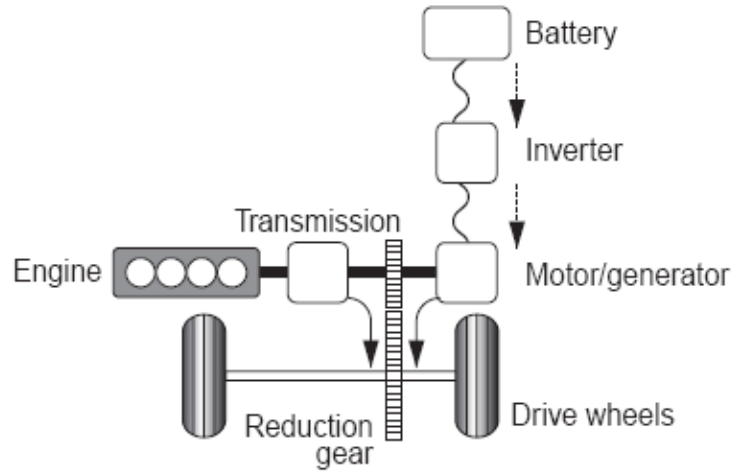


Figure 2.6. Parallel Hybrid EV [23].

C. Series/Parallel Hybrid Electric Vehicles

The series/parallel hybrid system combines the advantages of both the series and the parallel hybrid. It has the ability to switch between ICE and the electric motor to drive the wheels depending on the operating conditions in order to maximize efficiency [25]. Figure 2.7 shows the configuration of the system.

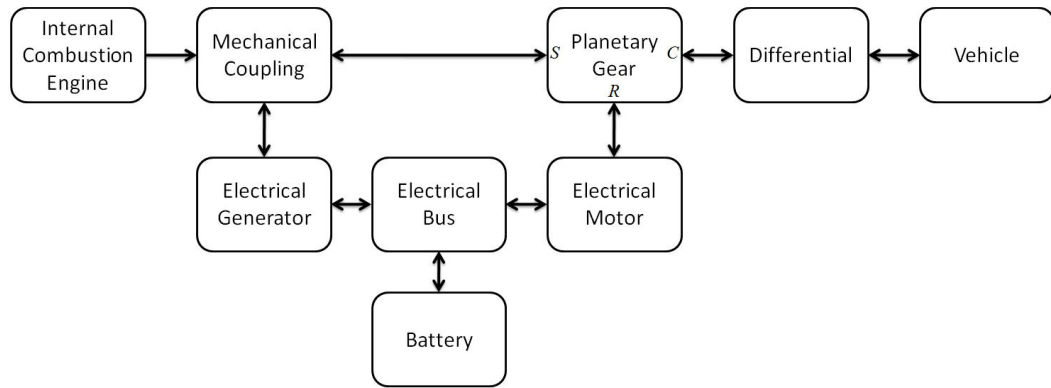


Figure 2.7. Series/Parallel Hybrid EV[25].

D. Plug-In Hybrid Electric Vehicles

Industrial, academic and government agencies consider plug-in HEVs (PHEVs) to be the most advanced form of HEV [26-29]. PHEVs use an external plug in order to charge the battery. This can be done overnight while the vehicle is in a garage. The batteries used in these vehicles store energy at high density when compared to the batteries used in regular HEVs. This allows PHEVs to run on electric power for longer [22, 30-33]. Figure 2.8 shows the configuration of parallel PHEVs.

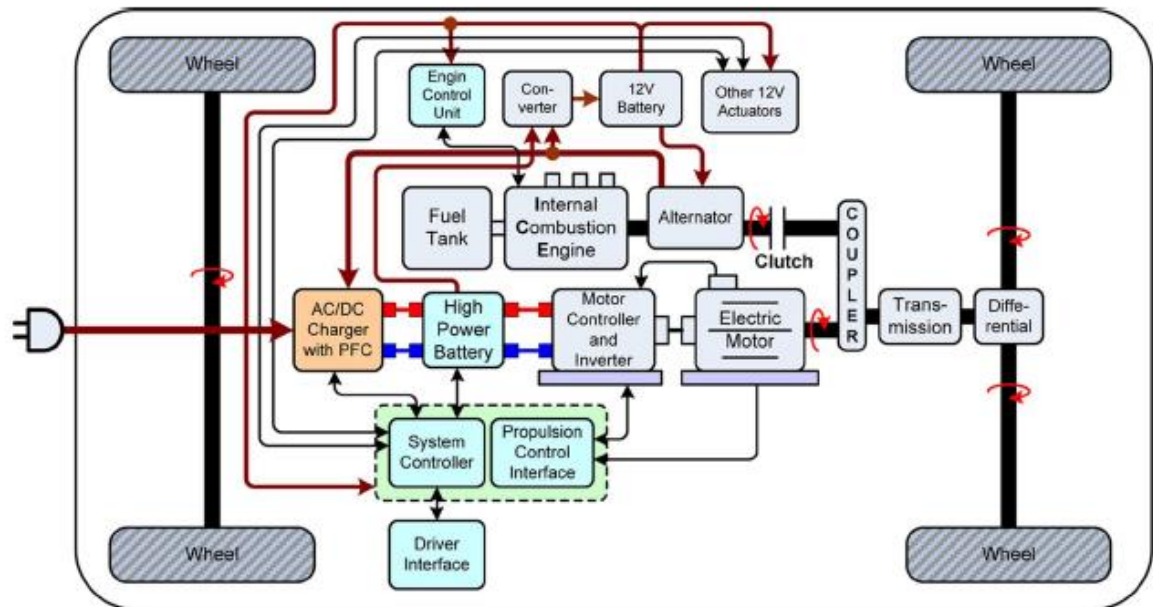


Figure 2.8. Plug-In Parallel HEV Configuration [21].

E. Crankshaft Mounted Integrated Starter/Generator (ISG) System-Based Hybrid Vehicles (Mild Hybrid)

The vehicle in this system has the architecture of a parallel hybrid, in which the torque to the drive wheels can be provided by either the electric motor or the ICE separately or even by both at the same time. This is done here in such a way as to boost the ICE off when it is less efficient in situations such as starting, stopping, hill climbing and overtaking. The configuration of this system is as shown in Figure 2.9.

Many companies are working on the development of these systems due to the fact they have many advantages. These include that they can start the engine in 200ms, and allow an automatic stop/start capability for the engine whenever the car is stationary with a high restart response from the throttle pedal. They also provide high torque that can be provided by the electric motor during acceleration and they have the ability for the electric motor to regenerate power to recharge the battery during braking [34-36].

There is also a side-mounted ISG system. This system uses a conventional generator that can also operate as a motor and provide torque to the drive wheels via a belt [21].

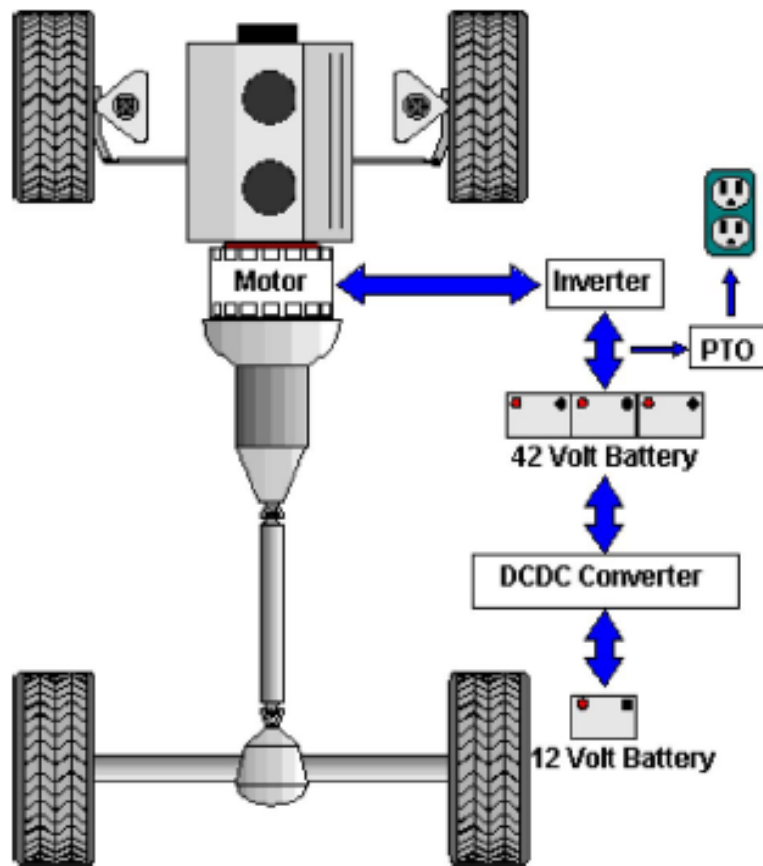


Figure 2.9. Crankshaft Mounted ISG System Based Hybrid Vehicles [21].

2.2.2 Pure Electric Vehicles

Pure EVs use one source of energy and are now becoming more prevalent. Companies such as Nissan, BMW and Tesla have commercially available systems. The Tesla has the best driving performance for a pure EV, achieving 0-60 mph in 3.2 seconds and a drive range of up to 312 miles [37]. Figure 2.10 shows the configuration of this system and Figure 2.11 shows a Pure EV that is made by Tesla (model X).

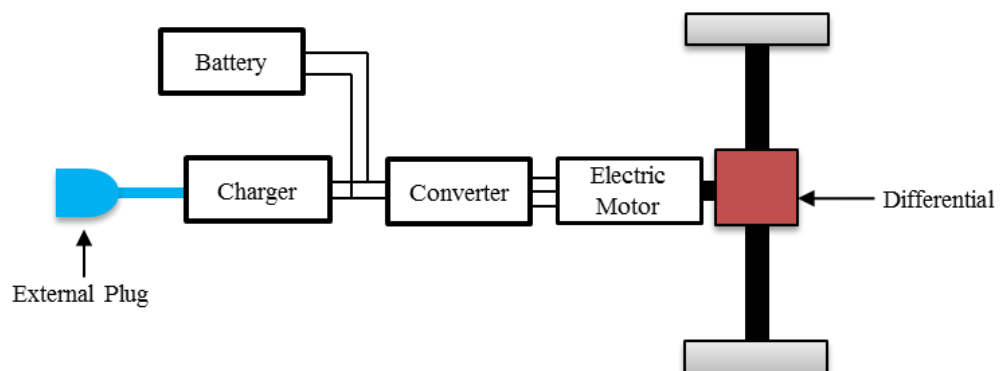


Figure 2.10. Pure EV System [32].

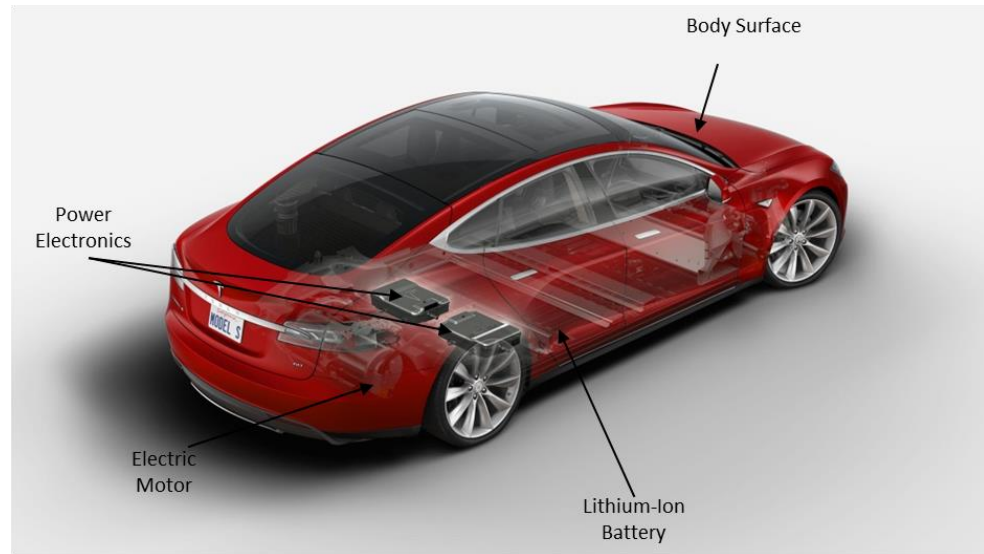


Figure 2.11. Pure EV Made by Tesla (model X) [32].

The pure EV operates at zero emission after it has been charged. However, there could be an indirect contribution to emissions with these pure EVs, which depends on the electricity source used to charge the battery. In addition, this can also be a zero emission source if renewable energy is used [38].

2.3 Challenges Facing the Design of EVs

The main challenges that face electric vehicles are as follows [14, 39-42]:

- Battery capability, size, lifetime and cost: Table 2.1 illustrates the low energy density of different batteries compared to that of fuel and hydrogen. Hence, in order for the battery to have a comparable level of energy storage to that of liquid fuels, the ratio of battery storage mass to full vehicle mass will be increased [43].

Table 2.1. Energy Density Comparison of Different Materials.

Type	Energy Density (MJ/Kg)
Lithium-Ion Battery	0.8
Nickel-Metal hydride Battery	0.288
Lead-Acid Battery	0.17
Hydrogen	60
Diesel	48
Gasoline	44.4

- EV charging stations: The limited driving range per charge for pure electric vehicles needs to be improved, especially considering the long charging time associated with them. Although Tesla motors has started to build new supercharge stations that are capable of delivering 120kW and are able to charge a battery up to half full in 20 minutes, this is still considered to be too long. Also it is only available for one of Tesla's models and only a limited number of these stations are available
- Performance (torque density and efficiency), size and cost of the electric motor used to drive the vehicle.
- The complexity of the power electronics associated with controlling the electric motor, especially with an in-wheel drive.
- The cooling system: the battery and power electronics operate at temperatures of 70-75°C, and hence it is essential to ensure an operating temperature within that range.
- Software: An electric vehicle comes with the challenge of designing appropriate communicational software between different parts of its system [44].

2.4 Electric Machines for Electric Vehicles

EVs have two different types of drive train: direct and geared. In the latter, the drive is connected to the wheel shaft through differentials, while in the direct type the motor is placed inside the wheel for a direct in-wheel drive. Each layout has its own advantages and disadvantages.

An ICE uses a geared transmission to extend the torque speed characteristics, but that can be accomplished when using an electric motor since the vehicle torque speed curves can be achieved electronically and by the use of appropriate motor design characteristics. This on its own can show the great advantage of having fewer parts and less weight on board the vehicle as a result of the elimination of the gearbox and clutch systems [27, 28]. Modern EVs use electric motors that are linked to a fixed gear ratio box and designed in such a way that both the electric motor and fixed gear ratio box come in one assembly.

The in-wheel motor design eliminates the differential. However, this type of in-wheel EV requires a complex control system in order to control the four motors in synchrony, especially in the case of faults occurring in one or more of the motors. It is also very costly when it comes to the implementation of more than one electric motor for one

vehicle, especially considering the complex control system required. In-wheel drives are designed to operate at high torques of more than 200 Nm and low speeds of less than 1500 rpm, and Figure 2.12 shows an in-wheel drive train [45-53].



Figure 2.12. In-Wheel Drive Train[53].

2.5 Electric Motor Performance Requirements for EVs

Designing an electric motor for EVs requires knowledge of all the forces that act upon the vehicle [10, 37]. This will help in giving the correct motor ratings since the motor and the chosen traction have to overcome the weight of the vehicle, aerodynamic drag forces, rolling resistance and gradient. These four forces are briefly below:

- The weight of the vehicle: it is very important that the vehicle's weight is kept to a minimum. The battery packs in EVs add extra weight to the car and this needs to be compensated for by machine efficiency and using lighter materials when constructing the car body.

Equation 2.1 below shows Newton's second law of motion, which can be used to determine the forces, F_a , required to increase the speed of a vehicle of given mass over a given period of time:

$$F_a = k_m m_v \frac{dv_T}{dt} \quad 2.1$$

where k_m is the compensating factor for the added inertia caused by the rotating components of the vehicle, m_v is the mass of the vehicle, v_T is its velocity and $\frac{dv_T}{dt}$ is its acceleration.

F_a equals zero if the vehicle is not accelerating ($\frac{dv_T}{dt} = 0$).

Using F_a above, Equation 2.2 can be determined as:

$$F_a = F_{TR} - F_{RL} \quad 2.2$$

F_{TR} is the traction force produced by the electric motor and the traction system, and F_{RL} is made up of the road forces and can be obtained by adding the following three forces to each other.

- Aerodynamic drag forces: these represents the viscous resistance of the air when it is acting against the vehicle's motion, and Equation 2.3 below shows how to calculate it:

$$F_{AD} = \frac{1}{2} \rho (v_T + v_0)^2 C_D A \quad 2.3$$

where F_{AD} is the aerodynamic drag force, ρ represents the air density in kg/m^3 , v_0 is the wind's velocity, C_D is the vehicle's drag coefficient (between 0.2 and 0.4) and A is the front area of the vehicle [17, 54].

- Rolling resistance forces: rolling resistance occurs because of the vehicle's contact with the surface and it is very important that it is accurately determined. Equation 2.4 below shows how to calculate the rolling resistance force F_{roll} .

$$F_{roll} = f \times m_v \times g \quad 2.4$$

where f is the resistance coefficient for a rolling tyre, which changes with different speeds and surfaces and g is the acceleration constant due to gravity.

- Gradient force: this is the force caused by the vehicle climbing up a hill and can be calculated as shown in Equation 2.5 below:

$$F_g = m_v \times g \times \sin \alpha \quad 2.5$$

where F_g is the gradient force, m_v is the mass of the vehicle, g the acceleration constant due to gravity and α the angle between the road and level ground.

Using Equations 2.6 below, the torque required of the electric motor, T_{motor} , can be calculated where r_w is the wheel radius

$$T_{motor} = F_{TR} \times r_w \quad 2.6$$

The power required by the motor can also be calculated using equation 2.7 and 2.8 where ω_w is the angular velocity of the vehicle:

$$Power = T_{motor} \times \omega_w \quad 2.7$$

$$Power = F_{TR} \times v_T \quad 2.8$$

2.6 Challenges of Electric Motors for EVs

When designing an electric motor for EV applications, some challenges have to be given careful consideration. The most significant challenges are the following requirements [17-21]:

1. High power and torque density.
2. A wide speed range is required at constant power, of the order of 3-4 times the base speed as can be seen in Figure 2.13.
3. High starting torque.
4. A high level of reliability.
5. Robustness.
6. Intermittent overload capability (for overtaking).
7. Acceptable cost.
8. Minimal torque ripple and audible noise.
9. Controllability.
10. High efficiency at all speed and torque ranges.
11. Good voltage regulation needed over a wide range of speeds.

Figure 2.13 also shows that the ideal torque and power-speed curves for a traction machine need to be considered carefully when designing a machine for EV application.

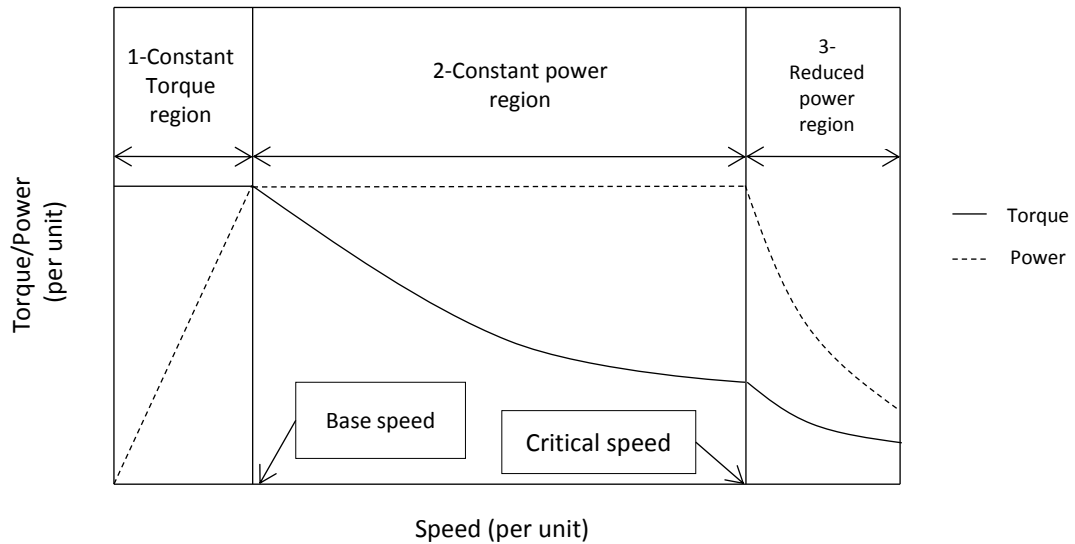


Figure 2.13. Ideal Torque and Power-Speed Curves [55].

The three operating regions illustrated in Figure 2.13 are, firstly the constant torque region (1) where maximum torque is applied. This is fixed to the current rating of the inverter, and it lasts until the point at which the rated torque starts to drop at the base speed point.

At the base speed, the inverter voltage limit is met [17, 55]. The constant power region (2) then starts at that base speed point where the inverter voltage and current are limited. However, in order to allow the machine to increase its speed further, a field weakening region is employed through which the angle between the current and the back EMF is changed, for the purpose of introducing a negative d axis current. This creates a demagnetizing field in the armature reaction field at the air gap to weaken the field produced by the magnets and hence increases the constant power region. Note that by introducing a negative d axis current, the rated torque is reduced.

The torque during field weakening will gradually drop at the same rate of the increase in speed for the purpose of keeping the maximum rated power of the machine constant. The machine phasor diagrams at base speed and during field weakening are shown in Figure 2.14 a) and b) respectively.

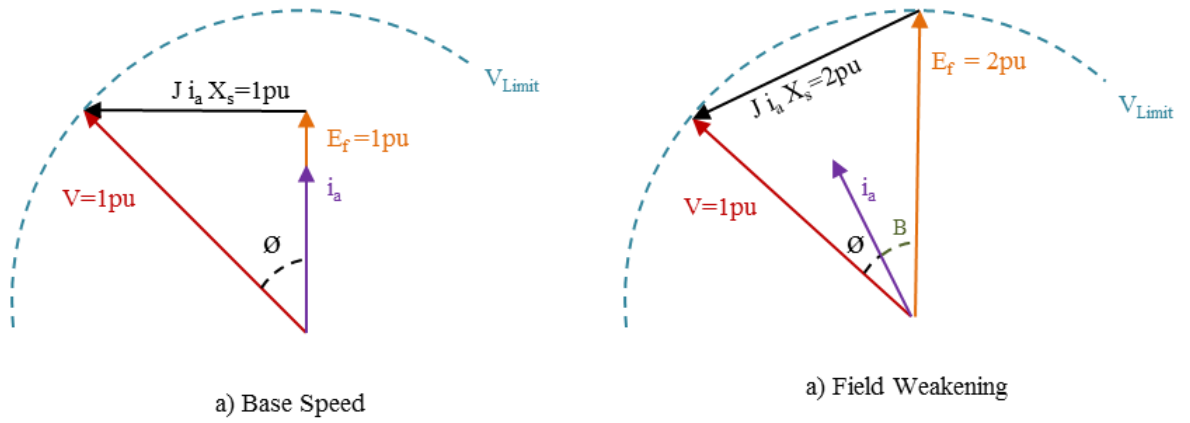


Figure 2.14. Phasor Diagrams at Base Speed and During Field Weakening.

At the start of the reduced power region (3), the speed at that point is classed as the critical speed of the machine. The increase in the back electromotive force (EMF) decreases both the rated power and torque if the machine reaches speeds over that point. The torque drops by the square of speed in this region [17, 18, 20, 55].

2.7 Drive Cycle

The driving cycle referred to here is the test driving cycle that is composed with standardized speed and road slope profiles. This is used in order to evaluate the pollution emissions and fuel economy of the ICE.

This cycle can also be used for the comparison of HEVs with ICEVs in terms of dictating cost, fuel consumption and battery contribution to run distances.

The New European Driving Cycle (NEDC) shown in Figure 2.15 represents the driving pattern of vehicles within the European region.

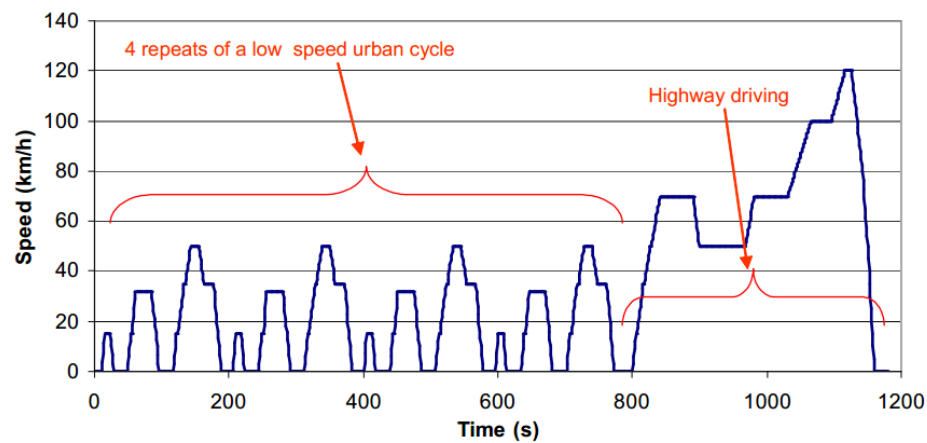


Figure 2.15. The New European Driving Cycle [56].

It can be seen from the figure that the NEDC is made up of two regions. The first is made up of four repeatable cycles, which represent the low speed urban cycle with a maximum speed of 45 km/h, and the second section represents the highway driving cycle with a speed up to 120 km/h [56]. The NEDC was proposed in order to be used for testing vehicles for the measurement of emissions and performance [57]. The electric motor should be tested with the battery using this cycle in order to validate efficiency, speed, and battery consumption for EV use.

2.8 Conclusion

The numbers of EVs developed has been increasing year by year because of their advantages when compared to ICE vehicles, such as the use of direct energy conversion, quieter operation, fuel flexibility, higher efficiency, lower energy consumption and reduced CO₂ emissions. Careful consideration must be given to the design of an EV system. The system design must have a specific weight, volume, and power density, and critical requirements include high performance, rapid acceleration, good fuel economy, low cost and a transient response similar to that of ICEVs. There are various types of electric vehicles, and the HEV is currently the most popular type because it uses two different sources of energy by combining the ICE with an electric motor. This combination has been found to save energy and minimize pollution when compared to ICEVs because the ICE is designed to run in a narrow power band, and can achieve greater efficiency by using the Atkinson cycle. However, this mode of the Atkinson cycle is not suitable for transients (high power and high torque) which are handled by the electric motor. The pure EV is another type of electric vehicle that operates at zero emissions after its battery has been charged. Although pure EVs operate at zero emission, indirect emission effects may be involved depending on the source of energy used to charge the battery. The design of EVs is faced with challenges that must be taken into account, such as the capability, size, lifetime and cost of its battery, safety features, the availability of charging stations, the performance of the electric motor, the cooling system and the software used to communicate between the different part of the system. EVs can use a drive train that is direct or geared, where the former is sited inside the wheel and the geared type is connected to the wheel's shaft through differentials. Although in-wheel drive trains eliminate the use of differentials, they require complex control systems. The weight of the vehicle, aerodynamic drag forces, rolling resistance forces and gradient forces should be determined in order to give the ratings of the motor required. Also various other challenges should be taken into consideration when designing electric motors for EVs, such as the demand for high power, high torque density, a wide speed range, high starting torque, reliability, robustness, overload capability, cost, minimal torque ripple, controllability, high efficiency and good voltage regulation. A drive cycle is shown to represent the driving pattern of vehicles within the European regions which is used when testing vehicles for emissions. The electric motor should also be tested using this cycle in order to validate its performance.

The following chapter highlights different topologies for EVs along with a finite element (FE) comparison between the most commonly used types. Some of the principles involved in the design of a permanent magnet (PM) machine are also shown and discussed.

Chapter 3. Electrical Machine Topologies for EVs

A survey of existing EVs has been presented in Chapter 2. The aim of this thesis is to describe research conducted in designing a high torque density electrical machine for EVs, and hence the different topologies of electric motors used for EVs are discussed in this chapter. This includes the advantages and disadvantages of each type, and a comparison of the different types using FE analysis is discussed.

3.1 Introduction

Among all of the different types of electric drives that are available, there are four major types which are viable for EV applications. They are [24]:

1. DC machines.
2. Induction Machines (IM).
3. Switch Reluctance Machines (SRMs) and Synchronous Reluctance Machines (SyncRMs).
4. Permanent Magnet Machines (PMMs).

The topology of each of the machines mentioned above is as shown in Figure 3.1.

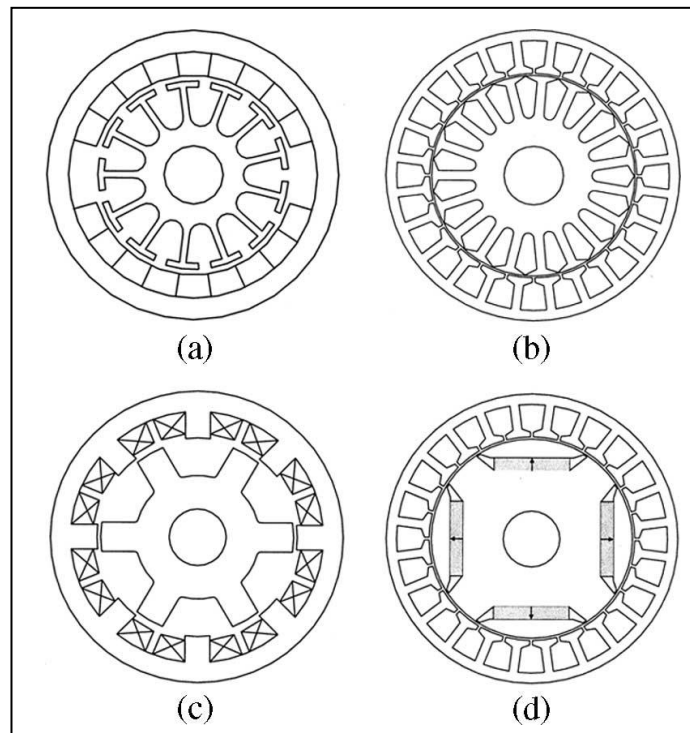


Figure 3.1. (a) DC Drive, (b) Induction Machine, (c) Switch Reluctance Machine and (d) PM Machine [24].

It is also possible to divide EV drive types into two main groups: brushed drives and brushless drives. These can themselves be further classified into subgroups as shown in Figure 3.2.

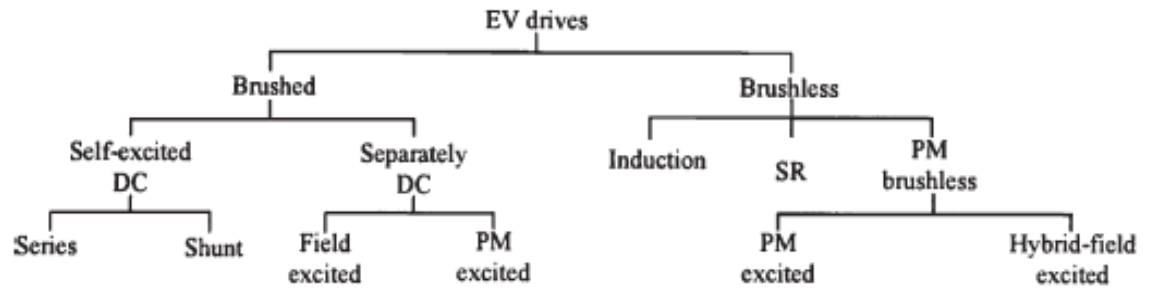










Figure 3.2. Classifications of the EV Drives [24].


A wide range of these machines are used by various manufacturers of EVs and HEVs. Modern vehicles tend to use either a PM machine or an IM due to their high operating efficiency and reasonable cost. DC drives were favoured when electric vehicles were introduced in 1900 due to their simple control and efficiency, but due to their low reliability they are not favoured in the current market. More research has been carried out recently in order to improve the operation of SRMs and to minimise their cost [58]. Different topologies have been proposed and these are described later in this chapter. Table 3.1 shows the different drives used in previous and latest EVs and HEVs by leading manufacturers, including sports vehicles, suburban utility vehicles (SUVs), and sedans.

Table 3.1. Drives Used by Different Manufactures Until Present [18, 24].

<i>EV models</i>	<i>EV motors</i>	<i>Country</i>	<i>Electric Range</i>	<i>Battery Size</i>	<i>Charging rate</i>	<i>Body Type</i>
Toyota Prius 	PM machine	Japan	11 miles	4.4kWh	3.3kW	Sedan
Ford focus Electric 	Induction motor	United States of America	76 miles	23 kWh	6.6 kW	Sedan

<p>Tesla Roadster</p> 	Induction motor	United States of America	244 miles	53kWh	16.8kW	Coupe
<p>Nissan Leaf</p> 	PM machine	Japan	84 miles	24 kWh	6.6kW	Sedan
<p>Mitsubisii-MiEV</p> 	PM machine	Japan	62 miles	16 kWh	3.3 kW	Sedan
<p>BMW i3</p> 	Hybrid Synchronous Motor	Germany	100 miles	22 kWh	6.6 kW	Sedan
<p>BMW i8</p> 	Hybrid Synchronous Motor	Germany	22 miles	7.2 kWh	3.3 KW	Coupe

Cadillac ELR 	Induction motor	United States of America	35 miles	16 kWh	3.3 KW	Coupe
Mercedes B-Class 	Induction motor	Germany	85 miles	28 kWh	10.0 KW	Sedan
Porsche Panamera S E-Hybrid 	Induction motor	Germany	22 miles	9.4 kWh	3.3 KW	SUV
Tesla Model X 	Induction motor	United States of America	210 Miles or 270 miles	60 kWh or 85 kWh	10.0 KW or 20.0 KW	SUV
Volkswagen E-Golf 	Induction motor	Germany	85 miles	24kWh	7.2KW	Sedan
Hyundai Kia Soul EV 	PM machine	South Korea	90 miles	27kWh	6.6kW	Sedan

Range Rover Defender EV 	Switch Reluctance machine	UK	50 miles	27kWh	606kW	SUV
---	---------------------------------	----	-------------	-------	-------	-----

Looking at Table 2.1 above, it can be seen that IMs were mostly used by US and European manufactures due to their desire to not use PM materials that are mainly controlled by the eastern world considering its availability and cost.

3.2 DC Drives

DC drives have been used for EVs and trains because of their simple control. However, they are less reliable because of brush and commutator wear and they have low efficiency. They were used in electric vehicle applications in the early 1980s, but are not used in modern vehicles.

3.3 Induction Machines

Induction machines (IMs) found in many EVs and HEVs because of their low cost, reliability, relatively maintenance-free status and reliable efficiency in the constant power region [55, 59]. However, they suffer from the following disadvantages:

- Low torque density, and hence they are preferable in high speed and low torque applications.
- Low efficiency at the low speed region.
- A vector control needs to be implemented in IMs in order to achieve the desired performance due to their variable frequency and voltage. The desired performance cannot be provided by conventional control because of the nonlinearities of the IM dynamic model [24].

IMs are undergoing continuous development in order to improve their performance [60, 61], and the following developments are of particular importance:

- A new strategy of efficiency-optimizing-control has been developed for IMs to be used in EVs, reducing the energy consumed and increasing levels of regenerative energy leading to the extension of the driving range of the vehicle [28].
- A new design incorporating an electrically pole-changing scheme has been developed for EV IMs. This extends the constant-power operating region to over four to five times the base speed [62].

3.4 Switched Reluctance Machines

SRMs have been accepted for use in EVs because of the following advantages:

- Their fault tolerance is very high due to their nature of energizing one phase at any given time.
- The rotor construction is robust, containing only iron with no magnet or copper.
- The cost is low due to its simple construction with only the need for iron and copper.
- The torque speed characteristics are suitable for an EV.

The main disadvantages of SRMs in comparison to other machines are lower torque density and that they exhibit high acoustic noise and vibrations which are caused by the machine high torque ripple.

SRMs are also faced by other challenges such as: the manufacturing difficulty due to the small air gap required and the requirement of a larger inverter for the controlling strategy due to the low resulted power factor which can increase the cost of the system as a whole [24, 63]. They also suffer from high iron loss at high speeds.

New design strategies have been introduced for EV SRMs and some examples of these are as follows:

- A mode of fuzzy sliding control has been developed for this type of drive in order to handle the machine nonlinearities and to minimize its control chattering [64].
- A phase advancing excitation technique has also been developed in the constant-power region in order to extend the base speed up to seven times [65, 66].

- A new concept has been developed to reduce acoustic noise by using a vibration cancellation technique that induces an antiphase vibration to cancel a specified vibration [67].
- An SRM with a segmental rotor topology has been demonstrated to produce more torque than that of the conventional configuration because more flux can be linked by each coil, as discussed by Widmer et al. [58] and this configuration is shown in Figure 3.3.

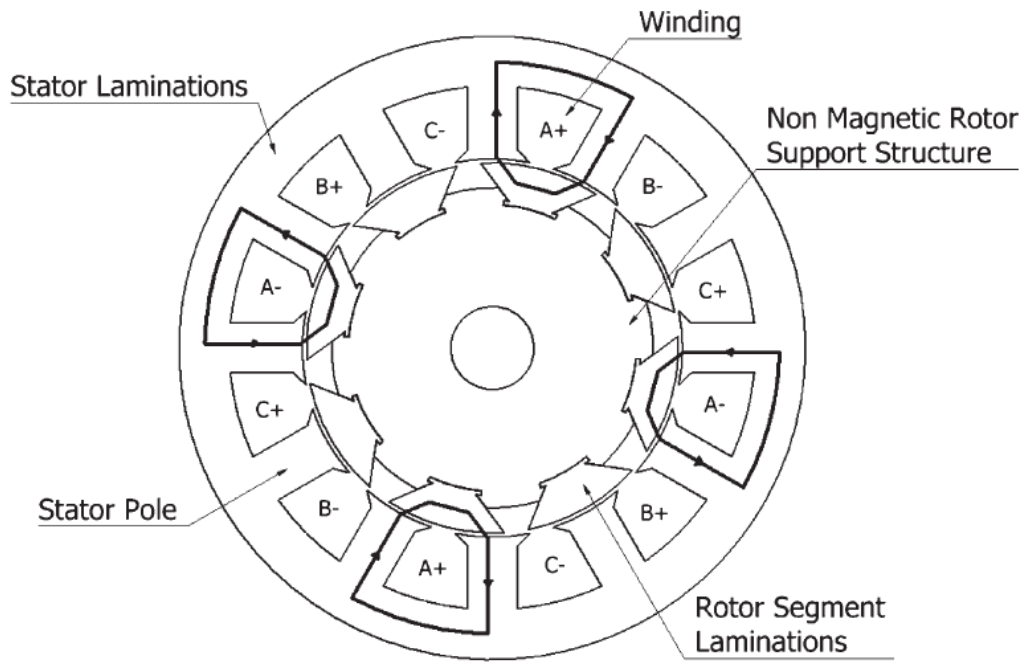


Figure 3.3. Segmental Rotor SRM [58].

Typical SRMs with one phase leg of an inverter are shown in Figure 3.4.

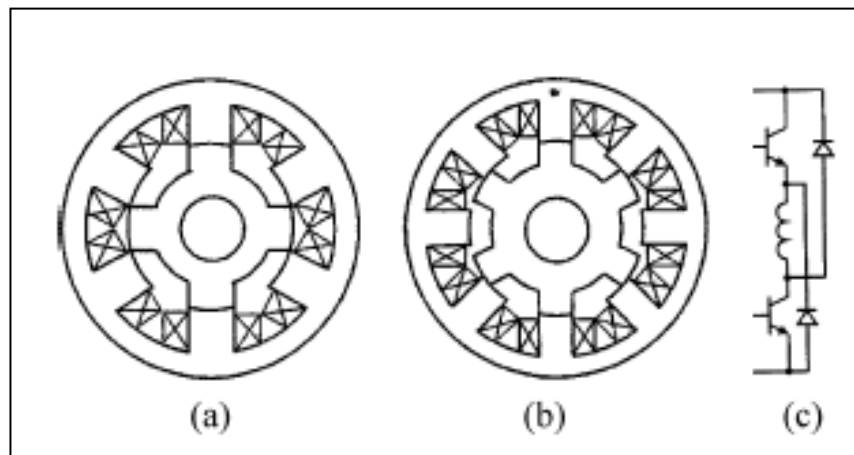


Figure 3.4. Three-Phase, 6/4 SRM. (b) Four-Phase, 8/6 SRM. (c) One-Phase Leg of Inverter [55].

Also, an example of an SRM which was developed for a HEV application is shown in Figure 3.5.

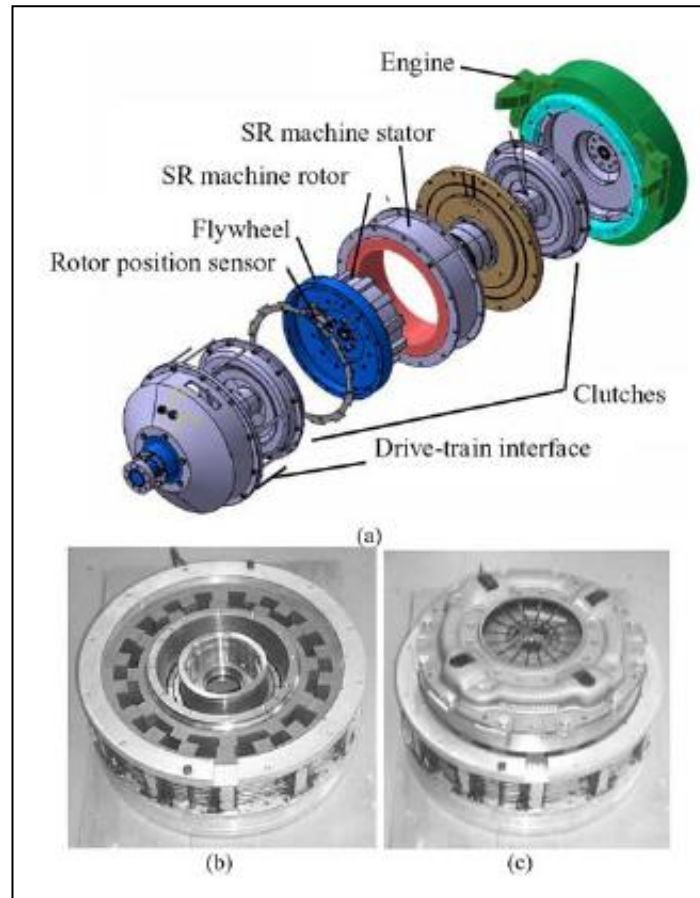


Figure 3.5. SRM with Integrated Flywheel and Clutch For HEVs: (a) the Machine's Schematic, (b) the Rotor/Stator Without Windings; and (c) the Assembled Unit [68].

3.5 Permanent Magnet Machines

PM machines are attractive in all types of EVs because of their high efficiency when compared to other types of machines, high torque density and high reliability. However, their cost is relatively high due to the price volatility of the material used. PM brushless drives have two types according to the operating current required and no-load EMF waveforms [33]. One is the PM sine wave machine that has sinusoidal back EMFs and armature current, which is known as the PM synchronous machine (PMSM). The other is the brushless DC machine that has trapezoidal back EMFs and current pulses. These two types of PM drive have much in common in practice. Figure 3.6 shows the schematic representation of a PM drive.

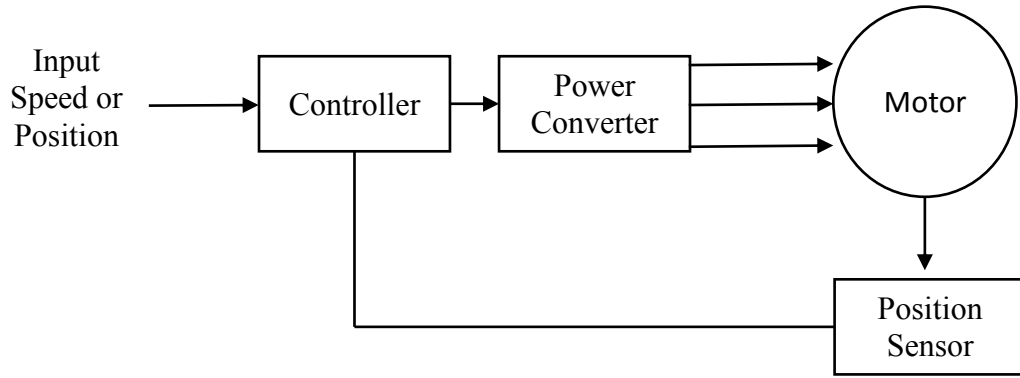


Figure 3.6. Schematic Representation of the PM drives.

The PM machine torque output is limited by the current rating of the machine and converter, while the speed is limited by the voltage limit of the power converter. The voltage can be controlled in order to obtain the desired current, but as soon as the machine reaches its base speed the voltage reaches its limit. Hence, to increase the speed further, field weakening is used.

Researchers are trying to develop improved PM machine designs to overcome these challenges, and more importantly, to improve power and torque density. The prevalent structures applicable for EVs are:

- The Radial Flux Machine (RFM), with magnets on the rotor and/or stator
- The Axial Flux Machine (AFM)
- The Transverse Flux Machine (TFM)

3.5.1 The Radial Flux Machine (with Magnets on the Rotor)

The RFM with magnets on the rotor is the most common topology of PM machines. A variety of magnet placements are possible which are broadly split into surface-mounted and buried.

The surface mounted rotor is the most commonly used in industry due to its simplicity. However, this type of machine has a low armature reaction field and a low phase inductance, where the magnetic gap is the combination of the physical air gap plus the magnet's thickness since its permeability is similar to that of air. Also, the magnets are directly exposed to the armature reaction field, which can cause some partial demagnetization. The d and q axis inductances are equal and hence there is no

additional reluctance torque. Inductance can be increased by means of a closed slot design. It is also important to note that surface-mounted PMs used in high-speed applications need a sleeve to retain the magnets under high centrifugal force.

Interior PM Machines have the advantage of non-equal d and q axis inductances and additional reluctance torque. The magnets are also shielded from the effect of the armature reaction field. This type of machine can introduce higher power output for the same magnet mass as a surface PM machine. It is most suitable for high-speed applications where the magnets are well retained. Furthermore, due to the high level and variation of the d and q axis inductances, this machine has a high level of suitability to extend its speed range beyond its base speed in the constant power region due to its flux weakening capability [69].

Figure 3.7 shows the alternative RFM topologies with magnets on the rotor with both surface placed PMs as seen in (a) and a general structure of interior placed PMs as shown in (b), (c) and (d) [55, 70, 71].

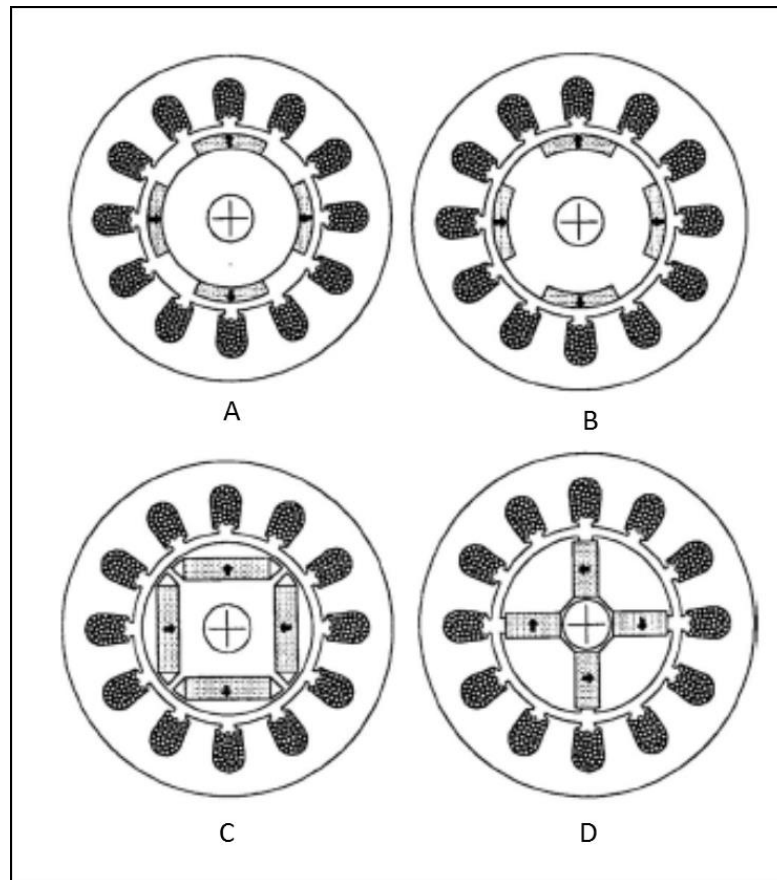


Figure 3.7. (a) Magnets on Rotor, (b, c and d) Magnets Inside the Rotor [55].

3.5.2 *The Radial Flux Machine (Magnets on Stator)*

These types of machines have PMs on the stator [72-78] [79], where the rotor has to be of a salient geometry. This can be very similar to SRMs, where both the latter and RFMs with magnets on the stator are very robust, simple and suitable for high-speed applications. In addition, placing the magnets in the stator has an advantage over placing them in the rotor, especially when it comes to the cooling system, as the magnets can be easily cooled through the stator core back. These machines can have three different topology arrangements regarding the placement of the magnets:

- Doubly Salient PM Machines (DSPMMs) with the magnets placed in the stator back iron as shown in Figure 3.8 (a). In this topology a magnet is required for every three teeth for a three phase machine while for every four teeth for a four phase machine. This topology is suitable for BLDC operation because the flux linkage variation with each coil is unipolar and the back EMF waveform is trapezoidal. However, a more sinusoidal back EMF can be achieved by skewing the rotor to make it more appropriate for a BLAC operation. The torque density of this topology is relatively poor in comparison to other conventional PM machines because of the unipolar flux linkage.
- Flux Reversal PM Machines (FRPMMs) with the magnets placed on the inner surface of the stator iron as shown in Figure 3.8 (b). In this topology two magnets of opposite polarity are mounted at each tooth surface so when the coil is excited, the field under one magnet is reduced while under the second magnet is increased and hence, this causes the salient rotor to rotate toward the stronger magnetic field and for the rotor to continue its rotation, the flux linkage in the coil reverses direction. This topology exhibits a low winding inductance because the flux linkage variation is bipolar while the back EMF waveform is trapezoidal. The magnet in this topology is vulnerable to irreversible demagnetization because of its location. In addition, the torque density is compromised here because the air gap flux density is limited by the magnets.
- Flux Switching PM Machines (FSPMMs) with circumferentially magnetised magnets sandwiched between a U shaped lamination segments in the stator as shown in Figure 3.8 (c). The magnetisation direction of the magnets is reversed from one magnet to the next. In addition, the armature reaction field on the magnet working point is minimal in this topology because of the magnet location. This

machine benefits from high torque density because of its increased electric loading. This topology is appropriate for a BLDC operation because of its sinusoidal back-EMF waveform.

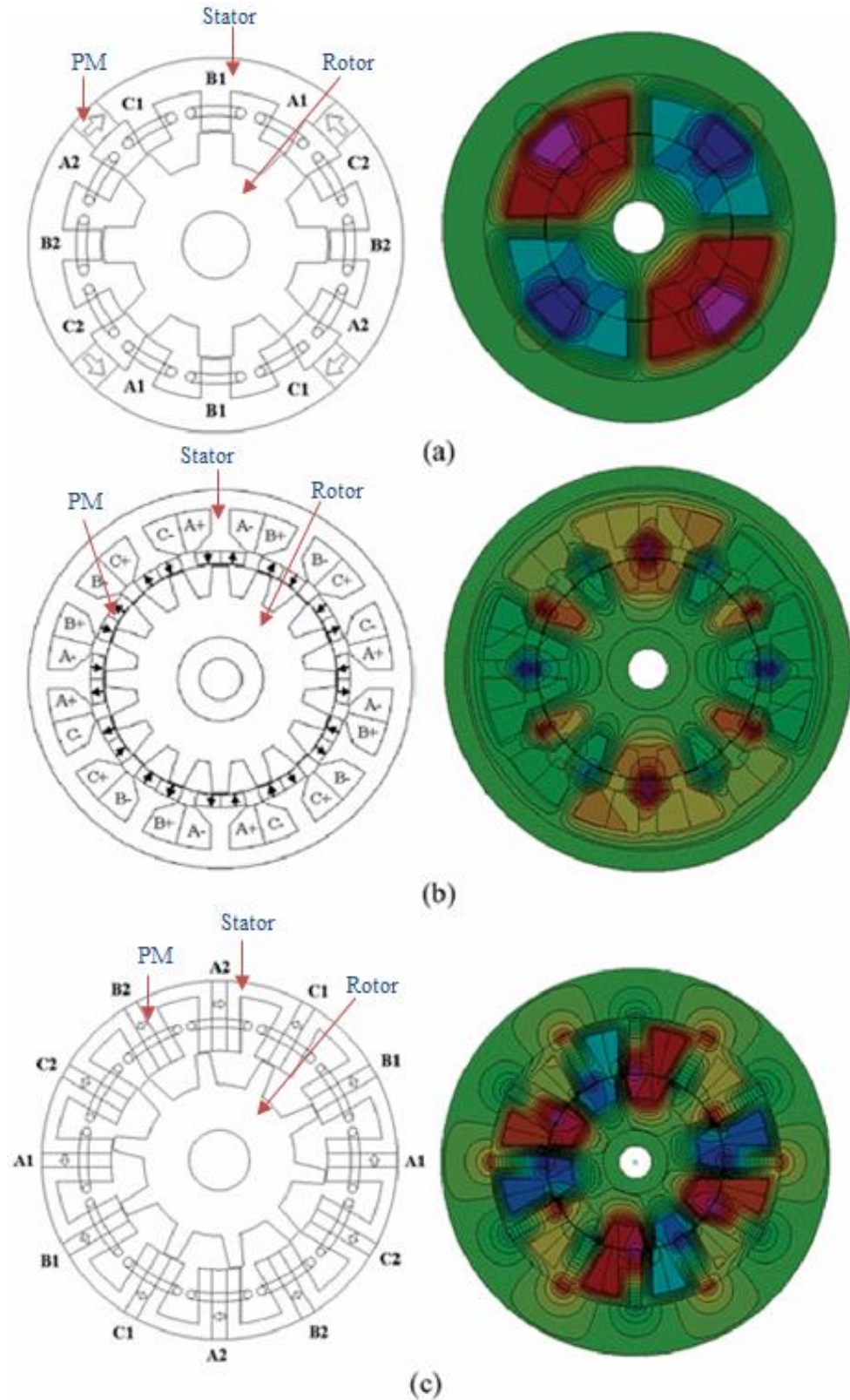


Figure 3.8. (a) Doubly Salient PM Machine (b) Flux-Reversal PM Machine (c) Flux Switching PM Machine [55].

3.5.3 Axial Field Machine (AFM)

AFMs have an air gap that allows the air gap flux to travel axially, and they may comprise of three different arrangements. These are a single stator and single rotor, a double-sided stator and a single rotor, or a double rotor and a single stator. All arrangements are on an axial stack [80-84]. A large axial force exists in all three arrangements. These types of machines can use either slotted or slotless stators, but due to manufacturing difficulties the slotless option is more commonly used in this type of machine.

AFMs have a high torque density, a slotless stator and a small cogging force. The main disadvantages are that they are expensive and that the winding inductance is small for the large effective air gap, which limits the constant power speed range [18, 85].

Figure 3.9 shows an example of (a) a double stator single rotor AFM and (b) a double rotor single stator AFM.

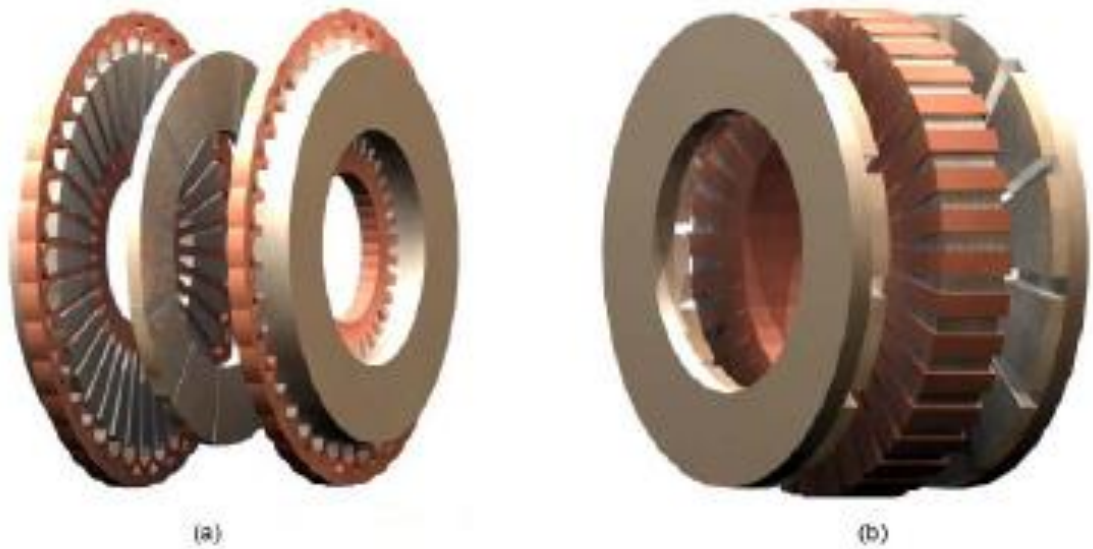


Figure 3.9. (a) Double Stator Single Rotor AFM, (b) Double Rotor Single Stator AFM. [83].

Figure 3.10 shows a novel design of an AFM that was published by Ho et al. [84], which was designed for in-wheel applications for EVs. In this figure, (a) shows the machine when assembled; while (b) shows a disassembled view. In this proposed design the machine must have an equal pole pair for both rotor and stator. The authors claim

that this novel design achieves higher torque density than RFMs at low speed and that it is simpler to manufacture.

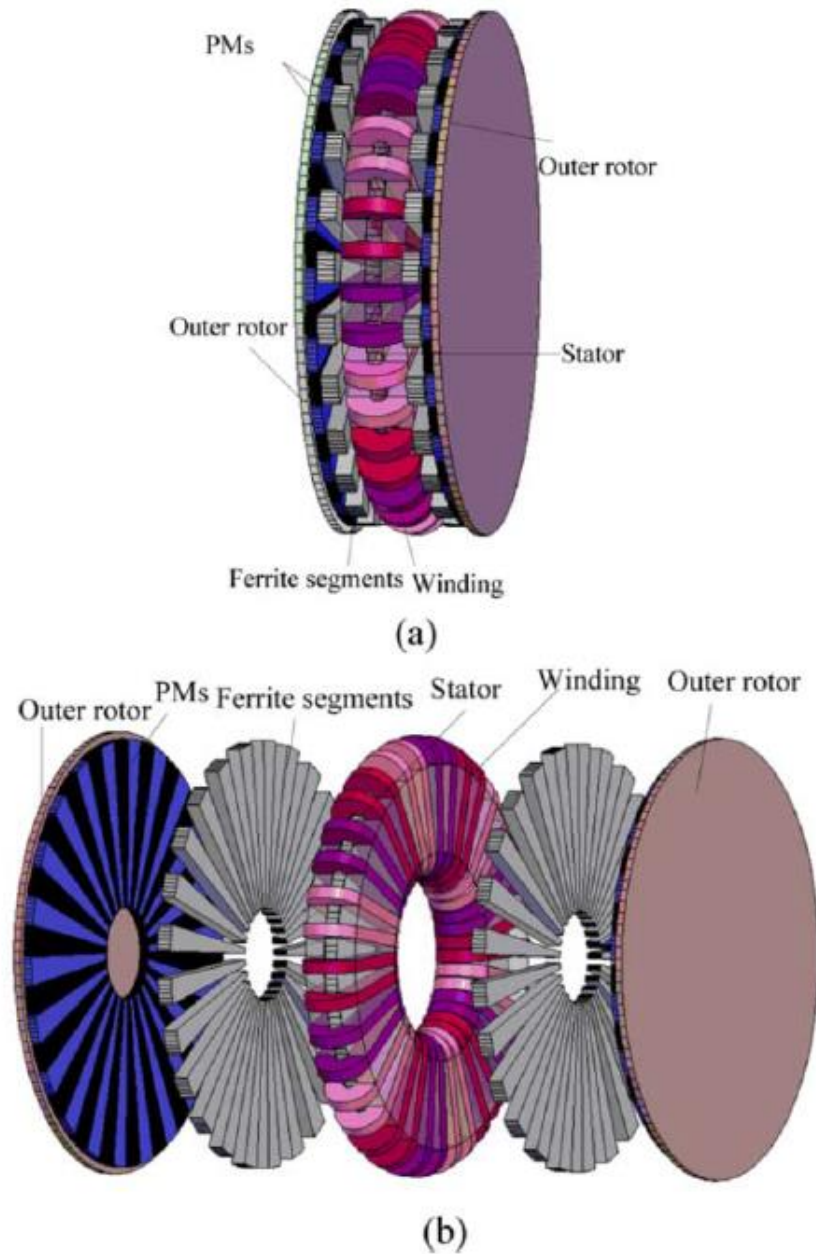


Figure 3.10. (a) Assembled View, (b) Disassembled View [84].

3.5.4 The Transverse Flux Machine (TFM)

TFMs [86-89] are known for their large pole numbers and for having structures that allow three dimensional flux paths across their sections, as shown in Figure 3.11. Also, due to their structure, the poles in these types interact with the total armature reaction flux of each phase. This enables a significant increase in the electric loading of the machine and hence allows a high torque density to be achieved [90-92]. Due to the large number of poles, these types of machine suffer from a large amount of leakage fluxes that contribute to the total losses of the machines. Furthermore a high winding inductance is present in this type of topology along with a low power factor [93, 94]. The low power factor is a significant disadvantage as it overrates the VA of the inverter and the large pole number requires a high operating frequency that has the effect of limiting the machines' speed ranges.

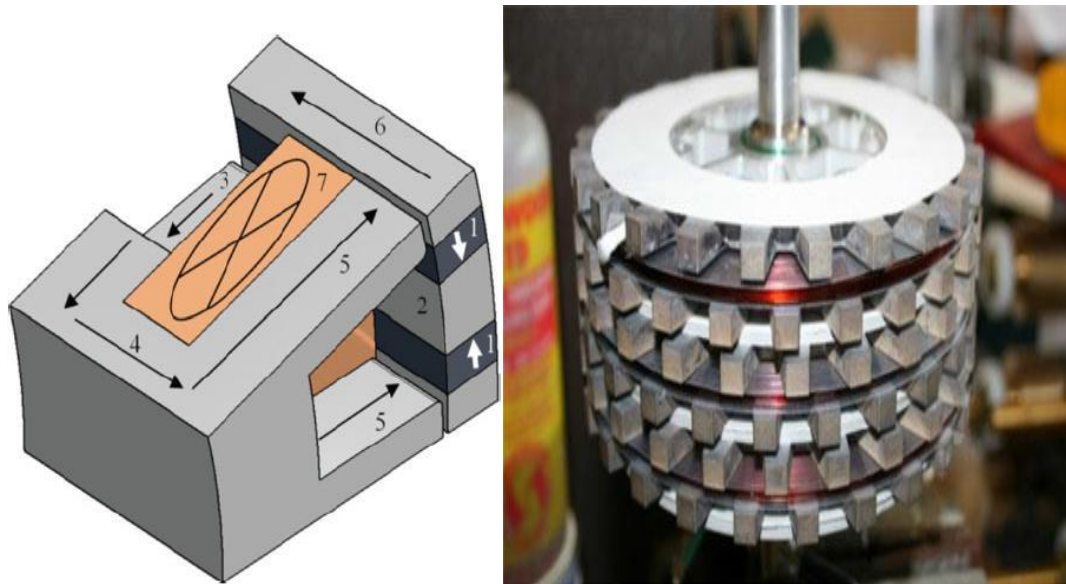


Figure 3.11. Two Pole Section of a Single Phase of TFM and an Axial View of a the Stator [88].

Comparisons between RFM, AFM and TFM have been published in three reviews [95-97]. All favour the RFM for best performance. TFM's have been shown to have a poor power factor, which limits their use to low speed applications.

3.6 FE Analysis Comparison Between a PM Machine Used in an Existing HEV and Other Investigated Alternatives.

In this section, a performance comparison of an interior PM machine, an IM and an SRM is carried out. The interior PM machine analysed is that of the Toyota Prius HEVs, whereas both the IM and SRM were optimized and developed to maximize torque output electromagnetically using 2D FE analysis solutions to investigate alternative drives for EVs. For the purpose of this thesis, the power electronic drives of all three machines are not discussed. However, it is important to note that all three machines use three phase windings in order to be comparable. Half of a cross-section of each of the three machine topologies is shown in Figure 3.12, where (a) shows an 8 poles PM machine that is used in the Prius HEV [98, 99], (b) shows an 8 pole IM that was validated for comparison in two studies [100, 101] and (c) shows an 18 /12 stator to rotor poles SRM discussed and validated for comparison in a further study [102].

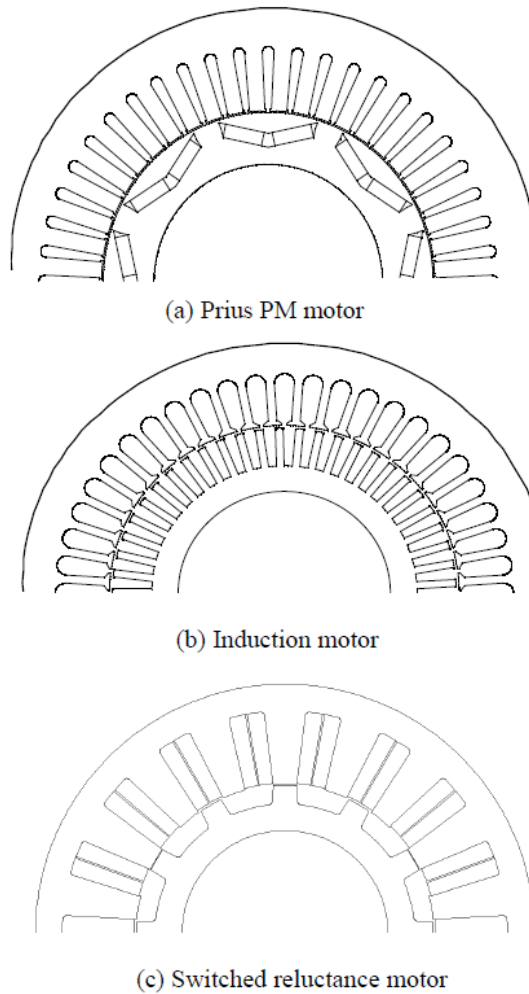


Figure 3.12. Half Cross-Section of (a) PM Machine, (b) SRM and (c) IM [100, 102].

Table 2.1 addresses the geometry and dimensions of the three machines and, in order to be comparable; all three share the same outer stator diameter, rotor inner diameter and axial length. However, they vary in the rotor outer diameter in order to meet the specifications. The SRM can be seen to have the lowest total weight because no rotor magnet exists, as in the PM machine and there is no rotor copper winding as in the IM. The efficiency varies between the three topologies with the PM machine achieving the highest efficiency. In addition, a cost comparison is shown in the table with the PM machine being the most expensive while the SRM is being the cheapest. This is due to the cost of the permanent magnet.

Table 3.2. Parameter Comparison of PM Machine, SRM and IM [101, 102].

Parameter		PM	SRM	IM
Outer Stator Diameter (mm)		269	269	269
Inner Rotor Diameter (mm)		111	111	111
Outer Rotor Diameter (mm)		160.5	170	180
Air Gap Length (mm)		0.73	0.3	1.5
Axial Length (mm)		84	84	84
Stator Core Weight (Kg)		18.65	14.11	11.86
Stator Copper Weight (Kg)		5.99	7.44	10.57
Rotor Copper Weight (Kg)		-	-	7.67
Rotor Core Weight (Kg)		5.22	5.16	6.15
Magnets Weight (Kg)		1.3	-	-
Total Weight (Kg)		31.6	26.7	36.25
Efficiency (%)	1500rpm (Base)	91	83	85
	6000rpm (Max)	96	95	88
Cost (£)		242	74	143

All three machines are designed for speeds ranging from 1500 rpm to 6000 rpm, and hence Figure 3.13 presents a performance comparison of the three machines at 1500 rpm and 6000 rpm while at maximum power.

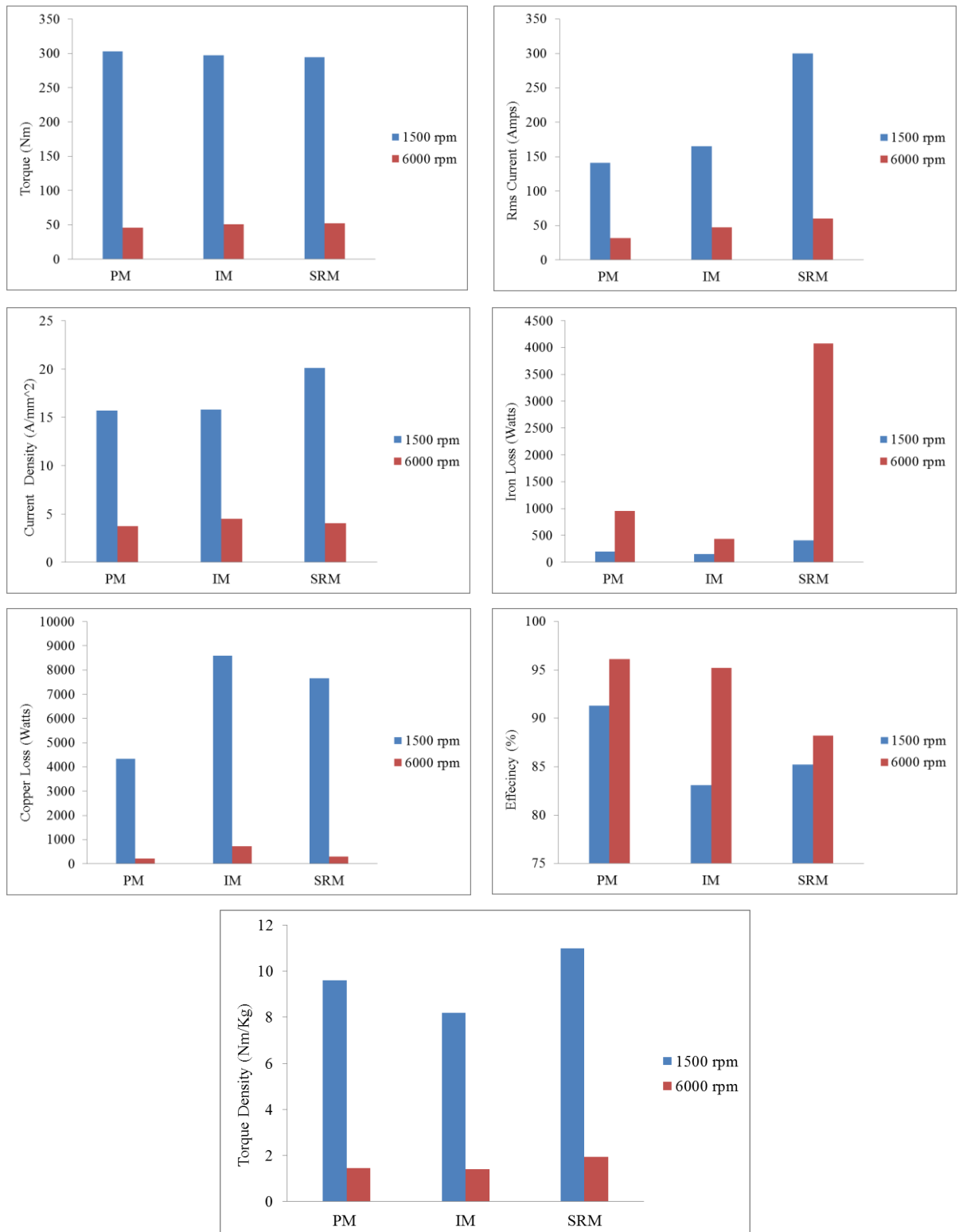


Figure 3.13. Performance Comparison at 1500 rpm and 6000 rpm at Maximum Power [102].

Figure 3.13 illustrates that the PM machine has the highest torque output, highest efficiency and lowest current density at 1500 rpm. However, the PM machine has less torque than the other two machines at 6000 rpm. This is because the torque drops in the

constant power region while increasing the speed. Also from the figures above, copper loss is shown to be the dominant type of loss in all of the machines at low speed because of the high current density applied. However, at high speed the iron loss is shown to be dominant, and this is because of the increased frequency at high speeds. The induction machine has very high copper loss, because it has copper winding in both the stator and rotor. The SRM, on the other hand, suffers from high iron loss due to the increased frequency of the flux. Although the SRM has the highest torque density achieved, it is not favoured in EVs because of the disadvantages mentioned in the previous sections. The PM machine, on the other hand, has been demonstrated to be a very strong candidate for EVs, considering the discussion in previous sections and based on the comparison and analysis in this section. The PM machine was thus chosen for the novel design topology explored in this thesis.

3.7 Principle of PM Machine Design.

Due to the high torque density and high efficiency of PM machines they have dominated large sectors of the variable speed drive market for the past two decades. PM machines are very important in the current and future market as they are favoured in aerospace, automotive and domestic applications, as well as in some of the largest machines available worldwide, such as direct drive wind turbines and large ships propulsion systems [103-106].

When a PM machine is designed, there are a number of optimisations that must be carried out within a series of constraints. The general constraints of any machine are:

1. The dimensions of the machine, such as the outer diameter and length of the machine. These are mostly dependant on the space envelope allowed by the specific application the machine is designed for.
2. The torque output that is required from the designed machine.
3. The range of speed that the machine is required to operate at.
4. The efficiency of the machine, the total machine losses and the resulting heat generated in the machine.
5. The voltage required, this specifies DC link rating and the ratings of the semiconductors required in the inverter.
6. The current rating of the machine in order to size the inverter devices and to

choose the best cooling method.

While the design constraints can be specified as follows:

1. Magnetic
2. Electrical
3. Thermal
4. Mechanical

And the general optimisation variables are:

1. The cost of the designed machine.
2. The performance of the designed machine to be increased to a maximum for the same cost.
3. The mass of the designed machine should be minimised for the same performance.
4. Inertia.
5. Reliability.
6. Ease of construction.

The design of machines for automotive applications has general requirements as shown in Chapter Two of this thesis, in addition to those requirements the following should also be considered:

1. It is important to choose the appropriate slot to pole combination.
2. Specifying the dimensions of the machine and the winding arrangements to achieve a specific power at the specified base speed for a known volume.
3. Evaluating the machine performance over the rated speed ('Overspeed').

Some of the theoretical and mathematical explanations involved in the principle of PM machine design are discussed in details in Appendix A for things such as magnetic loading, electrical loadings, winding arrangements, air gap depth, magnet thickness, tooth span, slot width, slot depth and coreback depth.

3.7.1 Torque Density

The torque (T) produced by any type of machine is mostly dependant on the type and size of the machine and its electrical and magnetic loading capabilities. The product of the flux density (B), length of the conductor (l) carrying a current (i) is a well known method to calculate the produced force. Also by multiplying the produced force in the equation above by the mean air gap radius (r), then integrate the results around the machine the torque generated can be found as shown in the following equation.

$$T = Bilr \quad 3.1$$

However, some of the more unusual topologies can't be defined using the above equation, hence another fundamental formula should be considered. The torque produced by any machine can be given by the rate of change of co energy with respect to position as can be seen in the following equation.

$$T = i \frac{d\psi}{d\theta} = iN \frac{d\phi}{d\theta} \quad 3.2$$

Change in the equation above indicates that the torque can be found using the product of the electric current i and the rate of change of the flux linkage per phase $d\psi$ with respect to angular displacement $d\theta$. The equation above is an approximation, as in reality it is only true in a wholly linear model. However, it is sufficient to illustrate the principles of torque production. Throughout this thesis theoretical torques will be evaluated using 2D FE simulation results. The torque equation used in any machine with saliency is:

$$T = \frac{3}{2}p [\psi_m I_q + (L_q - L_d)I_d I_q] \quad 3.3$$

T , is the torque output, p the pole pair number, ψ_m the flux linkage due to the PMs and I_q , I_d , L_q , L_d are the currents and inductances in the direct and quadrature axis. The equation above is used to show both the excitation and reluctance torques. In order to maximise the torque production the flux linkage has to be increased and the leakage flux reduced. This can be achieved by having flux barriers and interpole magnets as shown by four different topologies, where both flux barriers and interpole magnets are employed in Figure 3.14. Another way of increasing the flux linkage is by using a flux focusing technique [107].

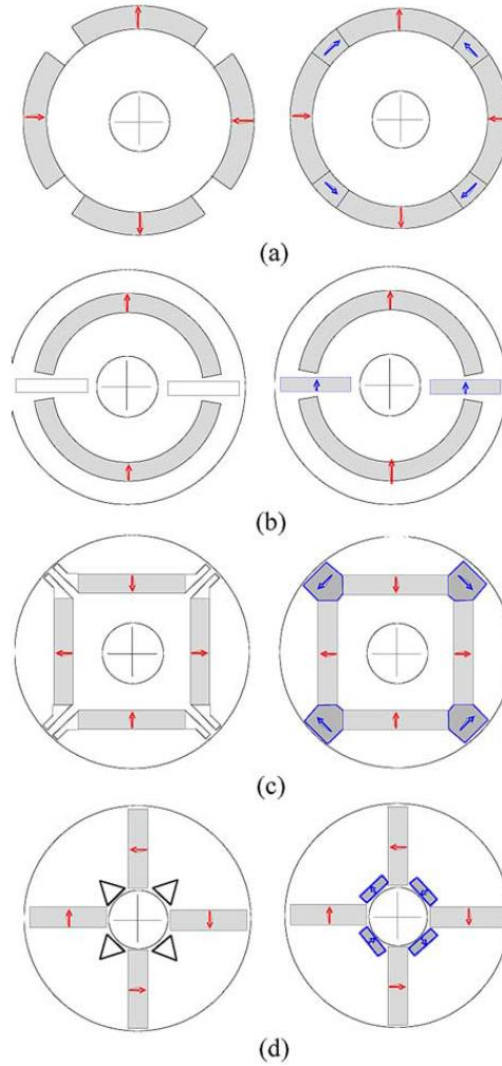


Figure 3.14. Some Examples of Ways to Reduce Leakage Flux by either Introducing Airspace Flux Barriers or by Using an Interpole Magnets [55].

The torque equation above can be seen as two expressions. The first expression represents magnetic torque generated from the magnet and current interaction, whilst the second expression represents the reluctance torque. This reluctance torque is driven from the difference in direct and quadratic axis inductances. Therefore, it can be evident from this latter expression that the torque will be increased by increasing the difference parameter $(L_q - L_d)$ between the inductances in both direct and quadratic axis where the capacity limit in the inverter is ignored. Increasing the difference between inductances in both direct and quadratic axis is referred to as improving the saliency ratio of the machine [108, 109] and Figure 3.15 shows some examples of topologies that improve the machine's saliency ratio.

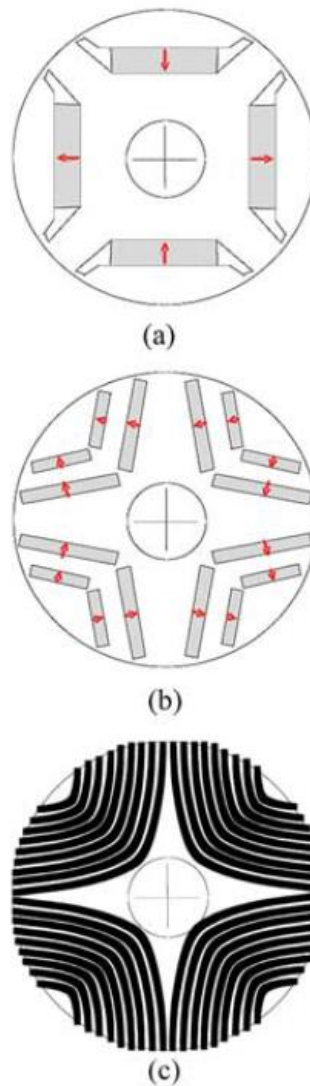


Figure 3.15. Some Examples of Ways to Increase the Saliency Ratio [55].

3.7.2 Efficiency and Machine Loss

As the level of efficiency of an electrical machine varies with the power rating and the operating load conditions, some other approaches can be applied to affect the efficiency of a motor. One approach is to target certain kinds of machines as some are generally more efficient than others [110]. Another approach to improve efficiency is by choosing a low loss material [111-113]. A third approach is by choosing a high efficiency configuration, as different configurations even of one type of a machine, affect the level of efficiency that can be achieved [112, 114]. For a machine with configuration constraints, optimising the machine dimensions for high efficiency can be also a valid approach for increasing efficiency [115-117].

Losses in an electrical machine can be categorised as:

- The copper loss in the form of I^2R loss in the winding resulting from the current carrying conductor, along with the skin and proximity loss in the slot.
- The iron loss which is caused by the changes in the magnetic flux in the lamination at a specific frequency.
- The magnet losses in the form of eddy currents.
- Bearing losses within the machine represented as a friction loss and windage loss in the surface of the rotor.

Reducing the losses is a big challenge but it's important to minimise them to avoid any unnecessary temperature rises in the machine.

When the machine is operating at low speeds at rated current, the copper loss is the dominant loss at this operating point.

Heat is naturally removed by conduction, convention and radiation. However if the losses are particularly high the machine may need to be force cooled. Improving the cooling system can increase the machine loading and hence performance, forced cooling can be achieved by blowing air through a fan to remove heat from the outer surface of the machine. A case with a large surface area can be used to remove the heat. Forced water or oil cooling by either spraying or using a jacket to remove any unwanted excess heat can be used where losses are particularly high, and are very popular in automotive applications and a radiator to remove heat already exists in current combustion engines.

3.8 Conclusion:

EVs require electrical machines with high efficiency and torque density and, because of the various machine types that can be used for EVs, the availability, advantages and disadvantages of each type have been shown and discussed in this chapter. Although DC motors have been used in EVs because of their simple control, they are not favoured nowadays because they are less reliable considering their levels of brush and commutator wear and have their low efficiency. Also, despite their low torque density, low efficiency at low speeds and need for vector control, IMs are widely used in EVs and HEVs because of their reliability and low cost. In addition, despite the low cost, high-tolerance operation and torque speed characteristics of SRMs that are ideal for EVs, their noise and manufacturing difficulties considering the small air gap required make them less favoured to be used in EVs. PM machines, on the other hand, have been favoured by various manufactures despite the high cost of materials because of their high power density, reliability and high efficiency. The availability of PM materials also plays a role when considering the choice of an electric machine for an EV, with USA and European manufacturers using IMs due to the cost associated with PM materials while Eastern manufacturers use PM machines due to the PM material availability in their region. A PM machine has been chosen for the novel design in this thesis because of its high torque density. Although there are different ways of calculating torque, they are mostly approximations; hence they will be used as an indication here, while MagNet software simulations will be used throughout this thesis to indicate the torque output. The dimensions of the PM machine design chosen for the purpose of this thesis should then be optimised using various numerical solutions using computing software such as MagNet. Below is a list of the main design aspects of the electric machine which can be optimised for applications such as EVs.

- Number of poles.
- Number of stator and rotor slots.
- The shape of the stator and rotor slots.
- Winding disposition.
- Dimensioning the machine.
- Designing the winding to achieve specified power.
- Simulating the machine performance over the full operating speed range.
- Magnet placement and saturation limits.

- The type of material used.
- Appropriate cooling method.

In the next chapter the theoretical and mathematical logic behind a novel split tooth PM (STPM) machine design is explained.

Chapter 4. Introducing the Split Tooth Permanent Magnet Machine

This chapter describes a method of deriving a greater torque per unit volume from a PM machine. The method involves splitting the stator teeth in order to introduce a magnetic gear ratio into the torque equation. The theory behind the design of the new split tooth PM machine (STPM) will be described. An initial design of the topology is developed using 2D FE methods and compared to a conventional brushless PM machine of the same dimensions.

4.1 Introduction:

Equation 4.1 states the product of the magnetic and electric loading specifies the torque output of a conventional machine.

$$T \propto A \times B \times \pi r^2 l \quad 4.1$$

Where T is the torque output, A is the electric loading, B is the magnetic loading and $\pi r^2 l$ is the volume of the machine (where r is the rotor outer radius and l is the axial length of the machine)

The saturation levels in iron of the machine's magnetic circuit limit the magnetic loading while the electric loading is limited by the machine's maximum permissible temperature at a given rated current. These limits can be significantly affected by the number of poles, apart from some secondary effects such as the core back depth and end windings. In order to increase the torque output for a given space envelope while considering the above limits, a departure from a conventional configuration is required.

When a high speed PM brushless machine and a speed reduction magnetic gear are combined within a highly integrated magnetic circuit, a high torque capability can be achieved. This can be combined with a low density loss as has been illustrated in [118], where a new topology of a PM machine has been built and tested for a high torque, low speed application. A cross section and different parts of this machine is shown in Figure 4.1 and Figure 4.2 respectively, it is made of two rotors rotating at different speeds. Despite the torque achieved by this topology, it suffers from under sized gear, under utilised stator and long flux paths.

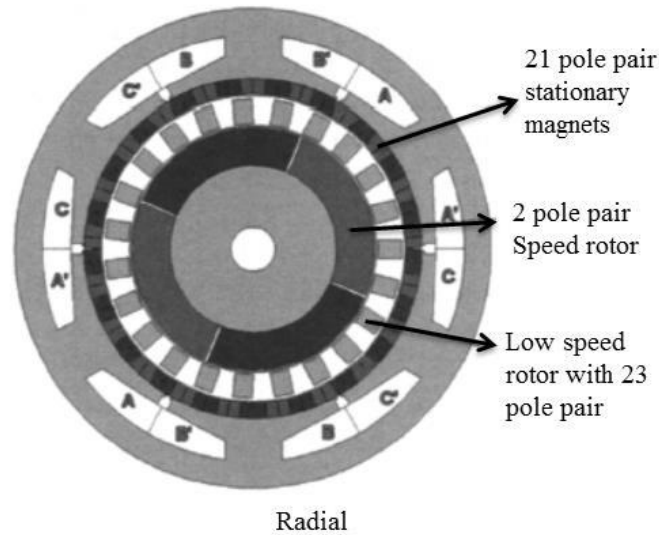


Figure 4.1. Cross Section of a High Torque Density PM Machine with Two Rotors [118].

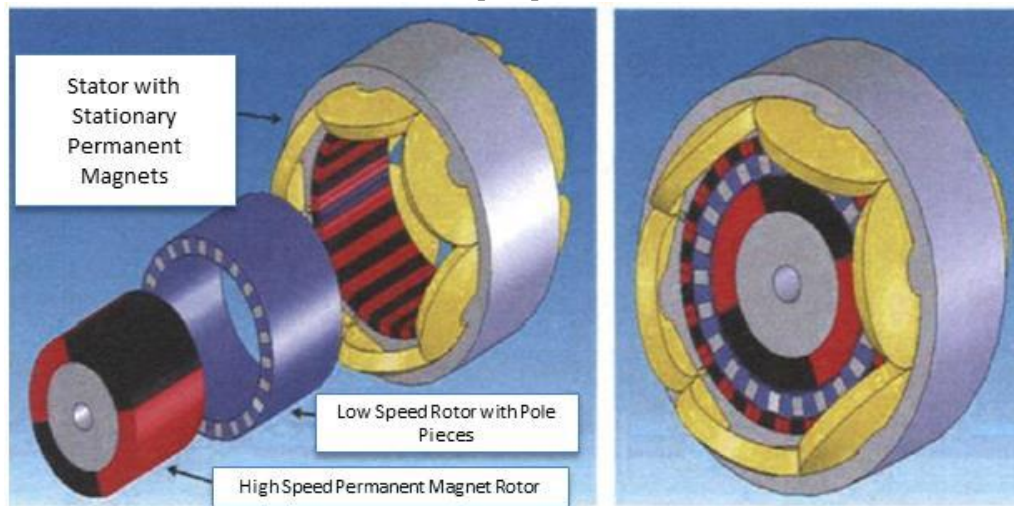


Figure 4.2. Parts of a High Torque Density PM Machine with Two Rotors [118].

In [119] an equivalent permanent magnet stepper motor design has been developed within the frame of a more conventional machine configuration of axial current and radial magnetic flux. It is compared in detail regarding the achieved torques to a more conventional permanent magnet machine configuration of the same dimensions and found to achieve higher torque density.

The concept behind the new design proposed in this thesis is that by splitting the stator teeth a higher torque output can be achieved. The new design is fully described theoretically and mathematically in this chapter. Two STPM machines have been designed, the second being a modified version of the first. The earlier is described in this chapter while the latter is described in the following chapter and both of them are compared in detail to a conventional brushless PM machines.

4.2 Design Concept

Consider a machine with no saliency, a magnetic field generated by the rotor, which generates a flux linkage per pole, φ_m , and a stator winding that has N_p turns and carries an instantaneous current i_p . The instantaneous power input P to the stator winding of the machine can be found as follows:

$$P = i_p \frac{d\Psi}{dt} \quad 4.2$$

This is also equal to the following:

$$P = i_p L_p \frac{di_p}{dt} + i_p N_p \frac{d\varphi_m}{d\theta} \quad 4.3$$

Where $i_p L_p \frac{di_p}{dt}$ corresponds to the rate change of energy stored in the magnetic field,

whilst the term $i_p N_p \frac{d\varphi_m}{d\theta}$ relates to the power input required to generate torque.

Hence the torque, T_p , produced per phase can be calculated as follows:

$$T_p = i_p N_p \frac{d\varphi_m}{d\theta} \quad 4.5$$

$$T_p = \left(\begin{matrix} \text{no of stator} \\ \text{windings} \\ \text{per phase} \end{matrix} \right) \times \left(\begin{matrix} \text{phase winding} \\ \text{MMF per} \\ \text{pole} \end{matrix} \right) \times \left(\begin{matrix} \text{rate of change of mutual flux} \\ \text{per pole with} \\ \text{relation to position} \end{matrix} \right)$$

From the equation above the following points can be observed:

- For a given slot area, conductor current density and therefore MMF, the torque per phase can be seen as independent of the number of turns as by reducing the number of turns the conductor size can be increased, hence larger current can be applied to maintain the same MMF.
- The torque can also be seen as independent of the number of phases, as the total MMF must drop when the number of phases increases.
- The number of poles does not affect the torque, as for a given magnetic loading

any decrease in pole pitch is accompanied by an equal reduction in the flux linking the coil (rate of change of flux is unchanged).

The concept behind the new design is to increase the total torque for a given electrical loading and magnetic loading. A way to increase the rate of change of the mutual flux with respect to position without reducing the stator phase winding MMF is required.

Increasing the rate of change can be achieved if the number of rotor poles of the same polarity can be linked by a specific stator winding MMF hence, the rate of change of the mutual flux will increase with respect to position. This is due to the smaller pole arc, whilst the total peak flux resulting from the high pole number and linking the winding is maintained.

This decoupling between pole number and stator winding MMF has been achieved by Hoffman and Landrath by applying a configuration with circumferential stator currents [120, 121]. A TFM design of circumferentially oriented magnets on a ring rotor in a flux concentrating type of configuration has been their preferred design. Optimum torques have been produced by having the rotor in a ring type construction with two parts of the stator, one inside the rotor and one outside. This design offers the potential to increase the torque output. However, it unavoidably suffers from some mechanical and electrical problems. The three dimensional nature of this machine's flux path within the core of the stator is one of the major electrical problems as the eddy currents against the effective lamination direction is found to be unavoidable. This topology can be seen in Figure 4.3.

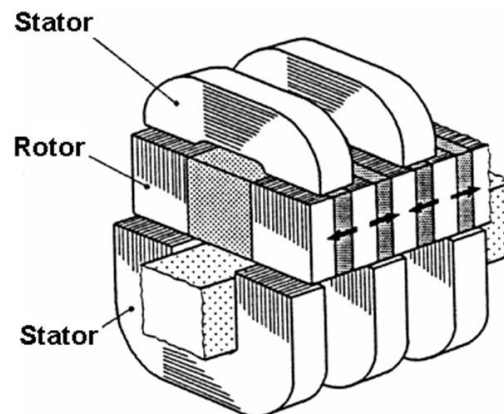


Figure 4.3. TFM Geometry With Flux Concentrated Magnets [120, 121].

An investigation into whether this can be implemented using a conventional machine

topology where the current can be employed in an axial direction and the flux in a radial/circumferential direction will be conducted.

The basic principle involved in the new design of the STPM machine has been illustrated in Figure 4.4 below, where a single stator coil is enclosed by an iron path that is common to three rotor poles identified as a, b, c, d and e, it can be seen that as the rotor moves through a full pole pitch, the mutual flux linking the stator windings will change from a maximum in one direction to a maximum in the other direction. So looking closely at the example, it's clear that for a given flux per pole, the rate of flux change is increased by a factor of five; this is known as the magnetic gearing ratio [122-127], which is five in this case. However only three poles are actually being utilised, which leads to a reduced magnetic loading of $3/5$, that will result in a net multiplication factor of three that is produced in the resulting torque per unit volume.

The basis of operation is essentially dependent upon the saliency of the stator iron path, by looking at the example it can be seen that a part from the three aligned poles there are another two unaligned poles of the opposite polarity. Which are assumed to be ineffective because of the high reluctance path, which their flux must traverse. In essence it is necessary for the unaligned permanent magnets to be driven back down their B-H characteristics in order for this configuration to work. Ideally a considerable increase in available torque results from the idea of this design. However, in practice it is very clear that's the rotor leakage flux and other effects should be taken into account and considered carefully. Hence it is essential to transfer the idea of this machine into an actual machine design and analyse it in some detail as will be seen in the following sections of this chapter.

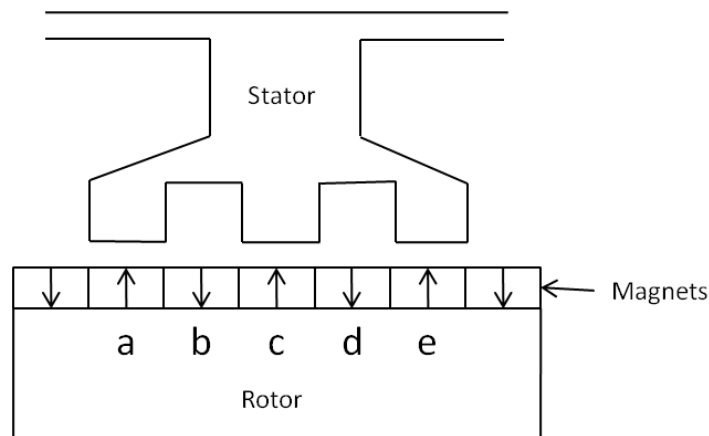


Figure 4.4. The New Split Tooth PM Machine Structure.

4.3 Machine Design

The split tooth design will be compared in detail to other more conventional configurations of the same dimensions in order to evaluate its performance. .

Two motor solve fully optimised radial PM brushless machines with 12 slots/ 4 pols and 12 slots /10 poles have been designed and analysed. Thereafter, the results obtained were compared to that of the new split tooth PM machine. Motor Solve has the ability to accurately deign the best module for a given specifications and topology because of its automated FE results module. Hence, it was found beneficial to use it in order to validate the results obtained.

The Split tooth PM has been designed to the same dimensions of both Motor Solve optimised radial PM brushless machines using the principles of PM machine design shown in Appendix A. it was then optimised using 2D FE methods for maximum torque output where a range of magnet thickness, magnet arc, tooth width and coreback depth have been applied.

The fixed physical dimensions and specifications used to design the three machines are listed in Table 4.1. These fixed dimensions and specifications have been chosen in order for the comparison machine to be used as a direct drive motor for an electric vehicle with a fixed rated speed of 6000 rpm and the maximum possible torque output.

Table 4.1. Fixed Dimensions and Specifications for Both Brushless PM Machine and Split Tooth PM Machine.

Machine	Both Brushless PM Machines	New Design with Surface Magnets
Stator outer/ inner diameter (mm)	200/50.5	200/50.5
Rotor outer diameter (mm)	100	100
Stack length (mm)	130	130
Speed (rpm)	6000	6000
Magnet	Neodymium Iron - Boron-	Neodymium-Iron - Boron

The conventional radial machines are a three phase brushless machines with the first one having a 12 teeth / 4 poles configuration and the second one having 12 teeth / 10

poles configuration. These are shown in Figures 4.5 and 4.6 below along with the winding arrangements, where also a surface mounted neodymium-iron -boron magnets were employed and magnetised in a radial direction for both machines.

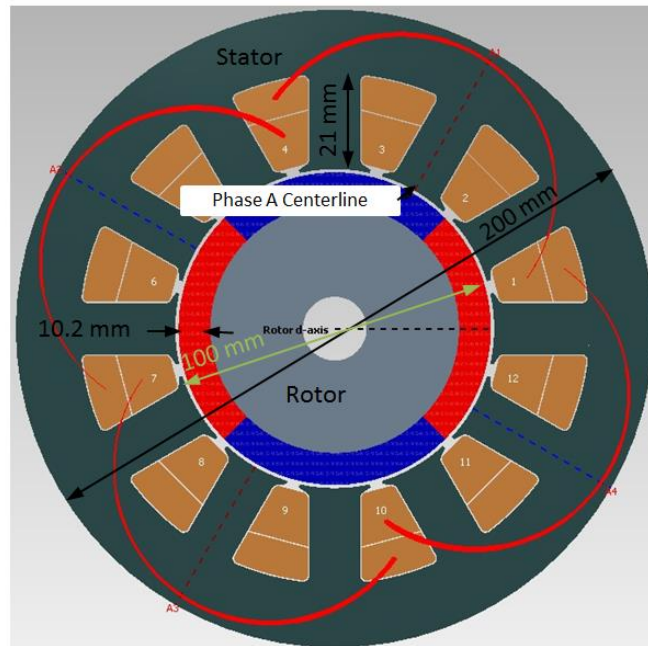


Figure 4.5. Optimised 12 Slots/ 4 Poles Brushless PM Machine Using Motor Solve.

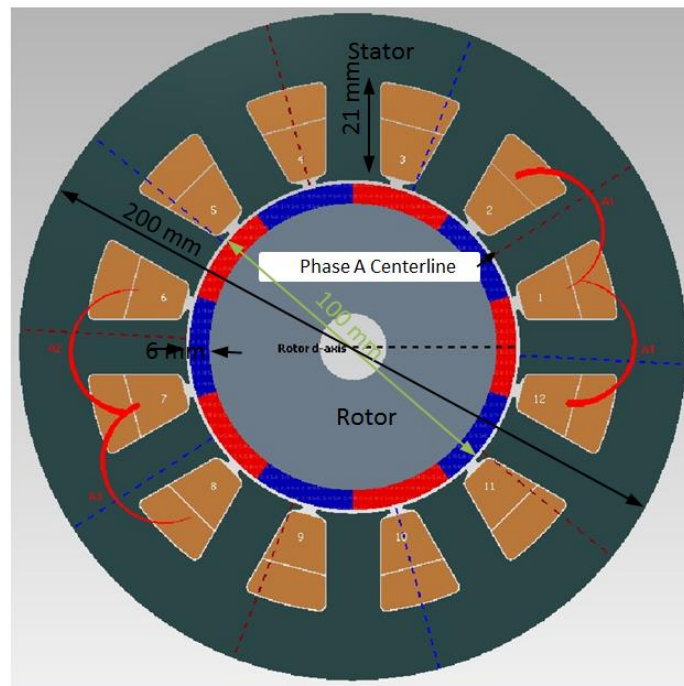


Figure 4.6. Optimised 12 Slots/ 10 Poles Brushless PM Machine Using Motor Solve.

The STPM machine configuration is designed as a three phase machine with 6 slots and

20 poles, where each tooth was split into two as illustrated in Figure 4.7, and surface mounted neodymium-iron-boron magnets are employed and magnetised in a radial direction.

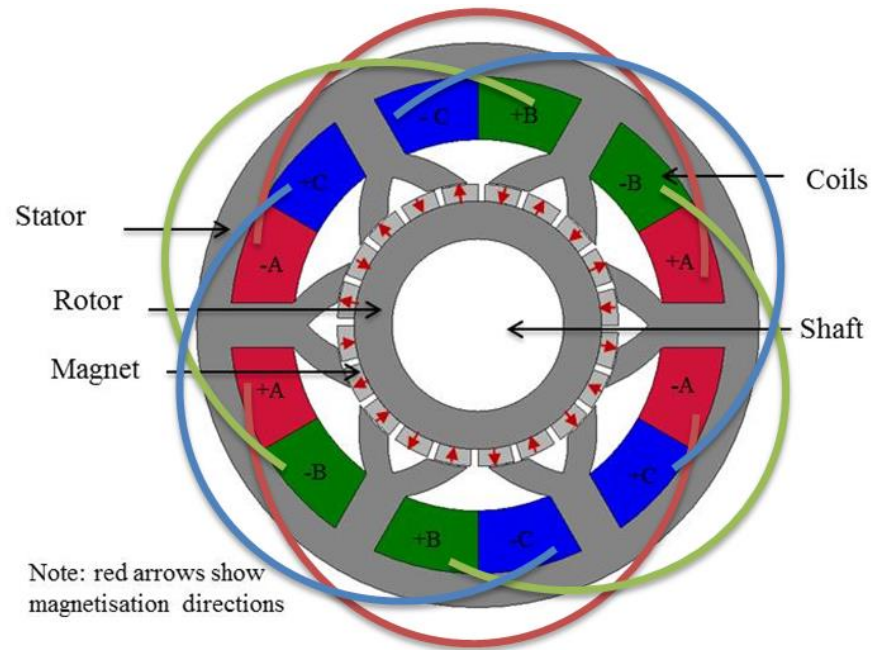


Figure 4.7. FE Cross Section of the Split Tooth PM Machine with 6 Slots and 20 Poles.

The 20 poles obtained here have resulted from the choice of 6 split teeth because this configuration requires three poles per tooth in order for the topology to work. This can be explained in Figure 4.8 where magnet 1 and 3 should be magnetised in the same direction, otherwise the flux will circulate back without linking the coil.

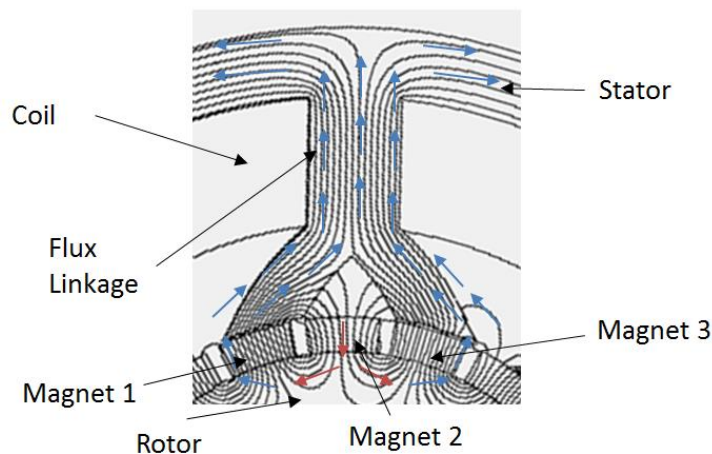


Figure 4.8. Magnet Required for Each Split Tooth

Although having 6 teeth would result in 18 poles, by taking the 120° electrical shift required between the three phases (for a balanced flux linkage) into consideration, two

extra poles were required, making a total of 20 required poles. This will be illustrated later in this chapter.

A fixed rotor diameter of 100 mm and an air gap length of 0.5 mm were chosen for both designs.

The higher pole number of the STPM machine, results in a high electrical frequency and consequently greater iron losses. This generally means this type of machines will need to operate at a lower speed.

The machine is modeled using 2D FE and due to the complexity of the magnetic circuit in the new design, the fringing (leakage) flux in between two magnets will be significant. Hence it is important to verify the sensitivity of the solution mesh before relying on the FE analysis.

The finite element method splits the geometry of the machine with a mesh of triangles called elements, where a polynomial with unknown coefficients represent each element, the solution of the set of equation for these unknown coefficients is the FE solution.

The elements in the 2D mesh have a triangular shape defined by three vertexes with a set of equations to be solved for the solution of the model's magnetic field. The mesh size and nature of the field indicate the accuracy of the FE solution, especially in areas where there are changes in the magnitude of the magnetic field and stored energy like in the air gap of the modelled machine.

In order to validate the accuracy of the FE solution, analysis of the mesh sensitivity was carried by reducing the element size until the rate of change of result with element size is minimal. This can also be done automatically by the software using auto adaption technique, which was used to validate the achieved element size. A finer mesh solution results in a longer solving time. However, due to the increasing power of modern computers; solution time is becoming smaller.

The air gap is more of a concern for refining its mesh as it has the most stored energy in the machine and is significantly affected by changes in the field directions; hence the mesh in the air gap is finer than that in the rest of the machine, as can be seen in Figure 4.9.

The air is split into four sections; stator air box, static air gap region, rotating air gap region and rotor air box, both stator and rotor air boxes extend to the air gap by 0.1 mm to insure they cover all stator and rotor components. This is necessary as the edges of the components have high field errors.

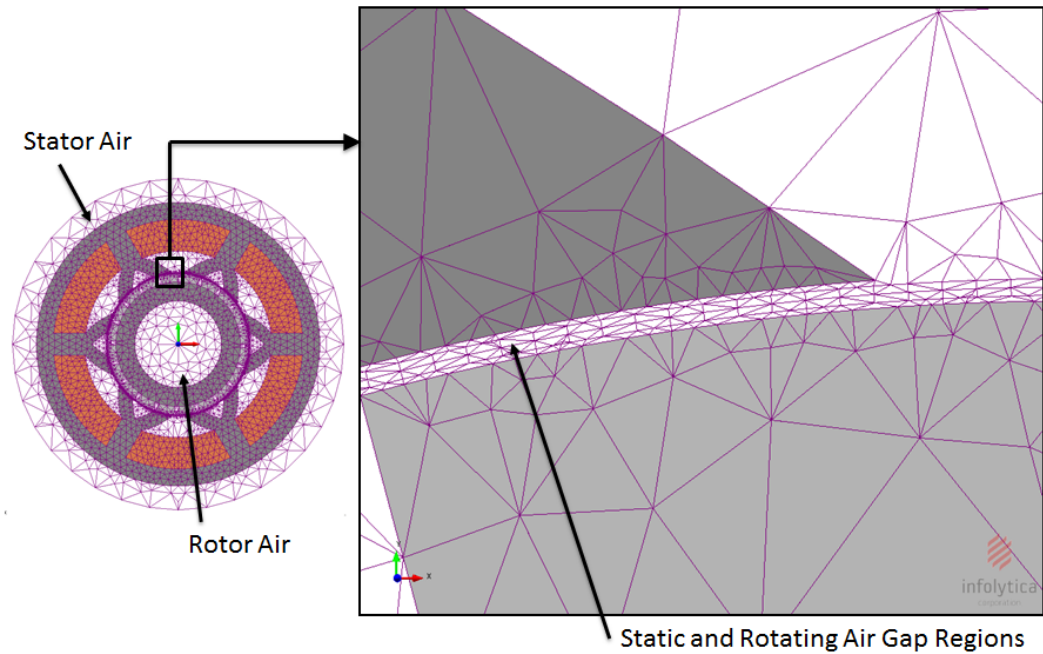


Figure 4.9. Mesh Distribution in a FE Cross Section of the Split Tooth PM Machine with 6 Teeth and 20 Poles.

4.3.1 Machine Dimensions

In this section the dimensions of the new STPM machine are shown in Figures 4.10. It has a frame size of 200 mm, a fixed air gap of 0.5 mm and a rotor outer diameter of 100 mm.

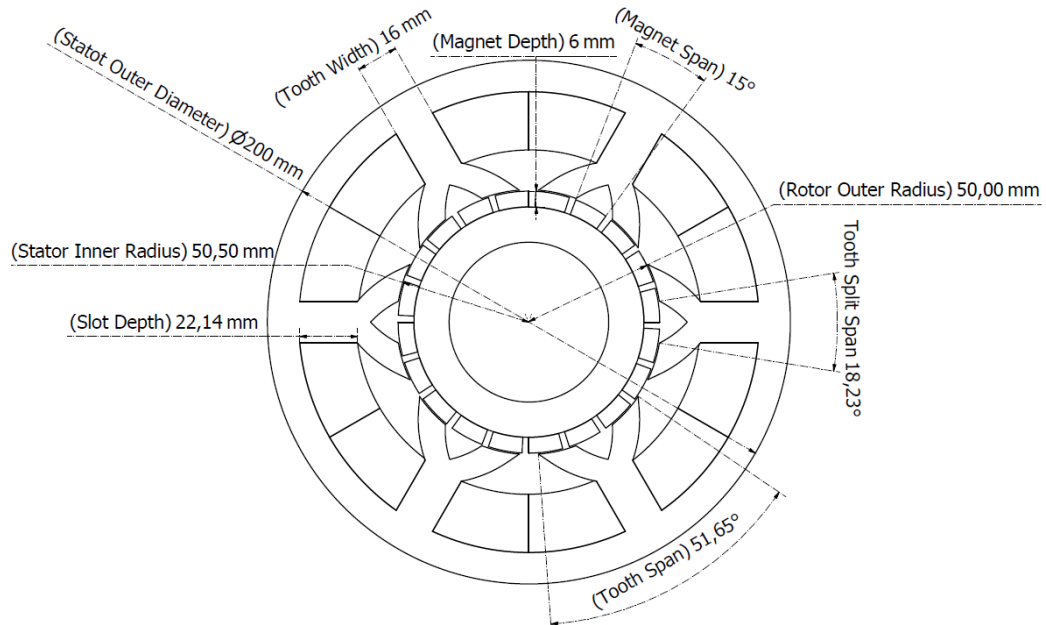


Figure 4.10. The Split Tooth Machine Considering a Frame Size of 200mm.

4.3.2 Winding Arrangements:

The STPM machine was wound using a single tooth, concentrated winding to form a three phase machine with short end windings and to give the maximum fundamental induced voltage. Figure 4.11 shows the winding arrangement inside the slots of the STPM machine. The STPM machine uses two teeth for each phase.

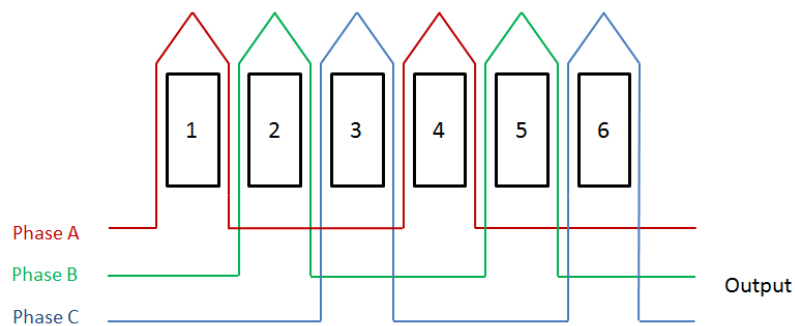


Figure 4.11. Winding Arrangement for the Split Tooth PM Machine.

4.4 No Load Analysis

A 2D FE no load simulation was conducted so that a flux path plot could be obtained and checked to ensure the correct flux path along with the correct three phase flux linkage balance. This solution involved rotating the rotor at the rated speed of 6000 rpm over one electrical cycle using 130 steps to obtain an accurate waveform.

4.4.1 Flux Density Distribution

Under no load condition with the rotor aligned at the d axis with respect to one phase, Figure 4.12 shows the mutual flux path of the STPM machine as indicated in by the red arrows along with the leakage flux path.

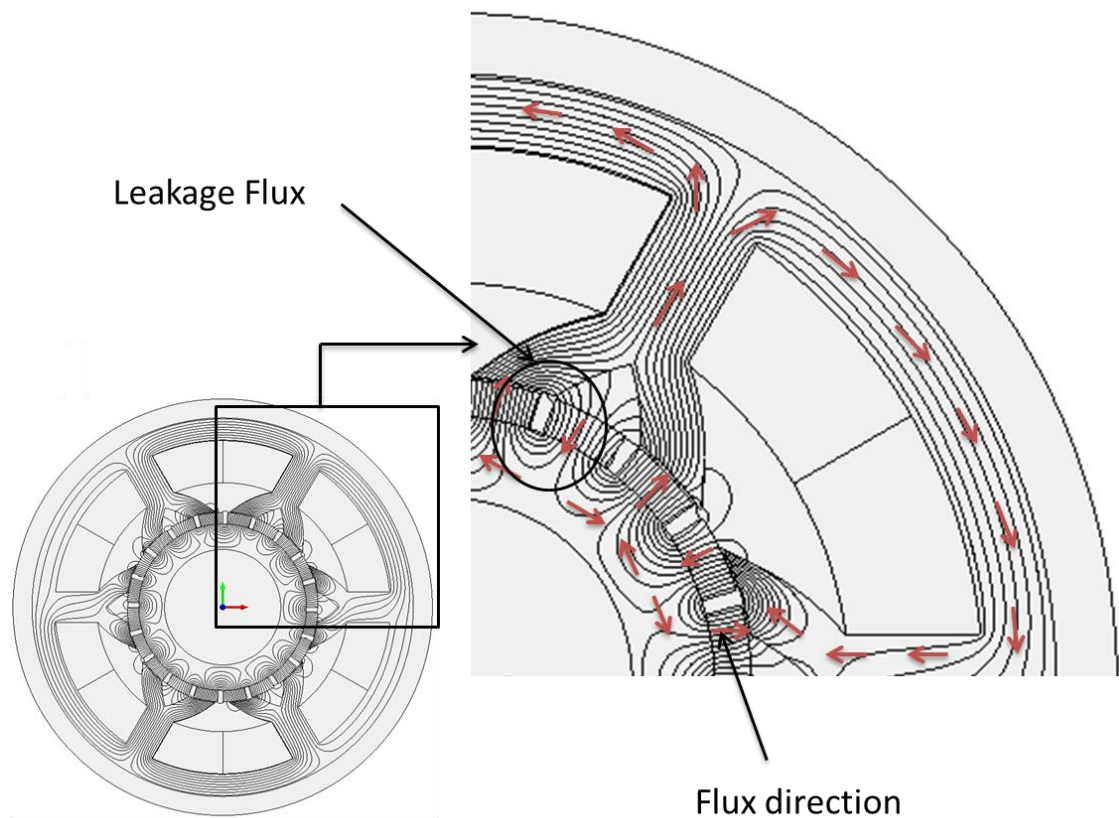


Figure 4.12. No Load Contour Flux Lines Plot of the Split Tooth PM Machine with 6 Teeth and 20 Poles of Surface Mounted PMs.

The no load flux linkage of the STPM machine over one full electrical cycle obtained is shown in Figures 4.13. It can be seen that the flux linkages are balanced with a 120° electrical between phases; this confirms the correct shift between phases for the new design.

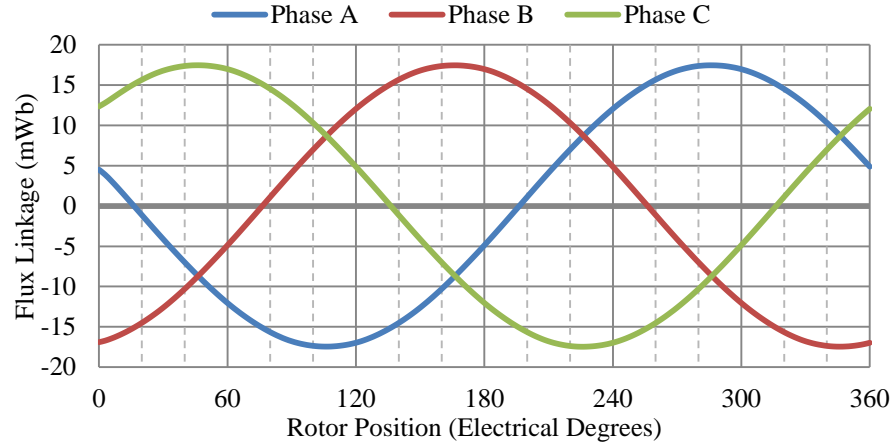


Figure 4.13. No Load Flux Linkage of the Split Tooth PM Machine Over One Full Electrical Cycle.

4.5 Load Analysis

The maximum permissible steady state conductor current density for an air cooling method is 10 A/mm^2 [128]. This current density can however be increased if an improved cooling method is used. For simplicity a fixed current density of 5 A/mm^2 has been used for the purpose of comparison between the designed machines here.

A 2D FE static simulation has been conducted for all three machines. This was done by moving the rotor angle to be aligned with the peak back EMF (q-axis) of phase A in a machine that is connected in star. Then a range of current was applied to phase A in series returning through phase B and C in parallel (giving a maximum 1pu current in phase A and -0.5pu in phase B and phase C). This arrangement can be seen in Figure 4.14.

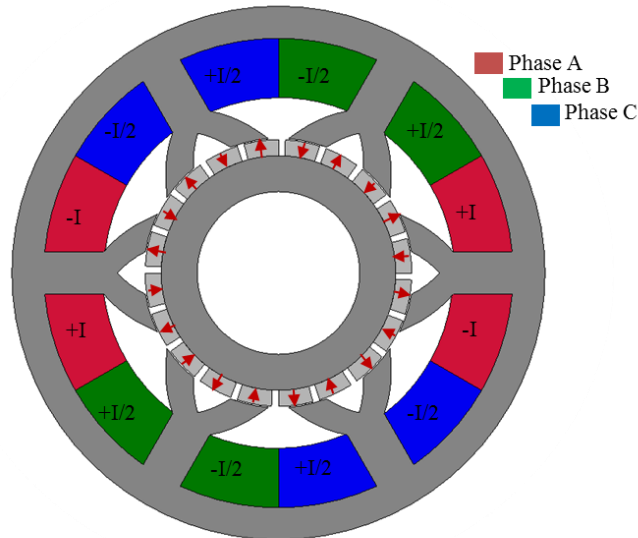


Figure 4.14. Static Simulation Coil Arrangements.

Before comparing the STPM machine to both brushless PM machines, different split tooth shapes are analysed and compared. Figure 4.14 shows a shaded flux linkage plots for the four most appropriate shapes.

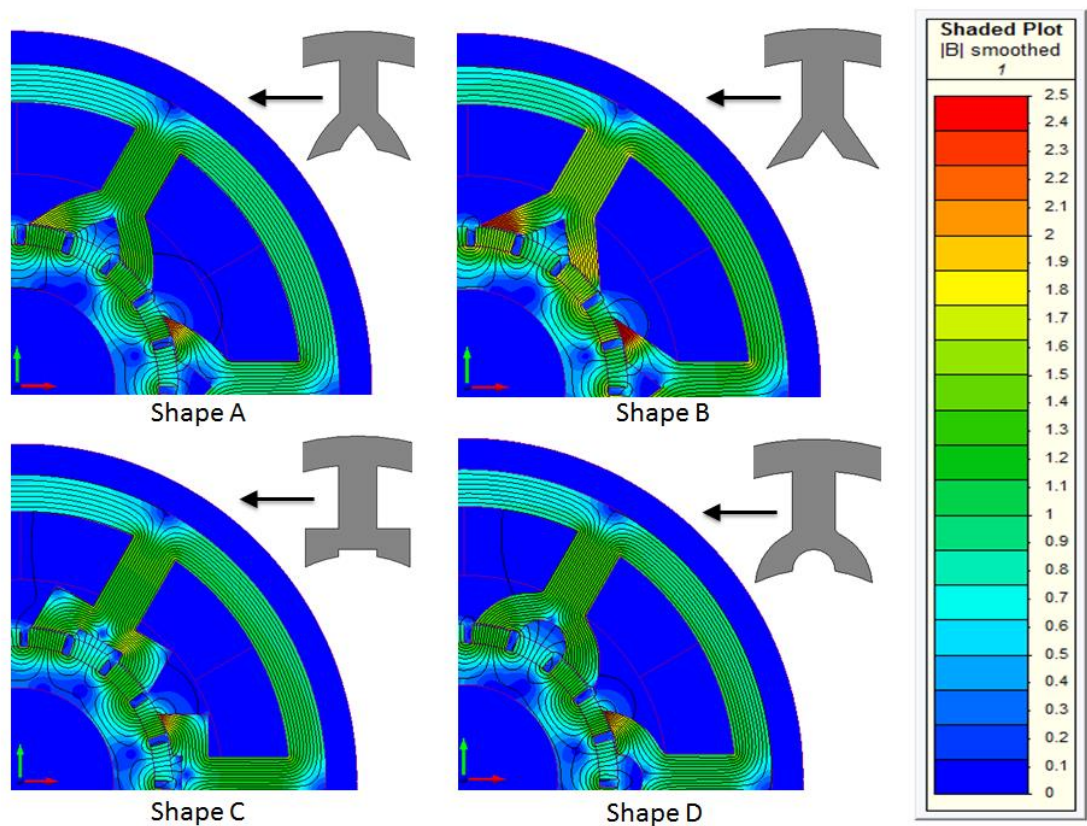


Figure 4.15. Shaded Flux Linkage Plots for the 4 Most Appropriate Split Tooth Shapes.

4.5.1 Static Torque

Comparing torque against current density is visible because it determines the maximum torque; the machine can operate at, considering the maximum permissible steady state conductor current density (5 A/mm² for the comparison). By using the analysis obtained using 2D FE along with slot area calculations for each machine, torque against current density was obtained for the four most appropriate split tooth shapes and are shown in Figure 4.16.

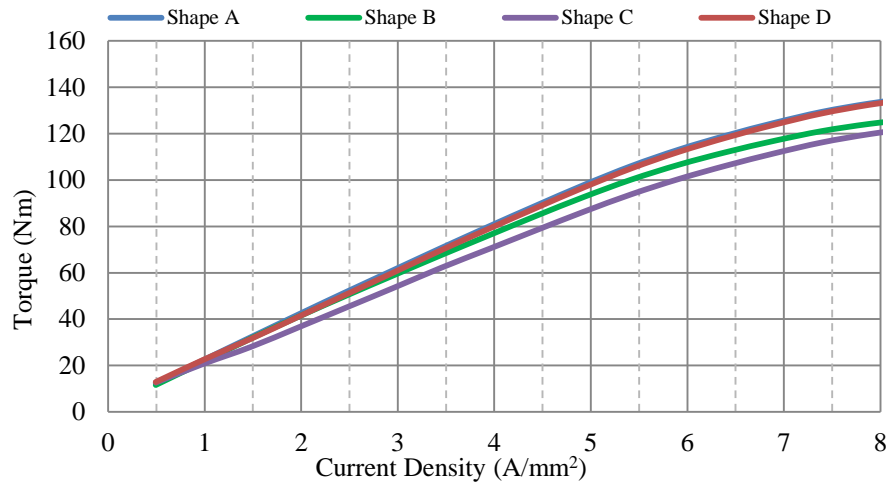


Figure 4.16. Static Torques Over a Range of Current Densities of the 4 Most Appropriate Split Tooth Shapes.

It can be seen from Figure 4.16 that the STPM machine with shape A and D split tooth have the highest achievable torque against current density. However, Shape A has a 2 % less mass than shape D, and hence it was chosen.

Also a torque against current density was obtained to compare the STPM machine and both of the optimised brushless PM machines shown in the previous section as shown in Figure 4.17.

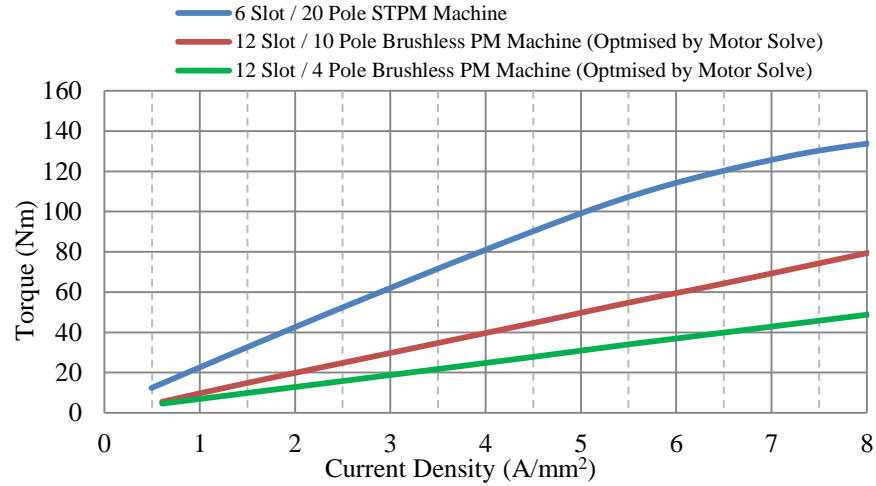


Figure 4.17. Static Torques Over a Range of Current Densities of Both the Split Tooth PM Machine and the Brushless PM Machine.

In Figure 4.18, the new STPM Machine showed a significant improvement in torque against a range of current densities.

Furthermore, 100 Nm, 34.1 Nm and 45 Nm were achieved by the STPM machine, the 12 slots/ 4 poles and 12 slots/ 10 poles brushless PM machine at the maximum conductor current density of 5 A/mm² respectively. This corresponds to a 193 % and 122 % increase in achievable output torque for the new split tooth PM configuration over the 12 slots/ 4 poles and 12 slots/ 10 poles brushless PM machine. This validates the concept of the new design.

The aim of this thesis is to improve torque density; hence it was essential to compare both designed machines using the achieved torque per unit mass as shown with a detailed comparison in Table 4.2.

Table 4.2. Comparison between the STPM Machine and the Brushless PM Machine.

Machine	12 slots/ 4 poles Brushless PM machine	12 slots/ 10 poles Brushless PM machine	New Design with surface magnets
Outer Diameter (mm)	200	200	200
Axial Length (mm)	130	130	130
Rotor Outer Diameter (mm)	100	100	100
Total slot area (mm ²)	10120	10120	8608
Current Density (A/mm ²)	5	5	5
Iron loss	440	460	650
Gear ratio	1	1	5
Torque (Nm)	34	45	100
Mass (Kg)	29.83	28.34	25.93
Magnet mass (Kg)	1.71	1.17	1.49
Torque density (Nm/Kg)	1.14	1.6	3.85
Torque to magnet ratio (Nm/Kg)	19.9	38.5	67.1

From table 4.2, it can be seen that the STPM machine has achieved 237 % and 141 % more torque density compared to the 12 slots/ 4 poles and 12 slots/ 10 brushless PM machines respectively. However, it has 47.7 % and 41 % more iron loss than the 12 slots/ 4 poles and 12 slots/ 10 brushless PM machines respectively.

4.6 Conclusion

A new method of driving greater torque density from a convention PM machine topology has been described and compared to two motor solved optimised brushless PM machines of the same dimension using 2D FE analysis. The method involved splitting the stator teeth in order to introduce a magnetic gear ratio into the torque equation.

The STPM machine introduced in order to be used as a direct drive motor for an electric vehicle. It was designed to produce the maximum possible torque output for a fixed physical dimensions and specifications.

The new machine has shown a significant improvement of 237 % and 141 % more torque density compared to the 12 slots/ 4 poles and 12 slots/ 10 brushless PM machines respectively.

The STPM machine has more iron loss and this is due to the higher electrical frequency required for the same speed.

One drawback for the STPM machine design despite its achievable high torque density is that as the machine rotates, and each rotor magnet moves from a position under a stator split tooth to one between them, it experiences a large change in flux density.

This changing flux density will inevitably induce eddy currents within the magnets and result in magnet losses. These losses can in certain cases be significant; indeed because of the degradation of the magnet properties at relatively high temperature. Hence, they must be regarded with some concern.

Within the next chapter an alternative design is developed in order to reduce this problem; by employing slightly different configurations. It also manages to further increase the achievable torque output.

Chapter 5. Development of the Split Tooth PM Machine

The STPM machine was discussed in Chapter 4 and found to suffer from the leakage from the aligned poles between the split teeth. To reduce this effect an improved design was developed and is discussed in this chapter. In this improved design, the magnets are alternatively magnetised in a circumferential direction in a flux concentrating arrangement. This chapter concludes with a comparison between the improved STPM machine, the initial STPM machine and the two brushless PM machines developed in the previous chapter.

5.1 Modified Machine Design

Higher transmission efficiency, lower acoustic noise and maintenance free operation have attracted attention to the concept of magnetic geared machines where double stator and single rotor machines are very popular. This is because of their high torque density and performance. Figure 5.1 shows different examples of such topology.[129, 130]

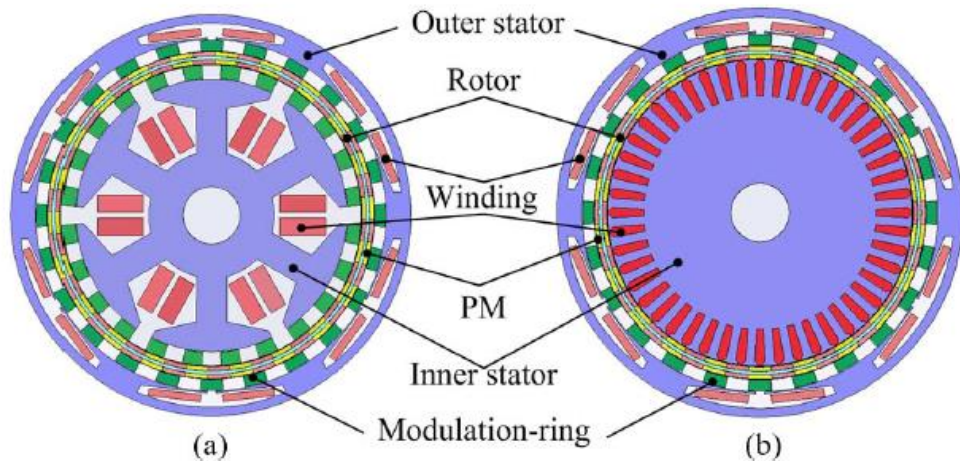


Figure 5.1. Double Stator and Single Rotor Machines (a) Dual Ring Type (b) Single Ring Type [129].

In the design considered in Chapter 4 the magnets are only used for a portion of the time. When they are aligned between the stator teeth they are actually detracting from the stator flux linkage, and hence act to reduce the total torque generated by the machine. A design where all magnets under a stator coil contributed to the coil flux linkage would be preferable; such a design is illustrated in Figure 5.2. The rotor contains permanent magnets magnetised in a circumferential direction in alternative directions in a flux concentration arrangements. The stator now must consist of two parts; an outer and an inner section; the rotor now forms an annular ring between. The outer stator is identical to before and the inner stator can operate in one of two ways; either as a second fully wound component, or, as a flux return path only. The basic path for the magnetic flux is now from the inner stator, across the air gap and into the rotor through the rotor magnets and radially outwards across a second air-gap into the outer stator. All magnets continuously carry approximately the same amount of flux, and therefore the losses within them are considerably reduced from the previous case.

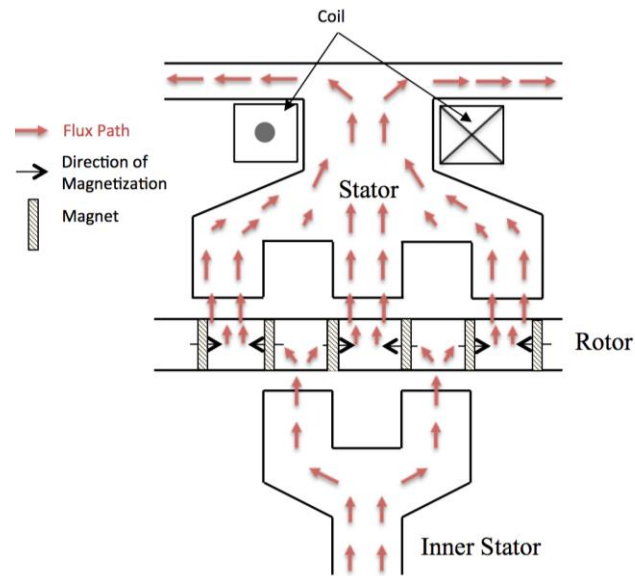


Figure 5.2. The New Modified Split Tooth PM Machine Structure.

Different configurations using different PM topologies have also been tried. However, they have shown no improvement to the new design due to the flux path, which allows the flux to circulate back to the rotor without linking the coil as can be shown in Figure 5.3.

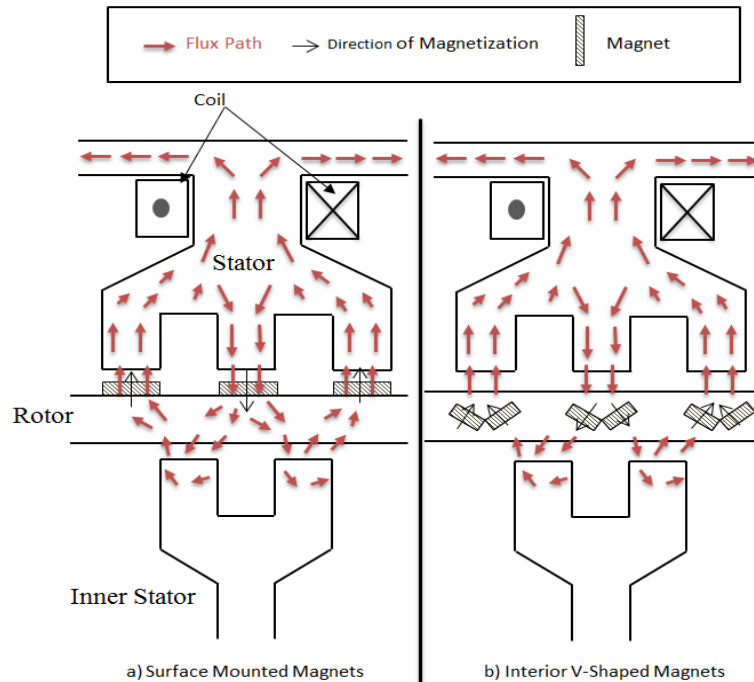


Figure 5.3. a) STPM Machine With Surface Mounted Magnets b) STPM Machine With Interior V Shaped Magnets.

It can be seen from Figures 5.2 and 5.3 that the flux concentrated magnets are most appropriate PM topology for the STPM machine with the inner stator.

Implementation of this principle into three-phase geometry is shown in Figure 5.4. The outer stator remains unaltered from before with the same winding arrangements. The 0.5 mm air gap depths have been used for both the inner and outer gaps.

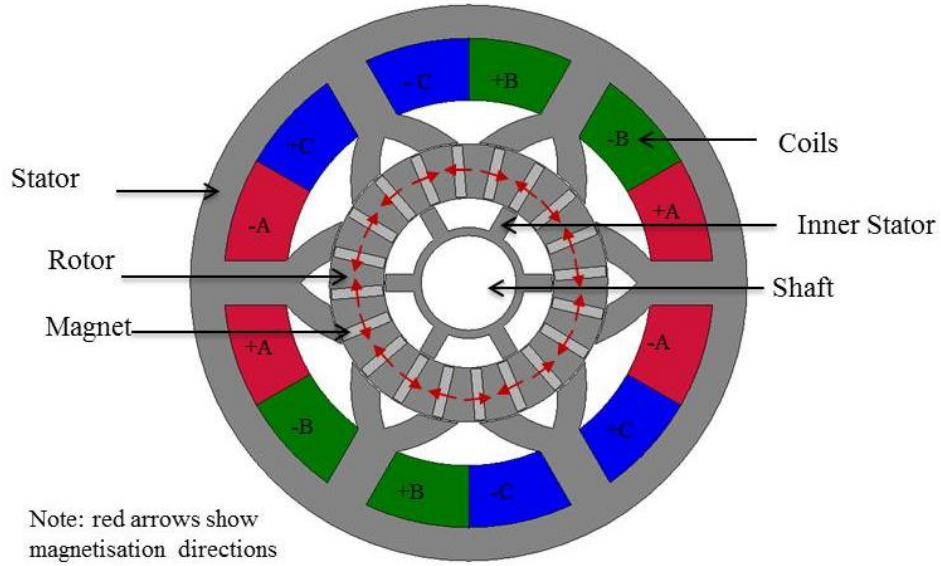


Figure 5.4. FE Cross Section of the Modified Flux Concentrated Split Tooth PM Machine with 6 Teeth and 20 Poles.

5.1.1 Modified Machine Dimensions

The dimensions of the outer stator, rotor and inner stator of the modified flux concentration PM STPM machine are as shown in Figures (5.5, 5.6, and 5.7) respectively (using the same space envelope used for both machines developed in Chapter 4).

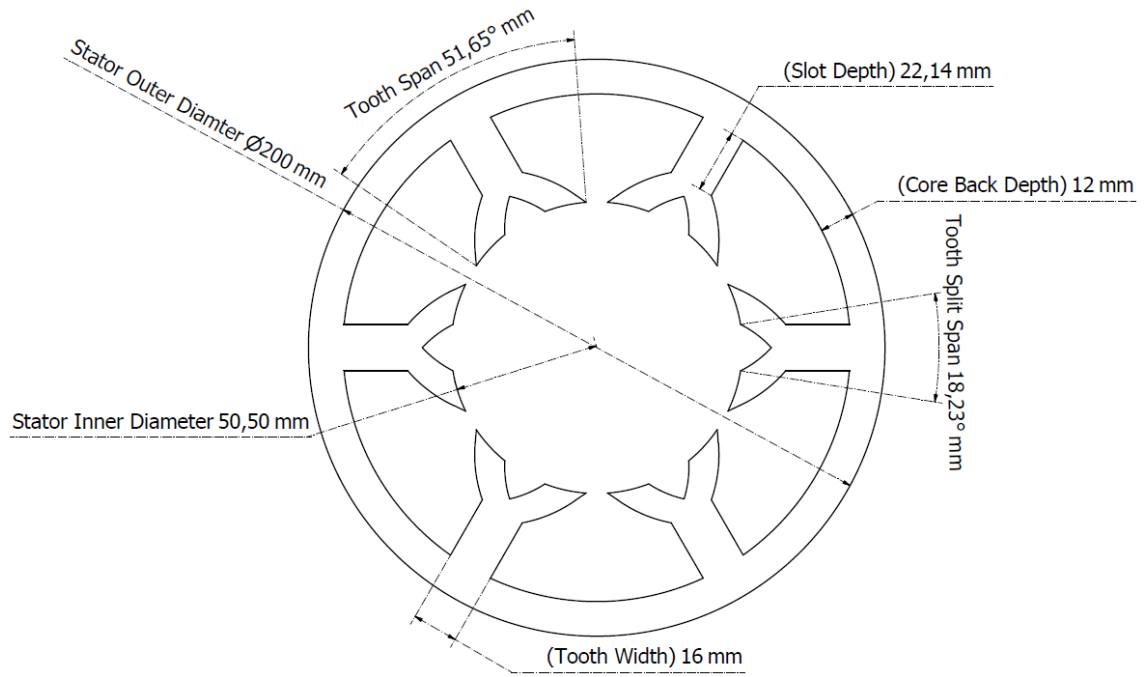


Figure 5.5. Stator Dimensions of the New Modified Flux Concentrated Split Tooth PM Machine.

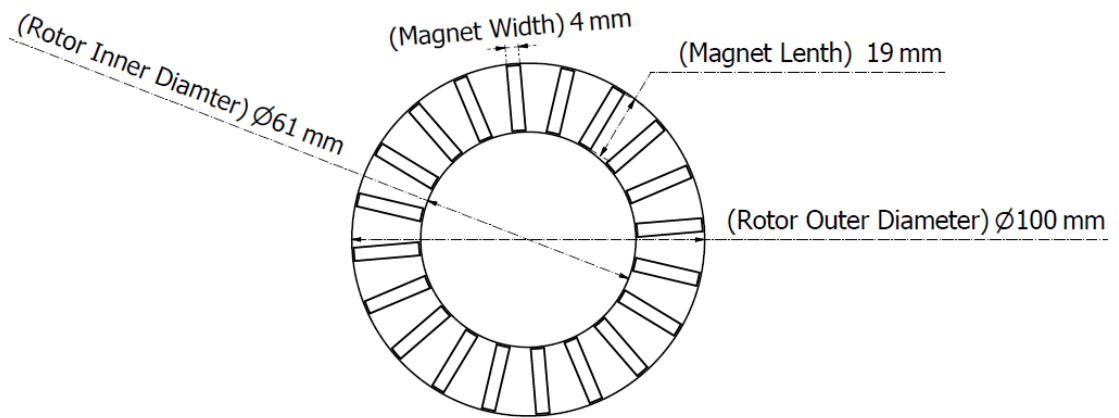


Figure 5.6. Rotor and Magnet Dimensions of the New Modified Flux Concentrated Split Tooth PM Machine.

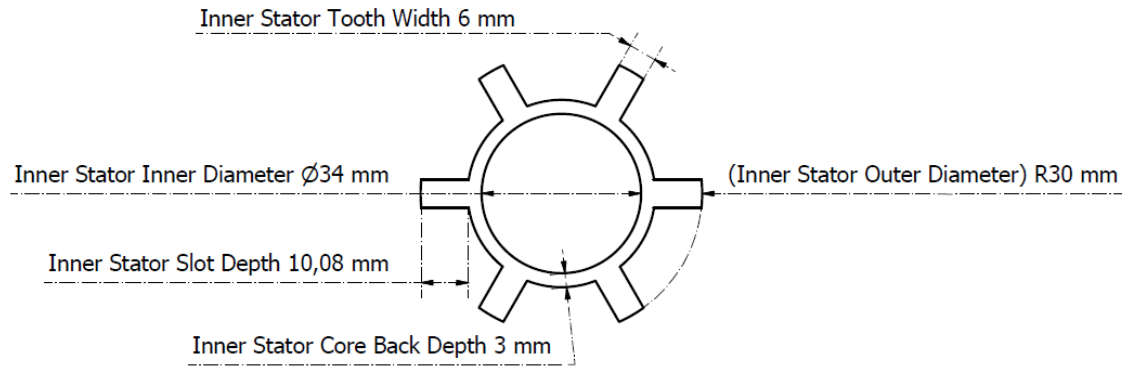


Figure 5.7. Inner Stator Dimensions of the New Modified Flux Concentrated Split Tooth PM Machine.

5.1.2 Modified Machine Mechanical Complexity

In the following sections, the new design is shown to be electromagnetically superior to that presented in Chapter 4; additional mechanical complexity is introduced by having an annular rotor between two stator components. However, such a configuration is feasible [131-133].

In order to mechanically restrain the rotor magnets it is proposed that the rotor lamination be made in one piece with bridges around the inner and outer radii of the magnets. This is shown in Figure 5.8. A bridge inevitably leads to increased rotor leakage flux, but such a feature is necessary for mechanical integrity.

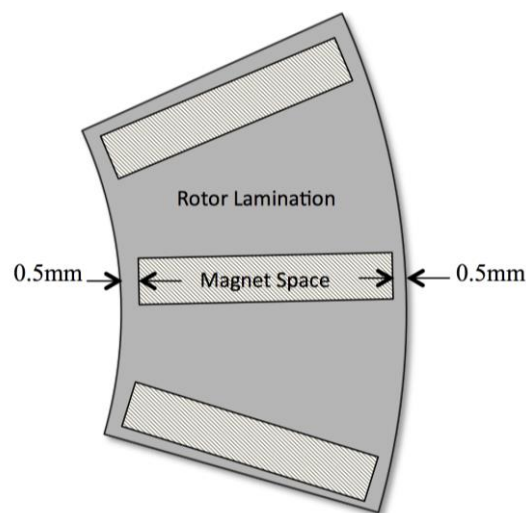


Figure 5.8. Rotor Lamination with Bridge Pieces Around the Inner and Outer Radii of One Magnet.

5.2 No Load Analyses of the Newly Modified Machine Design

No load analyses were obtained using 2D FE method where a transient with motion model was solved in order to observe the back EMF and obtain flux distribution plots and flux linkage waveform.

5.2.1 Flux Density Distribution

Figure 5.9 shows a no load flux contour plot at the position of maximum flux linkage with phase A. It can be seen from the figure that the flux linking this coil is comprised of two components; the first component is shown by the orange arrows where the first magnet finds a flux return path through the adjoining stator tooth. This path is essentially as in the earlier design however the second rotor magnet now also links the stator coil; whilst part of its return path is through the outer stator as can be shown by the purple arrows, the same flux also uses the stationary inner magnetic closure path. This second component of stator flux is additional to that in the earlier machine, and therefore results in an increase in total flux linkage and output.

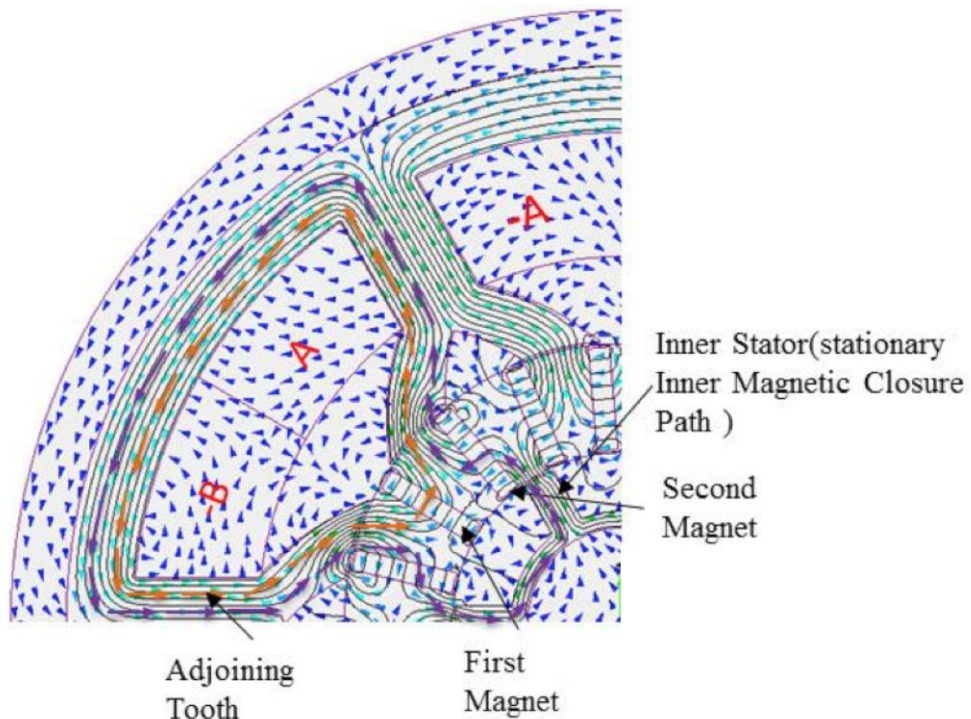


Figure 5.9. No Load Contour Flux Lines Plot of the Modified Split Tooth PM Machine with 6 Teeth and 20 Poles of Flux Concentrated Magnets.

5.2.2 Flux Linkage

The no load flux linkage of the modified STPM machine over one full electrical cycle obtained from the FE 2D simulations is shown in Figure 5.10. It can be seen that the flux linkages are balanced with a 120° electrical between phases which confirms the correct shift between phases.

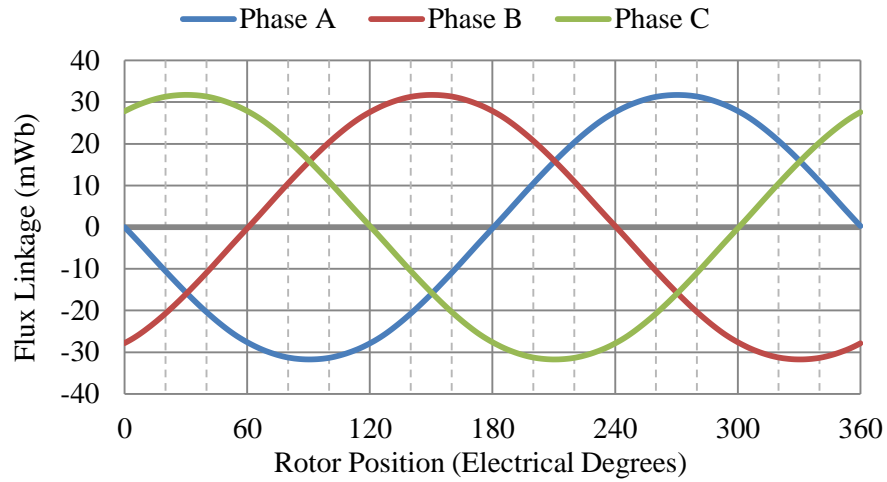


Figure 5.10. No Load Flux Linkage of the Modified Split Tooth PM Machine Over One Full Electrical Cycle.

A comparison between the peak flux linkages obtained by both STPM machines is shown in Figure 5.11.

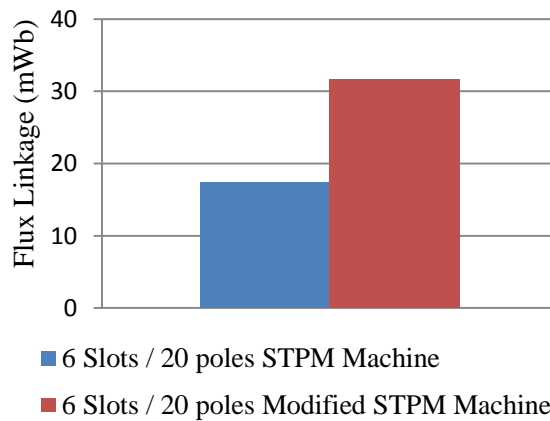


Figure 5.11. Peak Flux Linkage Comparison Between Both the Initial and Modified STPM Machines.

From Figure 5.11, it can be seen that the modified STPM machine has a 72 % increased peak flux linkage than that obtained by the initial STPM machine.

5.3 Load Analysis of the Newly Modified Machine Design

5.3.1 Static Torque

Figure 5.12 shows the modified STPM machine static torque against current densities when compared to the initial STPM machine with the surface mounted magnets.

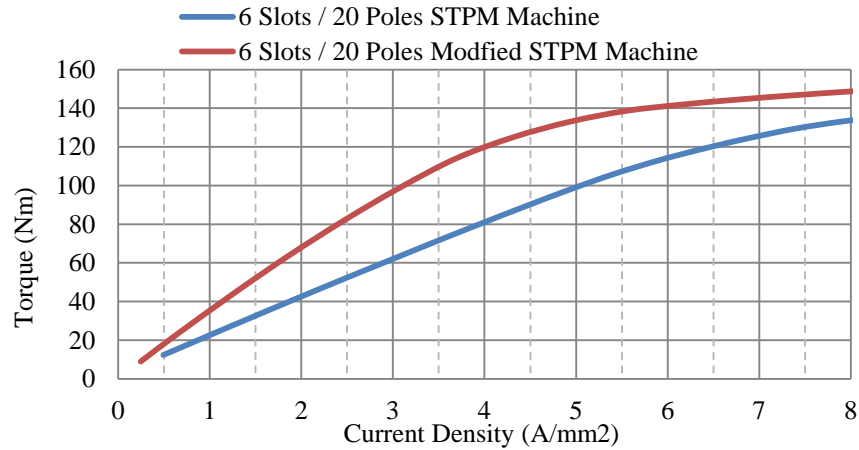


Figure 5.12. Static Torques Over a Range of Current Densities of the Initial and Modified Split Tooth PM Machine.

The modified STPM Machine shows a significant improvement in output torque. Also by specifying the point of the maximum permissible steady state conductor current density of 5 A/mm^2 , the modified design has 135 Nm, which is 35 % greater than that of the initial STPM machine with surface mounted magnets. In addition, The inner and outer air gap torques generated in the modified STPM machine can be seen in Figure 5.13.

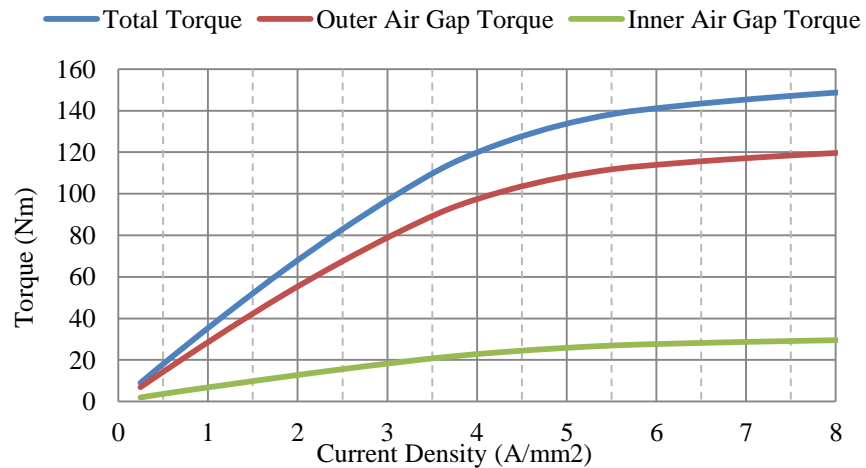


Figure 5.13. The Torque in Both Air Gaps of The Modified STPM Machine.

It can be seen from Figure 5.13 that the total torque generated by the modified machine is the sum of the torques generated by the two stators. The torque generated using the inner stator is only 18.5% of the total torque achieved.

5.4 Evaluation of Flux Concentration Topology over the Conventional Geometry

Because of the improved magnetic circuit of the new modified design shown in Figure 5.4, the magnetic loading is now increased as can be seen in Figure 5.11. It is also important to note the negative electromagnetic effect of the surface mounted magnet as it increases the effective air gap length while the flux concentration topology permits a flux density in the air gap much higher than that in the magnets and hence increased machine torque density. Also the implementation of the inner stator in the modified design has limited the leakage flux, so that more flux can be linking the phases, increasing the flux linkage. Since for the modified design the winding geometry and dimensions remain unaltered from the original STPM machine. However, there is no change in electric loading.

A maximum steady state output torque of 135 Nm that is 35% greater than the maximum torque achieved with the conventional flux STPM machine geometry, which was obtained by applying the same electric loading applied to the STPM machine with surface mounted magnets.

5.5 Comparison between the Four Machine Designs.

Table 5.1 summaries the important features of all four machines. Although the brushless PM machine geometries have greater magnetic and electric loadings than the new designs, but the influence of the magnetic gearing more than offsets this effect. The STPM machine designs flux concentration magnets consistently produced higher torques than both brushless PM machine and STPM machine with surface mounted magnets as can be seen from the table.

Table 5.1. The Important Features of All Four Machines.

Machine	12 slots/ 4 poles Brushless PM Machine	12 slots/ 10 poles Brushless PM Machine	New Design with Surface Magnets	New Design with Flux Concentration
Outer Diameter (mm)	200	200	200	200
Axial Length (mm)	130	130	130	130
Rotor Outer Diameter (mm)	100	100	100	100
Total slot area (mm ²)	10120	1020	8608	8608
Current Density (A/mm ²)	5	5	5	5
Iron loss (W)	440	460	650	697
Gear ratio	1	1	5	5
Torque (Nm)	34	45	100	135
Mass (Kg)	29.83	28.3	25.93	27.13
Magnet mass (Kg)	1.71	1.17	1.49	1.36
Torque density (Nm/Kg)	1.14	1.6	3.85	4.97
Torque to magnet ratio (Nm/Kg)	19.9	38.5	67.1	99.26

From Table 5.1, it can be seen that the developed STPM machine achieved 35 % more torque than the initial STPM machine. And although, the developed STPM machine results in a higher mass due to the inner stator, it was still able to produce 29 % more torque density than the earlier STPM. Furthermore, the developed PM machine reduced the magnet mass by 8.7 % and simultaneously increases the Torque to magnet mass by 48 % when compared to the initial STPM machine.

In addition, Iron loss has increased by 58 % from 12 slots/ 4 poles Brushless PM Machine to the STPM machine with concentrated magnets. This is because of the higher pole number of the STPM machine and hence the electrical frequency for the same speed.

5.6 Conclusion

A new PM machine design has been described and developed which shows an increased torque density over two optimised conventional brushless PM machines.

The performance of the new design has been compared with a conventional brushless PM machines of the same size. Also a further modified design of the new geometry that shows a further increase in torque density can be made using flux concentration magnets and an inner stator.

The new design requires the splitting of the stator teeth, so that a larger number of poles can be enclosed by the stator winding. The designs considered have stator teeth that split into two.

The advantages and disadvantages of the new designs:

1. The new machine has the advantage of introducing an additional factor into the output torque equation.
2. The new STPM machine produces a 193 % and 122 % than 12 slots/ 4 poles and 12 slots/ 10 poles brushless PM machines respectively.
3. A modified design of the new STPM machine with flux concentration magnets has shown a further 35 % increase in torque output.
4. The implementation of the inner stator in the modified design has harnessed more flux to link the phases, increasing the overall flux linkage.
5. The new design has a reduced electrical loading, as the slot area is reduced by the split tooth geometry.
6. Higher pole number in the new design results in a higher stator electrical frequency, and hence greater iron losses in the machine. This needs some consideration.

From the two split tooth designs considered here the first was found to be suffering from varying flux linkage within the magnets because of the large change in flux density when each rotor magnet moves from a position under a stator split tooth to one between them, which increases the danger of high magnetic losses, and overheating. However, the second modified design overcame this problem by allowing all magnets under a split tooth to be utilised at any one instant and simultaneously results in greater

torque output.

Table 5.2 compares both the Brushless PM machines with both STPM machines.

Table 5.2. Comparison between All Three Machines.

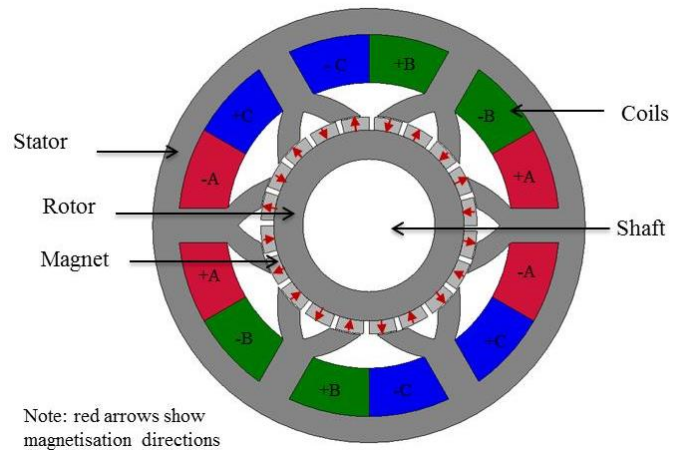
Machine	12 slots/ 4 poles Brushless PM Machine	12 slots/ 10 poles Brushless PM Machine	New Design with Surface Magnets	New Design with Flux Concentration
Torque (Nm)	34	45	100	135
Mass (Kg)	29.83	28.3	25.93	27.13
Iron Loss (W)	440	460	650	697
Magnet mass (Kg)	1.71	1.17	1.49	1.36
Torque density (Nm/Kg)	1.14	1.6	3.85	4.97
Torque to magnet ratio (Nm/Kg)	19.9	38.5	67.1	99.26

The STPM machine with concentrated magnets shows a factor of 2.9 and 2.2 increase in output torque when compared to 12 slots/ 4 poles and 12 slots/ 10 poles brushless PM machines; this is as a result of the improved magnet utilisation.

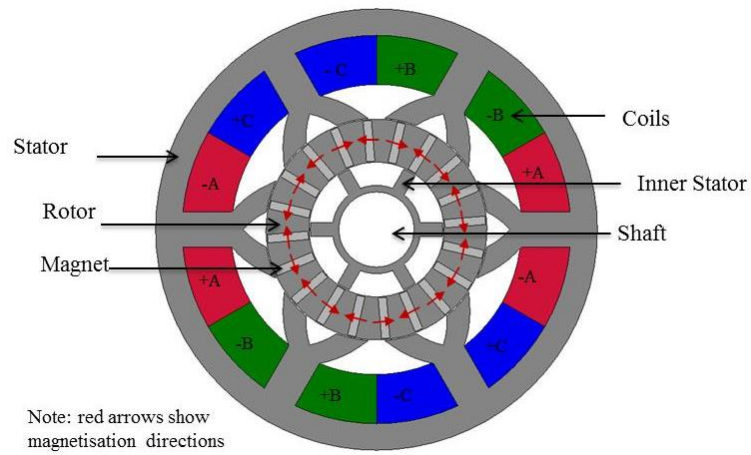
It can also be seen that the STPM machine with concentrated magnets has a factor of 4.4 and 3.1 increase in torque density when compared to 12 slots/ 4 poles and 12 slots /10 poles brushless PM machines. However, it has up to 54% more iron loss.

Figure 5.14 shows a geometry comparison of both initial and modified STPM machines compared in table 5.2.

a) STPM Machine with Surface Mounted Magnets (Initial).



b) STPM Machine with Flux Concentrated Magnets (Modified).

**Figure 5.14. Geometries of Both STPM Machines.**

The STPM machine with flux concentrated magnets will be further optimised. The optimisation method discussed in the following chapter.

Chapter 6. Design Optimisation

In this chapter the method used for designing, evaluating and optimising the STPM machine with concentrated flux magnets will be described.

The method involves writing a full script file to parameterise every vertex of the machine. This allowed a number of MagNet 2D FE simulations to be easily run for different designs. Descriptions of the effect of all the fixed and variable parameters used will be shown here. The possible slot and pole combinations for the STPM machine will be explained, evaluated and compared here in order to find the best combination with the highest torque.

6.1 Introduction

The initial design and evaluation of the STPM machine with concentrated magnets presented in Chapter 5 showed promise; it has therefore been decided to further improve its design to achieve a higher torque density by:

- Evaluating different slot and pole combinations in order to find the optimum combination.
- Investigating the machine's performance over a range of dimensions to find the optimum dimensions.
- Using the commercially available optimisation tool OptiNet™, to optimise the design.

In this optimisation, it is considered essential to keep the following dimensions fixed:

- Stator outer diameter.
- Air gap length.
- Axial length.

Other factors that must be taken into consideration are:

- The rotor has to rotate between two stationary stators and be connected directly to a shaft, this must be mechanically feasible.
- The pole number limit placed by the electrical frequency capability of the inverter.
- Single tooth winding will be used due to the shorter axial length.
- The rotor lamination bridges need to be thick enough for mechanical strength, yet small enough to saturate and reduce magnet flux leakage.

The design and optimisation methods are described in this chapter along with the machine's variable and fixed parameters, the script file and the optimisation process.

A range of feasible slot and pole combinations are also evaluated.

6.2 MagNet™ Software

MagNet™ is finite element electromagnetic modelling software; it can solve electromagnetic problems in both two and three dimensions. If a machine is known to have the majority of flux travelling in two dimensions, i.e. in the plane of the laminations then the 2D is acceptable with the advantage of substantial savings in solution times. Three dimensional analysis is then used if the end effect of the machine are to be analysed for a newer final design. The STPM machine is laminated, and hence has a mainly two dimensional flux path, hence 2D FE is used throughout.

6.3 Slot / Pole Combination

Increasing the number of poles for the concentrated magnet topology at a fixed diameter leads to thinner magnets.

Due to manufacturing difficulties a minimum allowable thickness of 2 mm is considered.

The slot to pole combinations chosen here based on an initial verification to ensure that they have a balanced rotating magnetic field in the air gap. This was achieved by first calculating the electrical angle of the slot pitch (ϑ_p) as follows:

$$\vartheta_p = \frac{360}{TN} \times pp \quad 6.1$$

Where TN is the number of teeth and pp is the number of pole pair. This is followed by drawing a phasor diagram that represents the electrical angle between all slots. Thereafter, the slots have been rearranged to make three phases with each phase having a resultant that is 120 electrical degrees away from the next phase [134, 135].

There are a number of requirements in the slot / pole choice specific to the STPM machine;

- Four poles have to be aligned to one specific tooth at any one time.
- The inner stator must have the same number of teeth as the outer stator. This is because each of the inner stator teeth has to be aligned with an outer stator slot opening. This reduces the amount of leakage flux redirecting it to link the

aligned phase.

Different possible combinations are shown in Table 6.1

Table 6.1. STPM Machine Different Slot to Pole Combinations.

Option	Outer Stator Number of teeth	Number of poles	Inner stator Number of teeth
1	6	20	6
2	12	40	12
3	24	80	24
4	48	160	48

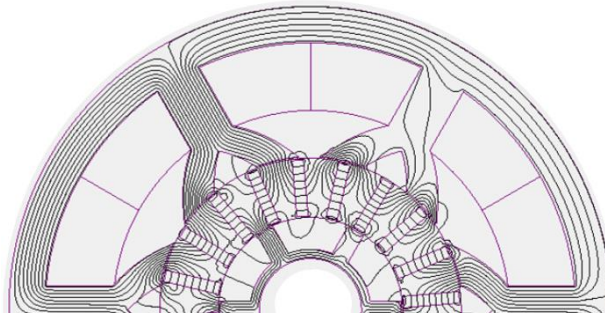
The combination of slots and poles influences both the machine's electrical and magnetic loading. Electrical loading depends on the slot area, while magnetic loading depends on the amount of flux linking the tooth of one pole. If the pole number is tripled, the flux per pole will be reduced to one third of its original value. The torque in an ideal case will not change by increasing the pole number if both the current density and rotor outer diameter remain unchanged. However, increasing the pole number can influence other design features that can contribute to increasing torque density as will now be explained;

1. Increasing the pole number means the coreback depth can be reduced, this is because a lower magnitude of flux has to travel shorter distances around the coreback. This contributes to increasing the torque as the rotor outer diameter can be increased for the same machine outer diameter. Less iron will be used, giving a reduction in mass hence, increase in torque density.
2. Higher pole numbers mean a higher machine electrical frequency for a given speed, this increases stator iron loss. It will however reduce the magnet and end winding losses as the circumferential path of the magnet eddy currents is reduced, and the coil resistance is lower due to the end winding length is shorter. The windings may also have a reduced impact on the axial length of the machine therefore the effective torque producing length of the machine can be increased for the same overall space envelope.

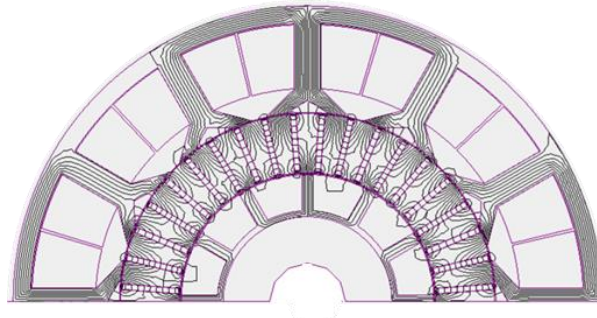
3. Fringing and leakage of flux between neighbouring magnets and from magnet to tooth will be increased by increasing the number of poles as they are spatially closer.
4. Increasing the pole number minimises the risk of magnet demagnetisation because the armature reaction is reduced.
5. The machine construction becomes more difficult with a higher pole number as there is a larger number of components.
6. Larger magnets are less expensive than smaller magnets of the same mass, because there is less processing and handling.

An optimal slot/ pole combination for a specific size frame has to be chosen; hence a comparison has been carried out between two STPM machines with different slot and pole numbers. A 6 slots/ 20 poles and a 12 slots/ 40 poles are considered. The combination of 24 slots/ 80 poles has been ruled out because it results in a magnet thickness that is less than 2 mm for a 200 mm outer diameter.

The 6 slot / 20 pole machine is the same as that described in Chapter 4. The 12 slot / 40 pole machine is an initial design that was achieved by using the same process of designing the 6 slots/ 20 poles machine. A single tooth winding has been chosen for both machines. The two machines share the same air gap length, stator outer diameter, magnet material, magnet mass and lamination properties. The winding of the 6 slots/ 20 poles machine was shown in Chapter 4 where two slots make up one phase. The same winding style has been applied to the 24 slots/ 40 poles machine which has four slots per phase. Figure 6.1 shows flux contour plot lines that have been obtained from no-load 2D FE simulation for the two designs.



a) 6 Slots/ 20 Poles Machine.



b) 12 Slots/ 40 Poles Machine.

Figure 6.1. Flux Contour Plot Lines Obtained from No-Load 2D FE Simulation for the Two Designs.

Figure 6.2 shows the dimensions of the 12 slots/ 40 poles machine.

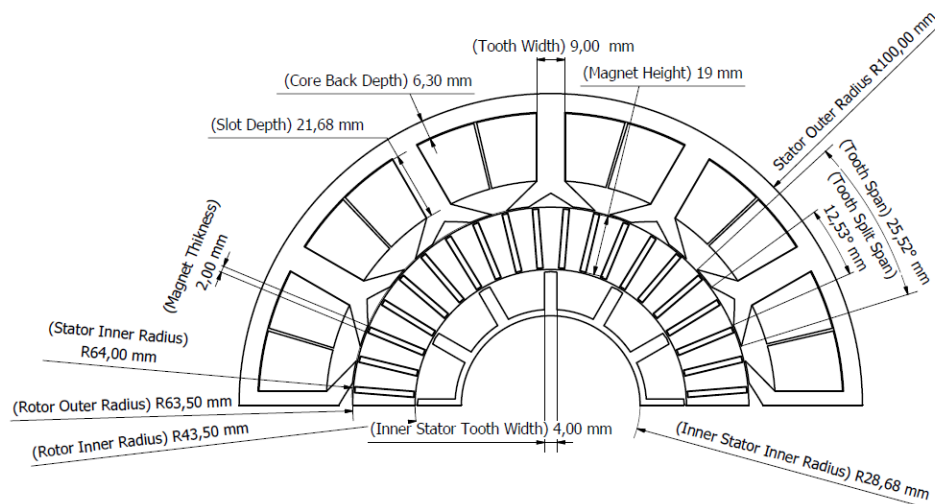


Figure 6.2. Dimensions of the 12 slots/ 40 Poles First Design

6.3.1 Evaluation of the 6 Slot / 20 Pole and 12 Slot / 40 Pole Designs

In this section both machines will be evaluated and compared with regard to their electromagnetic performance.

6.3.2 No-Load Back EMF Comparison

The back EMF amplitude of both machines has been kept constant by setting the number of turns. However, an increase in the frequency rating of the power electronics is needed for the higher pole number machine. The relation between the back EMF, number of turns and frequency is described by Equation 6.1.

$$E_{rms} = 4.44 \times \hat{\Phi} \times N \times f \times k_w \quad 6.1$$

Where E_{rms} represents the phase RMS value of the back EMF, $\hat{\Phi}$ is the peak flux of the linked phase, N is the number of turns, f is the electrical frequency k_w is the winding factor of the machine.

Figure 6.3 shows the simulated line to line back EMF waveform of the 6 slots/ 20 poles and 24 slots/ 40 poles machines at 3000rpm.

The fundamental winding factor of both machines is 0.866 with no distributed winding as all the coils that make up one phase are at the same electrical angle.

It is worth noting from the harmonic spectrum of the line back EMF of both machines shown in Figure 6.4 that the 3rd and other triplen harmonics are not present in both machines line back EMF waveforms. This is because both machines are balanced three phase machines that are connected in star; hence all triplen harmonics are in phase.

The only common harmonics of concern here are the 5th, 7th and 11th harmonics. However, looking at Figure 6.4, it can be seen that the 5th harmonic in the 6 slots/ 20 poles machine is 0.011 per unit, which is 1.1 % of the fundamental and only 0.5 % in the 12 slots/ 40 poles machine while 7th and 11th harmonics represent less than 1 % in both machines, hence they are small and can be neglected for the purpose of this study.

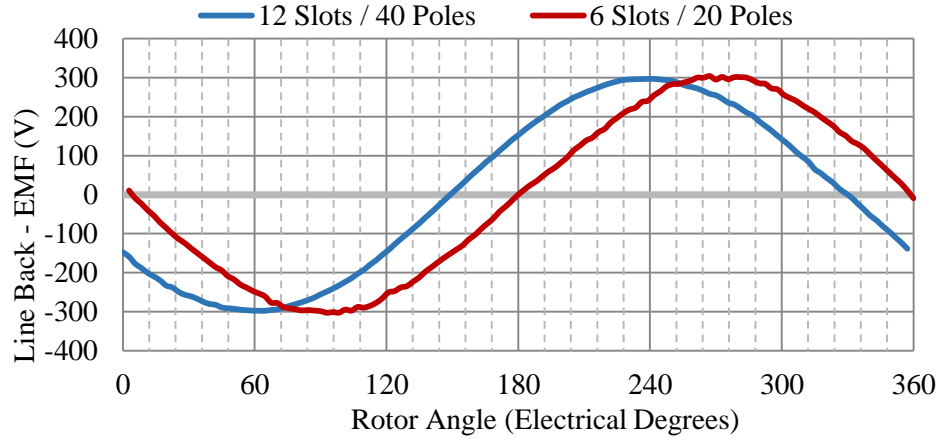


Figure 6.3. Line Back EMF for 6 Slots/ 20 Poles and 12 Slots/ 40 Poles STPM Machines with Concentrated Magnets.

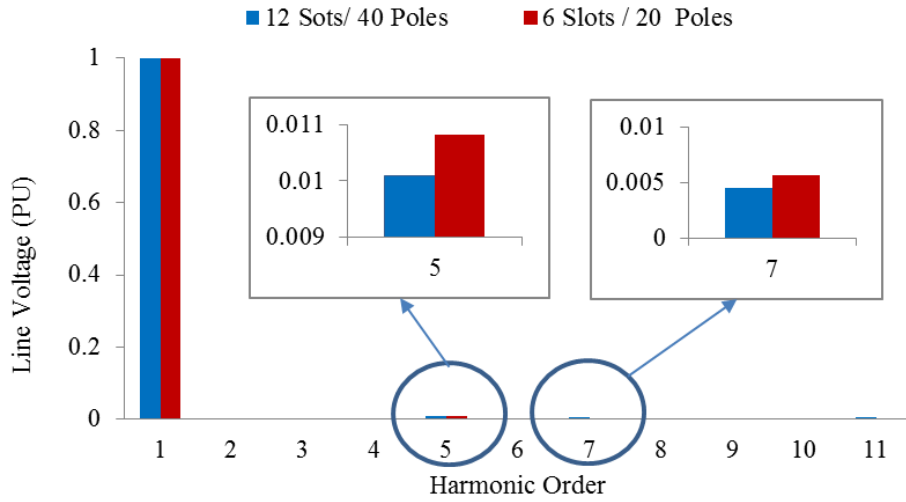


Figure 6.4. Harmonic Spectrum for 6 Slots / 20 Poles and 12 Slots/ 40 Poles STPM Machine with Concentrated Magnets.

6.3.3 Cogging Torque Comparison

One of the most important requirements of EVs is to reduce noise to a minimum in order to achieve the maximum possible comfort for passengers; reduced cogging torque contributes to minimising this noise.

Cogging torque is not included in the optimisation process. However, it is assessed post optimisation.

Cogging torque is a result of the interaction between both permanent magnet MMF harmonics and the air gap harmonics due to slotting [136]. The frequency of the cogging torque can be obtained using Equation 6.2:

$$\text{Cogging}_{pp} = \frac{N_{\text{slot}} \times PP}{\text{HCF}\{N_{\text{slot}}, PP\}} \quad 6.2$$

Where N_{slot} is the number of stator slots, PP the number of pole pairs and $\text{HCF}\{N_{\text{slot}}, PP\}$ is the highest common factor between the number of slots and number of poles. Table 6.2 shows the cogging torque lowest cogging torque frequency for different slot to pole combinations.

Table 6.2 Cogging Torque Frequency for Different Slot/Pole Combinations.

Outer Stator Number of teeth	Number of poles	Cogging torque pole pair number
6	20	60
12	40	120
24	80	240
48	160	480

Cogging torque waveforms for the 6 slots/ 20 poles machine and 12 slots/ 40 poles machine were obtained using 2D FE transient with motion simulations and are shown in Figure 6.5. It can be noticed from the figure that both machines produce very low cogging torque: less than 2 % of full load torque. The cogging torque frequency is in agreement to the values obtained in Table 6.2. A reduced cogging torque was observed with the higher slot/pole combination.

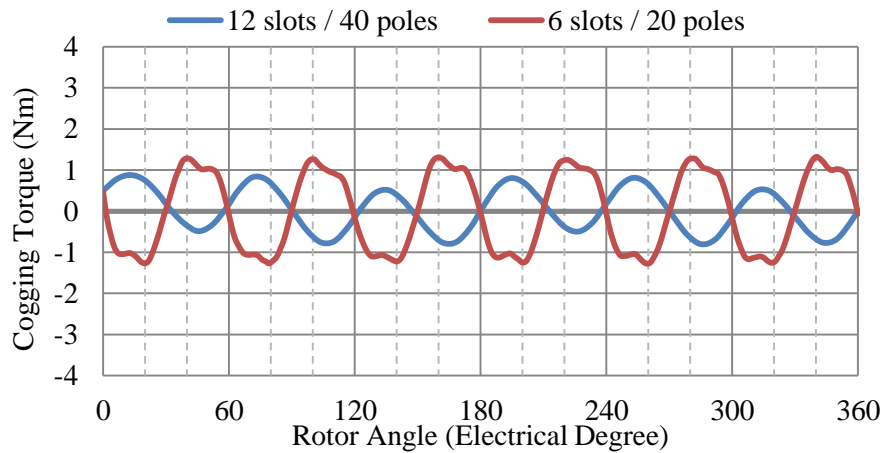


Figure 6.5. Cogging Torques for 6 Slots / 20 Poles and 12 Slots/ 40 Poles STPM Machine with Concentrated Magnets.

Although there has been no investigation into the relation between the amplitude of cogging torque and slot to pole combination, from Figure 5.10, it has been found that the higher slot to pole combination achieved the lower cogging torque amplitudes.

6.3.4 Mean Torque Comparison

Torque can be calculated using Equation 6.3:

$$T_m = \frac{3E_{rms} I_{rms} \cos \beta_{ph}}{\omega_{mech}} \quad 6.3$$

Where T_m is the mechanical Torque, E_{rms} is the phase back EMF, I_{rms} is the rms current in the winding, β_{ph} is the current and back EMF waveform phase displacement and ω_{mech} is rotor velocity at a given time.

Torques verses current density is shown in Figure 6.6 for both machines. The higher pole number machine produces more torque at 1.5 A/mm² onwards and has the ability to increase torque to 122 Nm at 5 A/mm² and 156 Nm at 10 A/mm². The torque increases up to 167Nm at 15A/mm² current density. The low pole number machine achieves near linear increases in torque up to 100 Nm at 5 A/mm² and while there is also a visible increase up to 130 Nm at 7A/mm² it has already started to level off. By taking the maximum achievable torques for both machines at different current densities, an increase of 22 %, 7.5 %, 4.5 % is achieved by the 12 slots/ 40 poles machine at a loaded current density of 5 A/mm², 10 A/mm² and 15 A/mm² respectively. This is partially because the torque is proportional to the square of the rotor diameter, which has been increased in the 12 slots and 40 poles machine as a result of reducing the coreback depth.

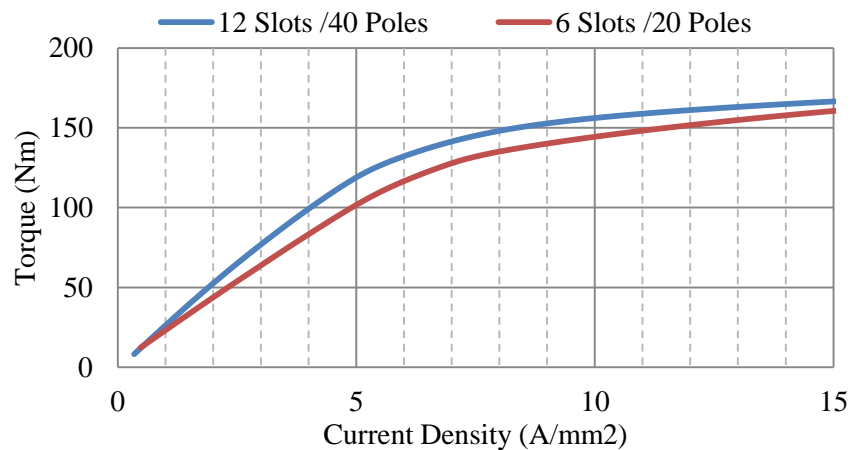


Figure 6.6. Peak Torque Versus Current Density for the 6 Slots/ 20Poles and 12 Slots/ 40 Poles Split Tooth PM Machines with Concentrated Magnets.

6.3.5 Torque Ripple Comparison

Torque pulsations are not desirable because they produce vibrations and acoustic noise in the machine [137, 138]. A torque ripple is caused by [139]:

- The interaction between time and asynchronous spatial harmonics between two air gap fields, where one is a creation of the armature excitation and the other is of the rotor magnets. Although the current applied to the stator winding is sinusoidal, spatial harmonics are created in the air gap field due to slotting effect and tooth tip saturation.
- Due to the reluctance variation between the tooth and slot (cogging torque).

Torque ripple can be found by Equation 6.4:

$$T_{ripple} = \frac{T_{max} - T_{min}}{T_{mean}} \times 100 \quad 6.4$$

Where T_{ripple} is the torque ripple, T_{max} and T_{min} are the maximum and minimum torques, respectively and T_{mean} the mean value of torque over one electrical cycle. Figure 6.7 shows torque obtained from the two machines when loaded at current density of 15 A/mm².

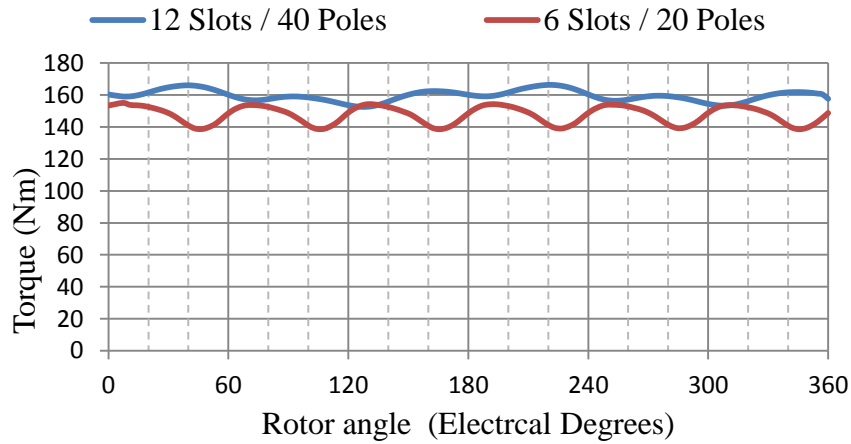


Figure 6.7. Torque Waveform for 6 Slot / 20 Pole and 12 Slots/ 40 Poles Split Tooth PM Machines.

The machine with 12 slots/ 40 poles exhibits a lower torque ripple, which has been calculated using Equation 6.4 as 6.5% of the machine output torque. The torque ripple for the machine with 6 slots and 20 poles is 11.2% which is higher in this case. This is because of the small distortion in the waveform of the back EMF.

Table 6.3 shows a comparison between both machines.

Table 6.3. A Comparison between 6 Slots/ 20 Poles and a 12 Slots/ 40 Poles STPM Machines.

Subject	6 Slots/ 20 Poles	12 Slots/ 40 Poles
Outer diameter (mm)	200	200
Rotor Outer diameter (mm)	100	144.53
Iron Losses at 15 A/mm ² & 3000rpm (W)	2017	2672
Peak Cogging Torque (Nm)	1.2	0.8
Torque Ripple (%)	11.2	6.5
Max Torque (Nm) (@15A/mm ²)	>160	>166
Mass (Kg)	27.13	18.8
Torque Density (Nm/Kg)	5.9	8.8
Speed (base)	3000	3000

From Table 6.3, the 12slots/ 40 poles STPM machine has 27.5 % more iron loss than the 6 slots/ 20 poles STPM machine at 15 A/mm² and 3000 rpm. This is because of the higher electrical frequency required at the same speed by the machine with the higher pole number. In addition, the copper loss was calculated for the 12 slots/ 40 poles machine and found to be 2177 W, which is lower than the iron loss by 18.5%.

In addition, the higher slot to pole combination has less cogging torque at 0.8 Nm when compared to 1.2 Nm by the lower slot to pole combination. Also less torque ripple is achieved by the higher slot to pole combination with only 6.5 % torque ripple.

The 12 slots/ 40 pole machine has been chosen for the purpose of this thesis because it increases torque density by 49 % when compared to 6 slots/ 40 poles machine, hence it will be further investigated as will be shown in the following sections and chapters.

6.4 Design and Optimisation Methods

The key optimisation parameter is the mean torque per unit mass that can be achieved at a specific frequency, temperature rise and for a specific set of dimensional constraints. Nevertheless parameters such as cogging torque and torque ripple must be kept within acceptable limits. The critical design points are:

- 1 Maximum continuous operating torque. This is important when it comes to electric vehicles, especially at the critical thermal point during driving up a steep hill.
- 2 Over load torque. Higher than rated torque and available for fast acceleration, for a period much less than the thermal time constant of the motor.

The MagNet drawing script parameterises every vertex of the Split tooth PM machine for the optimisation process. Inside the script file, MMF is calculated as a function of slot area.

The optimisation aims to maximise the torque capability of different designs for a fixed current density.

6.4.1 Optimisation Parameters

The optimisation considered some fixed constraints and some variable parameters as seen in Table 6.4.

Table 6.4. The Range of Fixed and Variable Parameters.

Parameter	Range	
	Minimum	Maximum
Stator Outer Diameter	200mm (fixed)	
Axial Length	130mm (fixed)	
Outer Air Gap Length	1mm (fixed) (initially 0.5mm)*	
Inner Air Gap Length	1mm (fixed) (initially 0.5mm)*	
Magnet Upper Bridge	1.5mm (fixed) (initially 0.5mm)**	
Magnet Lower Bridge	1mm (fixed) (initially 0.5mm)**	
Slot Depth	4 mm	26 mm
Tooth Width	4 mm	24 mm
Core Back Depth	4 mm	16 mm
Slot Opening Width	2 mm	
Tooth Split Width	1 mm	11 mm
Tooth Split Depth	2 mm	12 mm
Magnet Height	3 mm	27 mm
Magnet Thickness	2 mm	7 mm
Inner Stator Tooth Width	2 mm	10 mm
Inner Stator Slot Depth	3 mm	14 mm
Inner Stator Coreback Depth	2 mm	12 mm

*Changed in order to count for enough clearance during construction. ** Required to mechanically restrain the magnets against the centrifugal forces for a prototype.

All the variable parameters are calculated as a function of the stator outer diameter (fixed). Hence, other parameters can be also varied accordingly such as: stator inner diameter, tooth span, rotor outer diameter, rotor inner diameter, inner stator outer diameter, Inner Stator Tooth span, inner stator slot pitch

A representation of the 6 slots / 20 poles STPM machine's three different parts cross sections are shown in Figures 6.8, 6.9, 6.10 for the outer stator, rotor and an inner stator respectively and a description of their dimensions represented in Tables 6.5, 6.6, and 6.7 respectively.

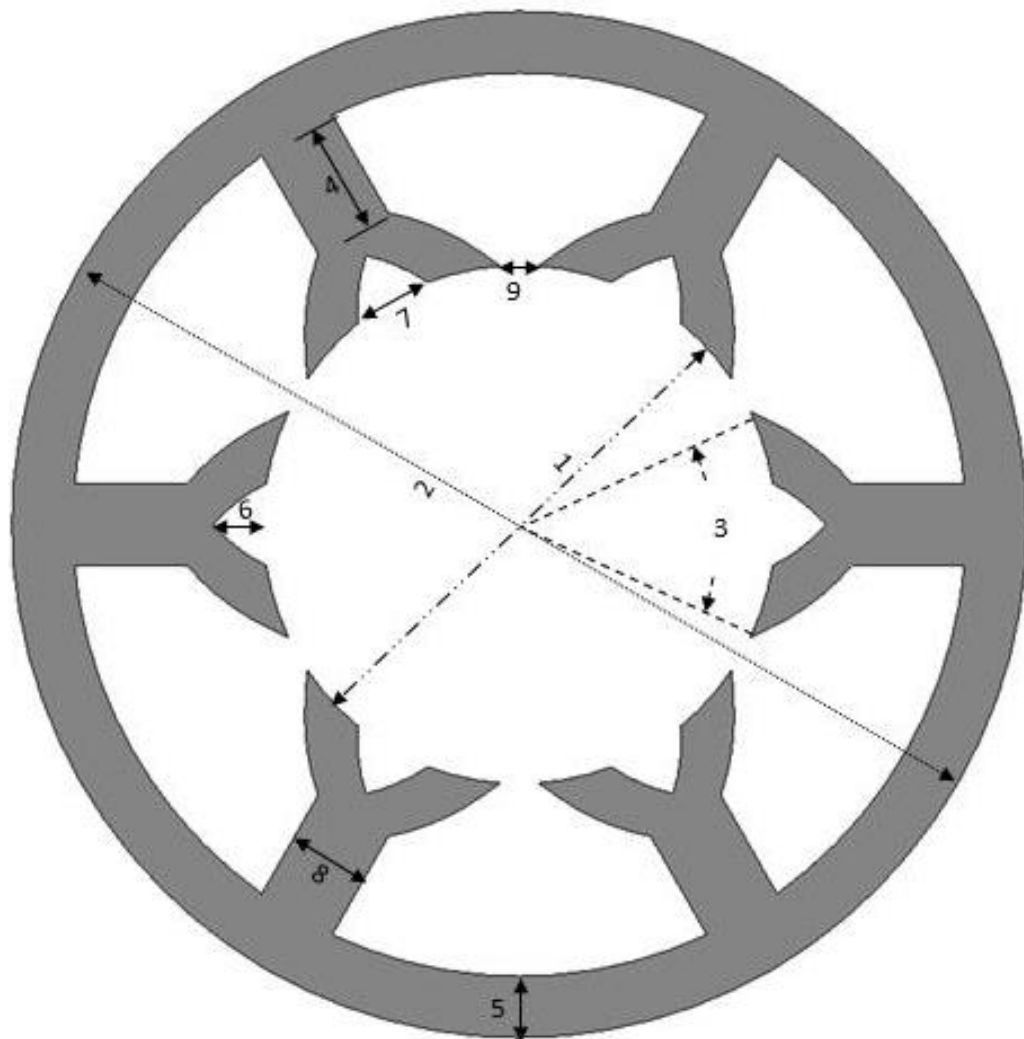
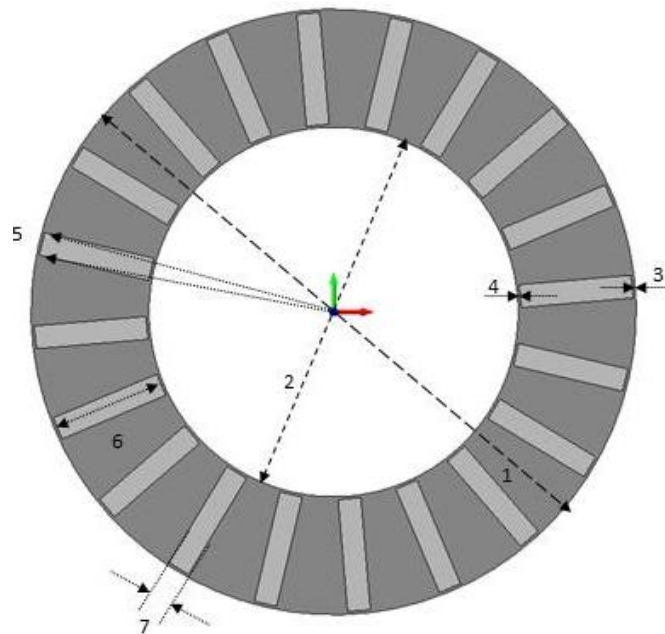


Figure 6.8. Outer Stator Dimensions of the STPM Machine.

Table 6.5. Outer Stator Dimensions Descriptions and Symbols.

Number	Description	Symbol
1	Stator Inner Diameter	D_{si}
2	Stator Outer Diameter	D_{so}
3	Tooth span	θ_t
4	Slot depth	d_s
5	Core Back Depth	d_{cb}
6	Tooth Split Depth	l_{ts}
7	Tooth Split Span	θ_{ts}
8	Tooth Body Width	w_{tb}
9	Slot Opening Span	θ_{so}

**Figure 6.9. Rotor and Magnet Dimensions of STPM Machine with Concentrated Magnets.****Table 6.6. Rotor and Magnet Dimensions Descriptions and Symbols.**

Number	Description	Symbol
1	Rotor Outer Diameter	D_{ro}
2	Rotor Inner Diameter	D_{ri}
3	Magnet Upper Bridge	B_{mu}
4	Magnet Lower Bridge	B_{ml}
5	Magnet Span	θ_m
6	Magnet Height	h_m
7	Magnet Thickness	t_m

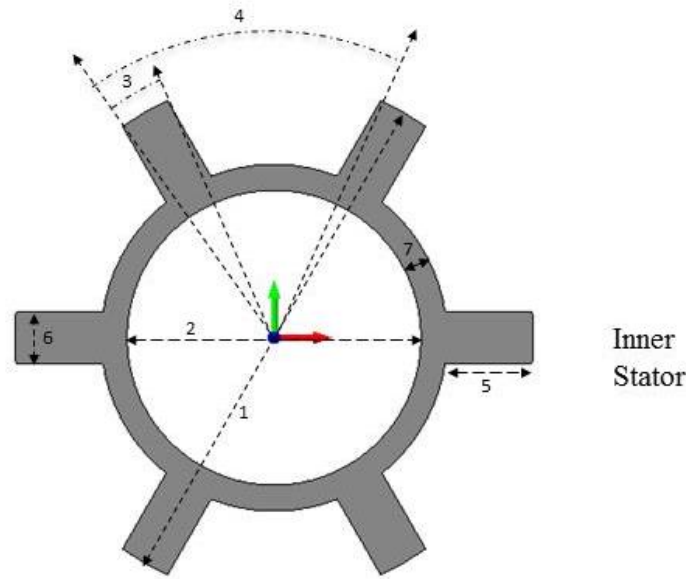


Figure 6.10. Inner Stator Dimensions of The STPM Machine.

Table 6.7. Inner Stator Dimensions Descriptions and Symbols.

Number	Description	Symbol
1	Inner Stator Outer Diameter	D_{iso}
2	Inner Stator Inner Diameter	D_{isi}
3	Inner Stator Tooth Span	θ_{ist}
4	Inner Stator Slot Pitch	θ_{iss}
5	Inner Stator Slot Depth	d_{ist}
6	Inner Stator tooth Width	w_{ist}
7	Inner Stator Coreback Depth	d_{scb}

6.4.2 Process of Optimisation:

The optimisation process is divided into two: the first method is the initial manual optimisation process and the second is the final optimisation process which is automated using OptiNetTM. Both optimisations were for maximum torque density at a fixed RMS current density of 15A/mm², which is a typical limit for a forced air-cooled machine. In order to reduce the solution time, the optimisation was undertaken using 2D static FE models.

The manual optimisation started by writing a script to parameterise the machine. A visual basic (VB) script was written in a text file which can be run by MagNet. Figure

B.1 in Appendix B shows the flow sequence in which the script was created in order to create and simulate the STPM machine in MagNet. Thereafter, the script file was run in MagNet, which was commanded to build and assign the appropriate material for each part of the STPM machine in FE. During this process, the script commands MagNet to build several models that vary one variable parameter at a time, and to solve it using 2D FE simulation. The simulation results are then obtained and transferred to Microsoft Office Excel for investigation. This process was repeated for all of the variable parameters to derive the dimensions of the initial optimal design. Figure 5.5 below shows a flow chart of the initial optimisation process.

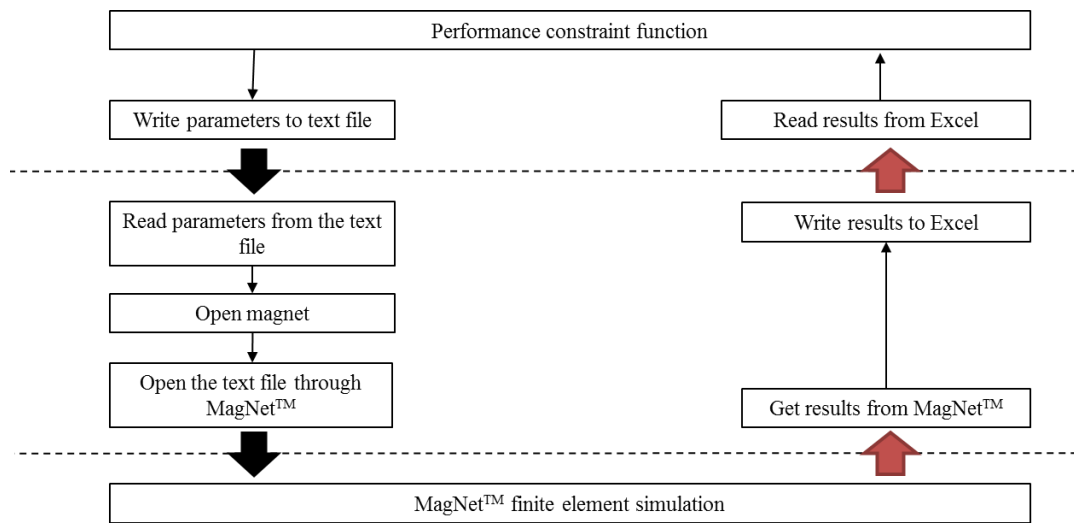


Figure 5.5. Flow Diagram for the Initial Optimisation Process.

After solving for the best-achieved design from the manual process of optimisation that has the maximum torque capability for a fixed current density, the simulation was saved in MagNet and then the final optimisation process was started.

In this process, software called OptiNet was used. OptiNet can be integrated with simulation packages such as MagNet, ElecNet and ThermNet to improve existing design models by optimising the electromagnetic and thermal characteristics of any parameterised model. OptiNet is very efficient because it uses an optimizer based on an evolutionary strategy.

In this process OptiNet was integrated with MagNet simulation to improve the saved parameterised model, which was the best design achieved through the initial optimisation. This was done by continuously varying the dimensions of the machine between fixed parameters; these limits were set to allow for only sensible geometries to

be considered during the optimisation. This was done in such a way as to avoid any overlap in the geometry which can be caused by the interdependence between different variables. It is also important to note that the optimisation was allowed to vary each variable cautiously outside of these limits in order to consider every possible combination. The process of the optimisation employed is summarised as shown in figure 5.6.

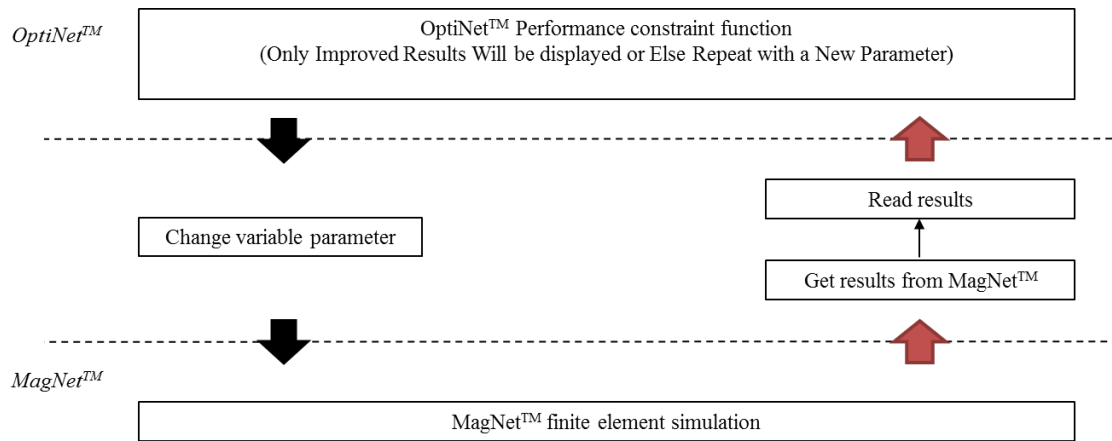


Figure 5.6. Flow Diagram for the Final Optimisation Process.

From the figure above, it can be seen that OptiNet worked in such a way as to command MagNet™ to change the parameterised model variables, to solve the model and to send the results back to OptiNet. The process was then repeated several times in order to obtain an improved torque output, and this cycle was repeated until no further increase in the output torque was noticed, hence the final optimal dimensions of the modelled design with maximum torque output were obtained.

The maximum number of solutions for OptiNet was set to 5000 with a time limit of 30 hours in order to allow it to run as many solutions as possible, to give the most accurate results possible.

6.5 Conclusion

Different slot-to-pole combinations of the STPM machine have been considered and compared in this chapter in order to find the optimum combination with the best torque density, which can be further optimised and built for the purpose of this thesis, 12 slots/ 40 poles was chosen, as this combination has been found to produce more torque per unit mass than the 6 slots/ 20 poles machine. A higher combination could not be considered because the resulting thin magnets are too difficult to handle during construction.

The coreback was reduced as a result of increasing the slot to pole combination. This is because the flux around the coreback becomes lower in magnitude and travels shorter distances. This effect contributes towards increasing the torque; hence the rotor's outer radius can be increased for the same overall outer diameter. However, increasing the pole number has the disadvantage of increased stator iron loss due to the higher electrical frequency of the machine at the same speed.

A script file was written to create the 12 slots/ 40 poles STPM machine and to define each of its vertices as a function of the outer stator outer diameter in order to parameterise the model of the machine in MagNetTM. This made the process of optimising the machine dimensions a lot easier and quicker. The optimisation included some fixed parameters such as the outer diameter and the axial length, due to the size restrictions of the application chosen. Two optimisation processes to maximise torque output at fixed current density were carried out as explained in this chapter. The first method was conducted manually by varying each of the variable parameters individually and to investigate their impact on torque density. The second method was conducted using OptiNetTM.

In the following chapter, the manual optimisation method was used to investigate the impact of varying each parameter on the achieved torque density and an optimum achieved design was chosen.

Chapter 7. Investigative Design

In this chapter, the impact of changes to the 12slot/40pole STPM machine's stator, rotor, magnets, and inner stator on torque density was explored. As a second order, the effect on torque ripple was observed. In addition, the impact of the inclusion of the inner stator was assessed. The parametrised model from Chapter 6 was used to vary the dimensions.

7.1 Introduction

In order to mathematically understand the effect of varying the machine physical dimensions on torque output it is important to understand the torque T_m to rotor radius r relation, which can be demonstrated in the general torque equation shown previously in chapter 4, which for clarification is more detailed in Equation 7.1:

$$T_m \propto B_{g \text{ fundamental}} \times A_{rms} \times \pi r^2 l_a \quad 7.1$$

Where $B_{g \text{ fundamental}}$, is the peak air gap flux density, l_a is the machine's axial length, and A_{rms} is the electrical loading that can be calculated using Equation 7.2 where I is the phase current and N is the number of turns per phase:

$$A_{rms} = \frac{6 N I}{2 \pi r} \quad 7.2$$

From Equation 7.1 and 7.2 the effect on the torque produced for different dimensional changes can be estimated as follows:

- Increasing the magnetic loading increases torque output, which can be achieved by increasing the air gap flux density.
- Increasing the electric loading by increasing either the number of turns or the current applied increases torque, this would require an increase in slot area fill factor or current density.
- Better cooling allows an increase in torque as the machine can operate at a higher current density.
- Torque is proportional to the square of the rotor radius; therefore increasing the air gap radius will have a large effect on torque.
- Torque output is proportional to the axial length of the machine, although the axial length is fixed in this investigation.

7.2 Investigation Methodology

The investigation was carried out using the parametrised model from Chapter 6. Static and transient with motion 2D FE was used throughout.

The static torque analysis has been conducted using the method described in Chapter 4. For each design variation the slot area is calculated, allowing torque to be assessed against current density ranging up to 20A/mm^2 in the conductor

The transient with motion simulation were conducted at both no load and load conditions with applied current density of 15A/mm^2 . During the no load condition, back EMF waveform and harmonic content, cogging torque and air gap flux density were measured. Also flux density was assessed for each variable. The load condition was used to obtain torque waveforms, and there by calculate the mean torque and torque ripple.

Torque density calculations are based on the mean torque at full load and divided by the magnetically active mass (laminations + magnets + windings). Torque ripple was also assessed.

7.3 Outer Stator Dimension Impact on Torque Density

The variable dimensions of the outer stator is shown in Figure 7.1 and Table 7.1

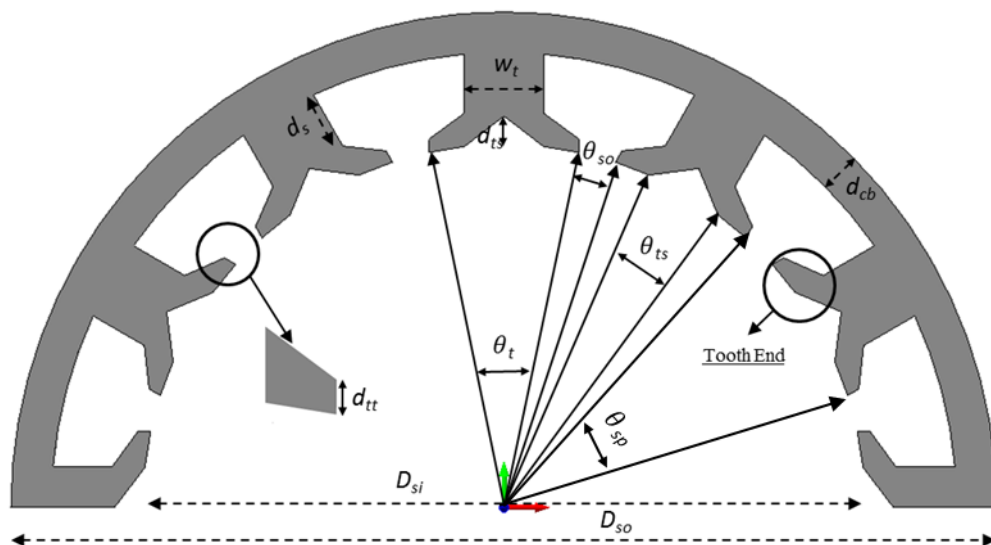


Figure 7.1. Outer Stator Dimensions of the STPM Machine.

Table 7.1. Outer Stator Dimensions Description.

Symbol	Description
D_{si}	Stator Inner Diameter
D_{so}	Stator Outer Diameter
θ_t	Tooth span
θ_{sp}	Slot Pitch Span
d_s	Slot depth
d_{cb}	Core Back Depth
d_{ts}	Tooth Split Depth
θ_{ts}	Tooth Split Span
w_t	Tooth Body Width
θ_{so}	Slot Opening Span
d_{tt}	Tooth Tip Depth

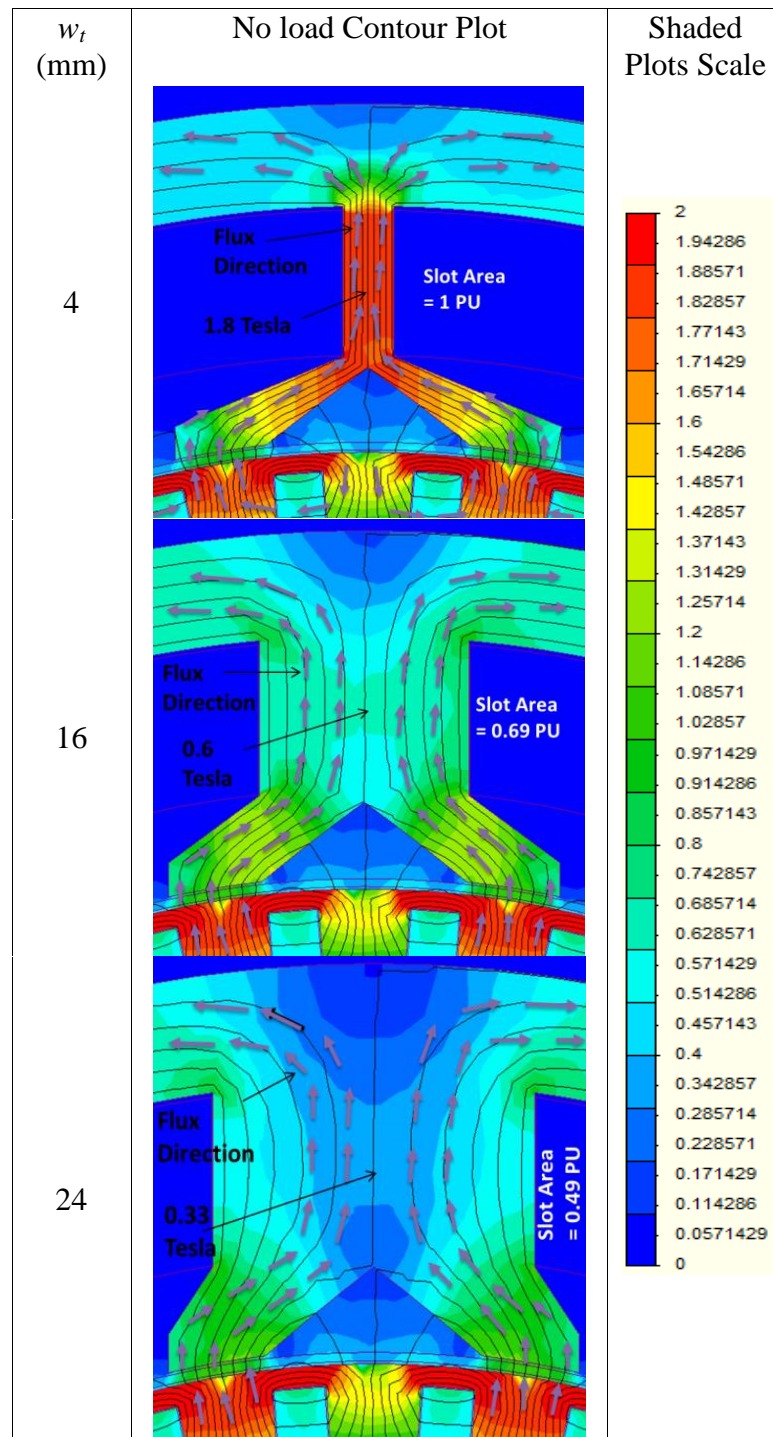
The outer diameter is kept constant at 200mm while the tooth width, slot depth, coreback depth, slot opening span, tooth split span , tooth split depth and tooth tip depth have been varied.

7.4.1 Tooth Body Width and Slot Depth

Since they have an effect on the total slot area, tooth body width and slot depth were chosen first for analysis.

A balance between the slot area, and hence MMF and saturation in the tooth body, and hence magnetic loading has to be taking into consideration when investigating the tooth body width because both of them are proportional to torque from Equation 7.1. Furthermore, a balance between the rotor outer radius and slot area has to be also considered when investigating various slot depths.

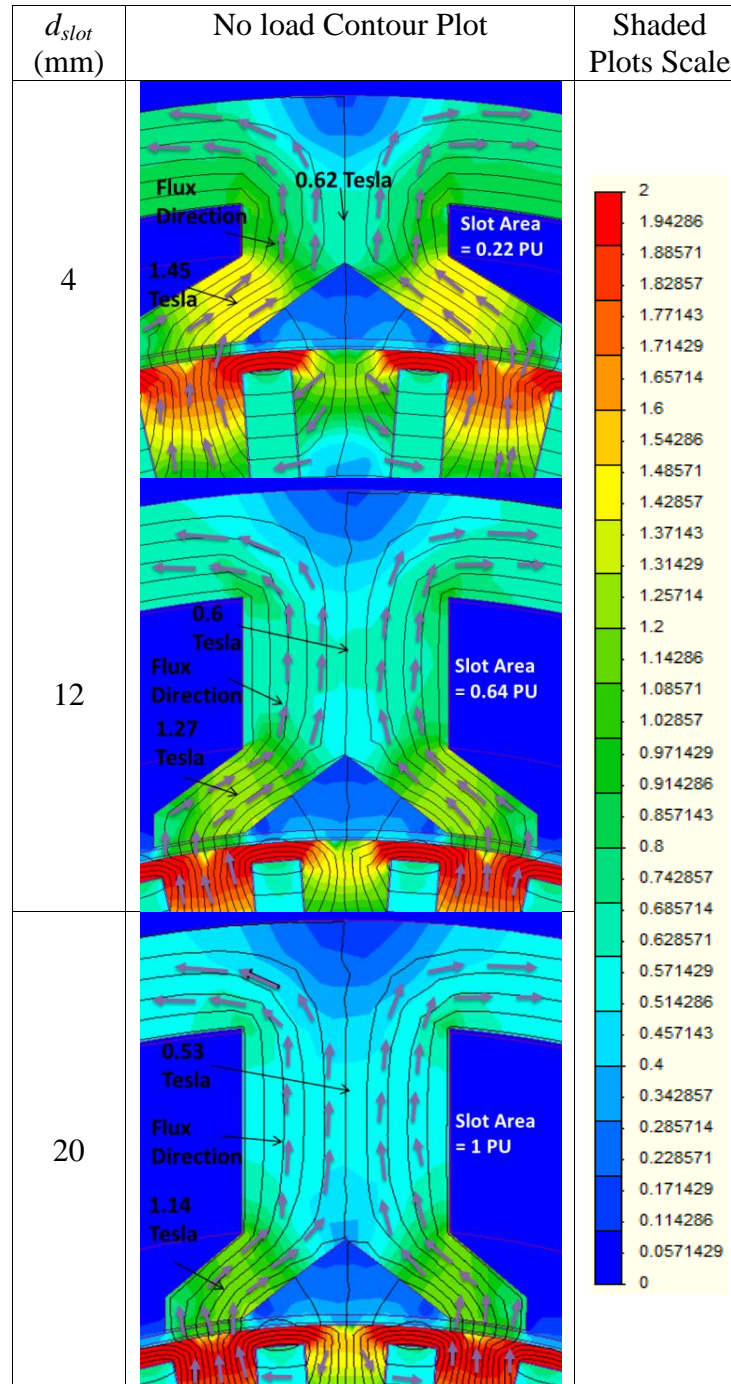
Table 7.2 and 7.3 show a no-load flux density distribution conducted for various tooth body width and slot depth respectively.

Table 7.2. No Load Shaded Flux Density Distribution of Various Tooth Body Widths.

It can be seen from Table 7.2 that a tooth body width of 4 mm has the highest flux density saturation in the tooth body, which limits the flux linking of the coils and increases iron loss. This width has also the largest slot area (1PU), and hence MMF that can be applied. However, a tooth body width of 24 mm has the lowest flux density saturation in the tooth, which increases the iron mass and has also the smallest slot area, hence electrical loading. However, a tooth width of 16 mm can be seen to have a

balance between the amount of distributed flux density across most of the stator tooth and the slot area available.

Table 7.3. No Load Shaded Flux Density Distribution of Various Slot Depths.



For varying slot depths shown in Table 7.3, a slot depth of 4mm can be seen to have the longest outer rotor radius. However, it has the smallest slot area, and hence electric loading for a fixed current density. In addition, slot depth of 20 mm has the largest slot area but the shortest outer rotor radius.

Moreover, a slot depth of 16 mm can be seen to have the most balance relation between both slot area and rotor outer radius than the other two depths shown in Table 7.3.

Torque for a range of applied current densities was obtained for various tooth body widths and slot depths and shown in Figures 7.2 and 7.3.

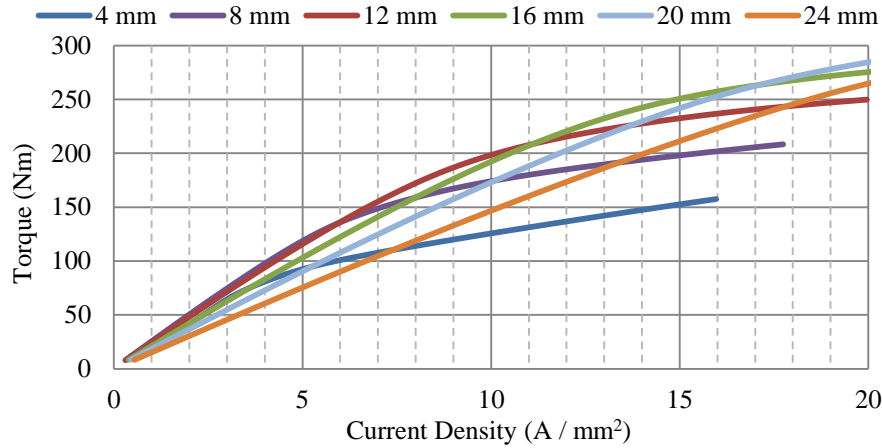


Figure 7.2. Torque Versus Current Density for Various Tooth Body Widths.

Looking at Figure 7.2 it can be seen that the 16mm tooth body width design is the best design as it has the higher achievable torque before it saturates and starts to level off. This is because tooth body widths lower than the 16mm width, get more saturated and hence limit the magnetic loading. Furthermore, tooth widths above 16mm result in smaller slot areas, which limit the electrical loading.

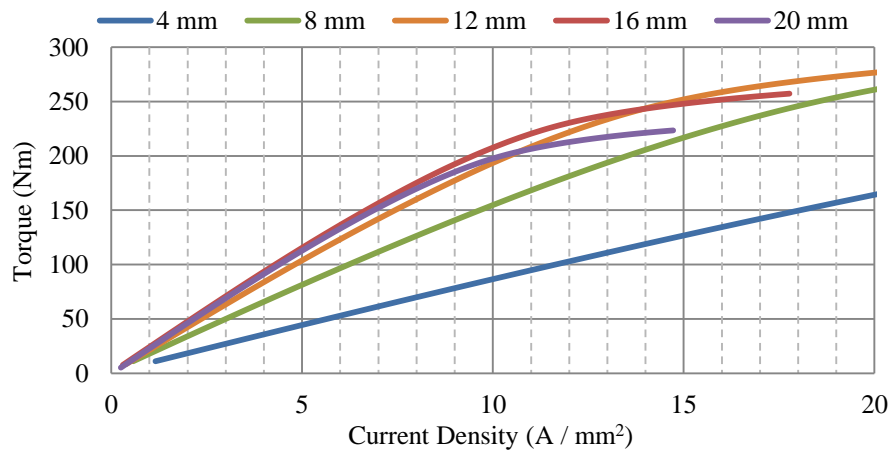


Figure 7.3. Torque Versus Current Density for Various Slot Depths.

Figure 7.3 shows that a slot depth of 12 mm achieves the highest torque output as it has a balance between the slot area achieved and hence MMF and the outer rotor radius than the other four depths shown in the figure. Also depths below 12 mm result in smaller slot areas. However, slot depths above 12 mm result in lower rotor radii.

For comparison, torque density for different tooth body widths and slot depths at a current density of 15 A/mm^2 are shown in Figures 7.4.

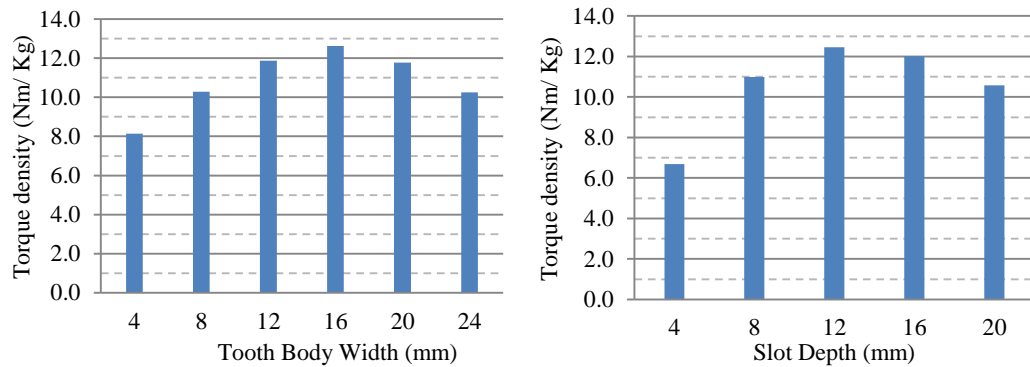
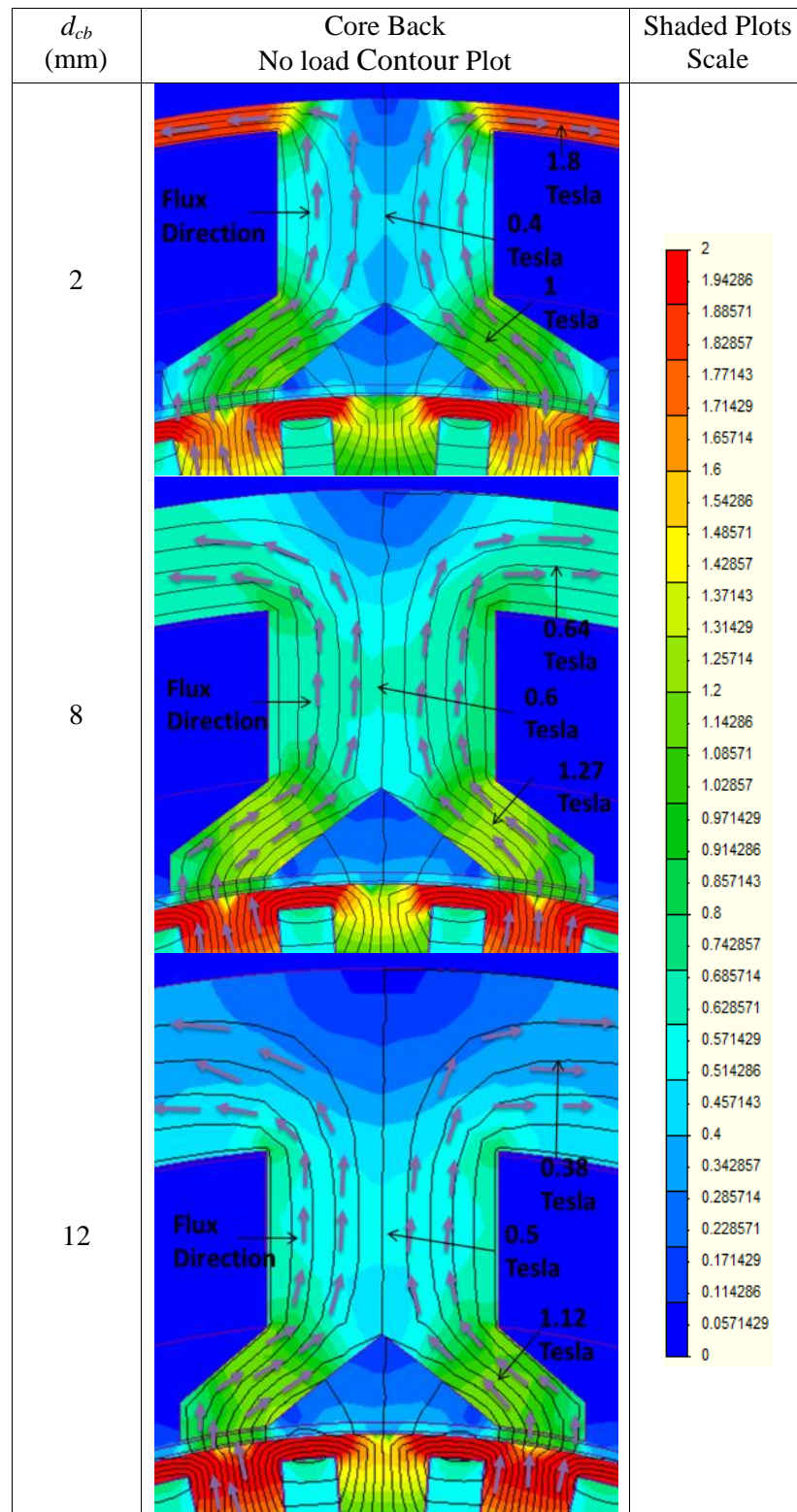


Figure 7.4. Torque Density at 15 A/mm^2 for Different Tooth Body Widths and Slot Depths.

Figure 7.4 shows that at 15 A/mm^2 a 16mm tooth body width achieves the highest torque density of 12.6 Nm/kg . Moreover, a slot depth of 12 mm has been found to have the highest torque density from Figure 7.4. A tooth width of 16 mm and a slot depth of 12mm are found to offer maximum torque and this is because the earlier achieves the ideal tooth body saturation and slot area ratio for maximum torque, while the latter achieves the optimum ratio between the rotor outer radius and the slot area.

7.4.2 Coreback Depth

The coreback depth has a large impact on torque as reducing the coreback thickness for the same outer diameter allows an increase in rotor radius, hence a large increase in torque. However, the coreback has to be thick enough to prevent saturation limiting the magnetic loading. Flux density distribution plots are shown for various coreback depths as shown in Table 7.4 and assessed alongside torque density.

Table 7.4. No Load Shaded Flux Density Distribution of Various Coreback Depths.

Torque for a range of applied MMFs was obtained at various coreback depths, then by using the slot area; torque against current density graphs were created. These are shown in Figure 7.5.

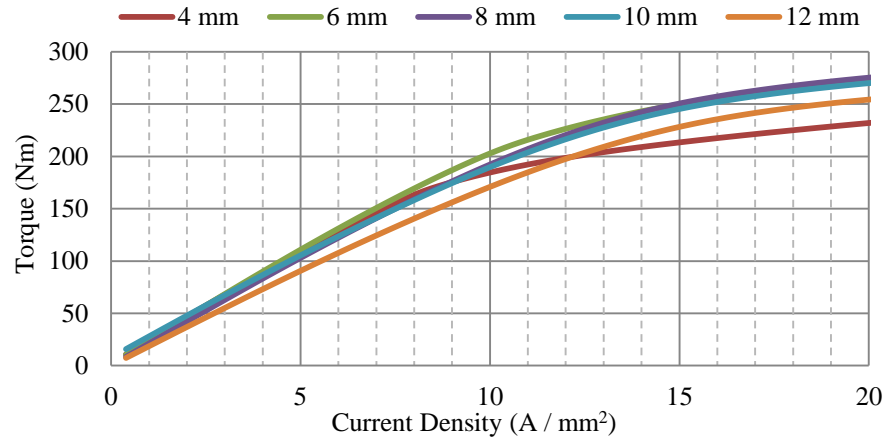


Figure 7.5. Torque Versus Current Density for Various Core Back Depths.

From Figure 7.5, torque can be seen to increase proportionally with current density until the magnetic circuit becomes saturated. Although the rotor radius is reduced, increasing the coreback depth up to 8 mm results in more torque. This is because the reduction in saturation is greater than the reduction in torque radius. However, increasing the depth to more than 8mm results in a reduced torque because the effect of reducing the rotor radius outweighs the benefit of reduced saturation. Figure 7.6 shows a chart of torque density and torque ripple resulting from different coreback depths obtained with 15 A/mm² applied current density.

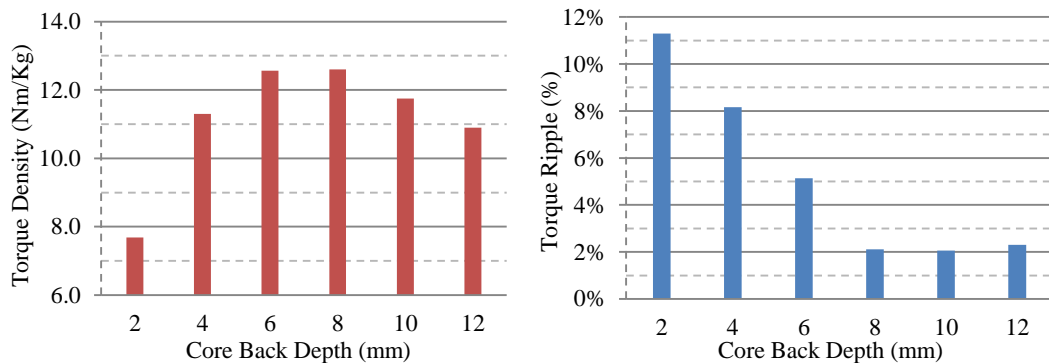


Figure 7.6. Torque Density and Ripple Achieved at 15 A/mm² at Various Coreback Depths.

From Figure 7.6, it can be seen that at 15 A/mm², the 6mm and 8mm coreback depth designs have the highest achievable torque density due to the increased rotor radius, improved magnetic loading and reduction in iron used. However, a lower torque ripple was observed at a depth of 8 mm, and hence it is chosen to be the optimum design of this machine.

7.4.3 Slot Opening Widths

It is apparent from the torque against current density for various slot opening widths shown in Figure 7.7 that torque increases in proportion to slot opening up to a width of 8mm. Above 8 mm width results in a torque drop. This is because lower slot opening widths in this particular machine allow an undesirable flux path in the tooth tip and very high widths limit the linking flux as both tooth ends become narrower. This can be illustrated by the shaded flux density distribution plots for various slot opening widths as can be seen in Table 7.5.

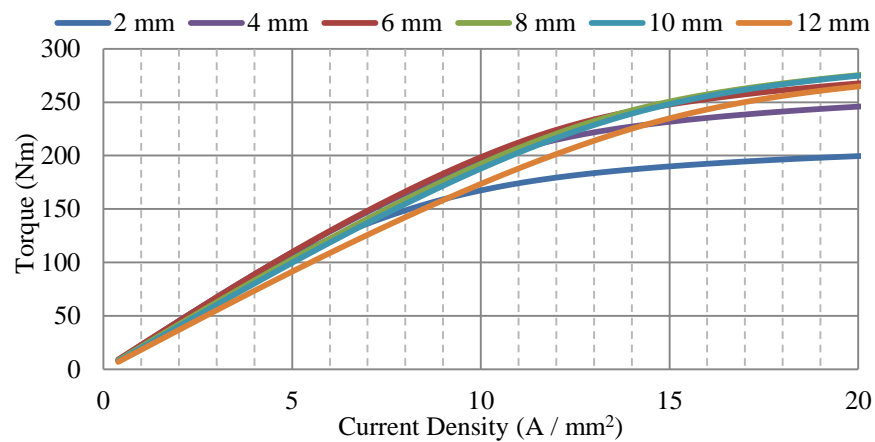
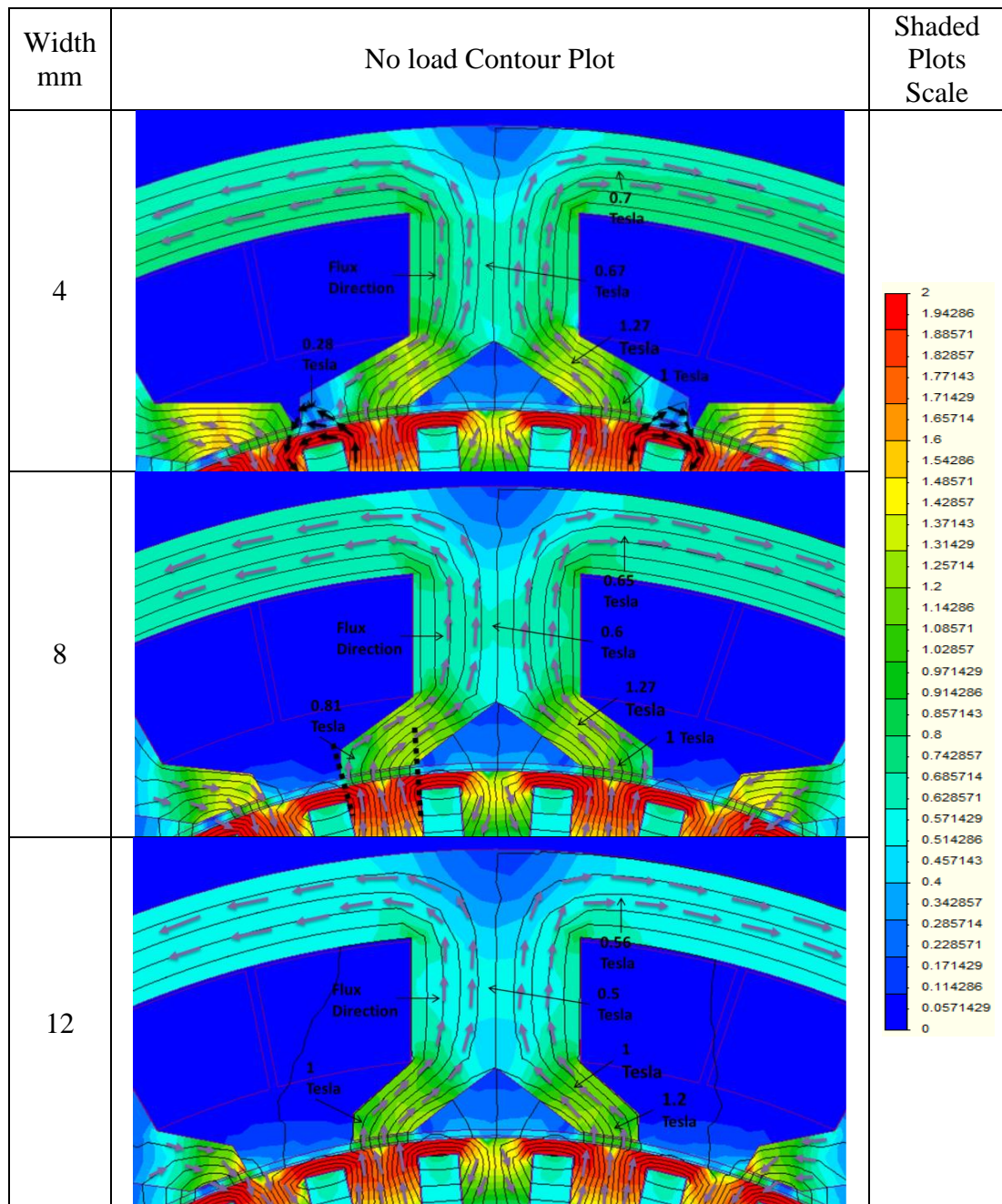


Figure 7.7. Torque Versus Current Density for Various Slot Opening Widths.

Table 7.5. No Load Shaded Flux Density Distribution of Various Slot Opening Widths.

By taking the saturation point in to account, a 6 mm wide slot opening width results in the highest torques in the region below 10 A/mm^2 and an 8mm width results in higher torques at the region above 10 A/mm^2 . Changing the slot opening width has an impact on the air gap harmonic spectrum; hence it is worthwhile investigating torque ripple. The torque ripple resulting from different slot opening widths at 15 A/mm^2 applied current density were obtained. Figure 7.8 shows the torque density and ripple with 15 A/mm^2 for different slot opening widths.

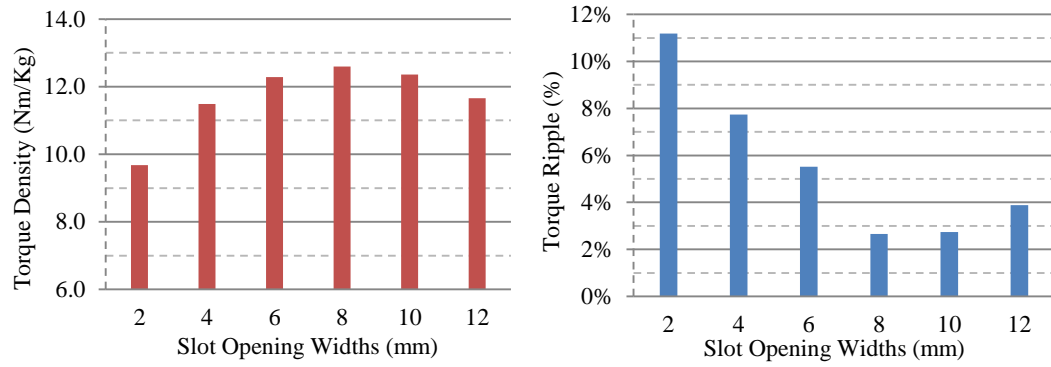


Figure 7.8. Torque Density and Torque Ripple at 15 A/mm² Applied Current Density for Various Slot Opening Widths.

From Figure 7.8, the highest torque density achieved at a slot opening width of 8mm because of the improved magnetic loading described earlier. The lowest torque ripple was also observed at this width due to its lower associated harmonic contents in the generated Back EMF. For these two reasons, 8 mm width was classified as the optimum design point here. During this investigation, it has been concluded that the iron of the tooth is best utilised when the inner surface of the tooth end is enclosed by the outer surface area in between the edges of any two magnet poles. This can be indicated by the dotted lines in the counter plot at 8mm slot opening width in the table.

7.4.4 Tooth Split Width

Torque against current density for various tooth split widths has been obtained and shown in Figure 7.9.

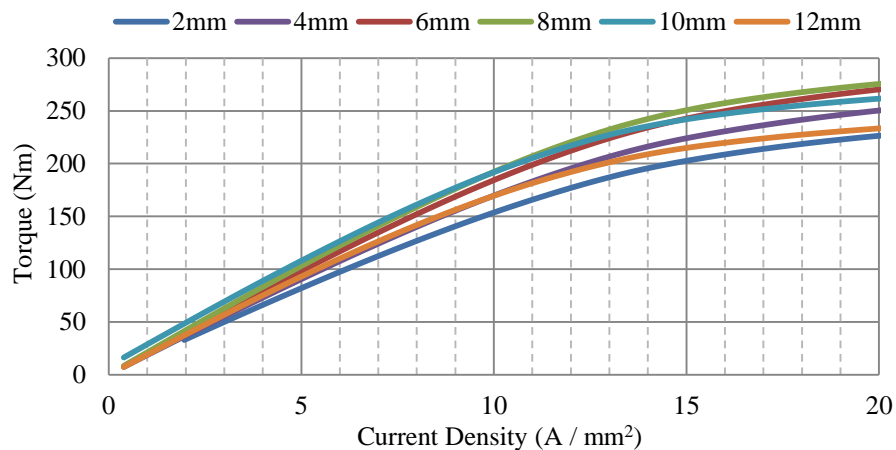
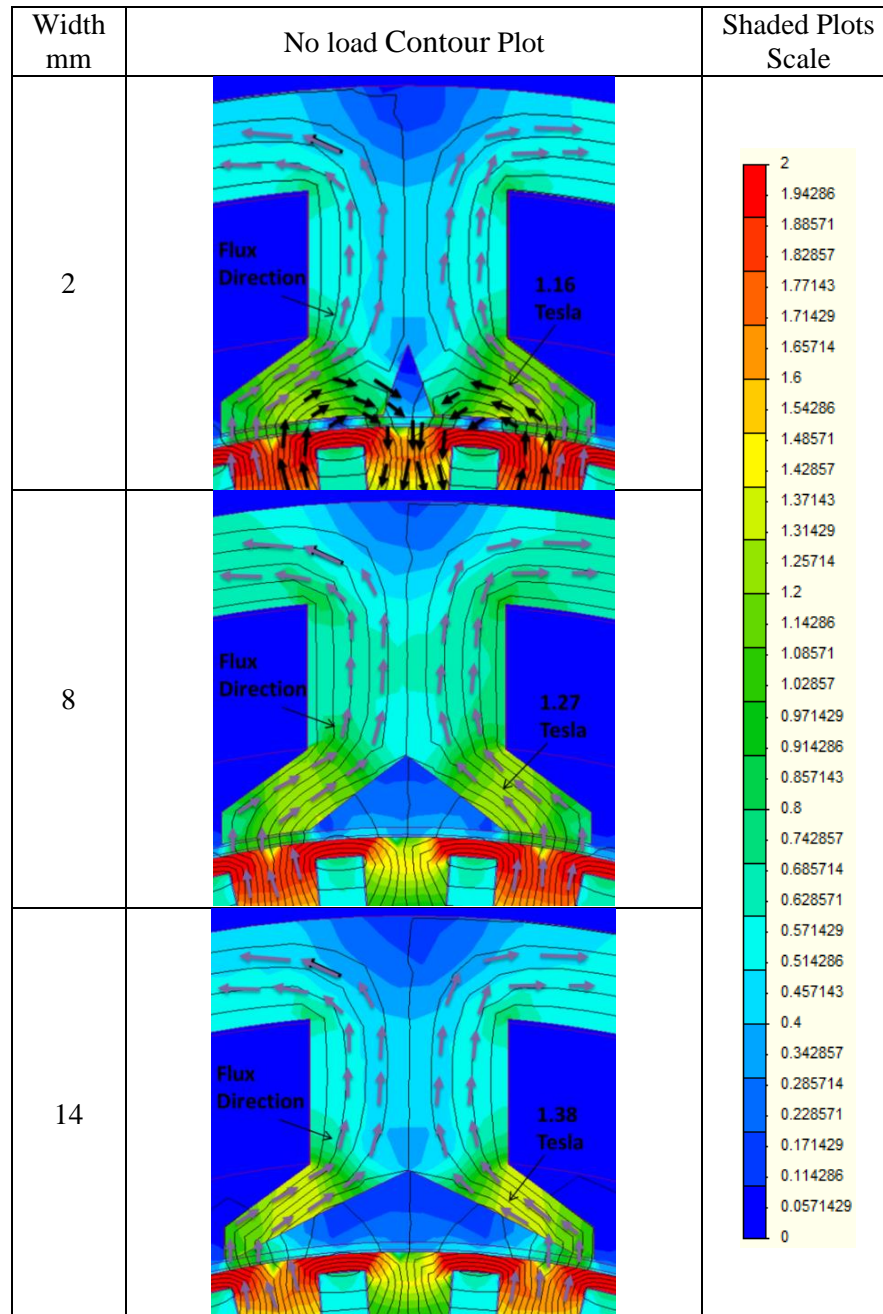


Figure 7.9. Torque Versus Current Density for Various Tooth Split Widths.

Figure 7.9 illustrates that increasing the tooth split width from 2 mm to 8 mm results in a significant increase in torque. This is because lower tooth split width allows the flux to circulate back to the rotor causing an undesirable leakage flux. In addition, increased widths of over 8 mm result in lower torques. This is because increasing the split width,

both tooth ends become narrower and hence less flux is going to be linked because they get saturated quicker. These two conditions result in a lower air gap flux density hence magnetic loading. This can be illustrated by the shaded flux density distribution plots for various tooth split widths in Table 7.6.

Table 7.6. No Load Shaded Flux Density Distribution of Various Tooth Split Widths.



The torque density and torque ripple resulting from different tooth split widths at 15 A/mm² applied current density were obtained, compared and shown in Figure 7.10.

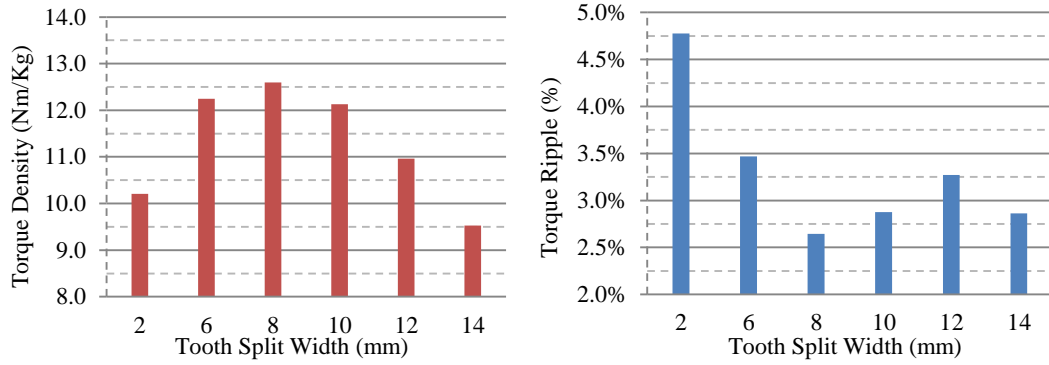


Figure 7.10. Torque Density and Ripple Achieved at 15 A/mm² at Various Tooth Split Widths.

Figure 7.10 shows that 8mm tooth split width has the highest torque density and lowest torque ripple, hence it was chosen as the optimal design.

7.4.5 Tooth Split Depth

Torque against current density for various tooth split depths has been obtained and shown in Figure 7.11.

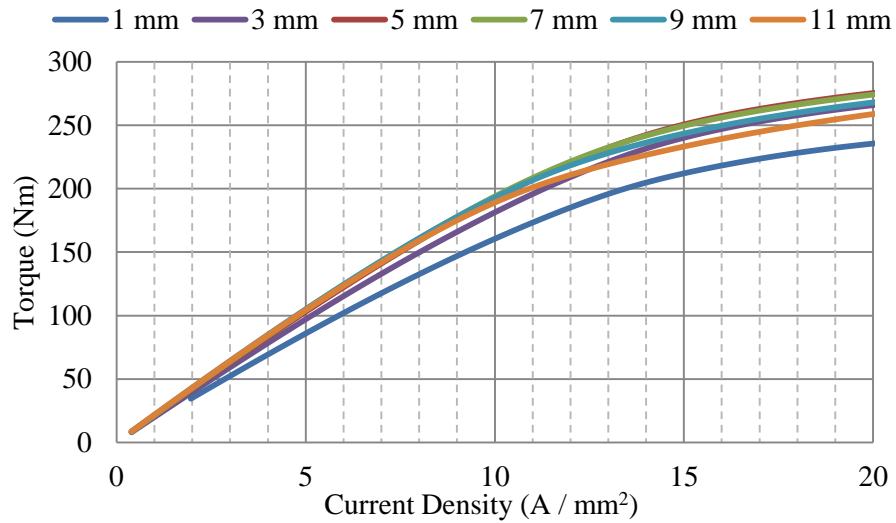
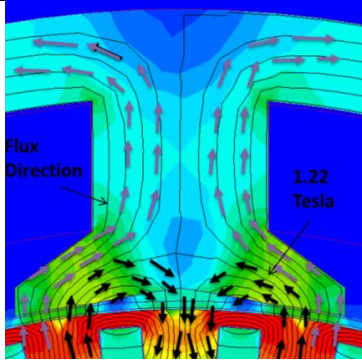
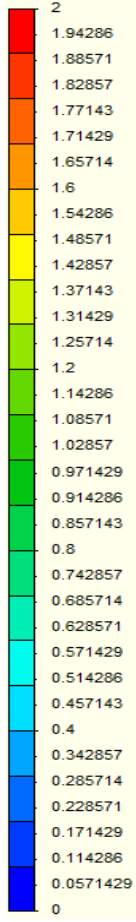
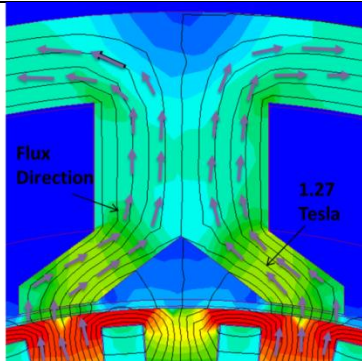
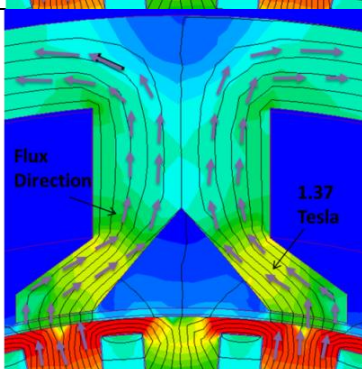


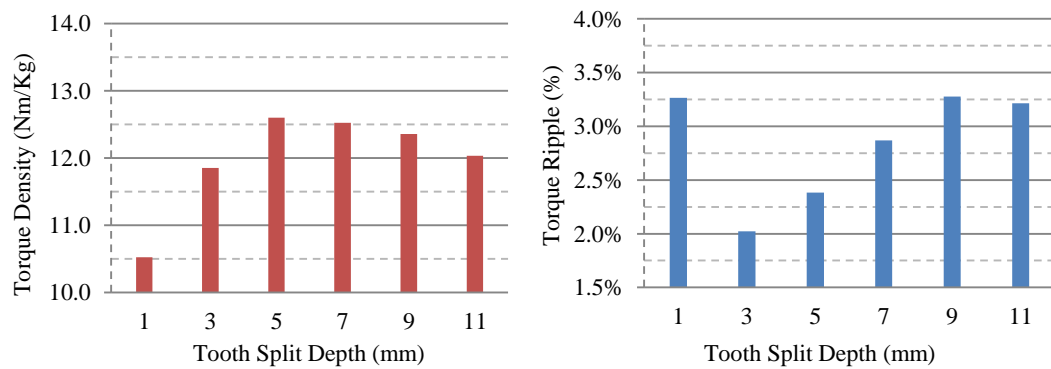
Figure 7.11. Torque Versus Current Density for Various Tooth Split Depths.

From Figure 7.11, it can be seen that the torque improves with increasing tooth split depths from 1 mm up to 5mm to where it starts to drop back. This is because of the reduced magnetic loading, as a tooth split depth below 5 mm allows the flux to circulate back to the rotor causing an undesirable leakage flux, and split depth above 7 mm makes the tooth ends narrower and hence they saturate easier. This is illustrated by shaded flux density distribution plots in Table 7.7.

Table 7.7. No Load Shaded Flux Density Distribution of Various Tooth Split Depths.

d_{ts} (mm)	No load Contour Plot	Shaded Plots Scale
1		
5		
9		

The torque Density and torque ripple obtained with a 15 A/mm^2 applied current density are shown in Figure 7.12.

**Figure 7.12. Torque Density and Ripple Achieved at 15 A/mm^2 at Various Tooth Split Depths.**

A tooth split depth of 5 mm achieves the highest torque density and a correspondingly low torque ripple as can be illustrated from Figure 7.12, and hence is has been chosen as the optimum depth at this investigation.

7.4.6 Tooth Tip Depth

The idea of the tooth tip was implemented after several attempts of trying to increase the width of the tooth end that is shown as B in Figure 7.13 in order to allow it to carry more flux (ideally to be half the tooth width). This was carried out after concluding the need of enclosing the inner surface area of the tooth end in between the surface area above the line A in the figure during the slot opening investigation. This was successfully achieved by an increase of 33 % as can be illustrated by the length of C in the figure.

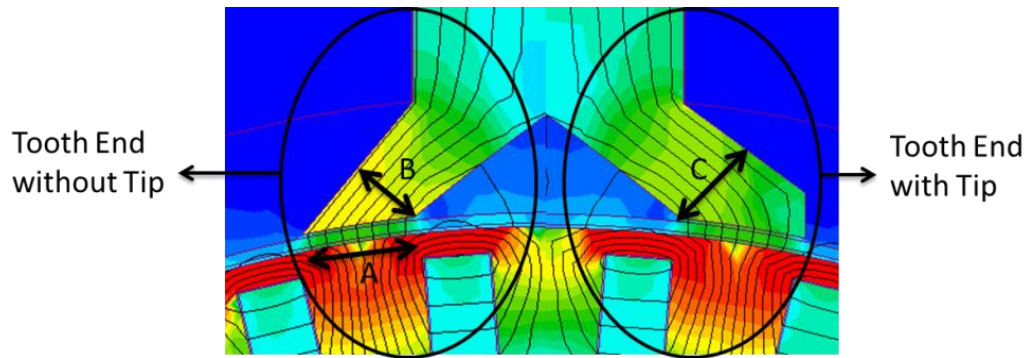


Figure 7.13. Split Tooth with and without Tooth Tip.

Torque against current density for various tooth tip depths has been obtained and shown in Figure 7.14.

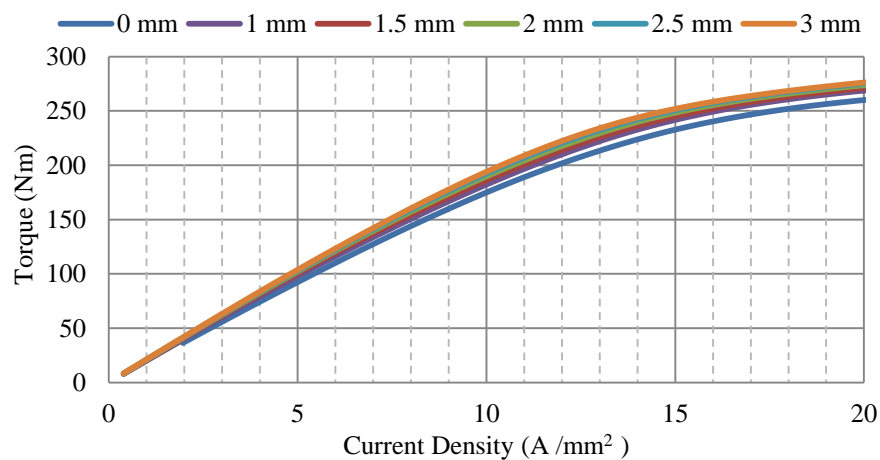
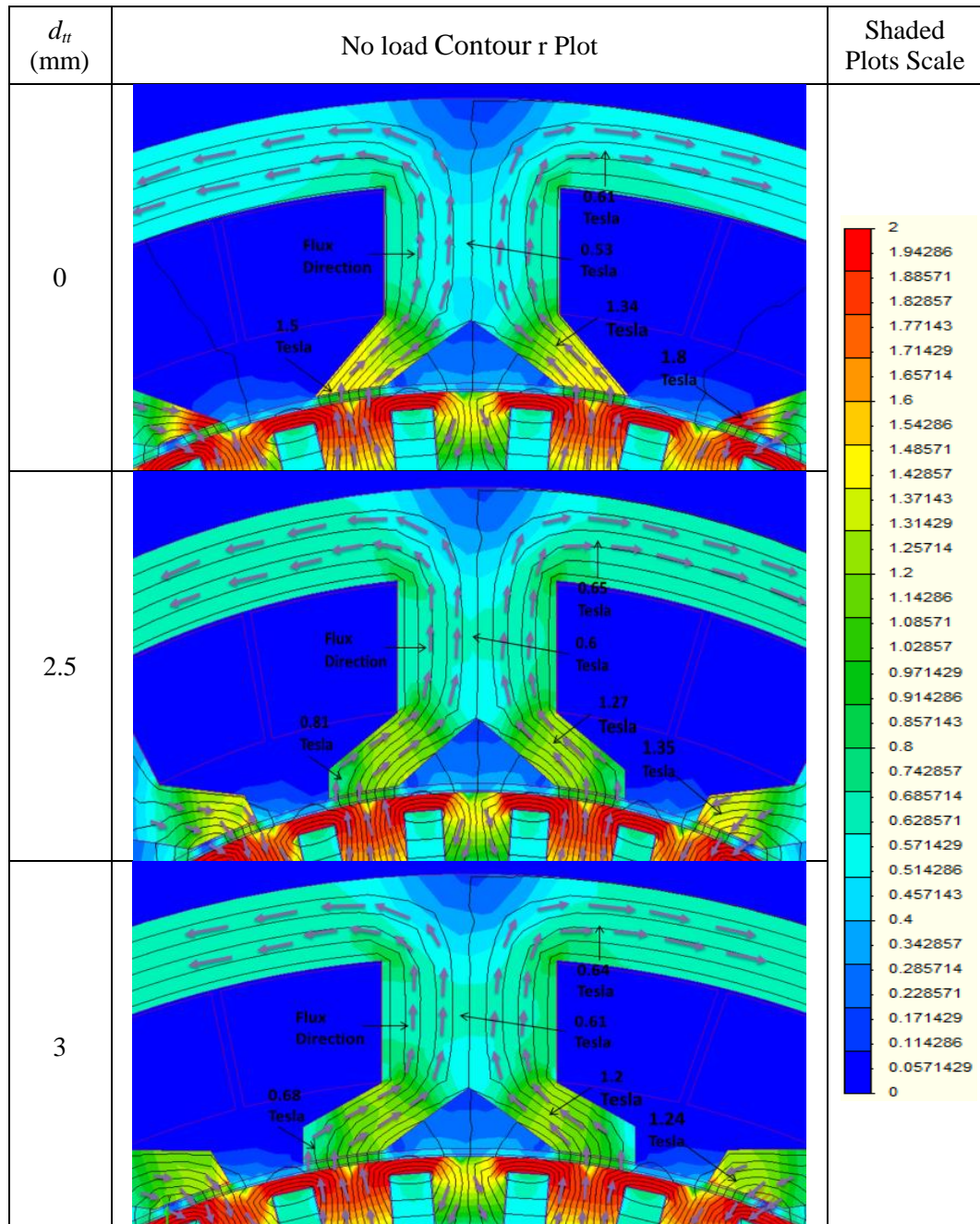


Figure 7.14. Torque Versus Current Density for Various Tooth Tip depths.

Figure 7.14 shows that by introducing a tooth tip, the machine produces 11 % more

torque. However, the increase is notable up to 2.5 mm depth, after this any further increase in tooth tip depth will only increase the iron mass. This is a result of allowing an improved flux path and hence magnetic loading. This can be illustrated by the shaded flux density distribution plots for various slot tip depths shown in Table 7.8.

Table 7.8. No Load Shaded Flux Density Distribution of Various Tooth Tip Depths.



From the contour plots shown in Table 7.8, it can be seen that more flux was allowed to be linked by introducing the tooth tip as less flux density saturation achieved at the tooth end iron and more flux at the middle of the tooth iron.

The torque density and torque ripple percentage for different tooth tip depths for 15 A/mm² applied current density are shown in Figure 7.15.

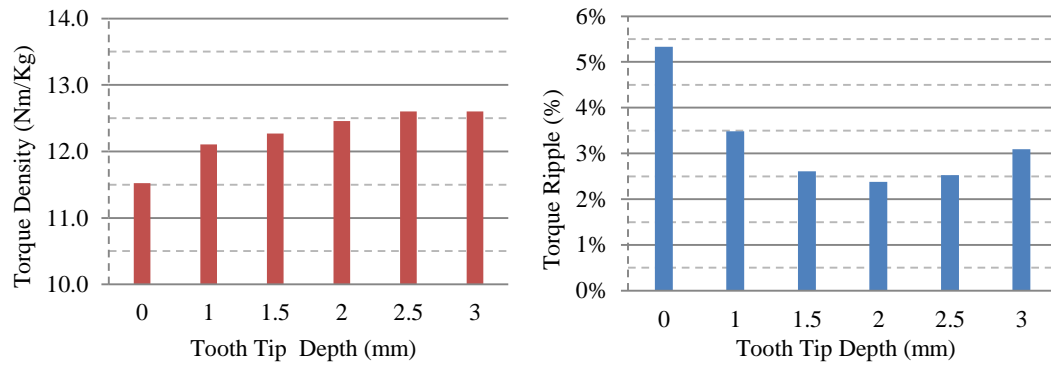


Figure 7.15. Torque Density and Ripple Achieved at 15 A/mm² at Various Tooth Tip Depths.

From Figure 7.15, a tooth tip depths of between 2.5 mm and 3mm achieve the highest torque density. However, a tooth tip depth of 2.5 mm showed less torque ripple, and hence it has been chosen as the optimum design here.

7.4 Rotor Dimension Impact on Torque Density

The key dimensions of the rotor are shown in Figure 7.16 and described in Table 7.9.

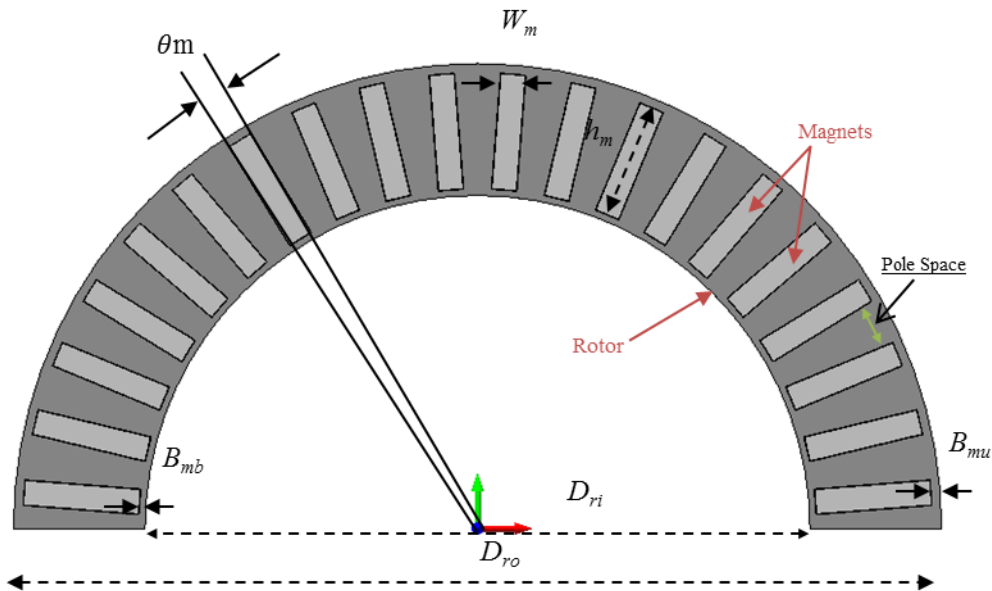


Figure 7.16. Rotor and Magnet Dimensions of the STPM Machine with Concentrated Magnets.

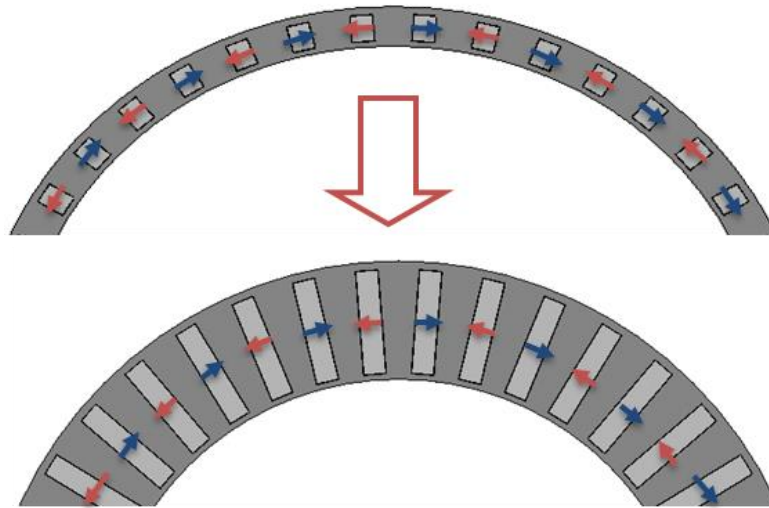
Table 7.9. Rotor and Magnet Dimensions Description.

Symbol	Description
D_{ro}	Rotor Outer Diameter
D_{ri}	Rotor Inner Diameter
B_{mu}	Magnet Upper Bridge
B_{mb}	Magnet Bottom Bridge
θ_m	Magnet Span
h_m	Magnet Height
W_m	Magnet Thickness

The magnet upper and bottom bridges have been fixed at 1.5mm and 1mm respectively in order to be mechanically strong; based on the analysis in Chapter 8. However, the rotor outer diameter, rotor inner diameter, magnet width and magnet height have all been varied.

7.4.1 Magnet Height

This section considers effective magnet utilisation through optimisation of the magnet height; Figure 7.17 shows the rotor structure when the magnet height is changed from 6mm to 18mm and the arrows show the direction of magnetisation.

**Figure 7.17. A Cross Section of the Rotor of Different Magnet Heights.**

Although several heights have been investigated during the simulation, only the viable solutions will be shown in this section. Figure 7.18 shows torque against current density for various magnet heights, which is increased by 6mm each time.

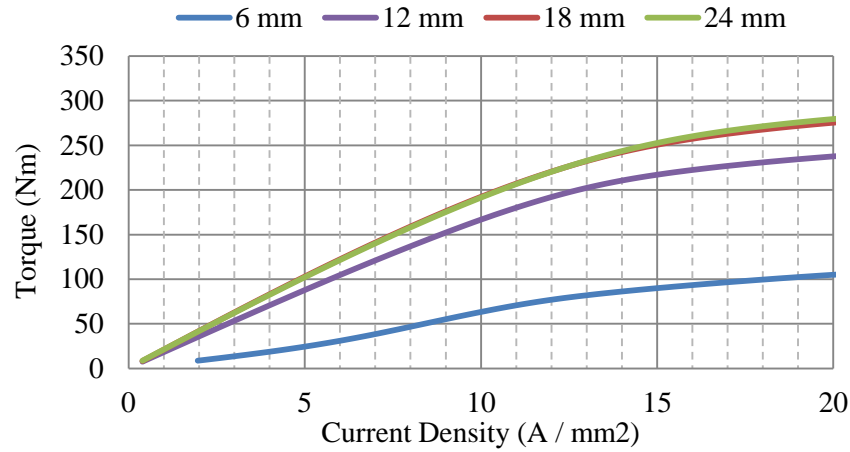


Figure 7.18. Torque Versus Current Density for Various Magnet Heights.

From Figure 7.18, it can be seen that increasing magnet height from 6 mm to 12 mm results in a significant increase in torque with longer magnets having a lesser effect. In addition, the ratio of increased torque to magnet mass was assessed at different heights at 15 A/mm² applied current density. It was found that increasing the magnet height from 6mm to 12 mm results in 143% increase in torque for 100 % increase in magnet mass. However, only 16.5% increase in torque for a 50 % increase in magnet mass was achieved by increasing the magnet height from 12mm to 18mm. Furthermore, less than 1 % increases in torque achieved by magnet heights above 18 mm.

This is because increasing the magnet height increases the mass and surface area of the magnet, and hence the flux density in pole piece, air gap and stator tooth. However, due to a fixed tooth's surface area, this increase in flux linkage with magnet height will eventually result in no further increase because the iron of the stator tooth becomes significantly saturated.

This can be illustrated from the peak flux linkage obtained per phase for different magnet heights as shown in Figure 7.19.

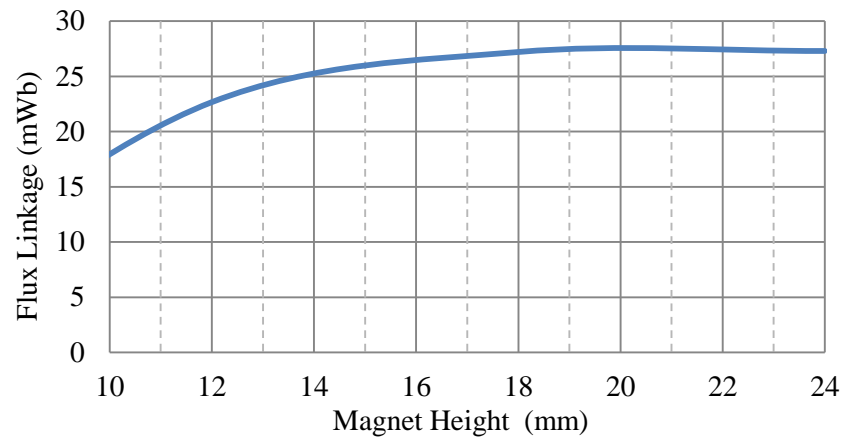


Figure 7.19. Variation of Peak Flux Linkage of the STPM Machine with Changing Magnet Heights.

From Figure 7.19, it can be seen that the flux linkage increased by 26 % from 10mm to 12mm heights, 20 % from 12 mm to 18 mm to where it starts levelling off and any further increase only results in less than a 1 % increase in flux linkage. Hence; it's decided that a tooth width between 18 mm and 20 mm should be considered to find the optimal height.

In Figure 7.20, comparison charts of torque density and torque ripple were obtained for different magnet heights with 15 A/mm^2 applied current density.

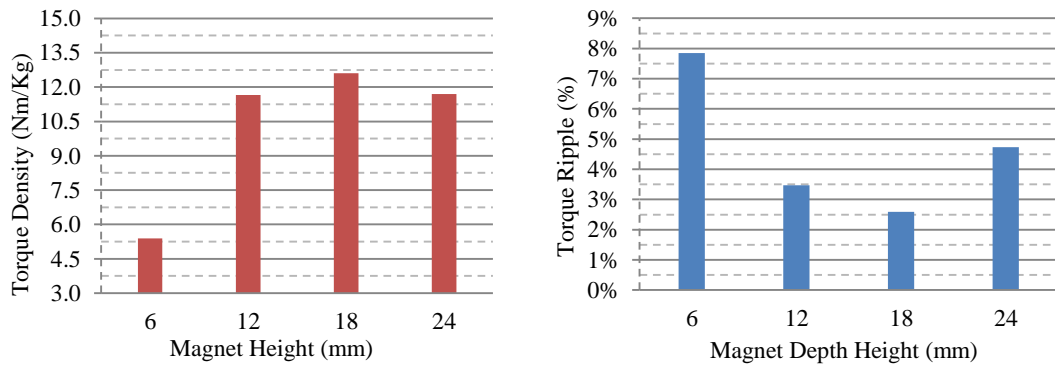


Figure 7.20. Torque Density and Ripple Achieved at 15 A/mm^2 at Various Magnet Heights.

From Figure 7.20, it can be seen that 18 mm height achieved the highest torque density and the lowest torque ripple because of the increased magnetic loading, and the smoother air gap field produced respectively.

The peak torque per magnet mass for different magnet heights at the optimised current density of 15A/mm^2 is shown in Figure 7.21 for indicating a ratio index to be considered for future work.

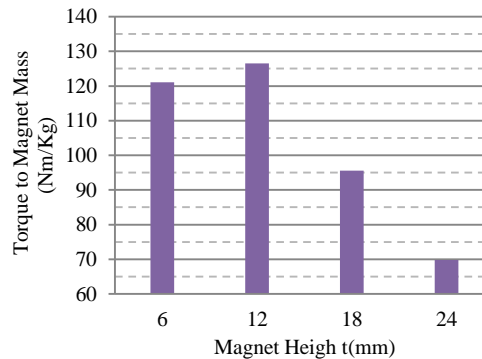


Figure 7.21. Torque to Magnet Mass Index at 15 A/mm^2 Applied Current Density for Various Magnet Heights.

From the figure, it can be seen that the highest torque to magnet mass is achieved at a magnet width of 12mm. This is due to the improved utilisation of the rotor magnetic circuit.

This rotor topology does not exhibit demagnetisation even during the over loading condition. This is because the bridges surrounding the magnets act to protect the magnets from any field strong enough to demagnetise. This is investigated further in the following chapter.

Although 12mm magnet height showed the best achieved torque to magnet mass ratio, 18mm has been chosen as the optimal height because of its higher torque to active mass ratio.

7.4.2 Magnet Thickness

The magnet thickness (in the direction of magnetisation) has been varied as can be seen in Figure 7.22 in order to conduct an investigation on the impact of magnet thickness on the achieved torque density.

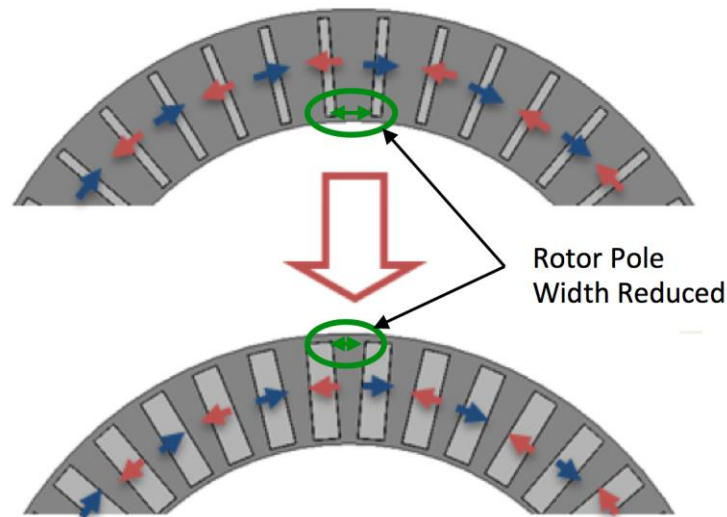


Figure 7.22. A Cross Section of the Rotor of Different Magnet Thickness.

The impact of changing the magnet thickness on the machine's flux linkage is investigated here. A wider magnet reduces the rotor pole width as shown in Figure 7.22. Figure 7.23 shows the no-load flux linkage per phase for different magnet thicknesses.

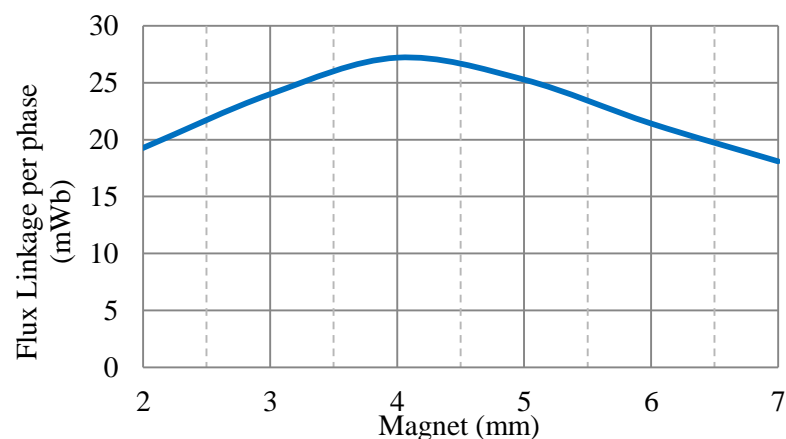


Figure 7.23. Variation of Peak Flux Linkage of the STPM Machine with Changing Magnet Thickness.

From Figure 7.23, the flux linkage can be seen to increase by 43 % for a range of 2 mm and 4mm for double the magnet mass. However, any increase beyond 4 mm thickness results in a reduced flux linkage.

This is because of the saturation in the new smaller pole piece from the excessive MMF generated by thicker magnets; this saturation also restricts the amount of flux that can be transferred through the new smaller outer pole piece.

Although, 4mm thickness has been found to achieve the best flux linkage before the saturation of the iron, an investigation on the magnet thickness impact on torque is essential. A comparison of static torque against current density for varying magnet thickness is shown in Figure 7.24.

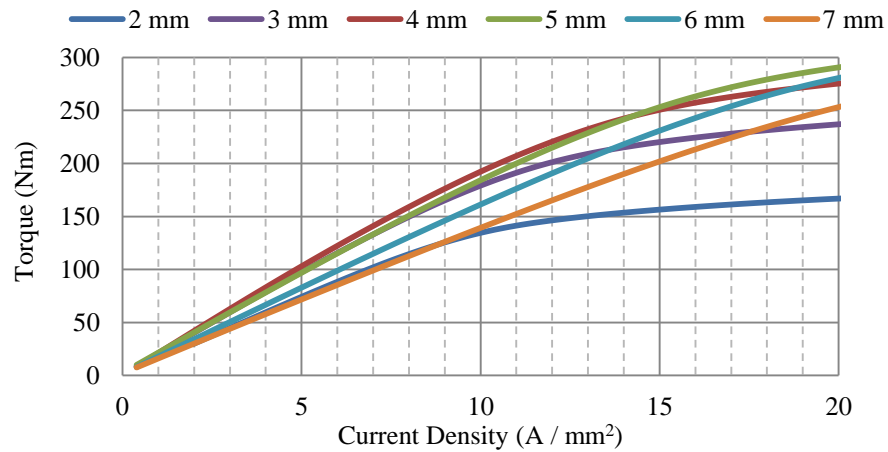


Figure 7.24. Torque Versus Current Density for Various Magnet Thicknesses.

At 15 A/mm² applied current density in Figure 7.24, it can be seen that, in the range of 2mm and 4 mm, an increased torque of 66 % is achieved for 50 % increase in magnet mass, and 12 % between 3 mm to 4 mm for 33 % increase in the magnet mass. However, any further increase in thickness results in a reduction in torque due to the saturation in the rotor iron. A comparison of torque density and torque ripple achieved at different current densities for varying magnet depths is shown in Figure 7.25.

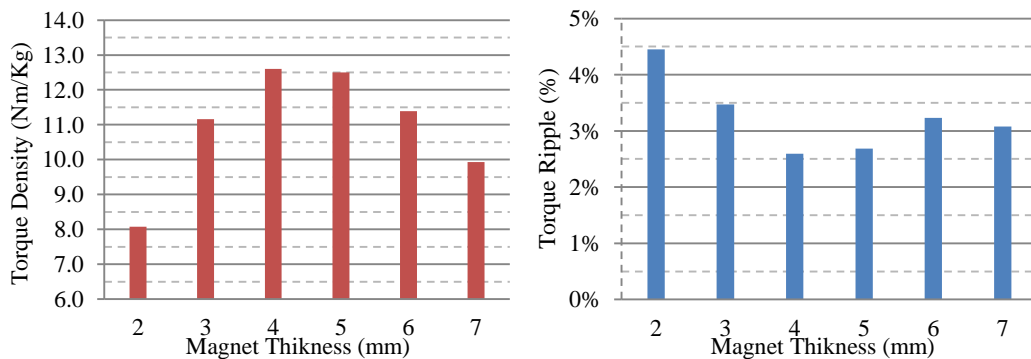


Figure 7.25. Torque Density and Ripple Achieved at 15 A/mm² at Various Magnet Thickness.

From the figure above, the highest torque density has been found at a magnet thickness of 4 mm. This is because of the high flux density and proper iron utilisation in this design. Moreover; the lowest torque ripple is achieved at 4 mm, and this is because of the smother spatial harmonics in the air gap from this thickness, resulting from the narrower pole piece.

Although Figure 7.26 illustrates that increasing the magnet thickness reduces the torque to magnet mass, a balance between the magnet mass and the flux linking of the coil is needed in order to achieve high flux density, improve iron utilisation and to avoid any waste in the costly magnets.

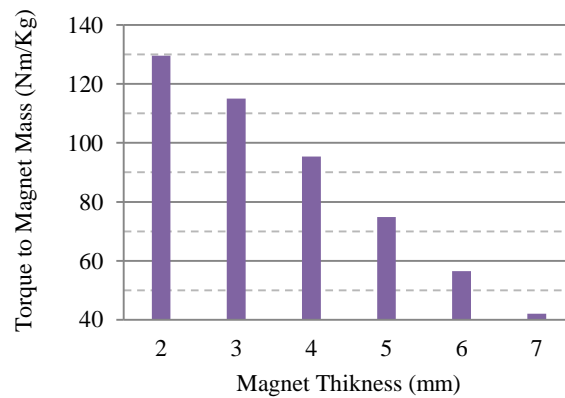


Figure 7.26. Torque to Magnet Mass Index at 15 A/mm² Applied Current Density for Various Magnet Thickness.

By considering the torque density, torque ripple and flux linkage, a 4 mm thickness is chosen to be the balanced optimal choice for this machine. In addition, this magnet thickness resulted in optimum rotor pole widths of 7.2 mm and 4.4 mm at the outer and inner radii respectively.

7.5 Inner Stator Dimension Impact on Torque Density

The inner stator is shown in Figure 7.21 and described in Table 7.10

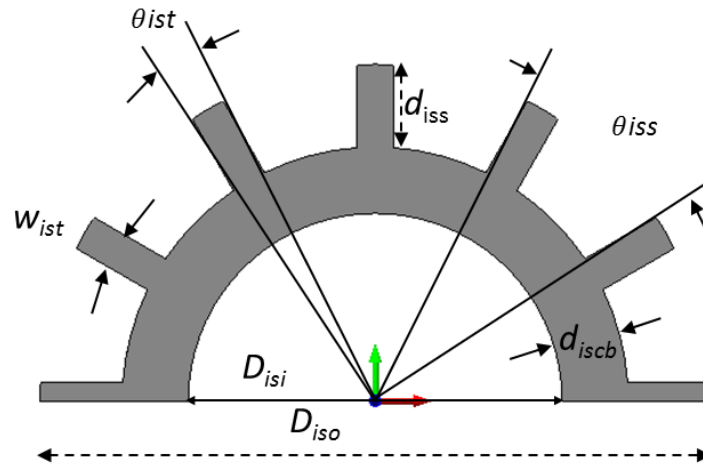


Figure 7.27. Inner Stator Dimensions of The New Split Teeth PM Machine.

Table 7.10. Inner Stator Dimensions Description and Definition.

Symbol	Description
D_{iso}	Inner Stator Outer Diameter
D_{isi}	Inner Stator Inner Diameter
θ_{ist}	Inner Stator Tooth Span
θ_{iss}	Inner Stator Slot Pitch
d_{iss}	Inner Stator Slot Depth
w_{ist}	Inner Stator Tooth Width
d_{iscb}	Inner Stator Coreback Depths

The inner stator tooth width, slot depth and coreback depth have been varied during this investigation and their impact on torque density explored.

7.5.1 Tooth Width

A torque against current density plot for differing tooth widths is shown in Figure 7.28.

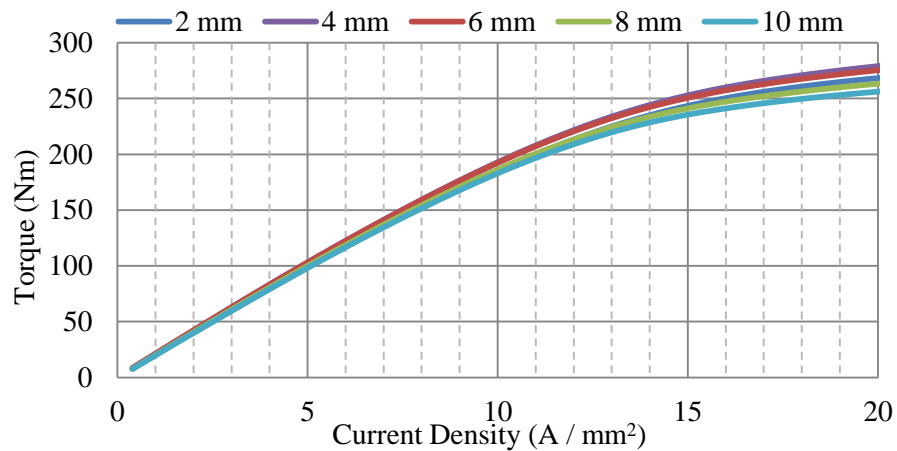
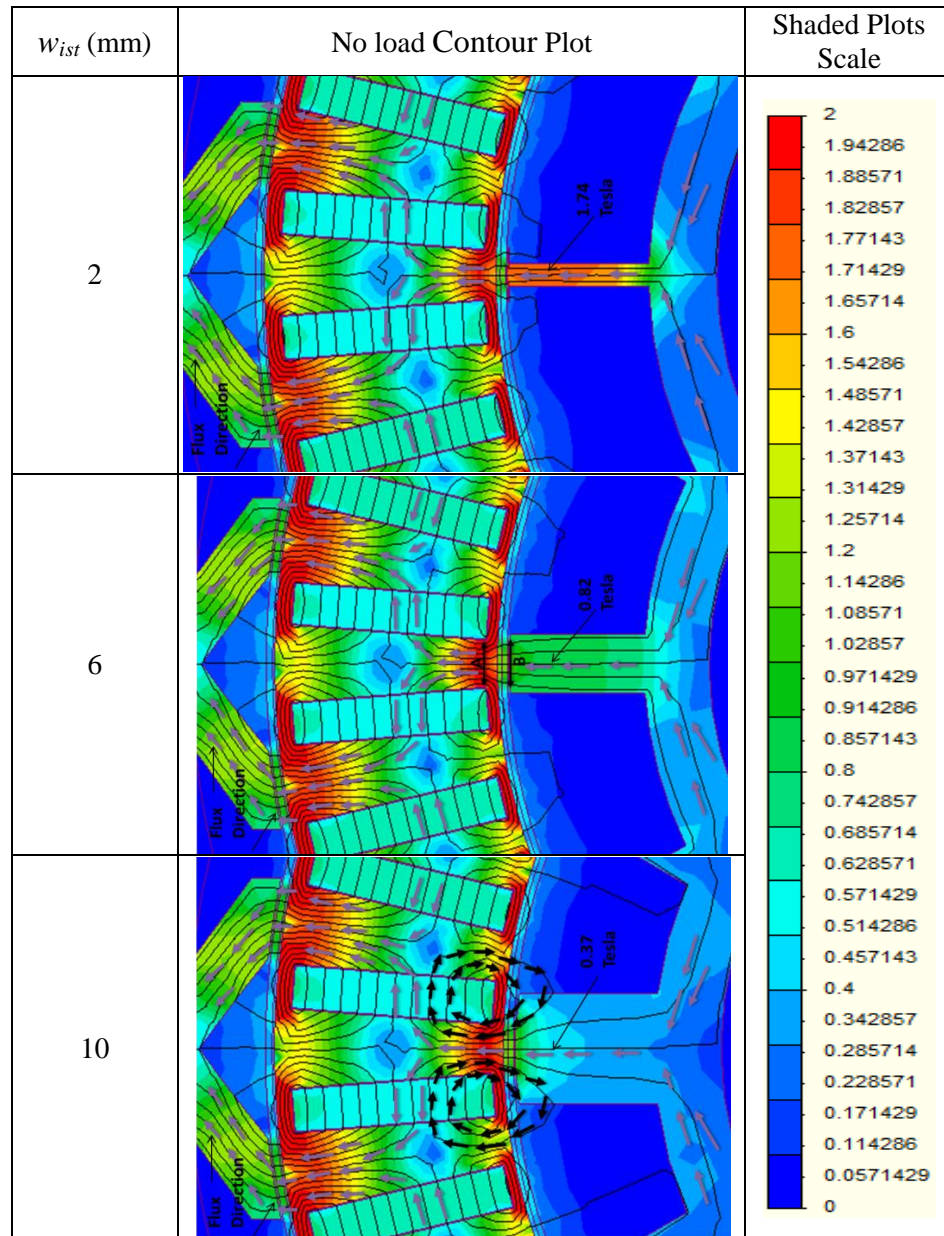


Figure 7.28. Torque Versus Current Density for Various Inner Stator Tooth Widths.

Looking at Figure 7.28, it can be seen that at an inner stator tooth width of 4 mm, the maximum torque is achieved. This is because this width directs the most flux to link the coil as can be illustrated by the flux density distribution plots shown in Table 7.11.

Table 7.11. No Load Shaded Flux Density Distribution of Various Inner Stator Tooth Widths.



From the table, at 2 mm tooth width, the inner tooth can be seen to be highly saturated, and hence can only redirect a limited flux to link the coil. However, 6mm tooth width allows for more flux to pass through the rotor. This is because it is less saturated, and the flux is evenly distributed across its iron. The outer surface area of the inner tooth width (shown as B in the second plot) in this type of machine has to be enclosed by the

inner surface area of the rotor in between two magnet edges (shown as A in the second plot) in order to link the maximum possible flux. This is essential as increasing the tooth width beyond these points result in a significant leakage flux as can be seen at an increased width of 10 mm.

Figure 2.29 shows the torque density and torque ripple achieved at 15 A/mm^2 .

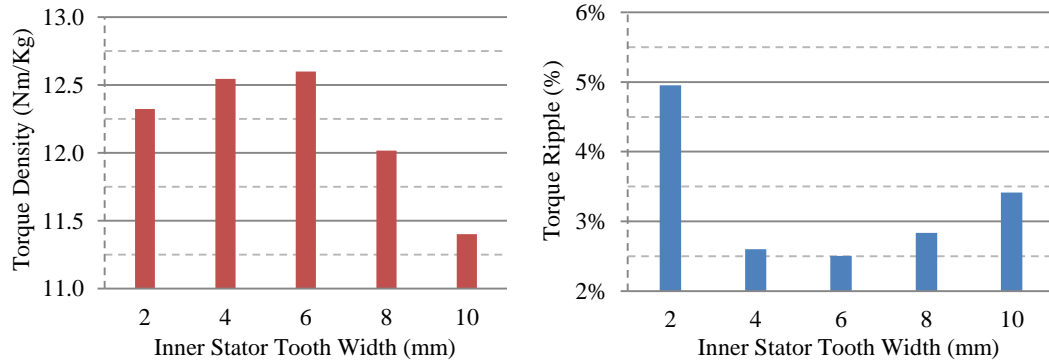


Figure 7.29. Torque Density and Ripple Achieved at 15 A/mm^2 at Various Inner Stator Tooth Width.

From the figure, it can be seen that the maximum torque density and lowest torque ripple were achieved at tooth width of 6 mm, and hence has been chosen as the optimal design.

7.5.2 Inner Slot Depth

Slot depth has a small effect on the achievable torque output as can be seen from the torque against current density shown in Figure 7.30. This is because there are no coils present in the inner stator. However, it is important to make it long enough to prevent a return flux path that causes undesirable leakage fluxes as can be seen from the shaded flux density distribution plots shown in Table 7.12.

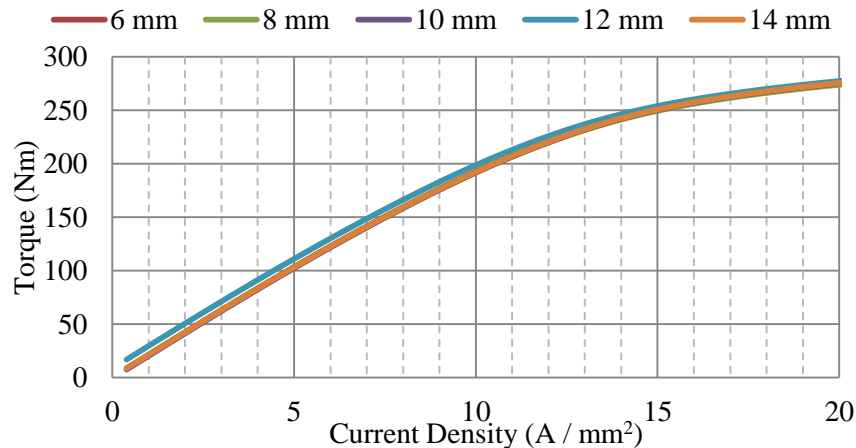
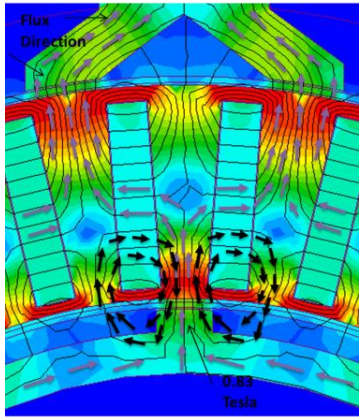
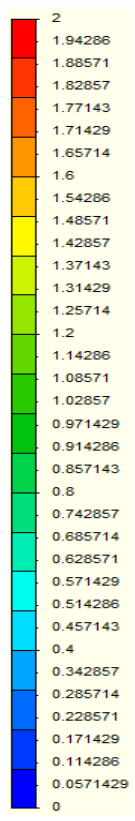
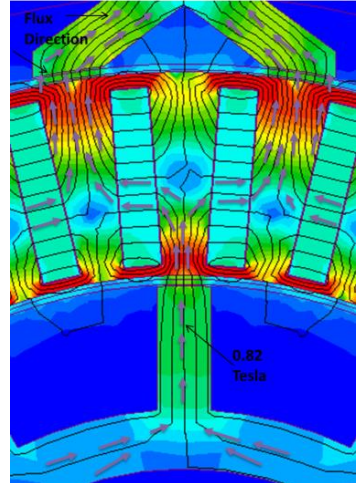


Figure 7.30. Torque Versus Current Density for Various Inner Stator Slot Depths.

Table 7.12. No Load Shaded Flux Density Distribution of Various Inner Stator Slot Depths.

d_{it} (mm)	No load Contour Plot	Shaded Plots Scale
2		
12		

To investigate the effect of various inner stator slot depths on torque density and torque ripple Figure 7.31 was obtained.

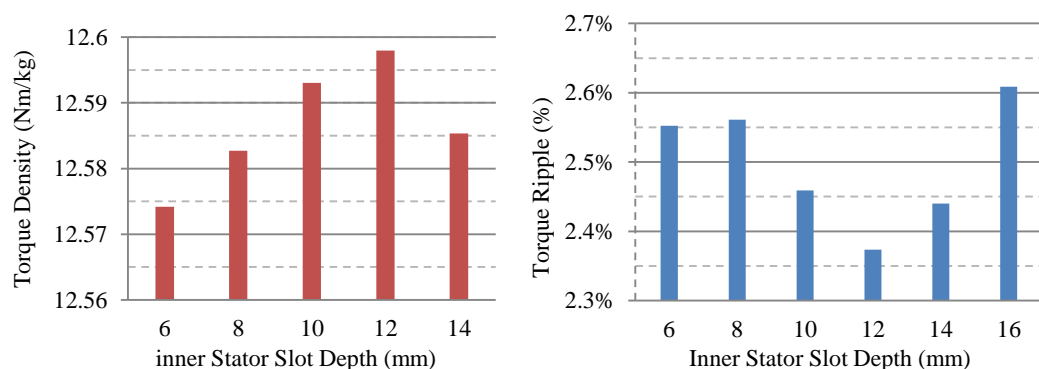


Figure 7.31. Torque Density and Ripple Achieved at 15 A/mm² at Various Inner Stator Slot Depths.

From Figure 7.31, it can be seen that the change in both torque density and torque ripple between different slot depths is almost negligible. However 12mm slot depth has been

chosen as the optimal design because of the advantage of achieving the highest torque density and lowest torque ripple.

7.5.1 Coreback Depth

The coreback must be large enough so as not to be over saturated but no larger to keep the mass down. Figure 7.32 shows the influence of changing the coreback depth on output torque against current density.

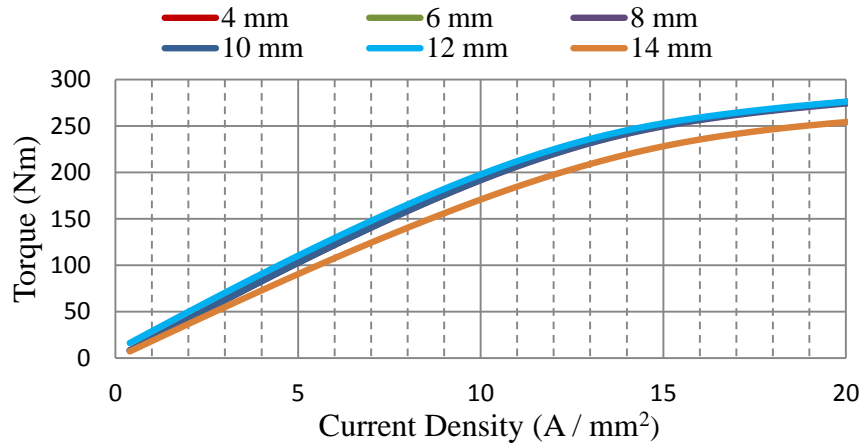


Figure 7.32. Torque Density Achieved by Various Inner Stator Core Back Depths.

From Figure 7.32, it can be seen that the coreback depths from 4 mm to 12 mm have only a small influence to the output torque. However, the mass of the machine increases, hence in order to choose the optimal depth, the influence of varying coreback depths on torque density must be analysed.

Torque density achieved at 15 A/mm² applied current density for varying coreback depths is shown in Figure 7.33.

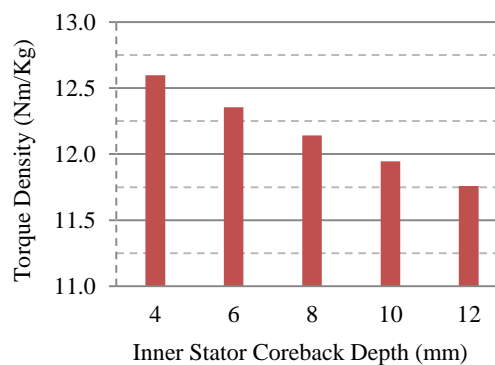


Figure 7.33. Torque Density Achieved by Various Inner Stator Core Back Depths.

From Figure 7.33, it can be seen that any increase in the coreback depth of 2 mm results in 1.5% reduction in the achievable torque density because of the increased iron mass. Hence, a coreback depth of 4mm is chosen here for the inner stator.

7.5.2 With and Without Inner Stator

A comparison is carried out to investigate the impact of using an inner stator. Figure 7.34 shows the effect of the inner stator on flux linkage;

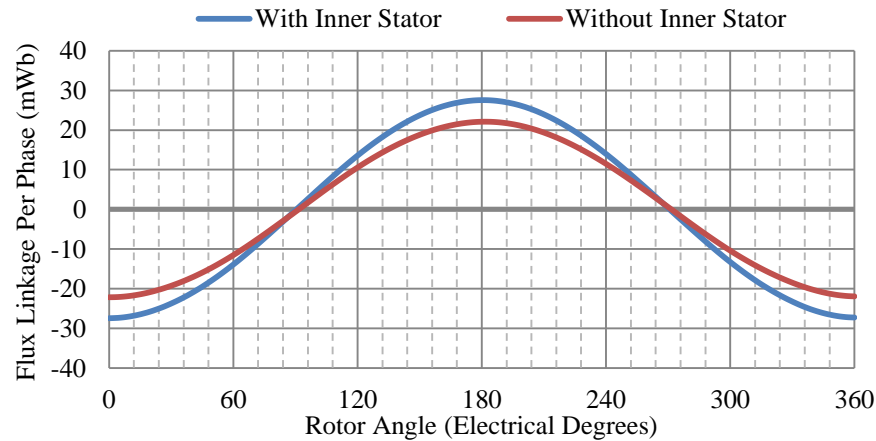


Figure 7.34. Flux Linkage Obtained with and without the Inner Stator

From the figure above, it can be seen that the presence of the inner stator increases the flux linkage by 24 %. This is because the inner stator is acting as a flux return path for the leakage flux as described previously in Chapter 5. In addition, Figure 7.35 shows the torque against current density for with and without the inner stator.

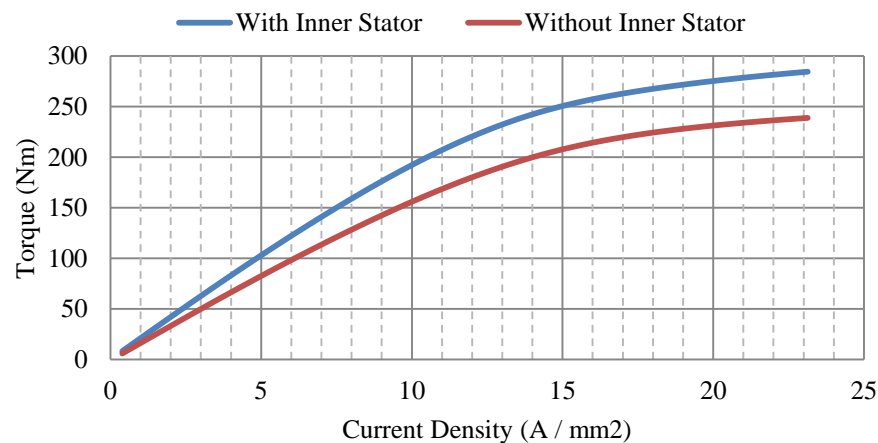


Figure 7.35. Torque Versus Current Density Obtained with and without the Inner Stator.

From Figure 7.35, it can be seen that adding the inner stator has improved the torque by 21 % at 15 A/mm² current density when compared to its absence.

In addition, of the inner stator increasing total mass but the torque increase of greater with torque density rising from 11.2 Nm/Kg to 12.6 Nm/Kg.

7.6 Conclusion

The impact of varying the machine dimensions on the torque density achieved has been investigated for each of the machine's various parameters. In addition to 2D FE solutions, the investigation has included theoretical and mathematical explanations to aid the general understanding of the behaviour of the STPM machine.

A balance between the slot areas, and hence the MMF, and saturation in the tooth and rotor radius has been considered when choosing tooth widths and slot depths since it was found that increasing the tooth width up to 16 mm resulted in increased peak torques. This is because of the increased magnetic loading. However, further increases in width resulted in a drop in peak torque because of the reduced electric loading. On the other hand, increased slot depth up to 12 mm resulted in increased torque because of the increased slot area and hence electric loading. However, a further increase in slot depth again resulted in a drop in torque because of reduced rotor diameter.

In addition, a balance between saturation and rotor radius was considered for the choice of the coreback depth, where reducing the coreback for the same outer diameter resulted in increased peak torque because of the increased rotor radius. However, this reached a point where the torque started to drop with further reduction in coreback depth because saturation it started to occur which limits the magnetic loading. The best torque density and lowest torque ripple were achieved at a coreback depth of half of the tooth width.

Torque increased with increasing slot-opening width up to 8 mm and then it started to drop back. This is because lower slot opening widths in this particular machine allow a fringing flux path in the tooth tip, and very high widths limit the linking flux since both tooth ends become narrower.

Furthermore, increasing the tooth split width and depth up to 8 mm and 7 mm respectively resulted in a significant increase in peak torques. However, the torque dropped with any further increase. This is because the tooth ends become narrower, and hence become saturated more quickly. Moreover, shorter tooth split width and length cause flux to circulate back to the rotor, causing fringing flux.

Furthermore, adding a tooth tip increased the torque by 11 %. This is due to the increased tooth end width which allows more flux to be linked. The choice of tip width

depended on a balance between the amount of increased flux linkage and the mass of the machine.

Also, increasing magnet height resulted in increased peak torques to a point where the ratio between the magnet flux generated by the magnet and the available inner area of the tooth ends increased and the tooth end iron became fully saturated. Any increase in magnet thickness above 4mm resulted in reduced torque because of the saturation of the rotor pole piece.

The implementation of the inner stator increased torque density by 12.5 %. This is because it resulted in an increase of 24 % in flux linkage. The different inner stator dimensions were also investigated here. Its tooth width was found to link the most flux when the outer surface was enclosed between two magnet pole edges, while varying slot and coreback depths had little effect.

After the manual optimisation had been carried out by investigating all of the different parameters and a manual optimum design was chosen, it was found that this design gave an increase by 43% in torque density when compared to the 12 slots/ 40 poles STPM machine that was initially designed in chapter 6.

Table 7.13 shows the different parameter values of the investigated and initially optimised STPM machine.

Table 7.13. Final Investigated STPM Machine Dimensions' Symbol, Descriptions and Values.

Description	Symbol	Value
Stator Inner Diameter	D_{si}	146.8 mm
Stator Outer Diameter	D_{so}	200 mm
Tooth Span	θ_t	24.77°
Slot Pitch	θ_{sp}	30°
Slot depth	d_s	12 mm
Core Back Depth	d_{cb}	8 mm
Tooth Split Depth	d_{ts}	5 mm
Tooth Split Span	θ_{ts}	12.50°
Tooth Body Width	w_t	16 mm
Slot Opening Span	θ_{so}	5.23°
Tooth Tip Depth	d_{tt}	2.5 mm
Rotor Outer Diameter	D_{ro}	72.35 mm
Rotor Inner Diameter	D_{ri}	51.85 mm
Magnet Upper Bridge	B_{mu}	1.5 mm
Magnet Bottom Bridge	B_{mb}	1 mm
Magnet Span	θ_m	3.23°

Magnet Height	h_m	18 mm
Magnet Thickness	W_m	4 mm
Inner Stator Outer Diameter	D_{iso}	50.85 mm
Inner Stator Inner Diameter	D_{isi}	34.66 mm
Inner Stator Tooth Span	θ_{ist}	6.8°
Inner Stator Slot Pitch	θ_{iss}	30°
Inner Stator Slot Depth	d_{iss}	12 mm
Inner Stator Tooth Width	w_{ist}	6 mm
Inner Stator Coreback Depths	d_{iscb}	4 mm

The inner stator slot depth doesn't have an impact in the achievable torque. However it has to be long enough to prevent a flux return path and to reduce the core back mass by reducing its diameter and hence increase the torque density. The inner stator coreback has to be thick enough to allow a full flux path for the linking flux.

In the following chapter an automated optimisation will be carried out using OptiNet to ascertain the effectiveness of the manual optimisation algorithm. Thereafter, mechanical and electrical evaluations will be carried out on the final design.

Chapter 8. Further Investigation of the Final STPM Machine

The final optimised and modified STPM machine is shown in this chapter. During the initial optimisation process (manual) of the STPM machine, the impact of changing the machine dimensions on torque output was investigated as shown in Chapter 7. This chapter describes the machine dimensions after the final optimisation process (Automated) using OptiNet. In addition, the method used to determine the mechanical strength of the rotor is explained, and further investigations on the final STPM machine using FE simulation are carried out.

8.1 Introduction:

A trade-off between parameters is required in electrical machine design, where by improving one aspect often degrades another. In this context, the optimisation of the STPM machine was conducted using two processes, initial manual optimisation, as described in previous chapters and a final automated optimisation. The optimisations focused on the highest peak torque for the specific volume of the machine, by varying a set of parameters. The results obtained from the final optimisation process are shown in this chapter and compared to the manually optimised design. Moreover, the dimensions of the final optimised STPM machine are presented. Due to centrifugal forces, rotors in high speed machines experience high mechanical stress. In order to ensure that the rotor in the STPM machine is mechanically capable at the maximum operating speed, mechanical stress analysis was carried out. The results are shown in this chapter. The winding arrangement for the final STPM machine is also described. The maximum operating current for the final design is then discussed and a torque-speed curve presented. The magnets of the final STPM machine were analysed for demagnetisation at the maximum operating temperature and maximum opposing field. These results are presented here.

8.2 OptiNet Optimisation (Final Optimisation Process)

The STPM machine model created using 2D FE simulations was optimised by the optimisation package, OptiNet here. Optimisation presented maximises the torque capability for a fixed current density. During this optimisation, some constraints were kept constant, such as stator outer diameter, axial length, air gap lengths and the magnet's upper and lower bridges. However, the other dimensions were free to vary by 30%. After thousands of simulations, the dimensions of the final design are shown in Table 8.1.

Table 8.1. Initially Optimised and OptiNet Optimised STPM Machine Dimensions

Description	Symbol	Manual Optimised Design	OptiNet Optimised Design
Stator Inner Diameter	D_{si}	146.8mm	146.5mm
Stator Outer Diameter	D_{so}	200mm	200mm
Tooth Span	θ_t	24.7°	24°
Slot Pitch	θ_{sp}	30°	30°
Slot depth	d_s	12mm	11.9mm
Core Back Depth	d_{cb}	8mm	8.2mm
Tooth Split Depth	d_{ts}	5mm	5.7mm
Tooth Split Span	θ_{ts}	12.50°	12.6°
Tooth Body Width	w_t	16mm	16.3mm
Slot Opening Span	θ_{so}	5.2°	5.9°
Tooth Tip Depth	d_{tt}	2.5mm	2.6mm
Rotor Outer Diameter	D_{ro}	72.3mm	72.2mm
Rotor Inner Diameter	D_{ri}	51.8mm	51.7mm
Magnet Upper Bridge	B_{mu}	1.5mm	1.5mm
Magnet Bottom Bridge	B_{mb}	1mm	1mm
Magnet Span	θ_m	3.2°	3.2°
Magnet Height	h_m	18mm	18.1mm
Magnet Thickness	W_m	4mm	4mm
Inner Stator Outer Diameter	D_{iso}	50.8mm	50.7mm
Inner Stator Inner Diameter	D_{isi}	34.6mm	34.2mm
Inner Stator Tooth Span	θ_{ist}	6.8°	5.5°
Inner Stator Slot Pitch	θ_{iss}	30°	30°
Inner Stator Slot Depth	d_{iss}	12mm	12.3mm
Inner Stator Tooth Width	w_{ist}	6mm	5.4mm
Inner Stator Coreback Depths	d_{iscb}	4mm	4.1mm

A comparison of torque output between the initial and final optimised designs is shown in Figure 8.1. It can be seen that the optimised machine obtained using OptiNet benefits from less than 2 % increase in torque output at 15 A/mm².

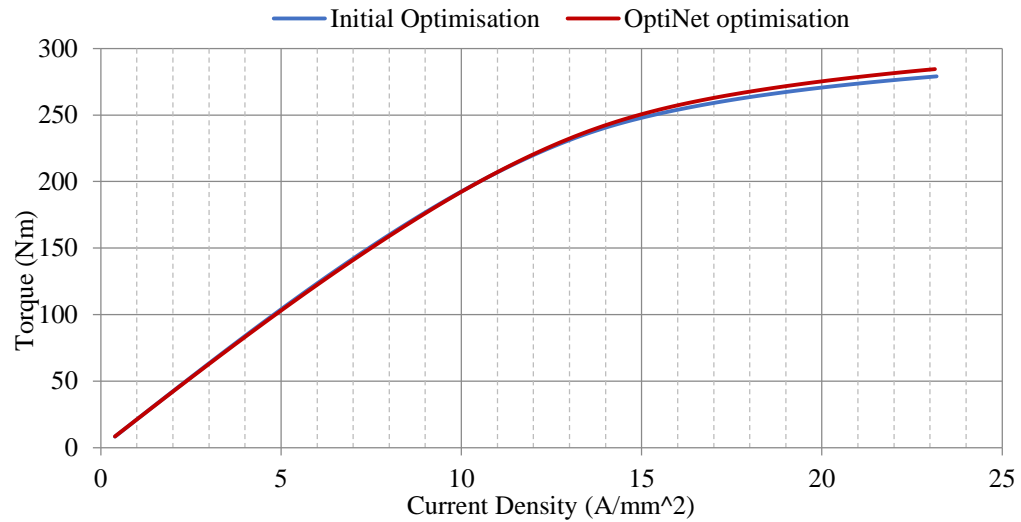


Figure 8.1. Torque against Current Density for the STPM Machines Resulting from Initial and Final Optimisation Processes

OptiNet optimised design has increased torque density from 12.6 Nm/Kg to 12.7 Nm/Kg when compared to the manual optimised design.

The final optimised STPM machine is chosen for construction and the results of further investigation are shown in subsequent sections of this chapter. The optimised dimensional drawings are as shown in Figures 8.2-8.4 respectively.

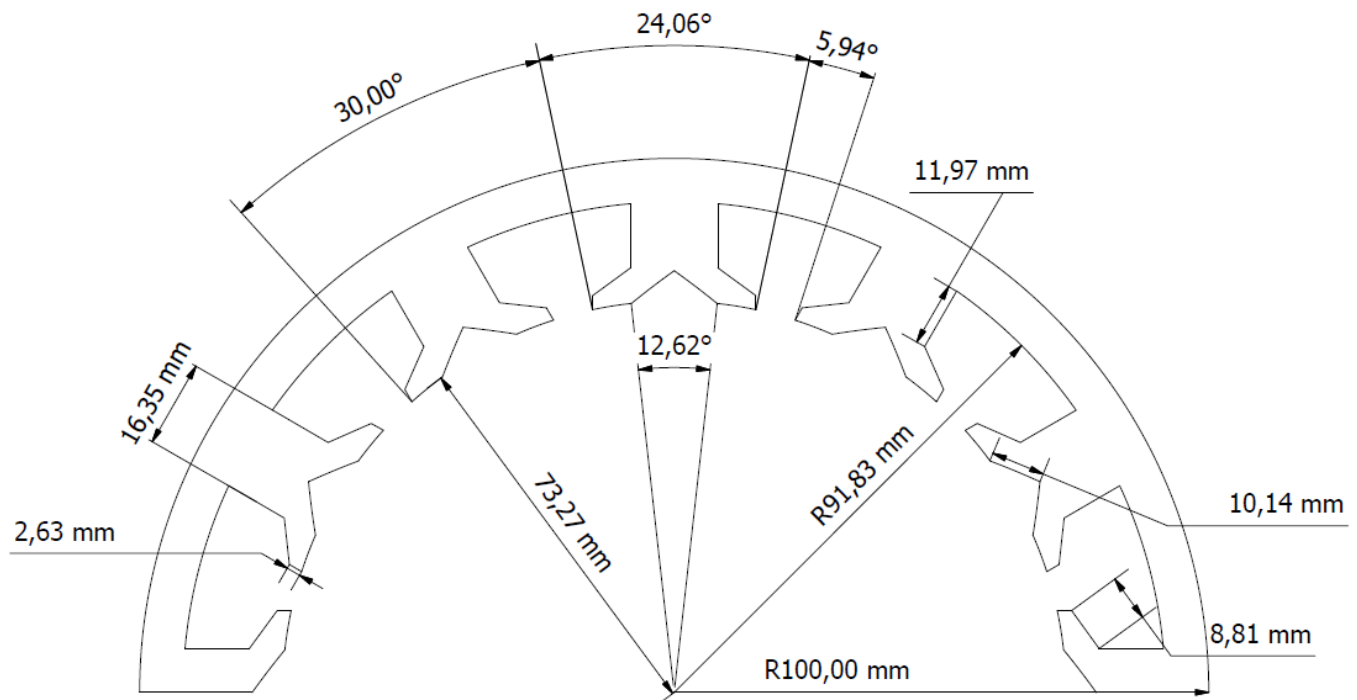


Figure 8.2. Final Optimised Stator.

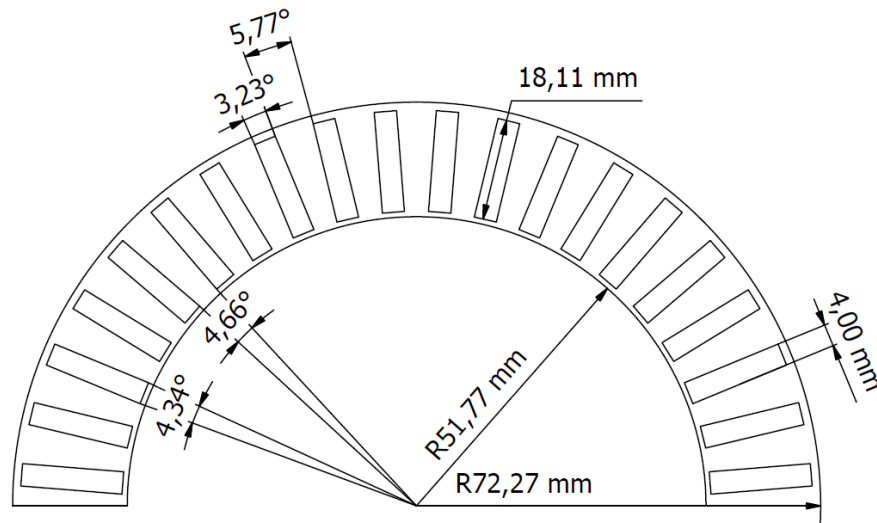


Figure 8.3. Final Optimised Rotor.

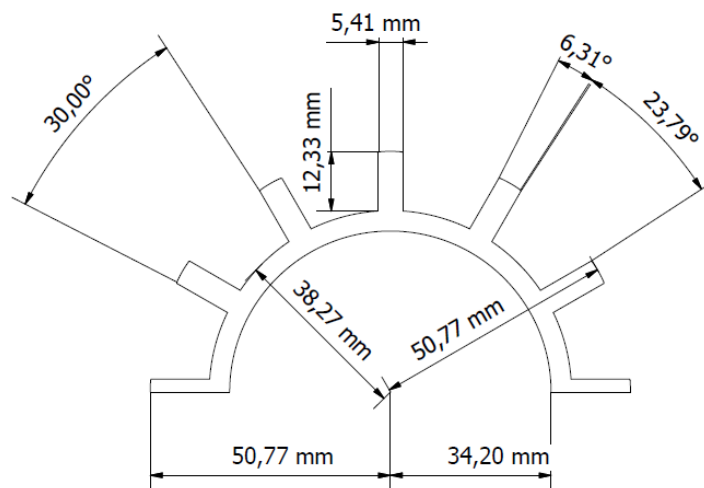


Figure 8.4. Final Optimised Inner Stator.

8.3 Rotor Mechanical Strength

In order to mechanically restrain the rotor magnets against the large centrifugal forces at high speed, it is proposed that the rotor lamination be made in one piece with bridges around the inner and outer radii of the magnets. These can be seen in Figure 8.5. Although a closure inevitably leads to increased rotor leakage flux, such a feature is unavoidable if mechanical strength is to be maintained.

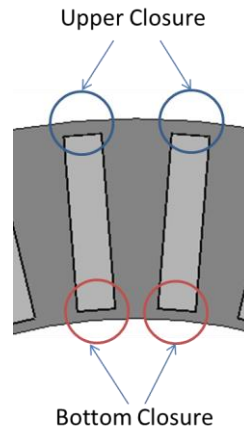


Figure 8.5. Bridges Around the Inner and Outer Radii of the Magnets.

Various mechanical restrains have been analysed. A sleeve to retain the magnets using various different materials (to replace the upper closure piece of the rotor) was considered with regard to the following properties:

- High yield strength (to be as thin as possible)
- Low electrical conductivity
- Good thermal conductivity (to allow for a good heat transfer)
- Non-magnetic properties (to reduce leakage flux).

The second property was particularly important in order to reduce eddy currents that could contribute to the demagnetising of the magnets.

The properties of the materials considered and analysed are as shown in Table 8.2.

Table 8.2. Properties of Sleeve Types under Consideration.

Material	Yield Strength (MPa)	Electrical Conductivity ($M\Omega^{-1}m^{-1}$)	Thermal Conductivity ($Wm^{-1}^{\circ}C^{-1}$)
Silicon Steel Laminations	450	0	25
Inconel (grade)	1100	0.8	11.4
Aluminium Alloy (grade)	415	23.26	155

Although a material with low electrical conductivity is preferable in order to minimise eddy current loss, it is also advantageous to have a high thermal conductivity so heat can be transferred away easily from the magnets. These two do not exist together so a compromise is sought

In order to start the comparison, the sleeve thickness required for mechanical integrity was determined using Equations 8.1 to 8.6:

The sleeve hoop stress(σ_{sleeve}) was calculated from:

$$\sigma_{sleeve} = \rho \cdot w^2 \cdot r_{ro}^2 \quad 8.1$$

Where ρ is the density of the material used, w is the speed in rad/sec and r_{ro} is the outer diameter of the sleeve. Then the force of the components under the sleeve should be calculated using Equation 8.2:

$$f = w^2 \cdot m \cdot r_{cm} \quad 8.2$$

Where f is the force of the component that is acting on the sleeve, m is the mass of the component under the sleeve and r_{cm} is the mean diameter of the component under the sleeve. Then the magnet pressure is calculated:

$$p_{componenet} = \frac{f}{2\pi \cdot r_{co} \cdot l_a} \quad 8.3$$

Where $p_{componenet}$ is the pressure generated by the component, r_{cm} is the outer diameter of the component under the sleeve and l_a is the axial length of the component under the sleeve. Now the hoop stress of the components can be calculated:

$$\sigma_{componenet} = \frac{p_{componenet} \cdot r_{co}}{t_{sleeve}} \quad 8.4$$

Where $\sigma_{componenet}$ is the hoop stress of the component and t_{sleeve} is the thickness of the sleeve. Now the total hoop stress can be calculated from Equation 8.5:

$$\sigma_{total} = \sigma_{sleeve} + \sigma_{componenet} \quad 8.5$$

For good design practice, the sleeve thickness is chosen to have a total that is not greater than 50% of the yield stress of the material, and this can be ensured by calculating the threshold using Equation 8.6:

$$Threshold = \frac{\sigma_{total}}{material\ yeild\ strength} \quad 8.6$$

Although the lamination bridge option is to be made in a single piece with bridges

around the inner and outer radii of the magnets, the thickness of the outer bridge is calculated assuming that it forms a separate sleeve placed over the magnets.

In all cases the sleeve thicknesses was calculated to achieve a hoop stress that is 50% greater than the yield strength at 6000 rpm. Table 8.3 summarises the results and the effect on flux linkage by the necessary change in magnetic gap to accumulate the sleeve.

Table 8.3. Sleeve Thickness and Flux Linkage of Various materials

Material	Thickness (mm)	Flux Linkage (PU)
silicon Steel Laminations	1.5	0.75
Inconel (grade)	0.6	1
Aluminium Alloy (grade)	8.5	0.3

From Table 8.3 it can be seen that the use of an Aluminium grade sleeve results in a significant reduction in the flux linking the coil. This is because of the resultant large magnetic gap.

Torque verses current density is analysed in Figure 8.6 for the Inconel sleeve and the silicon steel sleeve.

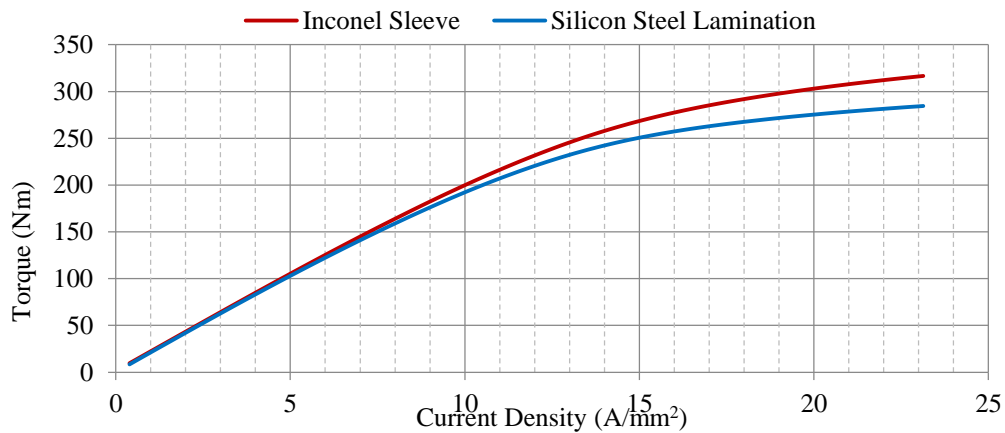


Figure 8.6. Torque Against Current Density for the STPM Machines Using Different Sleeves.

At 15A/mm, torque density is 12.6 Nm/Kg with the silicon steel and 13.5 Nm/Kg with the Inconel sleeve. Although using the Inconel sleeve increases the effective air gap depth, it results in 7 % increase in torque density. This is because using the Inconel sleeve allows for more flux to be linked by the coil whilst also minimising the leakage flux that results by using the silicon steel.

Although the Inconel improved the machine torque density, it was not considered for

the purpose of this research because of the limited time scale. However, it will be proposed to be used in future work.

8.4 Winding Arrangements

It is essential to choose the best possible winding arrangement, since this determines the amplitude and waveform shape of the MMF and the EMF. The windings of the optimised STPM machine have been arranged in three phases with a 120° phase shift.

For the tooth and pole arrangements every third coil is in phase, hence the condition shown in Figure 8.7 was most appropriate.

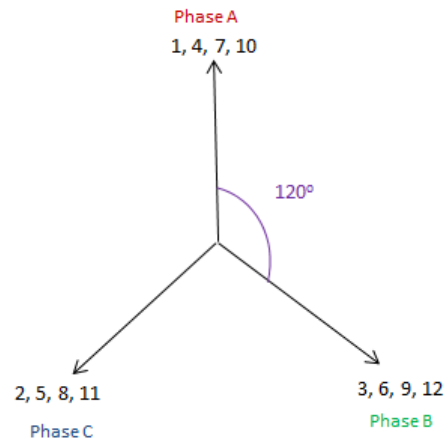


Figure 8.7. Electrical Degrees between the Slots of the STPM Machine.

This machine uses single tooth winding, which in the prototype is connected with three phases externally as shown in Figure 8.8.

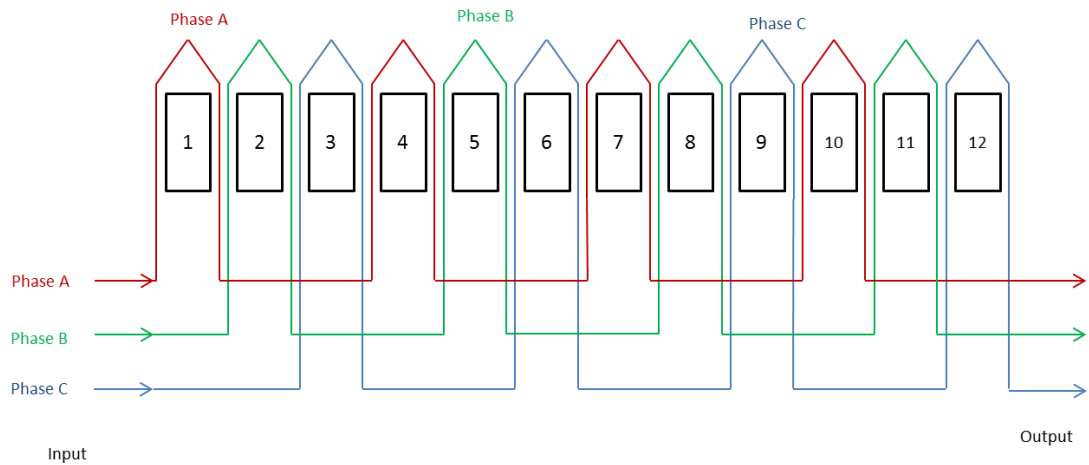


Figure 8.8. Winding Arrangement in the Slots of the STPM Machine.

8.5 Number of Turns

The number of turns depends on various important factors within the machine and the main factor considered was the supply voltage which should not be exceeded by the back EMF (300 volts). The back EMF can be adjusted by changing the coil's number of turns as illustrated by Equation 5.1 in Chapter 5, and hence 5 turns per phase have been chosen, with each turn including 10 strands which were chosen for simplicity. This allows easier winding construction when twisting the coils. This minimises the coil diameter, since a large diameter increases the end windings. Using stranded wire also minimises the coil skin effect. A fill factor of 45% has been chosen because the coils are wound by hand.

The available coil space is calculated to be 318.78mm^2 . Hence the effective area is $318.78\text{ mm}^2 \times 0.45$, which gives 143.45 mm^2 , and this means that the total area available for each turn is 28.69 mm^2 . Dividing this number by the number of strands results in each strand having a total area of 2.87mm^2 . From this, the radius of the strand can be found from:

$$r_{strand} = \sqrt{\frac{A_{strand}/2}{\pi}} \quad 8.7$$

Where r_{strand} is the radius of one strand and A_{strand} is the strand area which is divided by 2 because each strand has two sides. The diameter is hence calculated to be 1.35 mm. However, the coils available were of a diameter of either 1.3 mm or 1.4 mm. A choice of 1.4 mm will increase the fill factor to 48.2% as shown in Figure 8.9.

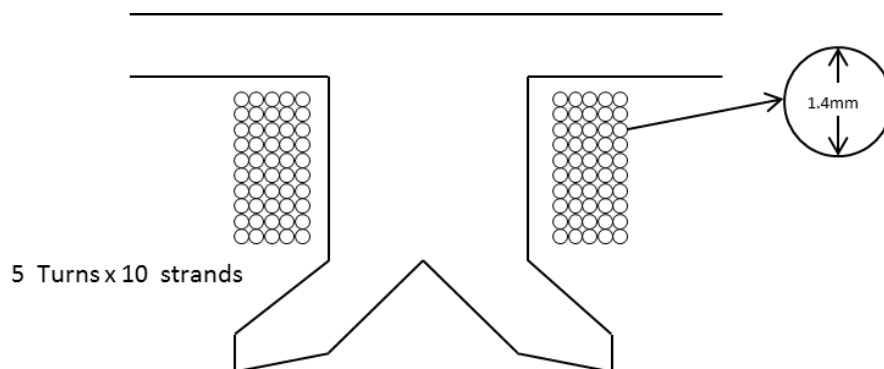


Figure 8.9. A Cross-Section View of the Coils Inside the Slots.

8.6 Electromagnetic Torque at Different Operating Currents.

The optimised STPM machine has three possible operational current ratings, as can be seen from Figures 8.10 and 8.11 and these are:

1. RMS current of 138.8 Amps where a torque of 197 Nm is achievable, this operating current does not require more than an external air cooling fan because the applied current density is 10 A/mm^2 [128].
2. RMS current of 226.3 Amps where a torque of 227 Nm is achievable. This operating current requires a self-fan air cooling because the applied current density is 12.5 A/mm^2 .
3. RMS current of 268.7 Amps where a torque of 250 Nm is achievable. This operating current requires forced air cooling because the applied current density is 15 A/mm^2 .

The STPM machine was built without a cooling system. However, it should be considered in future work as torque will increase with better cooling.

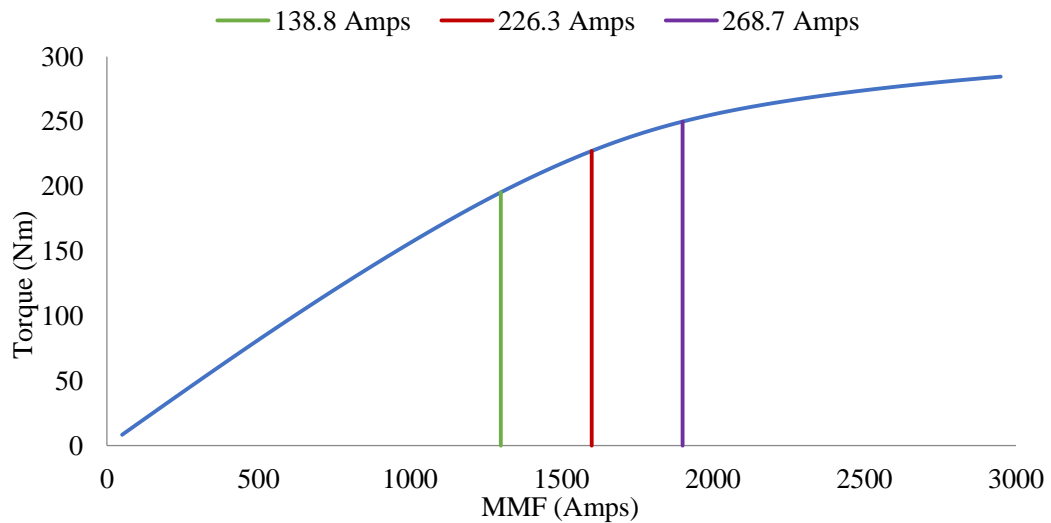


Figure 8.10. Current Ratings on a Torque Against MMF Plot for the Final STPM Machine.

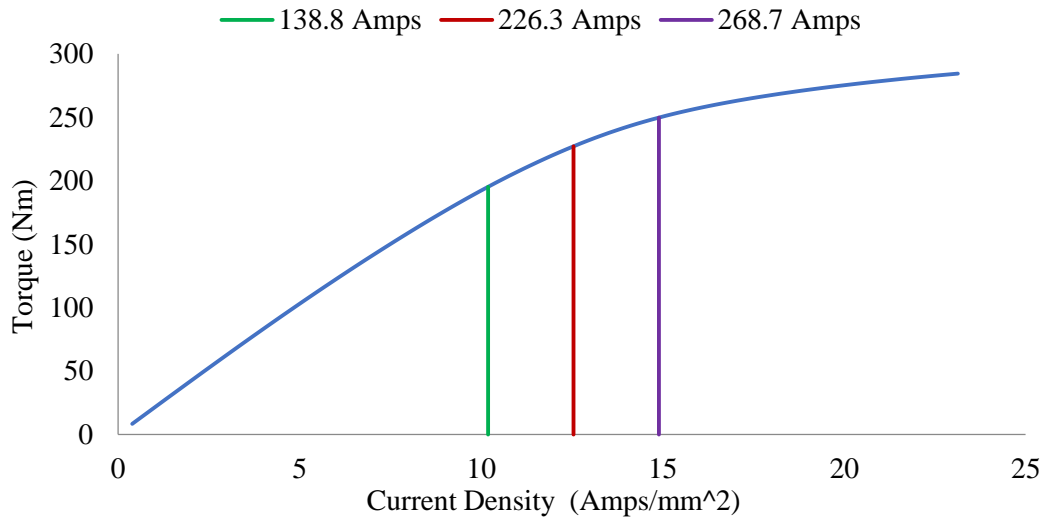


Figure 8.11. Current Ratings on a Torque Against Current Density Plot for the Final STPM Machine.

8.7 Torque-Speed Characteristics

The RMS current of 138.8 Amps is chosen as the prototype machine is naturally cooled. It is important to note that the back EMF increases with speed to a point where the inverter reaches its voltage limit. At this base speed, it is necessary to reduce the back EMF in order to increase the speed within the voltage limit. This can be achieved by using field weakening technique. This technique involves the application of a current component in the negative direct axis to oppose the magnet flux. This field weakening is determined by the inductance and current in the direct axis. Figure 8.12 shows a single phase phasor diagram for the PM machine in its direct and quadratic axis planes.

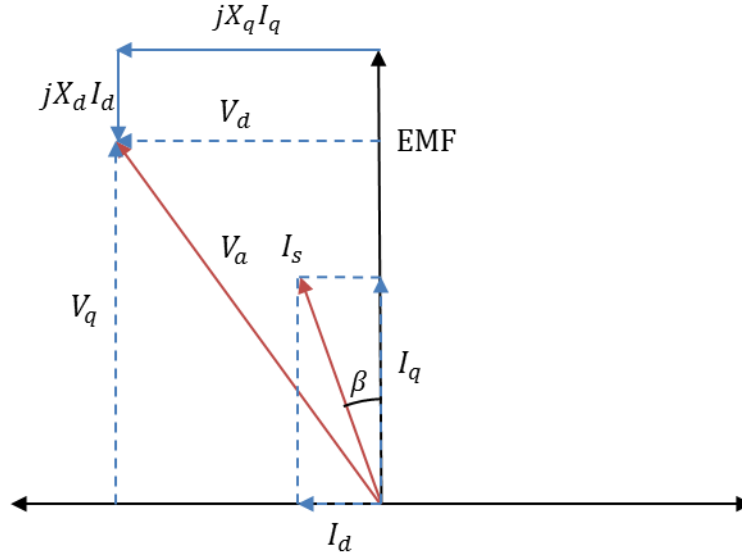


Figure 8.12. Phasor Diagram for a Single Phase of the PM Machine in its Direct and Quadratic Axis Planes.

From Figure 8.14, $-X_d I_d$ can be shown to be the field that oppose the field flux, and the set of Equations between equations 8.6 and 8.7 are also obtained from Figure 8.13 to calculate the field weakening angle β :

$$V_a^2 = V_q^2 + V_d^2 \quad 8.6$$

$$V_q = \text{EMF} - X_d I_d, \quad V_d = -X_q I_q$$

$$I_q = I_a \cos \beta, \quad I_d = I_a \sin \beta$$

$$V_a^2 = a_0 + (\text{EMF} - X_d I_a \sin \beta)^2 + (-X_q I_a \cos \beta)^2 \quad 8.7$$

The field weakening angle is calculated using equation 8.7, and then this angle is implemented in 2D FE transient with motion simulations and solved to obtain the torque-speed curve shown in Figure 8.13. Here it can be seen that the base speed is at 3900 rpm before the inverter reaches the supply voltage limit and the machine enters the field weakening region.

The output power(P_{out}) can be calculated at any point in the torque–speed curve using equation 8.8:

$$P_{out} = T \omega_{mechanical} \quad 8.8$$

Table 8.4 shows values of β at different speeds and the resulting per unit (pu) values of the inductance in the d and q axes.

Speed	L_q (pu)	L_d (pu)	β ($^\circ$)
0	1	0	0
1000	1	0	0
1500	1	0	0
2000	1	0	0
2500	1	0	0
3000	1	0	0
3500	1	0	0
3900	1	0	0
4000	0.99	0.087	5
5000	0.86	0.5	30
6000	0.7	0.7	44
7000	0.8	0.8	55

Table 8.4. Angle and Reactance of Field Weakening.

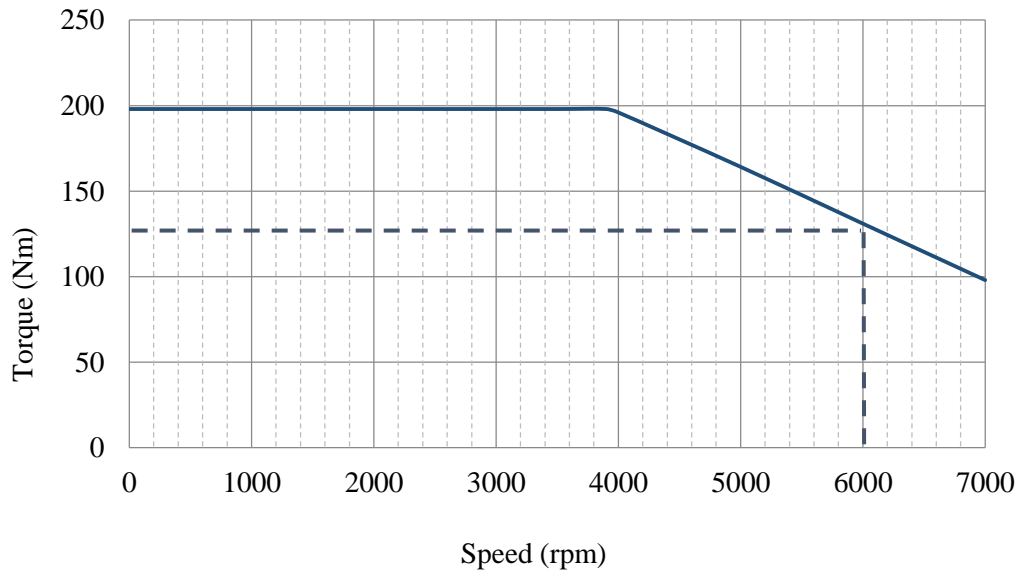


Figure 8.13. Torque vs Speed Curve Obtained by FE Calculations.

It can be seen from Figure 8.13 that the machine is capable of reaching a speed of 6000 rpm, which is the maximum speed required for the chosen applications for this project, while maintaining a torque of 131 Nm. Figure 8.14 shows how the current is applied in both d and q axes at different speeds. A d axis current of 96.4 Amps can be seen to be applied d axis at the maximum speed of 6000 rpm, while a reduced current of 99.8

Amps is applied in the q axis.

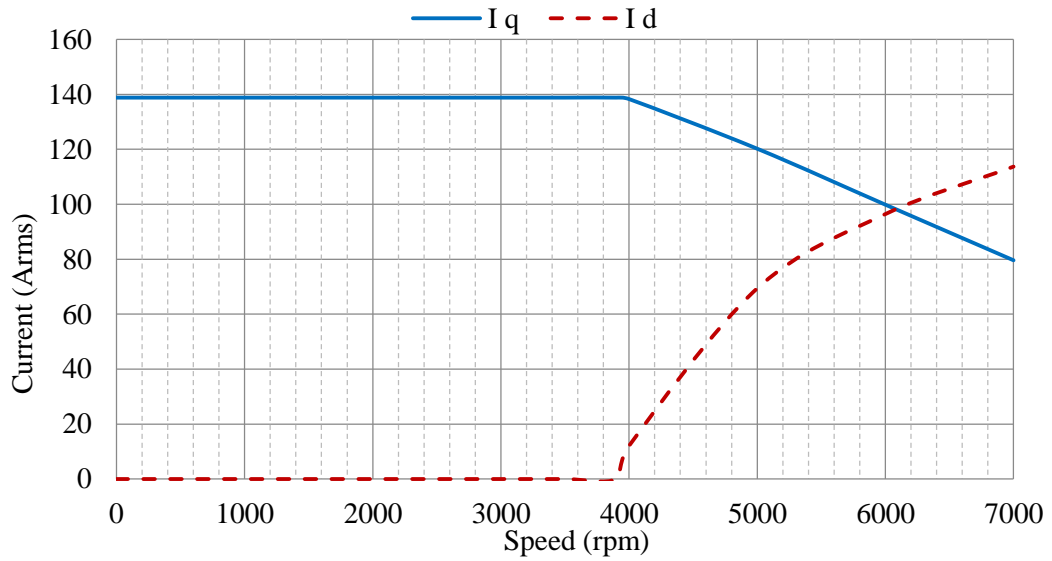


Figure 8.14. Direct and Quadratic Axis Currents Against Speed During Field Weakening.

8.8 Magnet Demagnetisation

This is a very important issue to be considered in permanent magnet machines. Apart from the operating temperature and the magnetic circuit, which can cause the magnets to be demagnetised, a large negative d-axis current applied for field weakening can cause demagnetisation. The demagnetisation curve in the second quadrant of the hysteresis loop for the neodymium iron boron magnet is as shown in Figure 8.15. This quadrant curve gives specific information about how the material performs under different magnetic loadings and temperature conditions, and it represents the specific material used to make the magnets and is independent of their shape. It is also important to mention that magnets can experience three different types of loss of output residual flux density, which are reversible, irreversible-recoverable and structural (irreversible-unrecoverable). Reversible loss is when the magnet is able to recover from its output loss as soon as it is returned to its original state. However, when the output change is permanent, the loss is called irreversible. Irreversible but recoverable loss is that where the magnet can be recovered by re magnetising the magnets. However, irreversible and unrecoverable loss is that of which the magnet cannot recover without reprocessing.

The machine will have a specific load line, which is also referred to as the operating slope and the slope of this line is the permeance coefficient (P_c). The load line

represents a line that starts from zero to the P_c value of the magnet in the circuit where it is placed with no field applied to the magnet by the machines stator windings. The intersection between the load line and the normal curve is called the operating point. The magnet will experience an irreversible demagnetisation if the operating point goes beyond the knee point of the normal curve. The knee point is a critical point for the magnet to operate around; and this point becomes higher with increased operating temperatures.

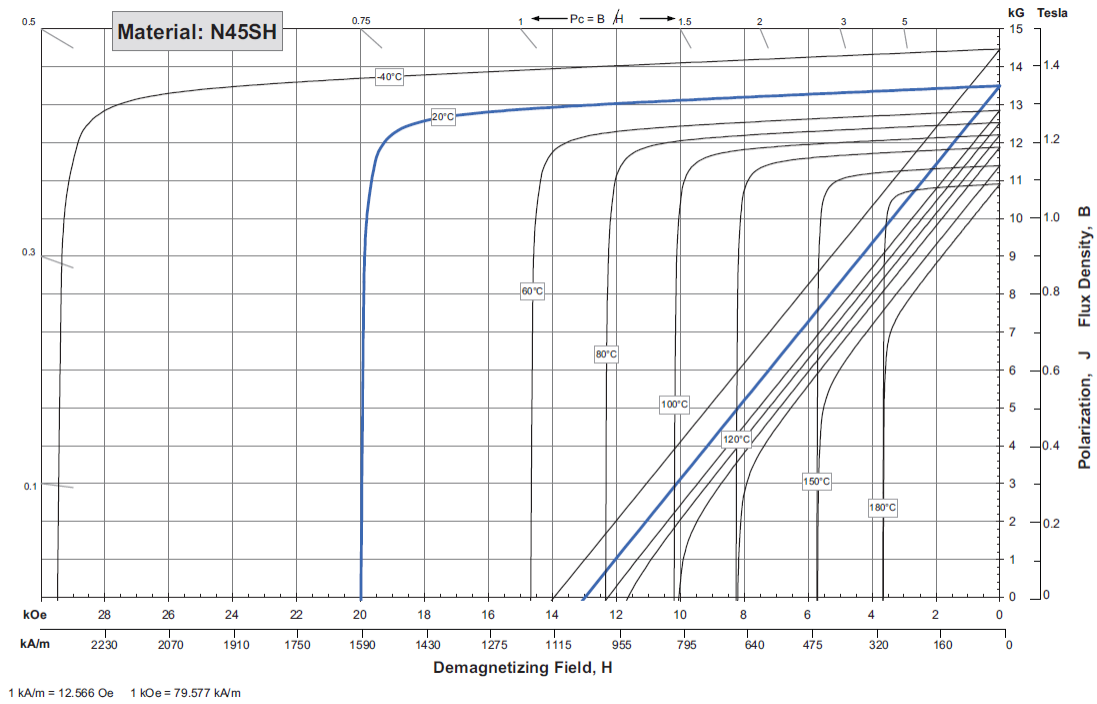


Figure 8.15. Magnet Characterisation B-H Curve[140].

It is very important to apply the maximum negative d axis current (to achieve the maximum speed is 96.4 amps) required in the field weakening region along with the expected maximum temperature of 120° in the 2D FE simulation, and to solve the model in order to check if any magnet demagnetisation occurs. A flux density plot of the magnet under the tooth at which the negative maximum d axis current is applied is shown in Figure 8.16. It can be seen from the figure that the flux density at the edge of that magnet is 0.5030 Tesla, which exceeds the flux density of 0.4 Tesla which would be expected to cause the permanent demagnetization of the magnets; hence demagnetisation is not a worry for this machine.

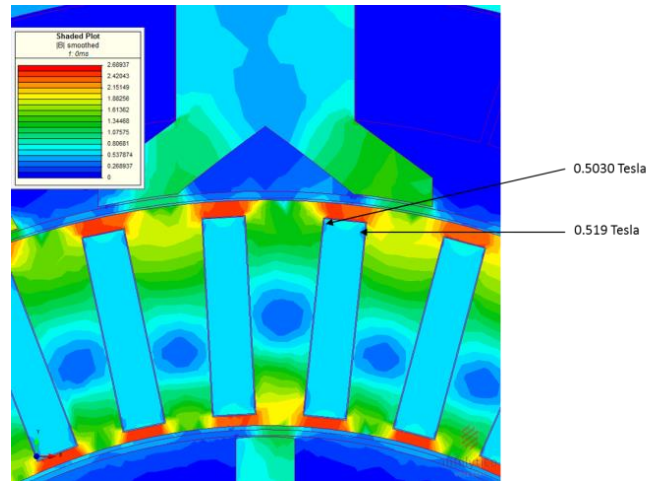


Figure 8.16. Flux Density Shaded Plot of the Magnet When a Current in the Direct Axis is Applied.

8.9 Conclusion

These following points summarise the conclusion of this chapter:

- The final optimisation process using OptiNet has improved the STPM machine torque output by 2 % at an applied current density of 15 A/mm^2 .
- All of the dimensions of the STPM machine have been finalised.
- The fringing flux can be reduced by using a sleeve of a non-magnetic and high-strength material such as Inconel to act as a mechanical component to retain the magnets against the large centrifugal forces.
- Single tooth windings were chosen for simplicity and low loss.
- The number of coil turns was chosen with a typical automotive inverter in mind.
- The final machine can operate at up to 15 A/mm^2 and achieve a torque of 250 Nm. At this torque, a cooling system will be required.
- An operating current density of 10 A/mm^2 can use natural cooling. However, densities of 12.5 A/mm^2 and 15 A/mm^2 require forced air cooling [128].
- An applied current density of 10 A/mm^2 was chosen for this thesis as the system will not have any cooling system. However, such a system is proposed in future work.
- Field weakening will allow the machine to reach 6000 rpm.
- 2D FE simulations show no demagnetisation at the design operating point.

Chapter 9. Design and Construction

All of the dimensions of the final STPM machine design were studied in chapter 8 and the structure was built and tested as shown in this chapter. An explanation is provided of the process of building several components of the final practical design. The final construction has proceeded through several stages starting from making the outer stator, the rotor and the inner stator components of the machine in the mechanical workshop at Newcastle University. The rotor was then sent away for the magnets to be cut and assembled inside the rotor by a magnet manufacturer. Finally different methods were tried to assemble the whole machine in an in-house build case, taking into consideration the mechanical difficulties involved in the operation of a rotor that rotates in between two stationary stators.

9.1 Introduction

The design and construction of the final STPM machine design included the following;

- Obtaining the full dimensions of the final optimised STPM machine shown in Chapter 8.
- Designing the required shafts, case and power connectors using an external socket holder.
- Creating 2D and 3D engineering drawings using Autodesk Inventor (AI) CAD software.
- Choosing the materials for the shaft and the case.
- Selecting the bearings.
- Ordering the laminations, coils, magnets, stainless steel (to make the shafts), aluminium (to make the case), bearings, crimps, cables, sockets and plugs.
- Manufacturing various components in house (Sending the rotor for manufacturing and magnet assembly).
- Winding the stator.
- Assemble the full machine.

The following sections describe the process of making each component in details and the assembly of the machine.

9.2 Stator Design and Construction

The stator outer diameter is 200 mm, and has the dimensions shown in chapter 8. In addition, a key of 3mm radius was added to the outer diameter on two opposite sides in order to lock the stator circumferentially as shown in Figure 9.1.

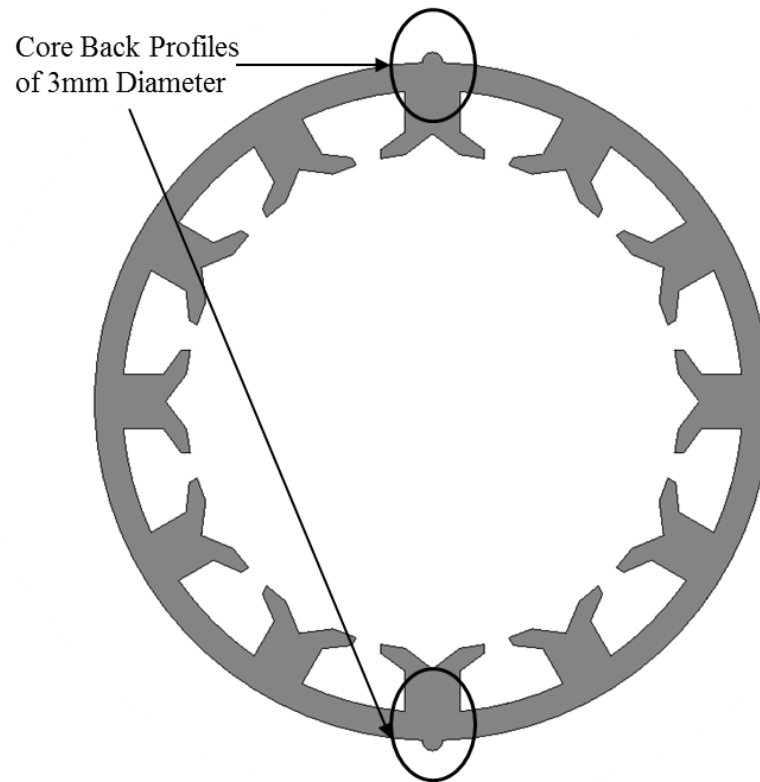


Figure 9.1. Stator Core Back Profiles.

The stator uses 0.35 cobalt iron laminations, 372 square sheets of laminations of 240mm width were stacked and bonded using epoxy to form the required stack length of 130mm. The stack was then compressed as shown in Figure 9.2, and left for the epoxy to cure for 24 hours. The laminations were bonded using MagnaTac (E645), a specialist epoxy resin with low viscosity resulting in a very thin layer of adhesive and consequently a strong stacking factor.

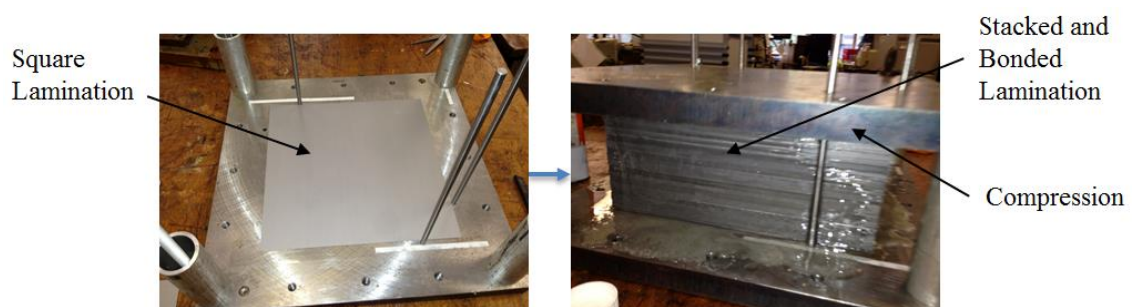


Figure 9.2. Lamination Stacked and Bonded Methods.

The bonded lamination stack was then located in the wire erosion machine. The AutoCAD drawings were used to control the cutting in order to form the stator, rotor and inner stator as shown in Figure 9.3. Wire erosion gives fewer burrs, and less

localised pressure points compared to the stamping, it also gives higher tolerance than using laser cutting. This was done in the mechanical workshop at the School of Electrical and Electronic Engineering in Newcastle University.

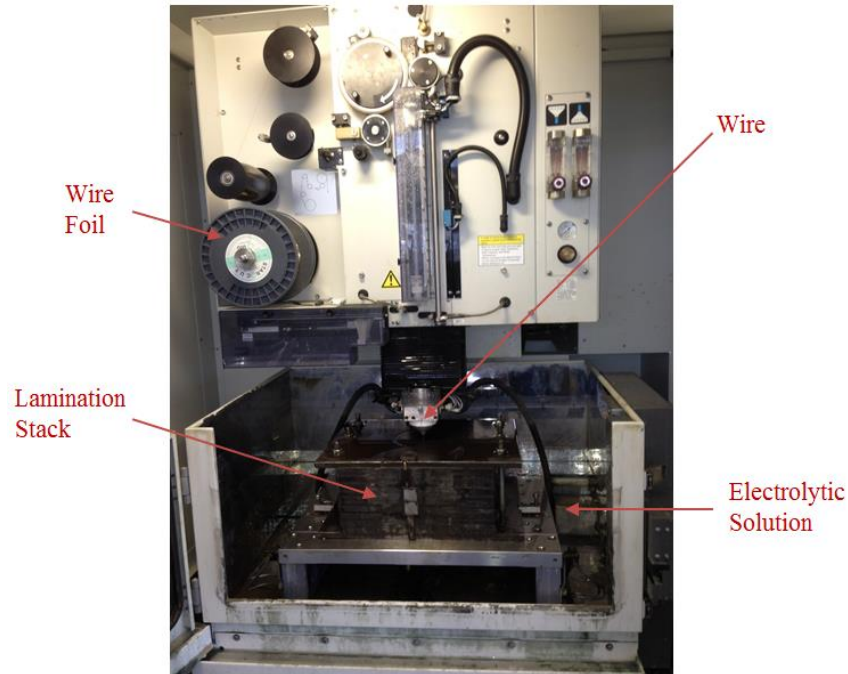


Figure 9.3. Lamination Stack While Inside the Wire Cutting Machine.

The constructed outer stator was placed inside the case, as shown in Figure 9.4.

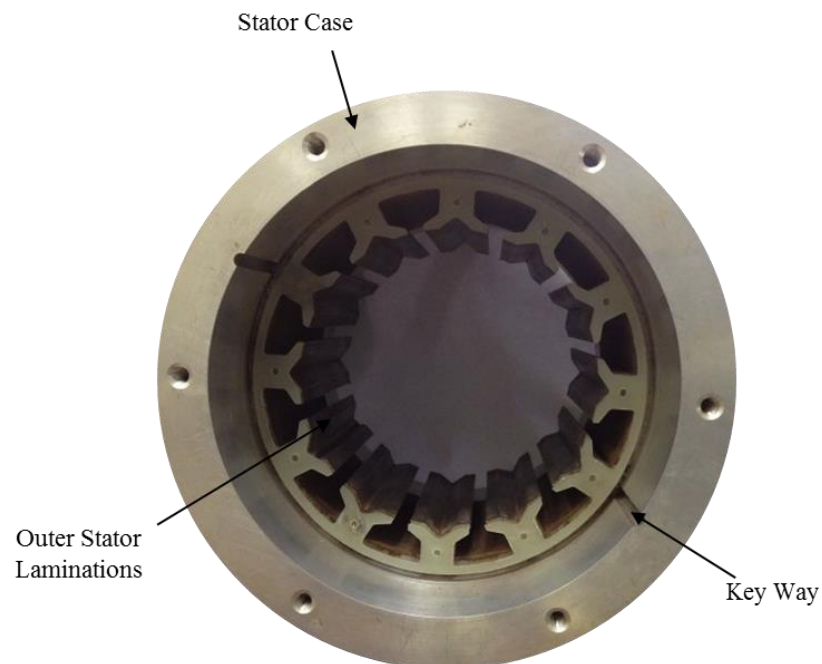


Figure 9.4. Final Constructed Outer Stator Inside the Case.

TUFNOL grade (natural glass fibre sheets) of 2 mm thickness were cut to shape the stator cross-section and glued to the ends of the stack in order to protect the end windings from the laminations

9.3 Winding Type and Arrangement

Single tooth winding were used and, each coil was wound by hand. However, due to the required fill factor of 45 %, and after several trials, a different winding technique tried. The coil was wound externally by hand around a wooden-former and compressed slightly. The former coil was then inserted into the slots via the slot opening. Although this technique can have the effect of slightly increasing the end winding length, it was found that this increase was only small.

A slot wedge was slid between the teeth. The wedge was made of TUFNOL and placed at the stator ends, in order to keep the coils in place as shown in Figure 9.5.

Type K thermocouples were placed inside three slots and in the top of three end windings in order to monitor the temperature. Two of these can be seen in Figure 9.5. These thermocouples have temperature range of -75 C° to $+250\text{ C}^{\circ}$.

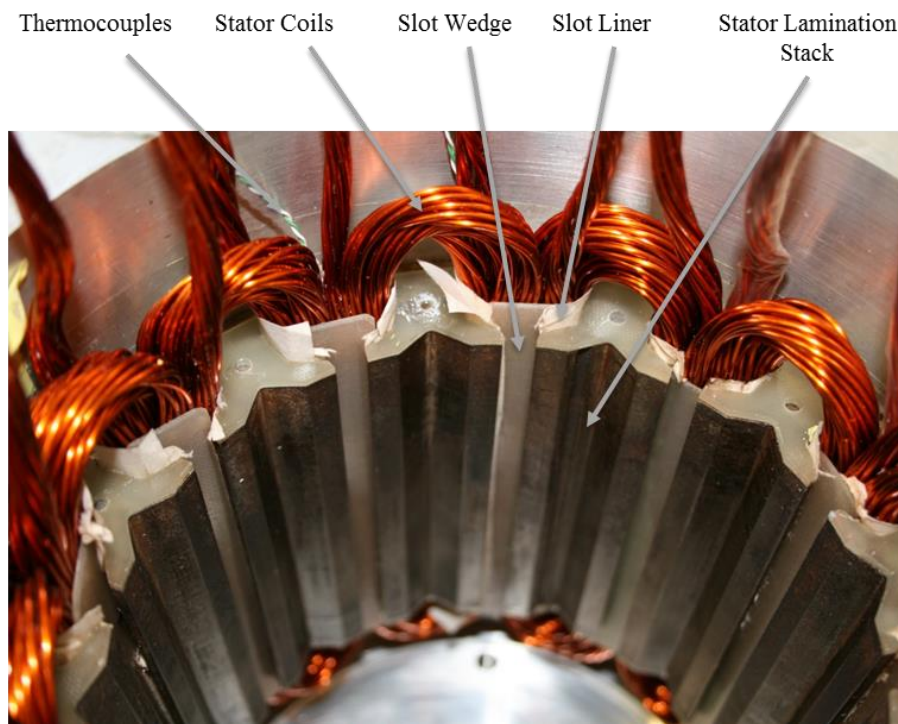


Figure 9.5. Stator Lamination Stack with the Stator Coils, Slot Wedge, Slot Liner and Thermocouples.

MAGNETEMP wire was constructed from 10 strands, each of which had a diameter of 1.4mm. This wire is THEIC polyesterimide enamelled copper wire over-coated with polyamide-imide insulation, with a temperature index of 210 C°, a good resistance to heat shock and high temperature overload.

9.4 Rotor Design and Construction

The rotor critical speed was set in excess of 6000 rpm. Hence, it is very important to consider the mechanical constraints of the rotor at that speed.

The rotor was constructed using the same laminations as the outer stator. However, the rotor laminations were sent to European Electrical Laminations based in West Midlands, UK to be stacked and cut due to their complexity.

The dimensions for the final rotor were slightly changed by +0.15 mm to allow a mechanical clearance for the magnets. Also 8 holes 3.15mm in diameter were drilled in between each 5 poles, as shown in Figure 9.6, in order to fix the rotor to both rotating shafts with pins of steel 3mm in diameter. These could be screwed at both ends of the rotating shaft in such a way as to allow the rotor lamination stack to be compressed in between the shafts.

The rotor was cut using a laser cutting method.

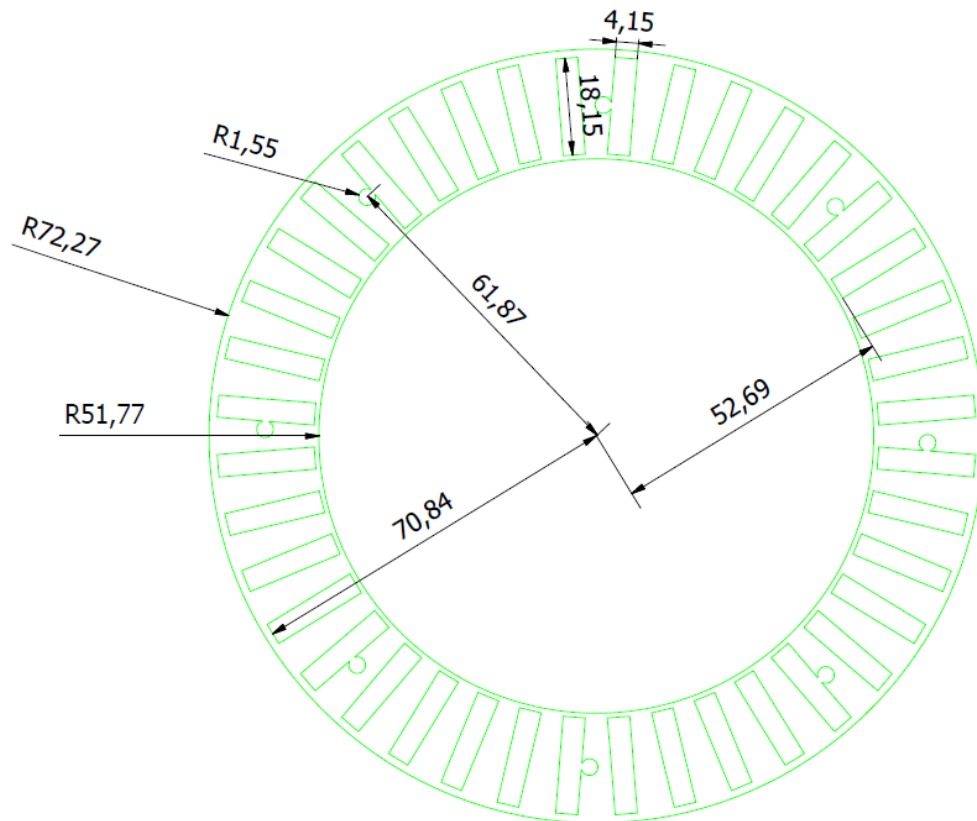


Figure 9.6. Constructed Rotor Cross Section Drawing.

As shown in Figure 9.6, it was necessary to ensure that the magnet slot size should be no less than 4.15 mm x 18.15 mm to give the required clearance, and also that the slot should be parallel down the whole 130 mm axial length in order to ensure that the magnet (4 mm x 18 mm x 130 mm) could be easily inserted.

The holes were designed in such a way to be in the centre of the rotor and to touch the slot of the magnet. This was done so that the laser can cut through both the magnet slot and the pin hole without having to be repositioned. This way has speeded up the cutting process of the rotor and avoided drilling a new hole for the pins, especially considering the small size of the hole.

Figure 9.7 shows a flux linkage contour plot comparison between the STPM machine with and without pins of steel.

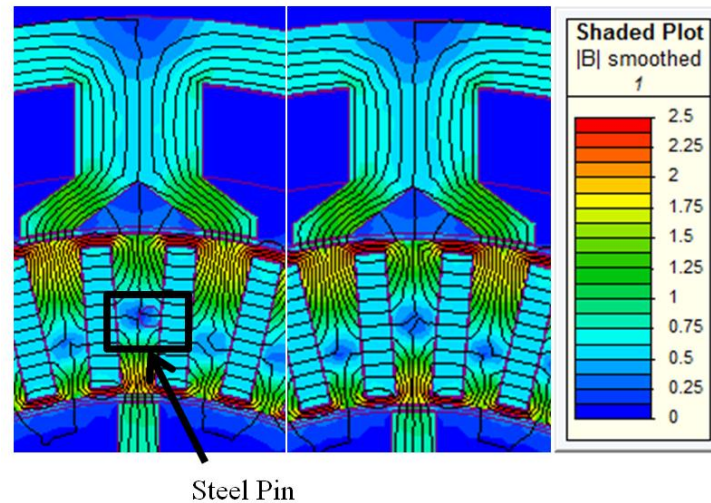


Figure 9.7. Flux Linkage Contour Plot Comparison between the STPM Machine with and without Pins of Steel.

From Figure 9.7, it can be seen that having pins of steel has no effect on the flux generated by the magnets. This is because the pins of steel are magnetic.

After the arrival of the final constructed rotor, it was attached to the rotating back end shaft and tightened by steel pins, as shown in Figure 9.8, and then sent to the magnet manufacturer for final assembly.

It is also important to note that, since achieving the correct holes size for the magnet was critical, it was deemed worth making a “dummy magnet” made to the top end of the tolerance band of 4.15 mm x 18.15 mm x 130 mm and running this through each of the magnets slots to ensure that they would pass through the lamination stack and sit properly in position. After several trials inserting different magnet dummy sizes, it was found that a magnet with the dimensions 4 mm x 18 mm x 130 mm would pass easily through all of the holes in the rotor.



Figure 9.8. Rotor Lamination Stack When Attached to the Rotating Back End Shaft by Steel Pins.

9.5 Permanent Magnets

The magnets were produced and assembled by Arnold Magnetic Technologies. The company suggested that the magnets should be inserted already magnetised and that if they were glued only at the ends this would be sufficient to hold the magnets in place, taking into consideration the reliance on the attraction of the magnet to the lamination stack.

Due to the high torque and high speed requirements of this machine, significant eddy currents were observed in the magnets during simulation. As a result the magnets were axially split into 3 sections along the 130 mm axis. Figures 9.9 and 9.10 show the magnet dimensions. A dimensional tolerance of ± 0.1 mm was advised by Arnold Magnetic Technologies Ltd.

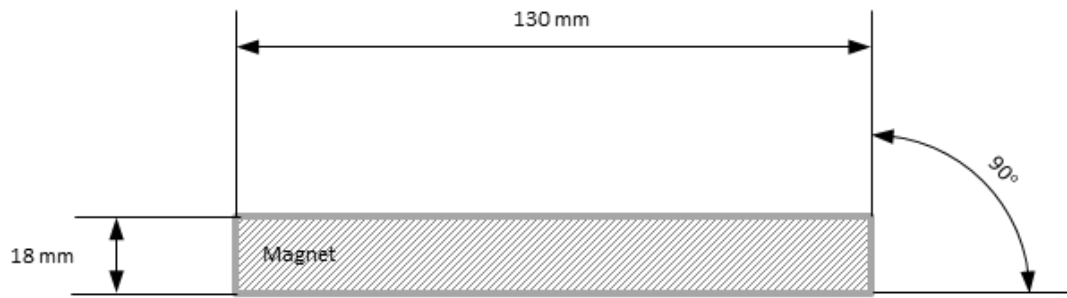


Figure 9.9. Magnet Axial Length.

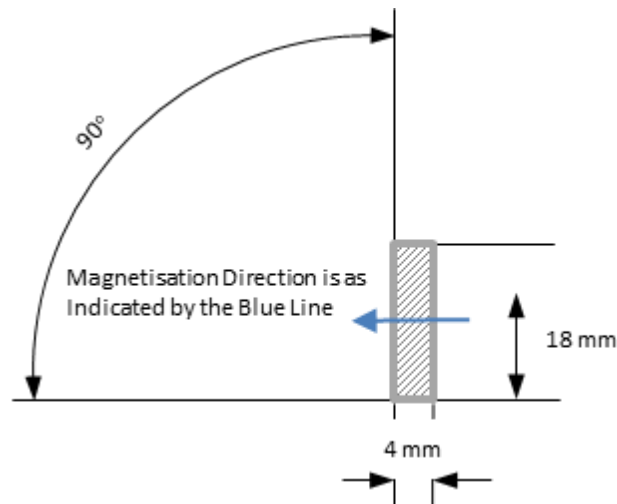


Figure 9.10. Magnet Cross Section.

Due to the imperfect alignment of the rotor laminations stack caused by using a laser cutting method rather than wire cutting, it was found that the magnetised magnets would not pass easily along. Due to time limitations, smaller magnets were used rather than rebuilding the rotor laminations stack.

In order to take into account this less than perfect alignment of the laminations stack holes, a new magnet thickness of 3.6 mm rather than 4mm and magnet height of 17.6 was found to be appropriate to fit the full length of the holes maintaining the same 3 axial length sections of 43.25 mm. The tolerance of the new smaller magnets was $+0.05/-0.1$ mm after plating. The final constructed magnets are as shown in Figure 9.11 when inserted inside the magnet holes.

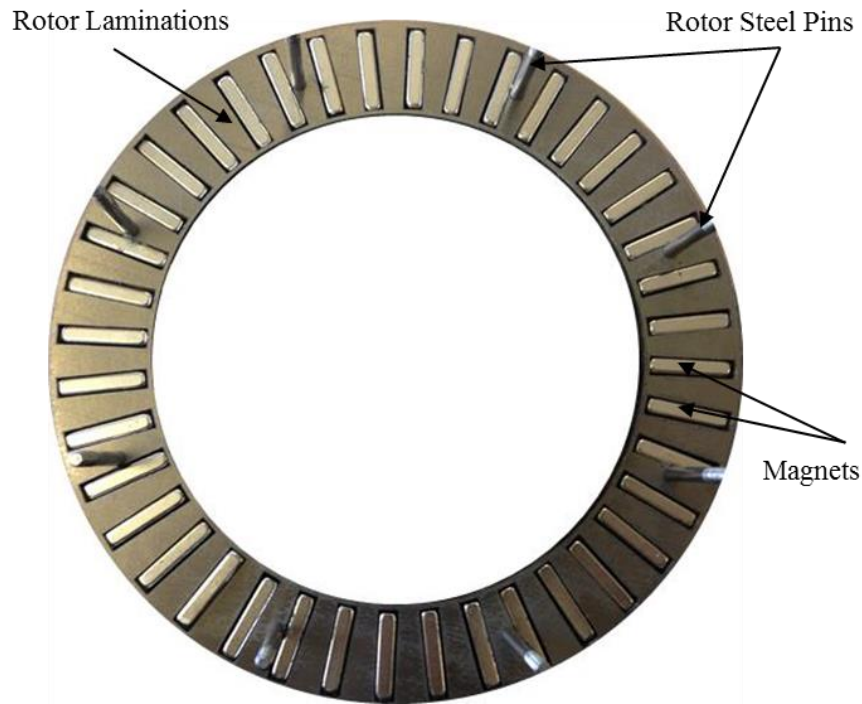


Figure 9.11. Rotor Lamination Stack Cross Section with Magnets Inserted.

Sintered Neodymium-Iron-Boron Magnets of grade N45SH were used, which are capable of operating at a maximum of 180° and have a minimal residual flux density (Br) of 1.32 Tesla, a maximum of 1.38 Tesla and a nominal value of 1.35 Tesla.

9.6 The Inner Stator

The inner stator was constructed using the same lamination material and method as the outer stator. The dimensions are shown in Chapter 8. However, a core back profile of 3 mm by 6 mm was added to the inner radius as a key to locate and lock circumferentially, as shown in Figure 9.12.

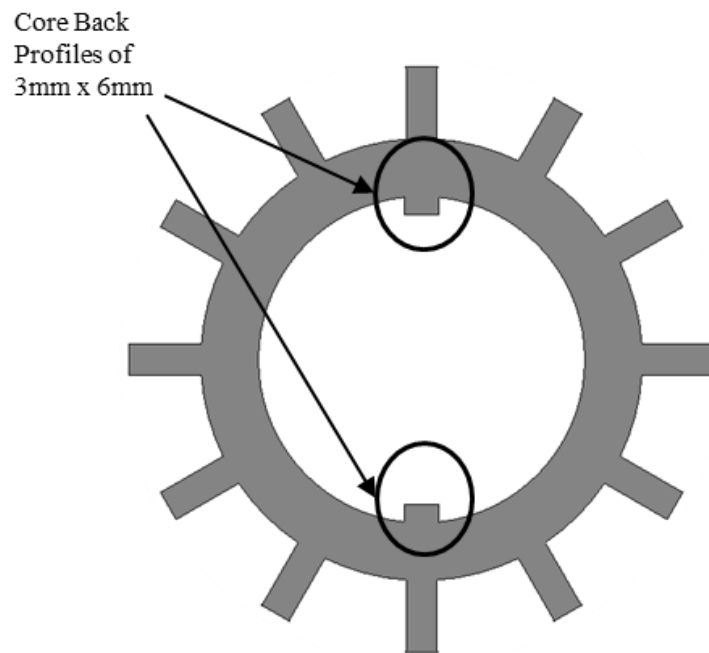


Figure 9.12. Inner Stator Cross Section to Show Core Back Profiles.

The inner stator was locked to the shaft by a TUFNOL ring and bearing, as shown in Figure 9.13.

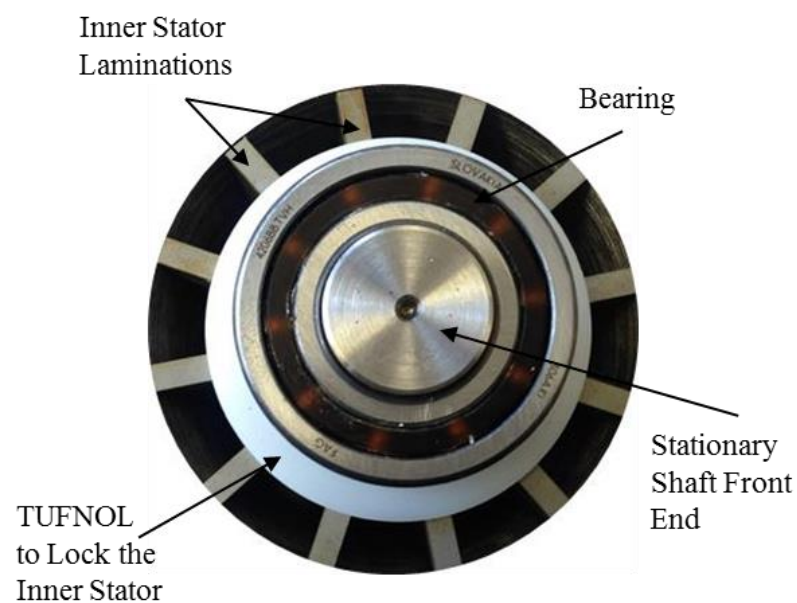


Figure 9.13. Cross Section of the Inner Stator Laminations Stack with a TUFNOL and Bearing to Lock it.

9.7 The Shaft Assembly

The shaft assembly consists of three parts: a stationary shaft onto which the inner stator is held, a front end rotating shaft, and a back end rotating shaft.

The stationary shaft locates the inner stator with respect to the outer stator. The rotating shafts connect via front and back end bearings.

Both rotating shafts are attached to the front and back ends of the rotor and connected axially by series of steel pins. This assembly allows the rotor and rotating shafts to rotate over the stationary inner stator.

The dimensions of the stationary shaft, front end rotating shaft and back end rotating shaft are as shown in Figures 9.14, 9.16, and 9.18 respectively.

All three shaft parts were constructed from a nonmagnetic stainless steel material (grade 303-S-31)

An overview of the constructed stationary shaft, front end rotating shaft and a back end rotating shaft are also shown in Figures 9.15, 9.17, and 9.19 respectively.

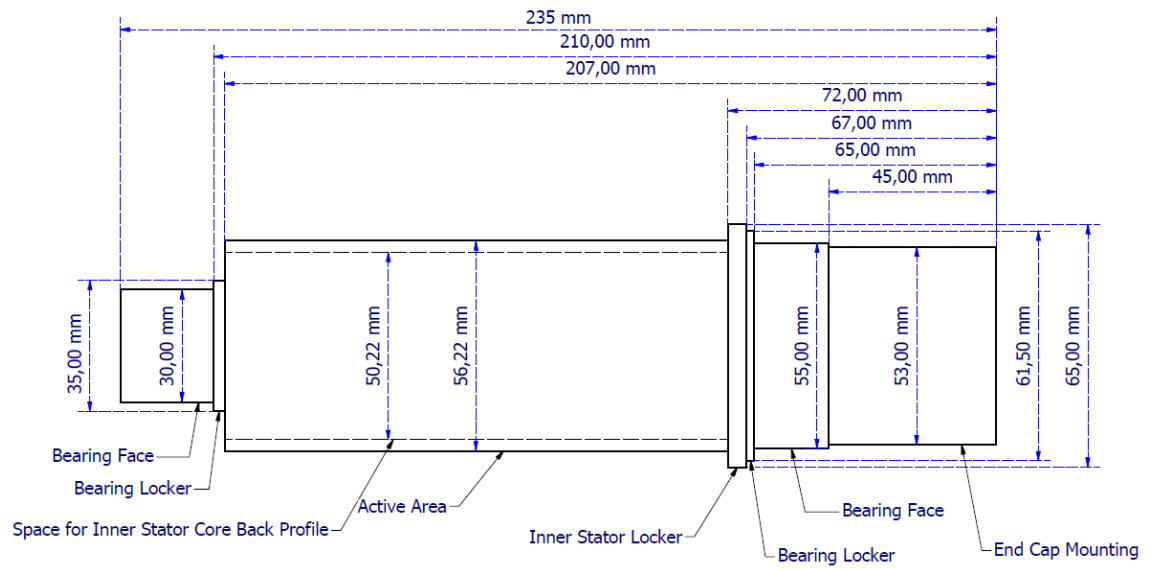


Figure 9.14. Stationary Shaft Dimensions.

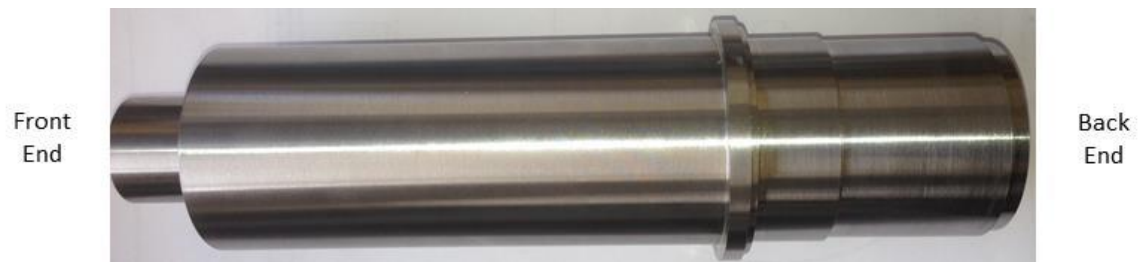


Figure 9.15. Final Constructed Stationary Shaft.

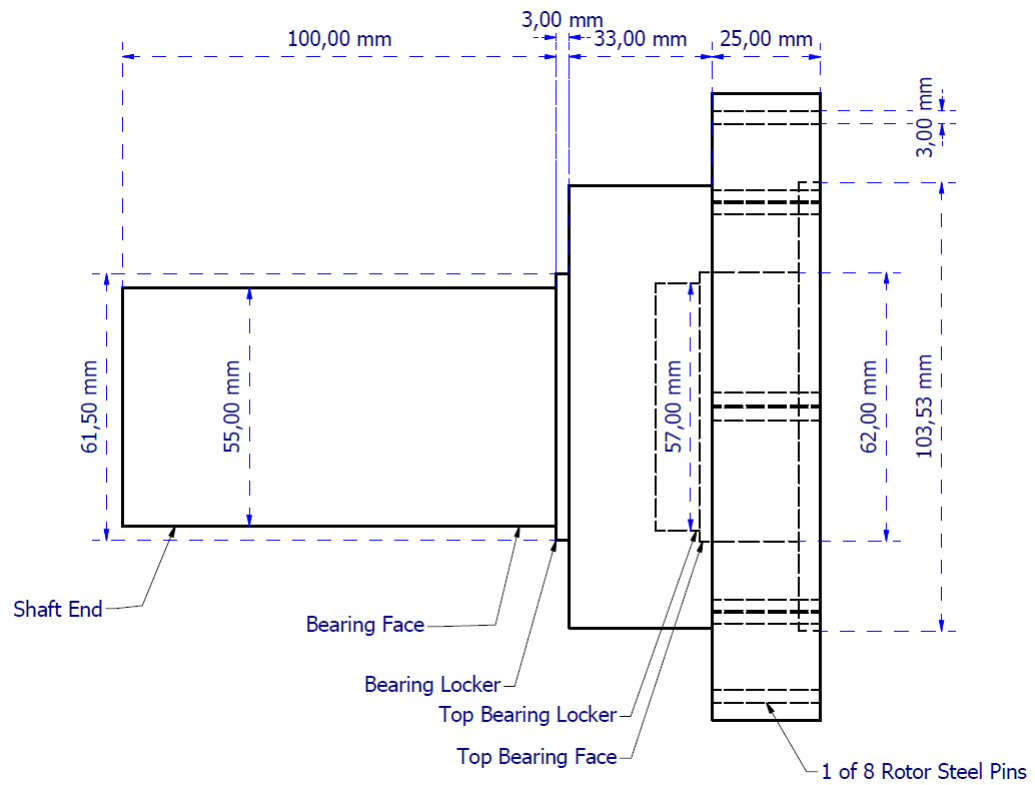


Figure 9.16. Rotating Front End Shaft Dimensions.



Figure 9.17. Final Constructed Rotating Front End Shaft.

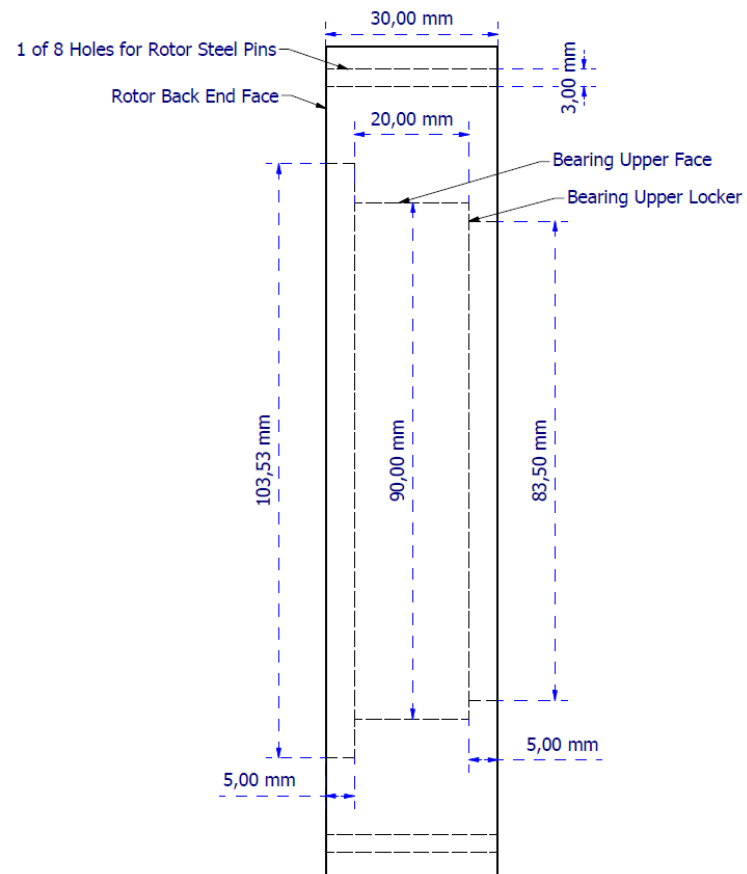


Figure 9.18. Rotating Back End Shaft Dimensions.

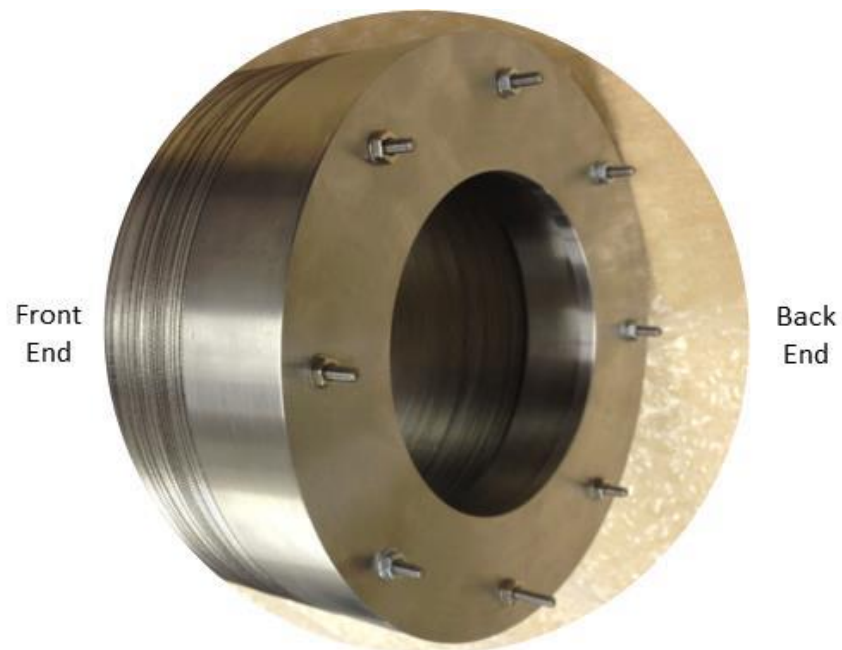


Figure 9.19. Final Constructed Rotating Back End Shaft.

9.8 The Rotor Assembly

Figures 9.20 and 9.21 show the full assembled rotor placed over the stationary shaft via bearings. The assembled rotor and inner stator is then held by the back end cap.

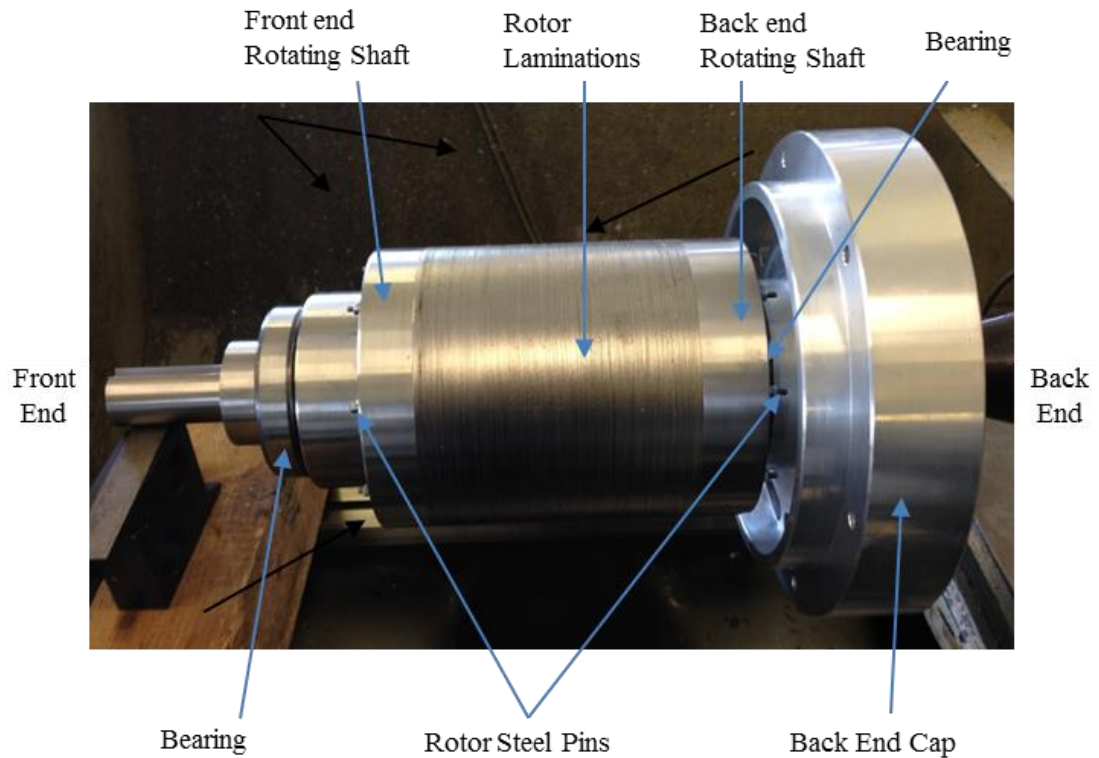


Figure 9.20. Side View of the Rotor Assembly.



Figure 9.21. Top View of the Rotor Assembly.

9.9 Case Design and Construction

The case is constructed from aluminium, 240 mm in diameter and can be seen in Figure 9.22. The case was made in-house, using the lasing machine after a cylinder of 260mm diameter had been ordered through one of the university's materials suppliers. Details are shown in Figures 9.23 and 9.24 and Table 9.1.

The case has a body which holds the outer stator, locking it axially and circumferentially with the windings and the thermocouples passing through. The two end caps are placed at either end of the case and bolted in place. The front end cap has a bearing case to allow the rotating shaft to exit for connection to an external load while the back end cap holds the stationary shaft in place and allows both power connectors and thermocouples to pass through.

Boring an axial shoulder into the case allowed the stator to be locked axially while the two keys on the outer stator coreback, as shown previously in the outer stator construction section, lock it circumferentially. It was heat shrunk before being bolted inside the case, in order for it to cool inside the case and be tightened in place.

Meanwhile, the inner stator was slid on top of the stationary shaft and also locked axially and circumferentially by means of shoulders and keys as shown previously in the inner stator construction section.

The rotor was inserted with the magnets and then compressed by the two rotating shafts using 8 steel pins that penetrate across the rotor core back in order to hold the lams and magnets in place.

Three bearings were used, two of which were placed on the stationary shaft and housed by both rotating shafts to allow for stability and any pre-loading, while the third bearing was placed on the front end rotating shaft housed by the front end cap. This method was found to be more mechanically secure than the method of using a cup rotor, given the axial length of 130mm.

The bearings were chosen depending on their load capability, speed ratio and the size required. Hence three bearings of two types were found to be appropriate and were purchased from SKF: one double ball bearing with a deep groove design; and two single ball bearings with a deep groove design.

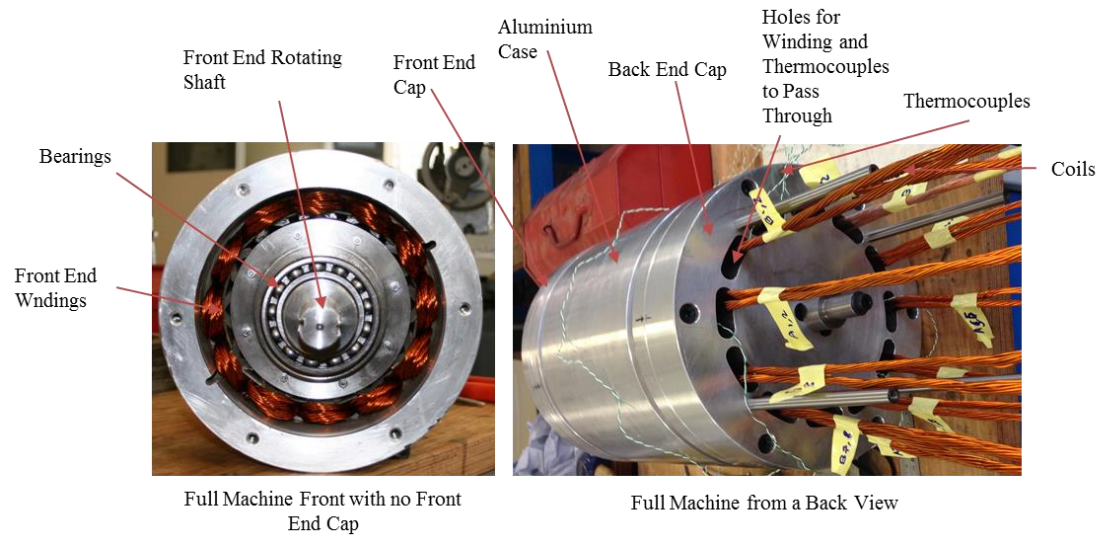


Figure 9.22. Front and Back Views of the Assembled Case.

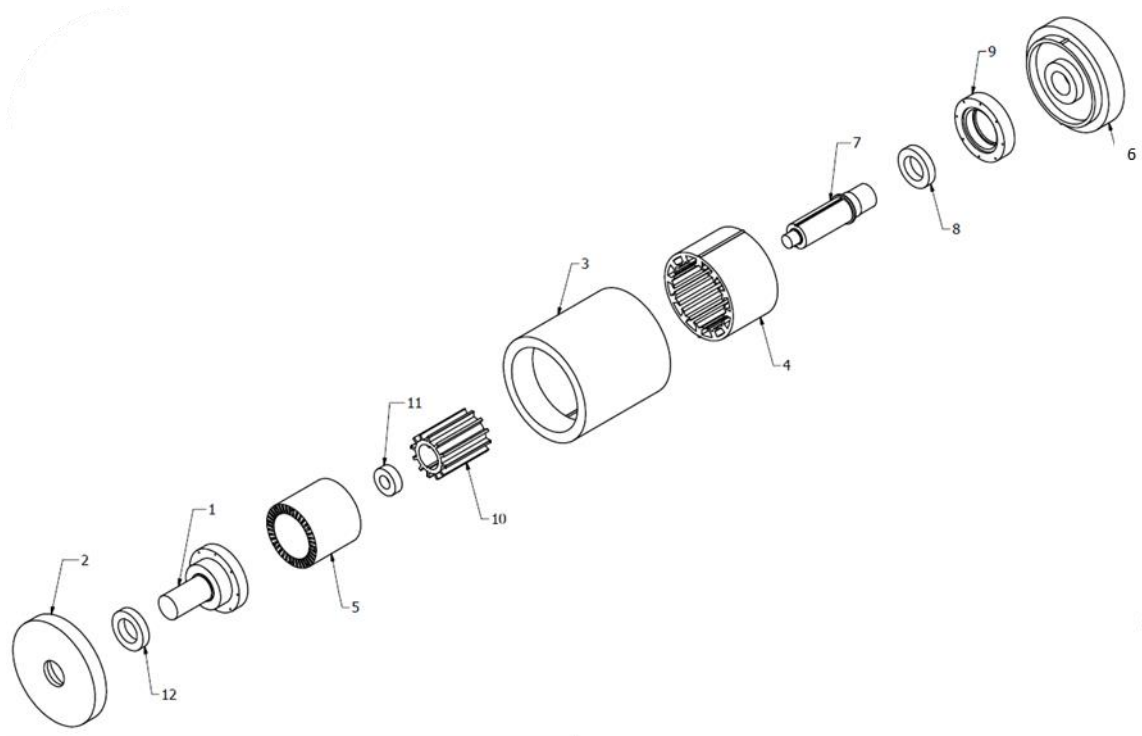


Figure 9.23. Case Contents When Separated.

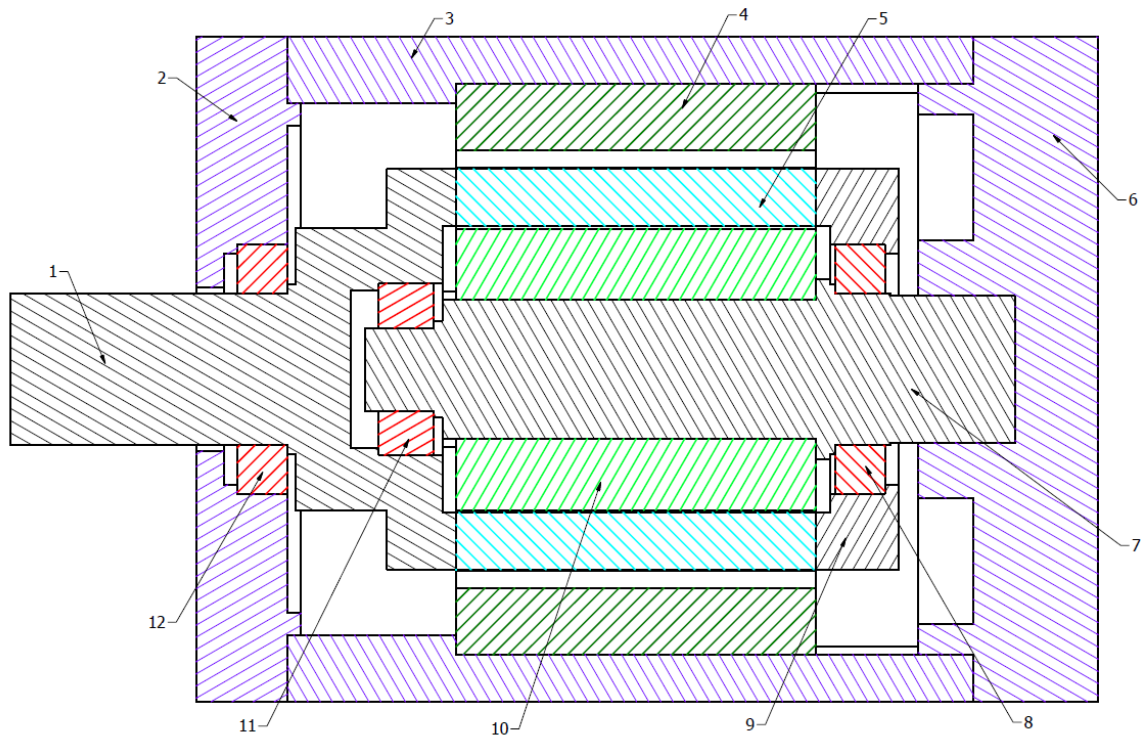


Figure 9.24. Case Contents Cross Section.

Table 9.1. Description of Each of the Case Contents.

Number	Definition
1	Front End Rotating Shaft.
2	Front End Cap
3	Outer case
4	Outer Stator
5	Rotor Lamination Stack
6	Back End cap
7	Stationary Shaft
8	Bearing Between the Back end Rotating Shaft and the Stationary Shaft
9	Back end rotating shaft
10	Inner Stator
11	Bearing Between the Front End Rotating Shaft and the Stationary Shaft
12	Bearing Between the Front end Rotating Shaft and Front End Cap

All parts of the machine are explained and shown in more details in the Design and Construction Appendix D.

9.10 Power Connector Design and Construction

The machine has three phases, each of which consists of 4 coils. These four coils are connected in series and a star connection made. An external connection arrangement was used for the following reasons:

- Each coil can be tested separately for faults.
- Various connection arrangements can be easily tested (Star, Delta, Parallel and Series).
- Current and voltage can easily be monitored for each individual coil.

The coil ends were striped using a power stripper, and then a crimp and a heat shrink sleeve used. The coils were then connected to the sockets, which were fixed to an external connection board. Thereafter, series and star connections were externally connected.

This arrangement limited the maximum current rating of the machine to $100A_{rms}$, due to the rating of the sockets.

Figure 9.25 shows the fully assembled machine with the complete construction of the power connectors.

Thermocouples also exit at this side. A top view of the connections on the socket holder is as shown in Figure 9.26. The connection star gives the electric circuit shown in Figure 9.27, where the numbers represent the slot number.

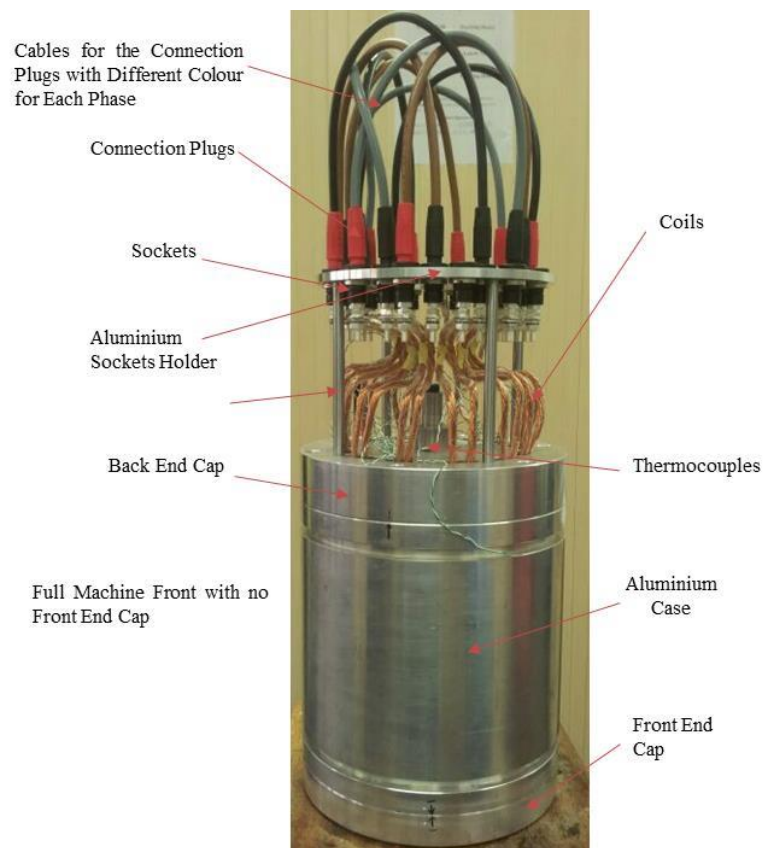


Figure 9.25. Final Case Assembly with the Final Winding Connection Box.

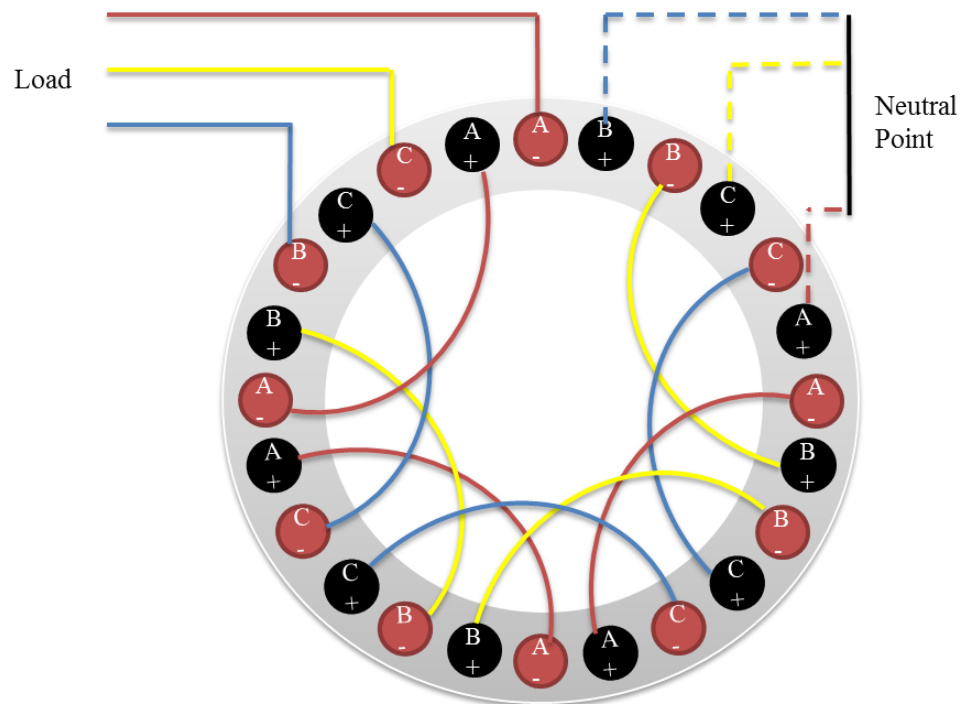


Figure 9.26. Top View of the Connections on the Socket Holder.

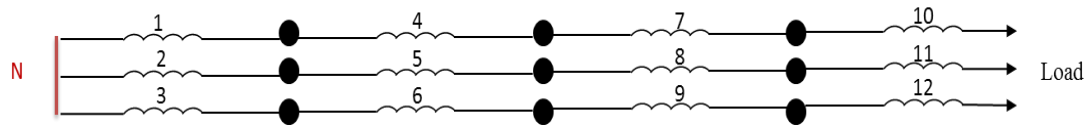


Figure 9.27. The Electric Circuit of the STPM Machine.

9.11 Test Rig

Two tests rig were set up as follows:

9.11.1 Static Torque Test Rig

The STPM machine was coupled to a rotary table using two shafts and a torque transducer as shown in Figure 9.28. The rotary table locks the rotor in position and allows for rotor movement as small as 0.125° . The motor here was connected to a DC power supply via the three phase power connector as shown in Figure 9.29.

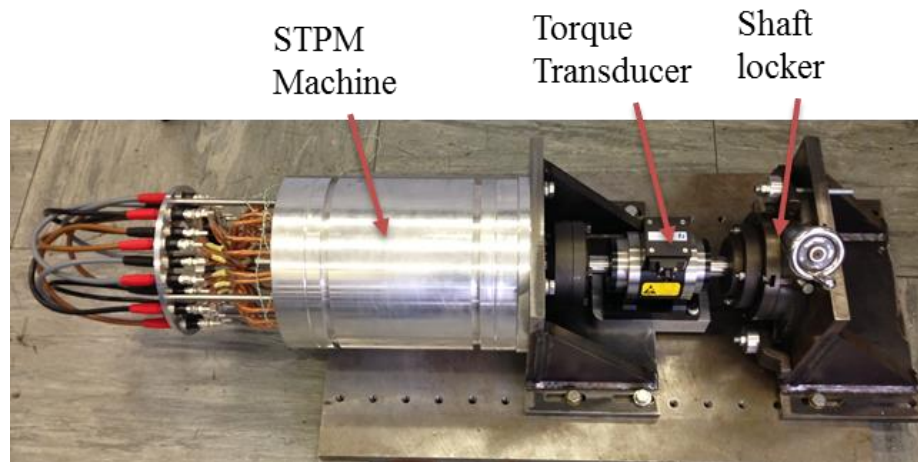


Figure 9.28. Static Torque Test Rig.

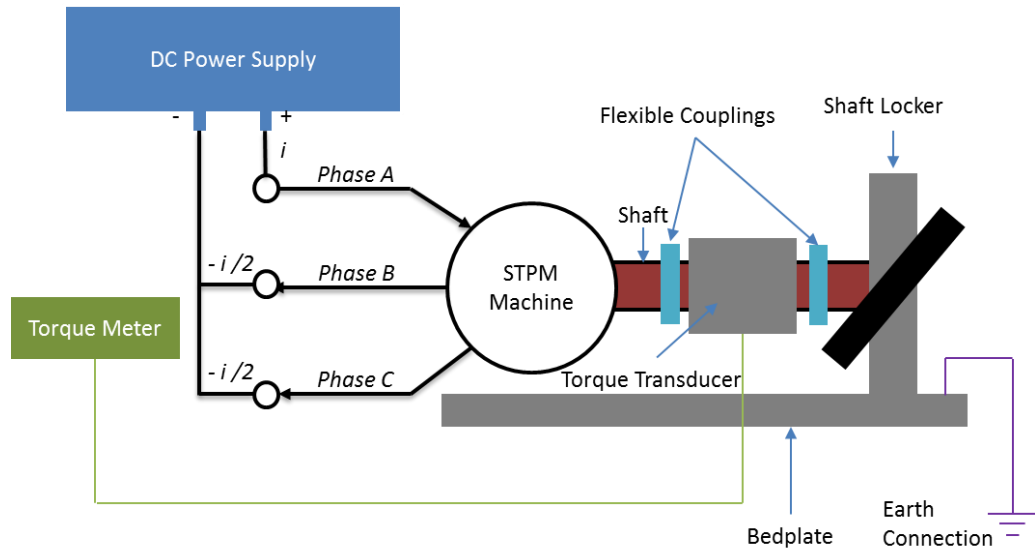


Figure 9.29. STPM Machine Connections to the Power Supply While Connected to The Static Torque Test Rig.

After placing the motor in the test rig and connecting it to the power supply as shown in Figures 9.28 and 9.29, static torque characteristics were obtained over a range of excitation currents. This was performed over 2 electrical cycles (36° mechanical) in steps of 0.5° mechanical. The torque measurements were obtained from the torque meter that was connected to the torque transducer.

9.11.2 High Speed Test Rig

The STPM machine was coupled to a high speed dynamometer test rig as shown in Figure 9.30. The coupling between both machines was via shafts, a geared toothed pulley, a torque transducer, and a pair of flexible couplings, which were placed under the safety shield and shown in Figure 9.31.

Two tests were performed on this rig; an open circuit test where the DC drive is used to drive the STPM machine, and a load test where the STPM machine is connected to a resistor bank.

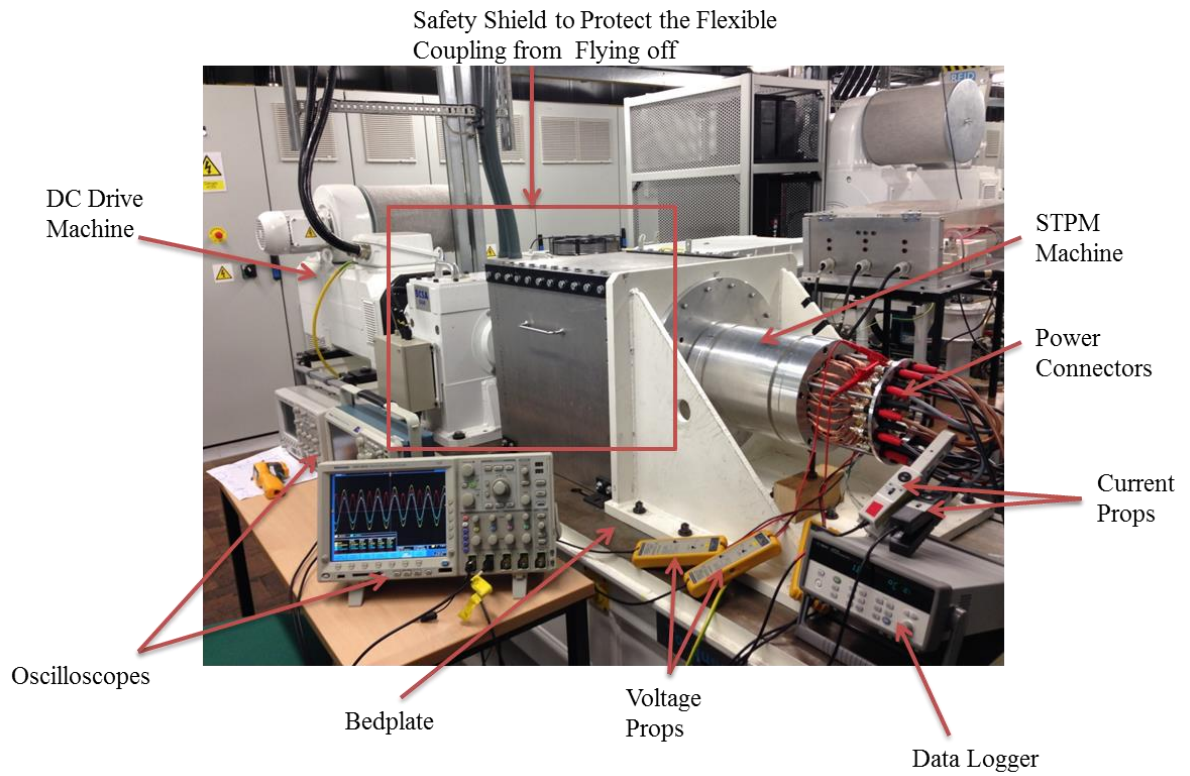


Figure 9.30. High Speed Test Rig.

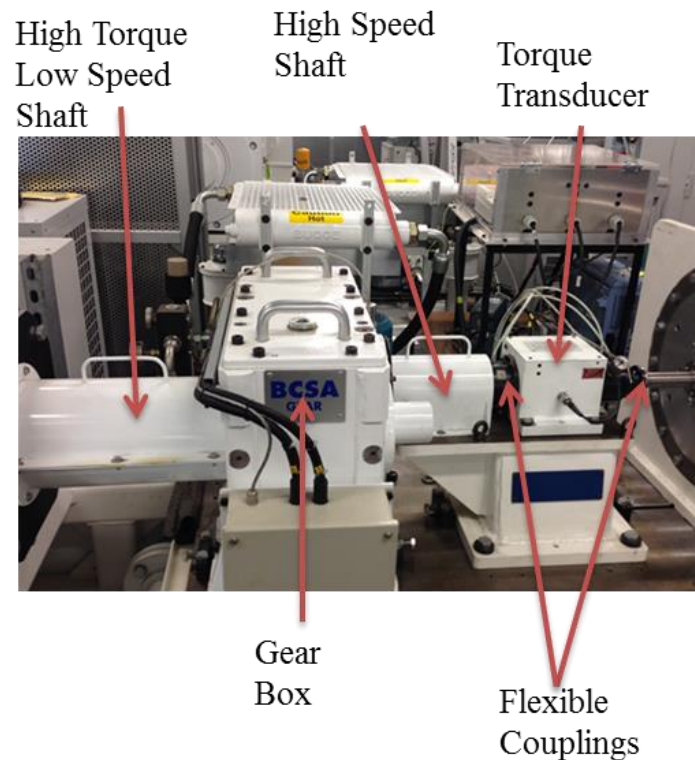


Figure 9.31. Gear Box and Torque Transducer.

An overview of the high speed rig is shown in Figure 9.32.

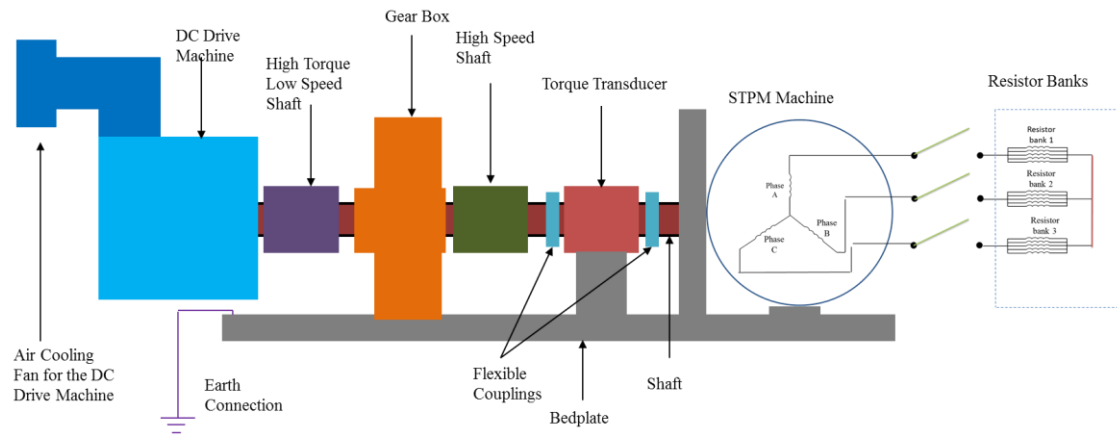


Figure 9.32. Overview of the High Speed Test Rig.

9.12 Conclusion

During the design and construction process, various points have been taken into consideration:

- A way of locking the outer and inner stator has been demonstrated by using shoulders and core back profiles.
- The wire cutting method has been proven to be the best method to cut laminations because it gives fewer burrs and less localised pressure points if compared to the stamping method, and it also gives higher tolerance than using laser cutting. However, great care must be taken to prevent laminations from being corroded. A different method has been tried to minimise corrosion, by cutting fewer laminations at any one time to speed up the cutting time and leaving the laminations in the water for less time.
- A new case structure has been illustrated in this chapter, which has been proven to be better than the typical cup rotor structure for machines with conventional rotors that rotate in between two stators. The new case structure allows the load of the rotor to be spread over both case ends whereas the load is only supported at one side in the cup rotor structure.
- Different power connection methods have been explained here, and a socket holder method was chosen due to advantages, such as allowing each coil to be tested separately for any type of fault, giving the opportunity of to change the connections in a simple manner and the ability to monitor currents and voltages for each coil individually.

- Two different test rigs were used. In the first one, called the static torque test rig, the rotor was locked, current was applied to the STPM machine, and measurements of torque were obtained. The second is the high speed rig, in which the STPM machine was tested and different results obtained at both no-load and load conditions.

Explanations of the results obtained for the machine designed and constructed here are shown in the following chapter.

Chapter 10. Experimental Testing and Evaluation

After constructing the STPM machine and carrying all the preparations for the test systems shown in chapter 9, the machine was tested and evaluated.

This chapter presents the analysis for the following experimental tests,

- Coil testing for faults.
- Resistance and inductance measurements.
- Static Torque test.
- Open circuit test
- Load test.
- Thermal test.

This analysis is compared to the 2D FE and theoretical results. Furthermore, the torque density of the STPM machine is compared to two interior PM machines; Toyota Camry and Prius electrical motors.

10.1. Introduction

The test was carried out in the Power Electronic Machines and Drives Laboratory at Newcastle University. Initial bench lap tests allowed coil and machine characteristics to be tested.

Thereafter, the machine was mounted to a static test rig and DC current applied. A measurement of torque against mechanical angles was obtained.

Then the machine was coupled to a high-speed rig where a set of no load and load tests were carried out and measurements of back EMF, efficiency and torque obtained.

The final stage was performing a thermal test by applying a current density of 10 A/mm² for a prolonged period of time.

Due to the limited equipment available, it was not possible to obtain a large enough drive for the motor, hence the machine was tested as a generator.

10.2. Coil testing

A mega-ohm, PI or Hipot test at 1kV was carried out for each coil individually using TTI,(1604, 40000 count digital multi meter) in order to test for coil to ground wall faults (ensuring no leakage current, and hence the dielectric strength of the slot liner).

A surge test was also performed using a coil testing equipment by Baker Instrument Company. This test detects any weakness between turns by applying a current impulse that induces a voltage difference between turns within a coil.

A distortion of the waveform measured would result between any two turns that cannot withstand the level of voltage difference, indicating a fault (weak insulation). The distortion of the waveform represents the voltage depiction across two testing leads that were connected to each of the tested coil ends, and hence any change in either or both waveform shifts and amplitude is an indication of a fault. The effect of the resulted distortion can be seen from a display on the test equipment as shown in Figure 10.1. All 12 coils were tested and passed and Figure 10.2 shows the surge waveform displayed by the test equipment for a healthy coil.

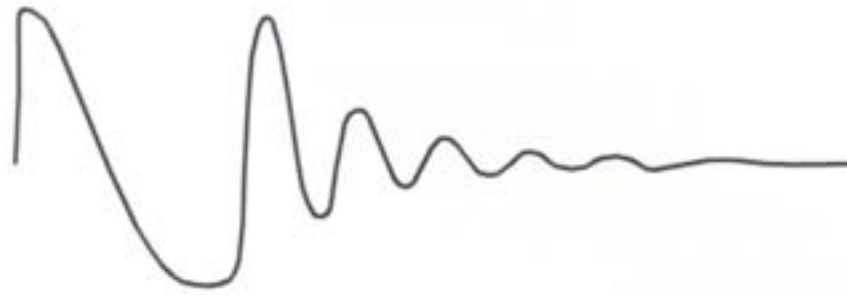


Figure 10.1. Surge Waveform During a Fault Between Two Turns.

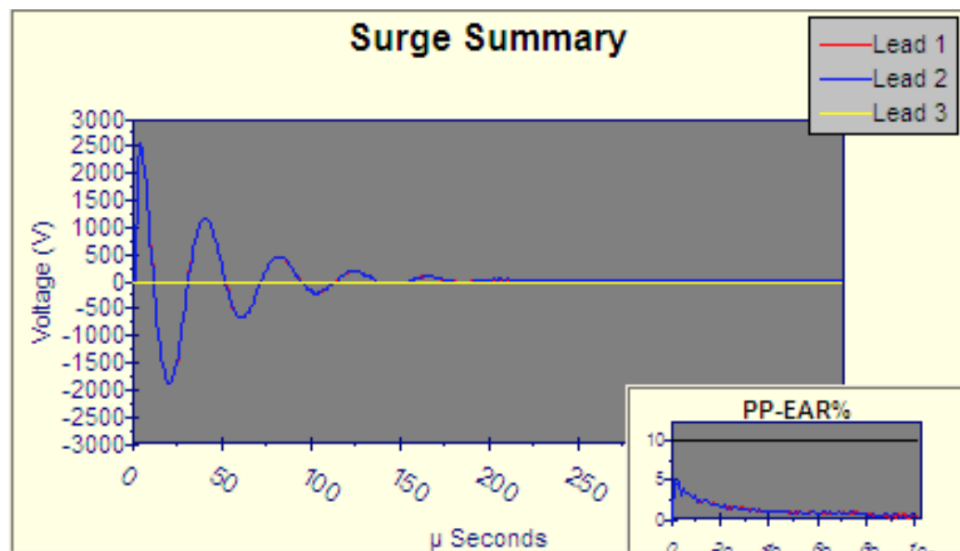


Figure 10.2. Surge Waveform Obtained for a Healthy Coil.

In order to understand the contents of Figure 10.2, it is worth discussing the process:

- Lead 1 and 2 are connected to the testing coil terminals, while lead 3 is connected to the case.
- A surge waveform was obtained for a known healthy coil.
- This surge waveform was then stored and used as a reference (master) for all other coils to be tested.
- A number of voltage pulses were applied to remaining coils and any surge waveform difference to that of the master was recorded and shown as the pulse-to-pulse error area ratio (PP-EAR) (This is done in order to ensure all coils have the same properties).
- Thereafter, in order for the coil to pass, its surge waveform should obtain no more than 10% difference to that of the master.

10.3 No Load Test

Two types of the no load test were carried out; with the machine stationary for the measurement of the general characteristics, and with the machine rotating at its rated speed for measurement of the back EMF.

10.3.1 Static No-Load Test

Inductance and resistance were measured here. They are very important in a newly build machine as they determine the integrity of the coils after being wound around the teeth (detect any short or open circuit of the coils).

For accuracy, the resistance was obtained using a DC supply, applying 100 A_{rms} and measurements of voltage were obtained in order for the resistance to be calculated, this was done for a coil and phase where the resistance found to be 11 mΩ and 23.3 mΩ respectively.

Furthermore, the calculated resistance is expected to be different due to the total estimations of the length of the coil during calculating the resistance using the general resistor equation:

$$R = \frac{l \rho_c}{C.S.A} \quad 10.$$

Where l is the total length of the coil, ρ_c is the resistivity of the material and $C.S.A$ is the cross section area of the conductor.

It can be seen from Figures 10.3 and 10.4 that the phase arrangements during the test used external cables and sockets for power connection. These can influence both resistance and inductance.

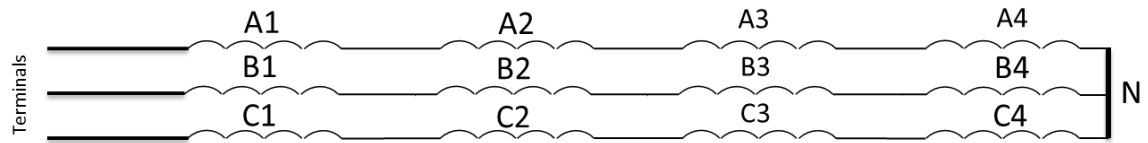


Figure 10.3. Phase Arrangements in 2D FE.

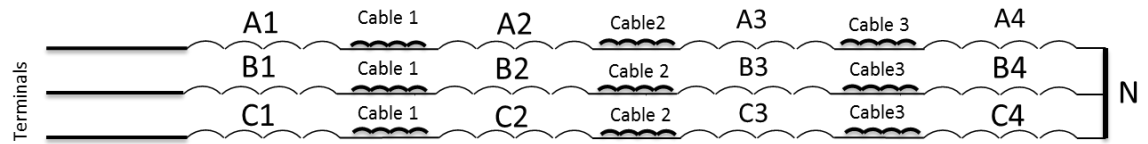


Figure 10.4. Phase Arrangements in Practical

Table 10.1 shows the maximum and minimum measured inductance for a phase that has all its coils connected in series and in star with other phases.

Table 10.1. Maximum and Minimum Measured Inductance.

		Phase
Inductance (μH)	Maximum	137
	Minimum	121

From Table 10.1, the measured inductances will slightly differ from the calculated. This is for the following reasons:

- Calculated inductance is obtained using 2D FE method and the end winding effect was not taking into account.
- The BH curve of the lamination will differ of the 2D FE model.
- The effect of the different layout of the phases shown above.

10.3.2 Open Circuit Test

This test was done after mounting the fully assembled machine into the high speed test rig as explained in Chapter 9 where measurements of back EMF over a speed ranging from 200 rpm to 6000 rpm were obtained.

A dynamometer was used to drive the STPM while the measurements were taking using Tektronix, (M50 4034 mixed signal oscilloscope).

Figure 10.5 shows voltage waveforms in each of the machine's three phases for a full electrical cycle obtained at 4000 rpm.

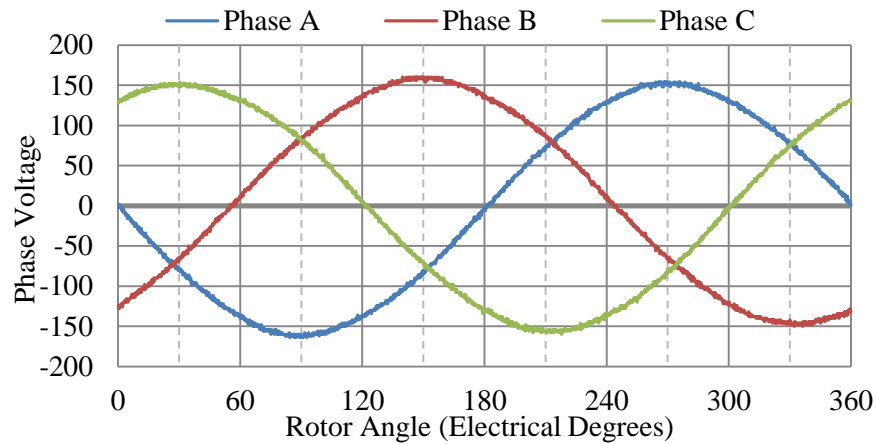


Figure 10.5. Three Phase Open Circuit.

Figure 10.6 shows the measured and calculated line back EMF waveform for one full electrical cycle obtained at 4000 rpm. Also Figure 10.7 shows the harmonic contents of the measured waveform.

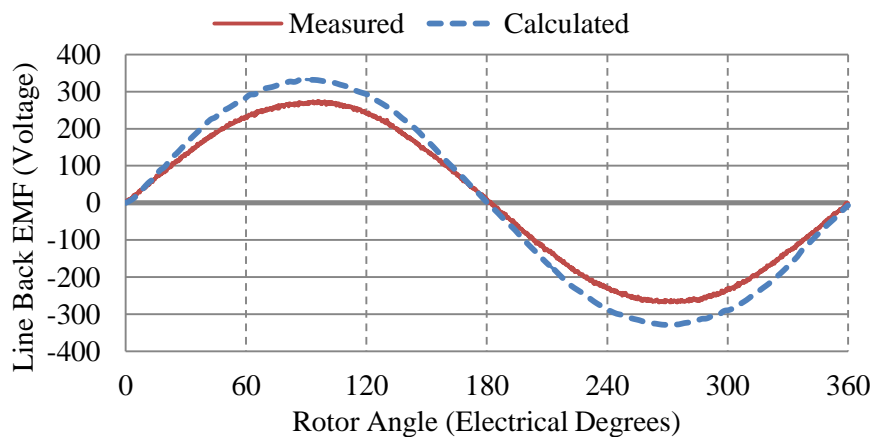


Figure 10.6. Measured Line Back EMF at 4000 rpm.

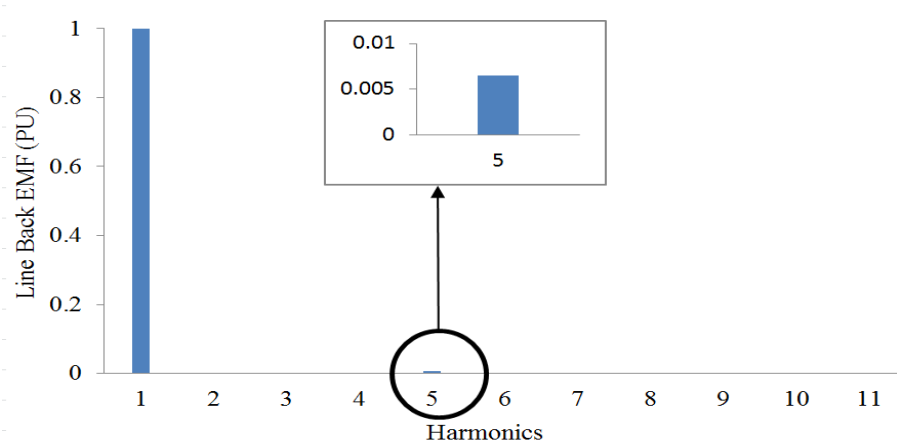


Figure 10.7. Harmonic Spectrum of the Measured Line Back EMF at 4000 rpm.

From both figures, it can be seen that the back EMF is close to a pure sinusoid, with a fifth harmonic of only 0.6 % of the fundamental.

The back EMF variation with speed is expected to rise linearly. Figure 10.8 shows the variation of the measured and the predicted line back EMF.

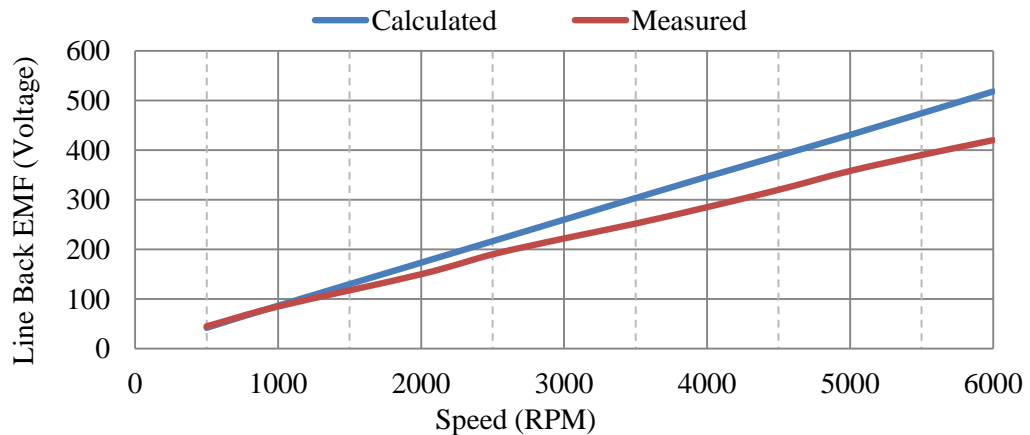


Figure 10.8. Measured and Calculated Line Back EMF versus Speed.

From the figure above, it can be seen that the measured back EMF is linearly rising with speed as initially expected. However, the measured values are reduced by 20 % (at the maximum rated speed) when compared to 2D FE. This difference is due to the followings:

- The reduced flux linkage caused by the reduction in magnet sizes during manufacturing than that of the simulated ones in 2D FE (as explained in chapter 9).
- The no-load loss generated in the machine increases with higher speed and is

expected to be more than the predicted using 2D FE method because of the 2D nature of not counting the end effects. These losses cause a rise in the magnet temperature which reduces the flux generated, and hence affect the Back EMF.

- The back end bearing had a slight unexpected misalignment during the test, which caused a further unexpected increase in temperature.
- The variation in the measuring equipment.

An investigation of the effect of the reduced magnet size was carried out and compared to that of the measured value as shown in Figure 10.9.

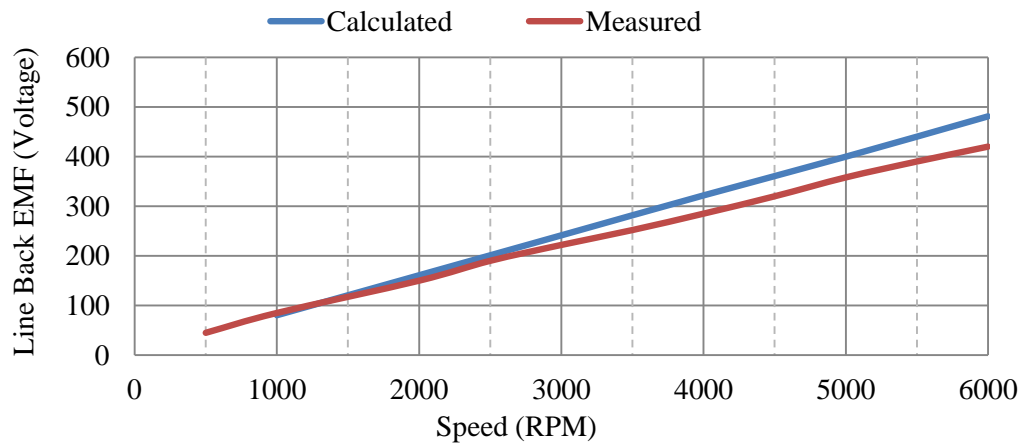


Figure 10.9. Measured and Calculated Line Back EMF Verses Speed.

The difference between the calculated and measured values is 14 %. It is postulated that the remaining difference is due to end effect, which has not been investigated here.

The increasing discrepancy between the measured and calculated values after 2000 rpm is due to the temperature raise, which affects the magnet performance, especially at a higher speed. This temperature raise cannot be accurately predicted by simulation due to the extra heat generated by the associated mechanical parts that are not counted for during simulations such as; the bearings.

Figures 10.10 and 10.11 show iron and magnet loss obtained at a range of speed and different temperatures.



Figure 10.10. Iron Loss at Different Temperatures and a Range of Speed.

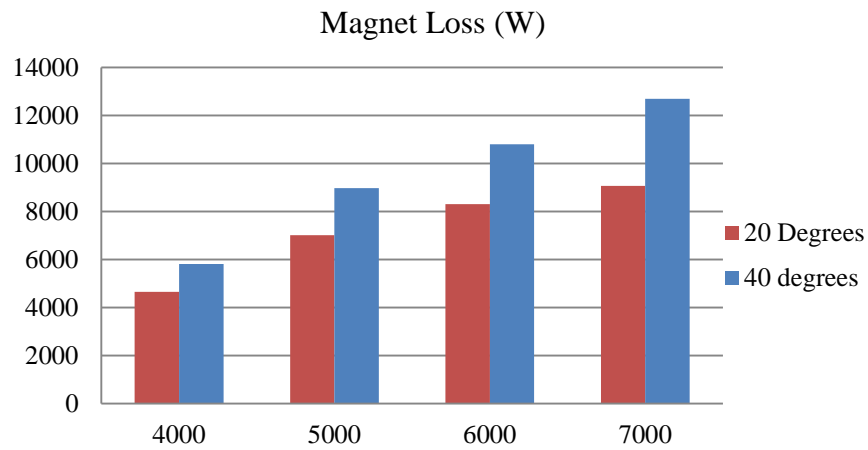


Figure 10.11. Magnet Loss at Different Temperatures and a Range of Speed.

Losses such as windage, friction and iron are generated when the machine is running on no load. The no-load losses of the machine were predicted using 2D FE method and shown in Figure 10.12.

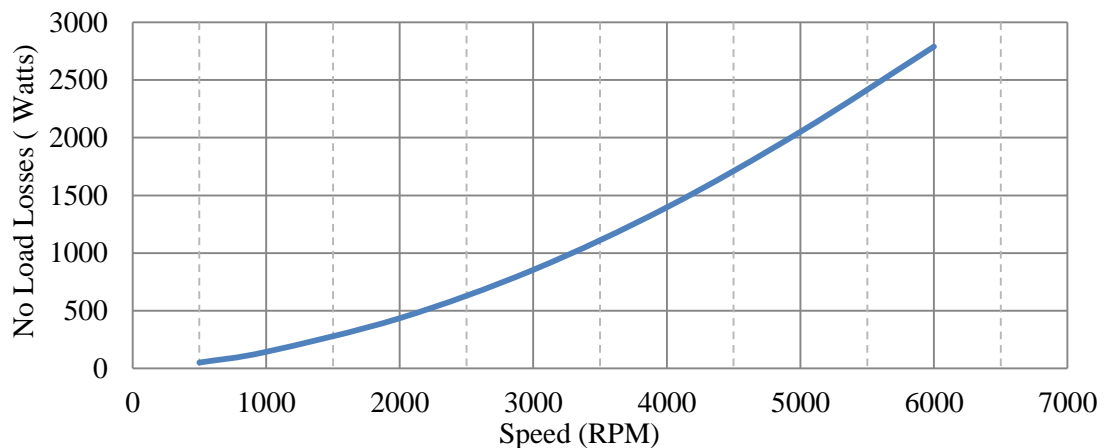


Figure 10.12. Predicted No Load Losses Versus Speed.

It can be seen from the figure that the no load loss increases with speed.

10.4 Load Tests

Two types of load tests were carried out; a static test and a rotating test.

10.4.1 Static Torque

The static torque test can accurately compare the result of the torque measurement with that calculated from the FE model. This is because, when the static torque is measured with various applied currents, any distortion of the torque, such as cogging or reluctance torque can be seen in the resulted waveform.

After mounting the motor into the static torque test rig and connecting it to the power supply as shown and explained in Chapter 9, the static torque characteristics were obtained from a torque meter (MAGTROL, Model 3410) connected to the torque transducer (MAGTROL, TM313) over a range of excitation currents from 0 to 100 Amps where one phase was energised with current I and the other phases with $-I/2$. This was done in such a way that the three phases of the machine were connected in star and phase A was energised with current I and allowed to split at the neutral point so that $-I/2$ results in phases B and C, as shown in Figure 10.13.

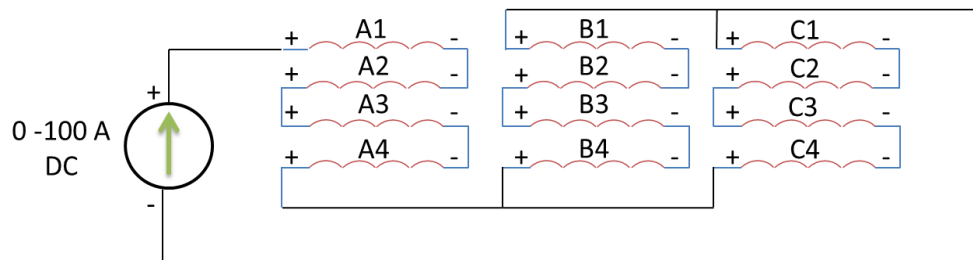


Figure 10.13. Phase Connections During the Static Torque Test.

This was performed over 1 electrical cycle (18° mechanical) in steps of 0.5° mechanical. The measured and calculated torque versus rotor angle is as shown in Figure 10.14.

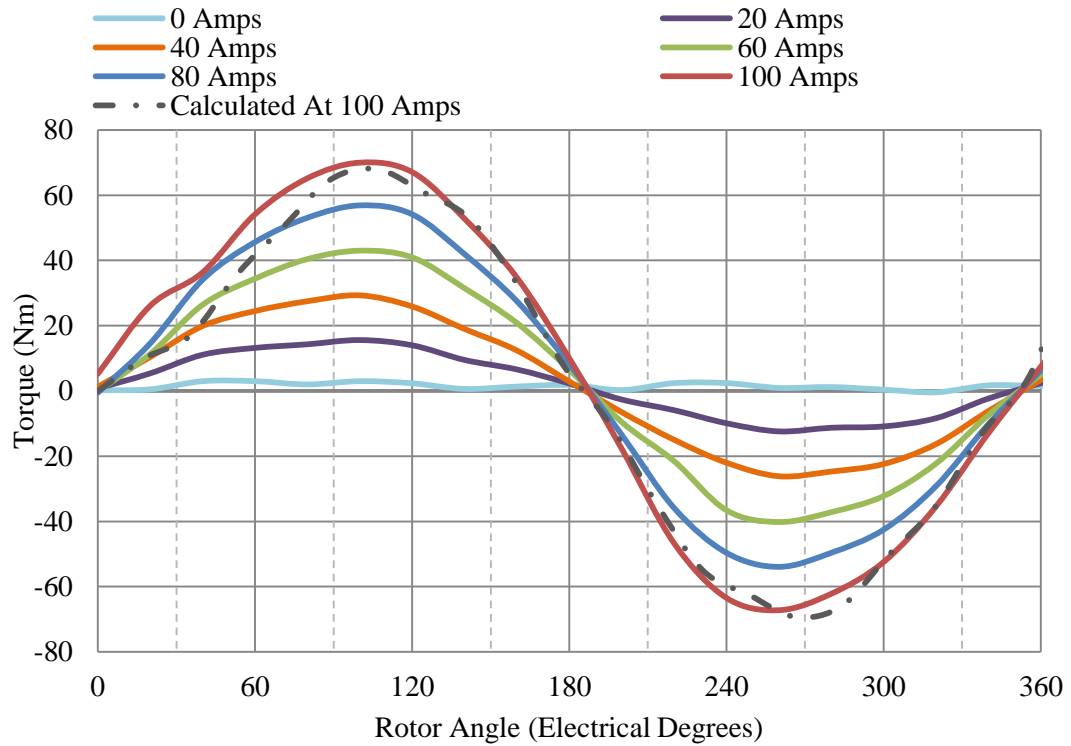


Figure 10.14. Measured and Calculated Torque Verses Rotor Angle.

From Figure 10.14, it can be seen that the torque measured throughout the experiment increases linearly with the current applied. This rise in torque is expected to continue at the same rate up to an applied current of 268 Amps before it starts to saturate and level off. However, due to the limited capability available for such a test, the full test was not carried out and will be considered for future work. A calculated result at 100 Amps was also added and only a small acceptable difference can be noted.

In addition, it can be seen from the figure that neither reluctance nor cogging torque were of significance. This is due to the low variation in phase inductance with respect to rotor position.

A comparison of these torque results with the values of torque obtained from 2D FE is shown in Figure 10.15 in terms of torque against applied current.

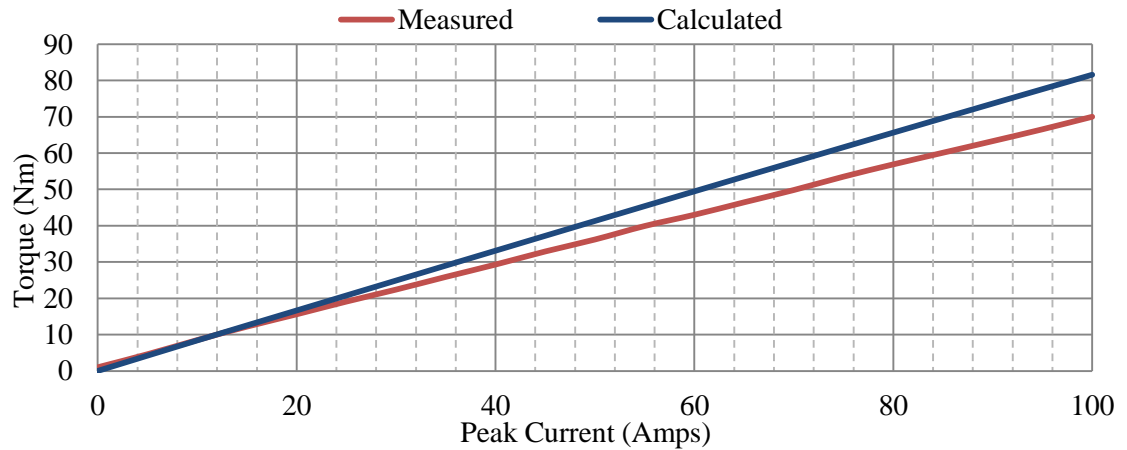


Figure 10.15. Measured and Calculated Torque Verses Applied Current.

From Figure 10.15, it can be seen that the calculated torque differs from the measurements, varying by 5% to 13.5% as machine load increases. This drop was expected for the following reasons:

- The reduction in magnet size during assembly.
- When the current is applied to phase A in series into phase B and C in parallel, it is assumed that the two phases in parallel are balanced, which is not always the case during operation.
- Error caused by the measuring instruments (torque meter, current probe) of between 2% to 4% was observed during the test.
- The value of inductance is lower than that predicted in the 2D FE model.
- According to the assumption made in the 2D simulation, end-winding effects are not accounted for.

In order to eliminate the first potential reason, a new model was simulated in 2D FE with the reduced magnet sizes. Predictions of torque against current were then obtained and compared again with the measured values, as shown in Figure 10.13.

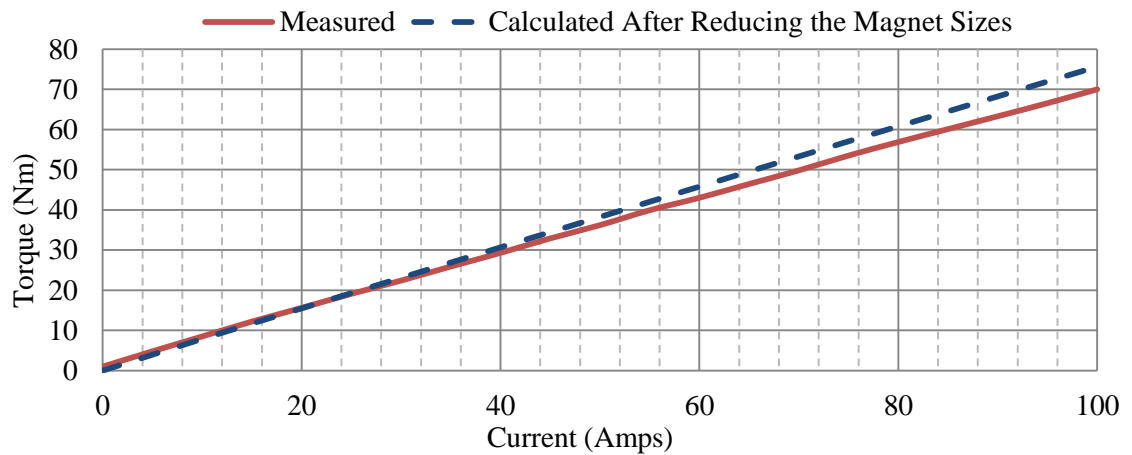


Figure 10.16. Measured and Calculated Torque Verses Applied Current.

From the figure, it can be seen that the measured values represent only 8% less torque than the calculated values resulting from the 2D FE model of the reduced size magnets. For the reasons mentioned above, the measured values can be said to agree with the simulation results despite the 8% reduction.

10.4.2 Running Load Test

The machine was driven using a dynamometer (DC motor rated to 30,000 rpm) with a speed controller to speeds ranging from 1000rpm to 4000rpm in steps of 1000rpm with various loads. The load was applied using a digital varying resistor bank (Hillstone, HAC415-20) that was connected to the machine terminals using cables. This was done in order to obtain measurements of power, current, voltage and torque at each load using Tektronix oscilloscopes and a torque meter that was connected to a torque transducer by Hillstone (Model, ET1303) that was mounted on the rig. The measured output power was observed to be proportional to the armature current generated, which was in agreement with theoretical expectations.

The results obtained were then used to calculate the efficiency of the machine and to generate plots of efficiency against both the armature current generated and power output, as can be seen in Figures 10.14 and 10.15 respectively.

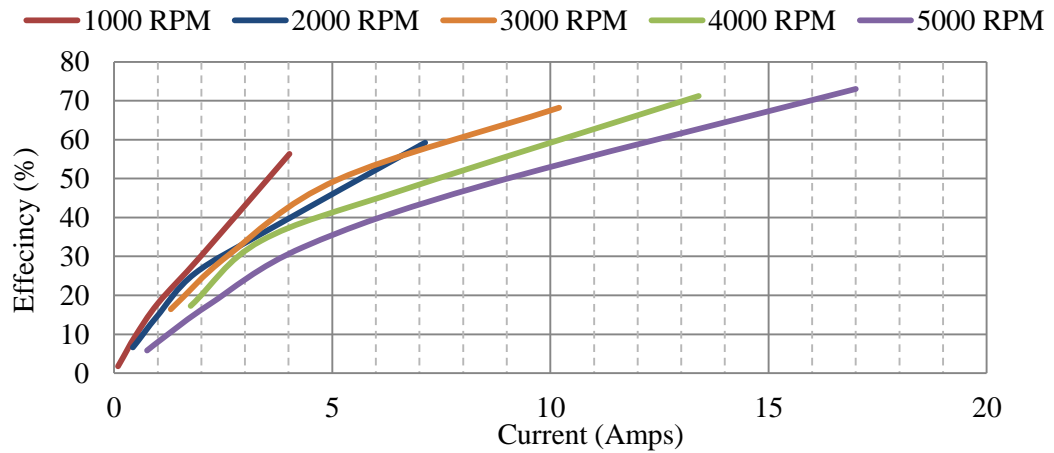


Figure 10.17. Measured Efficiency Against Armature Current Generated.

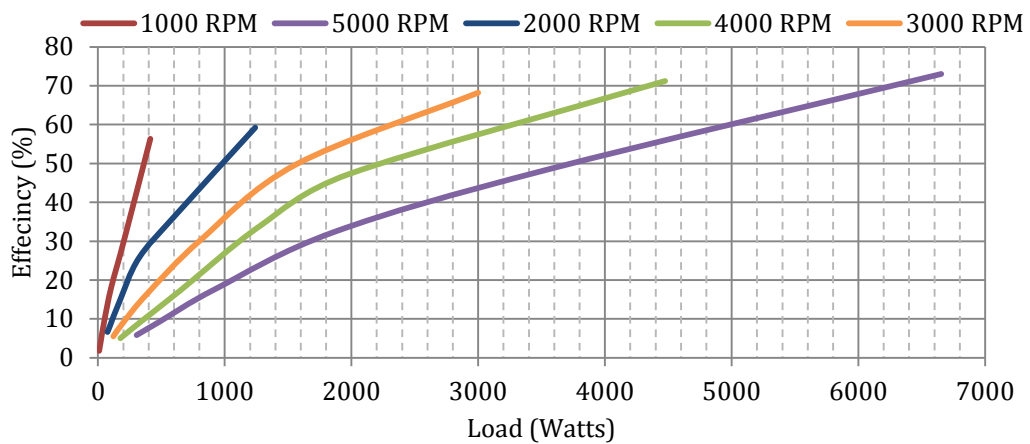


Figure 10.18. Measured Efficiency Against Output Load Generated.

From Figure 10.14, it can be seen that, although winding loss increases with the current through the stator windings, the machine's efficiency initially increases with increasing armature current. This is due to the small current applied in comparison to the rated current of the machine and hence, at this stage, the effect of winding loss is minimal with respect to the machine's total losses.

In addition, it can be seen from Figure 10.15 that efficiency increases with load at a fixed speed due to the small load applied in terms of the rated load for this machine (74.4Kw). However, it is reduced when the speed is increased for the same applied load. This is because of the increased iron, windage and frictional losses with increasing speed, as illustrated during the no-load test.

A maximum efficiency of 73% has been achieved with 6600 watts of applied load at a speed of 5000 rpm. This is expected to increase at higher loads. However, due to the limited load of the resistor bank available, no further measurements were taken, and this

will be proposed for future work.

10.5 Thermal Test (No-Load)

The machine has 7 K-type thermocouples located at:

- Centre of slot (phase A).
- End winding (phase A).
- Centre of slot (phase B).
- End winding (phase B).
- Centre of slot (phase C).
- End winding (phase C).
- Outer case.

The thermal characteristics were determined using a DC power supply as shown in Figure 10.16 where a current of 100 Amps was energized to one phase which was connected in series with the other two phases for a duration of 3 hours. Measurements of temperature were recorded at intervals of 30 seconds.

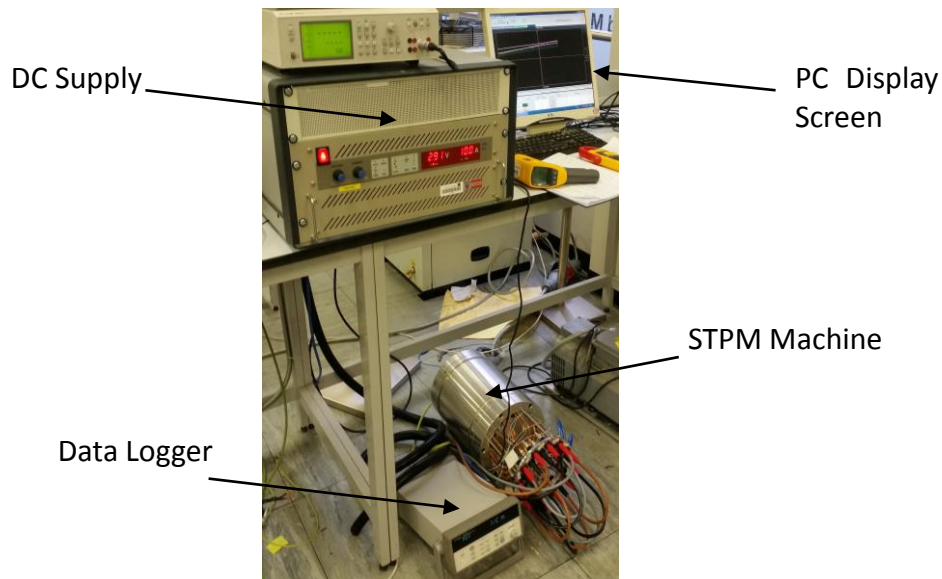


Figure 10.19. Thermal Test Bench.

The temperatures obtained on the outer surface of the case, inside the slot (Phase A) and at the end winding (phase A) are as shown in Figure 10.17.

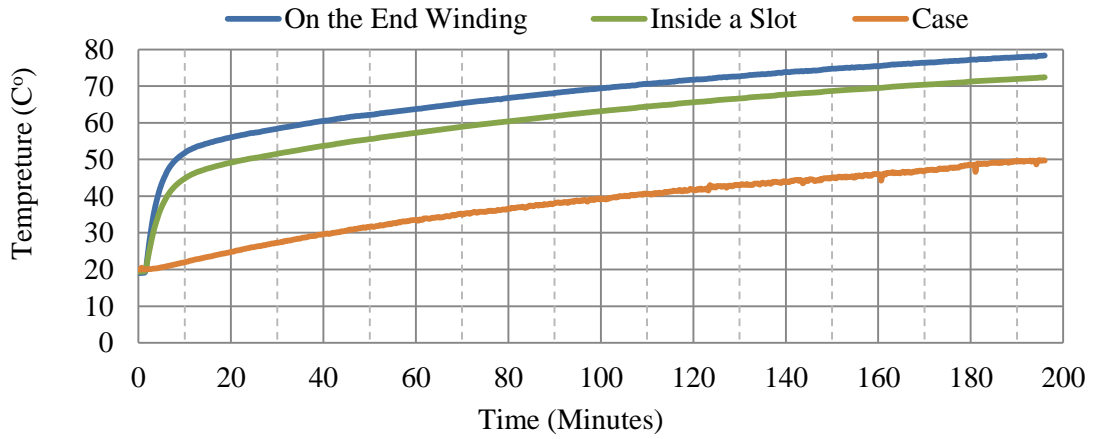


Figure 10.20. Temperature Rise with Time at 100Amps

It can be seen from Figure 10.17 that, in air, the maximum temperature at the end windings of the coils was just below 80°C. This can be compared to 72°C in the middle of the slot between the coils. In addition, the maximum temperature recorded on the outer case was 50°C. The higher temperature rise at the end winding of the coil is due to the thermal conductivity of the coil surroundings, and hence the thermal path in which the heat is transferred, to the air around the end winding (with low thermal conductivity, hence lower heat transfer) and to the lamination around the coils inside the slots (with higher thermal conductivity, hence better heat transfer).

Although it is possible to scale up the temperature rise with increasing current by assuming that the temperature is proportional to the square of the applied current (acting as a resistor), a more accurate method is proposed and used here. The test above was repeated using a different current (I_2) for the same duration and using the temperature obtained (T_2) along with the same assumptions above but with an added thermal constant (K_t) to act as an error adjuster:

$$\frac{I_1^2}{I_2^2} = K_t \frac{T_1}{T_2} \quad 10.1$$

Where I_1 and T_1 are the applied current and temperature obtained during the first test respectively. By solving for K_t and then using the equation, the maximum current that the machine can operate at without forced cooling is found to be 150 Amps. This is greater than the rated operating current (10A/mm²) for the natural air cooling method. It is also important to note that this machine is capable of operating at 15A/mm² before it becomes saturated. However, forced cooling is required, and this will be the subject of future research.

10.6 Comparing STPM Machine to Existing Machines.

This section gives a comparison between the final STPM machine and two interior PM machines, Toyota Camry and Prius motors [98, 99]. Table 10.2 highlights the different motor components of the three machines (the effect of the reduction gear used with the Camry motor is eliminated in this comparison).

Table 10.2. Comparison between the STPM Machine, Camry and Prius Motors

Parameter	STPM Machine	IPMM(Camry)	IPMM (Prius)
Lamination dimensions			
Outer Stator Diameter (mm)	200	264	269
Inner stator Diameter (mm)	73.27	161.93	161.93
Stator Stack Length (mm)	130	60.7	84
Outer Rotor Diameter (mm)	72.27	160.47	160.47
Inner Rotor Diameter (mm)	51.77	105	111
Rotor Stack Length (mm)	130	62	83.6
Air Gap (mm)	1 (Inner & Outer)	0.73025	0.73025
Lamination Thickness (mm)	0.35	0.31	0.33
Rotor Mass Including Magnets (kg)	7.6	9.03	10.2
Stator/ Mass Including Copper (kg)	10.8	18	25.9
Inner Stator	1.7	N/A	N/A
Total Mass (kg)	20.1	27	36.1
Stator Wiring			
Number of Stator Slots	12	48	48
Stator Turns Per Coil	5	14	9
Slot Depth (mm)	11.97	30.9	33.5
Slot opening (mm)	8	1.88	1.93
Total Mass of Stator Copper (kg)	2.4	5.6	6.8
Magnets (NdFeB)			
Magnet Dimensions (mm)	130x18x4	60.6 x 19.1 x6.6	83.1 x 18.9 x6.5
Magnet Volume (mm ³)	9360	7639.23	10208.83
Total Mass of Magnets (kg)	2.65	0.928	1.232
Performance			
Rated Torque (Nm)	254.5	270	400
Maximum dc-link voltage	650	650	650

Speed (rpm)	6000	12000	6000
Torque Density* (Nm/kg) (*Active mass)	12.7	10	11.1
Torque Per Magnet Mass (Nm/kg)	95	313.57	241

From Table 2.2, it can be seen that the STPM machine has the smallest outer diameter and the longest axial length. However all three machines are used for the same application.

The active mass of the STPM machine is 25.5 % and 44 % less than that of the Camry and Prius motors respectively. However, the STPM machine has more magnets mass.

Despite, the higher magnet mass achieved by the STPM machine, It was found that the torque to magnet mass ratio increases for a smaller magnet height than the optimum magnet design, during the investigations carried out in Chapter 7, and hence further investigation on reducing magnet mass will be recommended for future work.

Less number of slots and number of turns can be seen at the STPM machine, which indicated less overall coil length, and hence less resistance which reduces the winding loss (I^2R).

A V shape rotor has been used for the Toyota motors while concentrated magnets are used for the STPM machine.

The Prius motor has obtained the highest torque. However, the STPM machine achieves the highest torque density of 12.7 Nm/Kg that is 14.4 % and 27 % more than these achieved by the Prius and Camry motors respectively.

Although, reducing the magnet size wasn't under the scope of this research but due to the lower torque to magnet mass achieved by the STPM machine when compared to the other two motors, it is beneficial to compare the cost of all three machines. The comparison will be considered by calculating the cost of the active materials of each machine without taking manufacturing cost in to the account as shown in Table 10.3. (Prices as follows; for copper (London stock Exchange as of 01/2015) at 5.58 \$/kg, Neodymium-Iron-Boron (estimated) at 132 \$/kg and for lamination (estimated) at 1.3 \$/kg).

Table 10.3. Cost Comparison between the STPM Machine, Camry and Prius Motors

Machine		Lamination	Copper	Magnet	Total Price
STPM	Mass (Kg)	15	2.4	2.65	\$372.7
	Price (\$)	\$19.5	\$13.4	\$339.8	
Camry	Mass (kg)	20.5	5.6	0.928	\$180
	Price (\$)	\$26.6	\$31.2	\$122	
Prius	Mass (kg)	22.1	6.8	1.232	\$231.6
	Price (\$)	\$28.7	\$37.9	\$165	

The Camry and Prius are 51 % and 37 % cheaper than the STPM machine respectively; this is due to the higher magnet mass of the new design. In addition, it is also worth noting that if the magnet height is reduced to 12 mm, the magnet to torque ratio will increase by 33% as can be seen in Chapter 7 in Figure 7.21. This will correspond to a cost reduction of 27%, reducing the cost to \$269.18 while still maintaining a higher torque density than both Camry and Prius motors of 11.7 Nm/mm^2 . Reducing the magnet mass is viable and it will be proposed for future investigation.

Manufacturing costs could also add up to the STPM machine due to its mechanical structure. However, this can be minimised using the most appropriate cutting method and it will also be proposed for future investigations.

10.3. Conclusion

This chapter started by presenting five different tests and analysis that were carried out for the fully assembled STPM machine and ended with a torque density comparison between the STPM machine and two IPM machines that are commercially available.

Although the coils were pressed around a wooden former to achieve a higher fill factor, all coils were found to be healthy without any damage to their insulation during carrying tests to find any coil to ground wall fault and any inter-turn fault.

The machine resistance has been measured and found to be low at $23.3 \text{ m}\Omega$ per phase because of the short end winding and small number of turns, resulting in a reduced winding loss (I^2R).

Although the reduction of magnet sizes has resulted in 6% reduction in the line back EMF, a further 14% reduction in back EMF has resulted due to the increased temperatures at the rated speed. This is because of the end effect and the misalignment of the back end bearing. These have resulted in a magnet temperature rise and hence reduced flux.

The measured torque values are 8% less than that expected due to effect of the reduced inductance during the measurements, the end effect that isn't counted for in 2D FE, the error caused by the measuring instruments and the assumptions that all three phases are fully balanced.

During loading the machine at various speeds, the machine followed an expected trend as the efficiency increased at the same output load for a reduced speed.

A thermal test was carried in which the machine showed the capability of achieving the specified current without being over heated.

Out of the three compared machines in this chapter, the STPM machine can be more preferable in high torque density application where there is a more limited radial envelope because of its shorter radius. The STPM machine has shown to have the best torque density out of the two Toyota Motors by up to 27% achieving the purpose of his research. The STPM machine can be further improved by reducing its magnet mass in order to reduce its cost.

Chapter 11. Conclusion

The aim of this thesis was to introduce, describe theoretically and mathematically a high torque density Permanent Magnet (PM) machine design for Electric Vehicles (EVs). This was then designed, optimized, constructed and successfully tested. In addition, it achieved higher torque density than two commercially available PM machines.

11.1 An Overview of Electric Vehicles

The system design of EVs must have a specific weight, volume, and power density, and critical requirements include high performance, rapid acceleration, good fuel economy, low cost and a transient response similar to that of Internal Combustion Engine Vehicles (ICEVs). The design of EVs is faced with challenges that must be taken into account, such as the capability, size, lifetime and cost of its battery, safety features, the availability of charging stations, the performance of the electric motor, the cooling system and the software used to communicate between the different parts of the system. EVs can use a drive train that is direct or geared, where the former is sited inside the wheel and the geared type is connected to the wheel's shaft through differentials. Although in-wheel drive trains eliminate the use of differentials, they require complex control system. Also various other challenges should be taken into consideration when designing electric motors for EVs, such as the demand for high power, high torque density, a wide speed range, high starting torque, reliability, robustness, overload capability, cost, minimal torque ripple, controllability, high efficiency and good voltage regulation.

11.2 Electrical Machine Topologies for EVs

EVs require electrical machines with high efficiency and torque density and, because of the various machine types that can be used for EVs, the availability, advantages and disadvantages of each type have been shown and discussed. IMs are widely used in EVs and Hybrid Electric Vehicles (HEVs) because of their reliability and low cost. In addition, despite the low cost, high-tolerance operation and torque speed characteristics of the SRMs make them ideal for EVs. However, their noise and manufacturing difficulties considering the small air gap required make them less favoured to be used in

EVs. PM machines, on the other hand, have been favoured by various manufactures despite the high cost of materials because of their high power density, reliability and high efficiency. A PM machine has been chosen for the novel design in this thesis because of its high torque density. And although, there are different ways of calculating torque, they are mostly approximations; hence they were used as an indication here, while MagNet software simulations was used throughout this thesis to indicate the torque output.

11.3 Introducing the Split Tooth Permanent Magnet Machine

A new method of deriving greater torque density from a convention PM machine topology has been described and compared to two motor solved optimised brushless PM machines of the same dimension using 2 Dimensional (2D) Finite Element (FE) analysis. The method involved splitting the stator teeth in order to introduce a magnetic gear ratio into the torque equation. This Split Tooth Permanent Magnet (STPM) machine introduced in order to be used as a direct drive motor for an electric vehicle. It was designed to produce the maximum possible torque output for fixed physical dimensions and specification. The new machine has shown a significant improvement of up to 237 % and 141 % more torque density than the other brushless PM machines (12 slots/ 4 poles and 12 slots/ 10 brushless PM machines respectively), one drawback for the STPM is found in need of improvements, that as the machine rotates, and each rotor magnet moves from a position under a stator split tooth to one between them, it experiences a large change in flux density. This changing flux density will inevitably induce eddy currents within the magnets and result in magnet losses. These losses can in certain cases be significant; indeed because of the degradation of the magnet properties at relatively high temperature, and hence they must be regarded with some concern.

11.4 Development of the Split Tooth PM Machine

A further modified design of the new geometry was made using flux concentration magnets and an inner stator. The modified design showed a further increase in torque density, improved the disadvantage of the induced eddy currents within the magnets in the first design and allows all magnets under a split tooth to be utilised

The advantages and disadvantages of the new designs:

1. The new machine has the advantage of introducing an additional factor into the output torque equation.
2. The new STPM machine produces a 293.2% more torque than the conventional BL design.
3. A modified design of the new STPM machine with flux concentration magnets has shown a further 35% increase in torque output.
4. The implementation of the inner stator in the modified design has produced more flux to link the phases, increasing the overall flux linkage.
5. The new design has a reduced electrical loading, as the slot area is reduced by the split teeth geometry.
6. The higher pole number in the new design results in a higher stator electrical frequency and hence greater iron losses in the machine. This needs some consideration.

Table 11.1 compares the Brushless PM machine and both STPM machines.

Table 11.1. Comparison between All Machines.

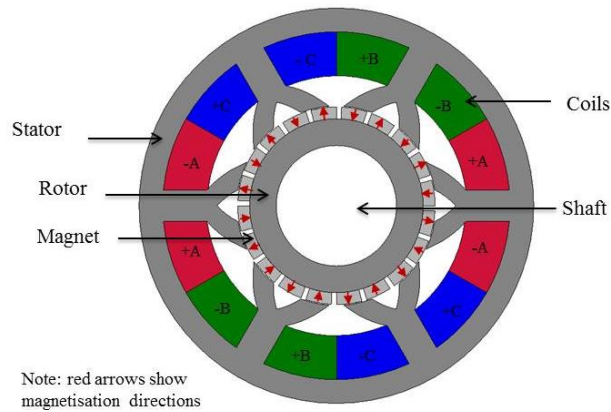
Machine	12 slots/ 4 poles Brushless PM Machine	12 slots/ 10 poles Brushless PM Machine	New Design with Surface Magnets	New Design with Flux Concentration
Torque (Nm)	34	45	100	135
Mass (Kg)	29.83	28.3	25.93	27.13
Magnet mass (Kg)	1.71	1.17	1.49	1.36
Torque density (Nm/Kg)	1.14	1.6	3.85	4.97
Torque to magnet ratio (Nm/Kg)	19.9	38.5	67.1	99.26

The STPM machine with concentrated magnets shows a factor of 2.9 and 2.2 increase in output torque when compared to 12 slots / 4 poles and 12 slots /10 poles brushless PM machines; this is as a result of the improved magnet utilisation

It can also be seen that the STPM machine with concentrated magnets has a factor of 4.4 and 3.1 increase in torque density when compared to 12 slots / 4 poles and 12 slots / 10 poles brushless PM machines.

Figure 11.1 shows a geometry comparison of both initial and modified STPM machines.

a) STPM Machine with Surface Mounted Magnets (Initial).



b) STPM Machine with Flux Concentrated Magnets (Modified).

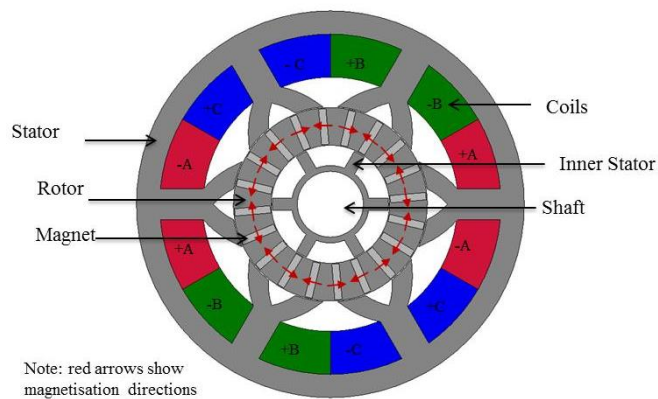


Figure 11.1. Geometries of Both STPM Machines

11.5 Design Optimisation

Different slot to pole combinations have been considered and compared to find the optimum combination with the maximum torque density that can be built for the purpose of this thesis. 12slots/ 40poles was found to produce up to 15 % more torque density than the other possible combination, hence chosen to be further improved using two optimisation processes that were explained and carried in order to investigate and

optimise the 12 slots/ 40 poles STPM machine. The first method was by changing the dimensions manually (single objective optimisation) and the other was by using OptiNetTM (multi objective automated optimisation). Increasing the slot to pole combination resulted in some advantages such as; less coreback depth, which increases the rotor radius for the same outer stator outer diameter, reduced magnet and end winding, shorter end winding, minimised risk of magnet demagnetisation. However, it results in increased stator iron loss because of the higher resulted machine electrical frequency for the same speed, increased flux leakage between neighbouring magnets and from magnet to tooth, reduced magnet sizes which make them more sensitive to handle and harder to manufacture.

11.6 Investigative Design

The impact of varying the machine dimensions on the achieved torque density has been investigated using the manual optimisation method for each of the machine's various parameters. Some theoretical and mathematical explanations have also been included to aid the general understanding of the behaviour of the STPM machine.

A balance between the slot areas, and hence the MMF and the saturation in the tooth, has been considered when choosing the tooth widths and slot depths. In addition, a balance between the saturation and rotor radius was considered for the choice of the coreback depth. Furthermore, slot opening widths in this particular machine can limit the linking flux by either having a short or a long width, where the former allows for a fringing flux path and the latter causes saturation on the tooth ends as they become narrower. The optimum width was found when a tooth end is enclosed in between any two magnet poles. On the other hand, shorter tooth split widths and depths allow the flux to circulate back to the rotor, causing fringing flux, while longer widths and depths mean that the tooth ends become narrower and hence become saturated more quickly. Thus, a balance has been considered in finding the optimum designs. Adding to tooth tip width increases the peak torque up to 11 %. This is due to the increased air gap flux density.

Also, increasing magnet height results in increased peak torques to a point where the magnet flux flowing circuit becomes fully saturated and any further increase becomes pointless. The saturation of the circuit flux flow path also limits the maximum magnet

thickness to 4 mm, where any further increase results in a reduced torque. Moreover, the bridges that lay on top of the magnets act as a shield to protect the magnet from the armature magnetising field strength.

The inner stator slot depth was found to have no impact on the achievable torque. However, it has to be long enough to prevent a flux return path and to reduce the coreback mass by reducing its diameter and hence increasing the torque density. On the other hand, the inner stator coreback has to be thick enough to allow a full flux path for the linking flux, and short enough to reduce the active mass of the machine.

The implementation of the inner stator increases the flux linkage by 24% and increased the torque by 12.5% compared to its absence.

11.7 Optimisation and Final STPM Machine Design

The values obtained by the manual and automated optimisation (OptiNet™) methods were compared, and the torque was found to only be improved by 2% using OptiNet at the optimised current density of 15 A/mm². Thereafter, the dimensions of the STPM machine have been finalised. Different sleeves were also studied and a sleeve made of Inconel grade was found to improve torque by 7 % and this will be the subject of future work. Single tooth windings were chosen for simplicity with a number of coil turns that took the automotive inverter constraint into account. The final machine can operate at up to 15 A/mm² and achieve a torque of 250 Nm. However, a forced cooling system will be required, and the machine can operate at a current density of 10 A/mm² with only natural cooling. Field weakening will allow the machine to reach 6000 rpm with no demagnetisation, and the design operating point was predicted from 2D FE simulations.

11.8 Design and Construction

During the design and construction process of the STPM machine; shoulders and keys were used to lock the outer and inner stator. The wire cutting method has been proven to be the best method to cut the laminations, A new case structure has been illustrated which has been proven to be better than the typical cup rotor structure for machines with conventional rotors that rotate in between two stators. Different power connection

methods have been explained, and a socket holder method was chosen. Reduced magnet sizes resulted during construction due to the uneven magnet space caused by laser cutting and the manufacturing difficulty which resulted in a magnet size less than that of the optimum design. Two different test rigs were used. In the first, called the static torque test rig, the rotor was locked, current was applied to the STPM machine, and measurements of torque were obtained. The second is a high speed rig, in which the STPM machine was driven using a DC drive and tested, and different measurements were obtained at both no-load and load conditions.

The manufacturing process has taken more time than it has expected. This is due to the new machine structure as it is the first trial to build one. However, this will improve in building a second or a developed one as the challenges has been pointed out and can be improved, especially after more knowledge about the building process is gained.

11.9 Results and analysis

Five different tests and analysis were carried out for the fully assembled STPM machine and the following was concluded:

- All coils were found to be healthy when testing for any coil to ground wall and inter-turn fault.
- Resistance measurements were carried out and it was found to be lower than expected at 23.3 m Ω , resulting in a reduced winding loss (I²R).
- Inductance was found to be less than that expected due to the end winding effect, the expected variation in lamination permeability and the different layout of the coils during the test.
- In addition, 14% reduction in back EMF has resulted due to the increased temperatures at the rated speed because of the misalignment of the back end bearing and the nature of the 2D FE method.
- The reduction in magnet size has resulted in a 6% reduction in the line back EMF.
- 8% less torque was measured due to the effect of the reduced inductance during the measurements, the end effect is not accounted for in the 2D FE analysis, the error caused by the measuring instruments and the assumption that all three phases are fully balanced.

- The machine showed the ability to achieve its rated current without becoming overheated in the thermal test.
- The STPM machine resulted in smaller outer diameter and longer axial length than both Toyota motors.
- The STPM machine has shown better torque density than the two Toyota Motors by up to 27%, thus achieving the main purpose of his research. However, it achieved the lowest torque to magnet mass.
- The STPM machine has the ability to produce 33% more torque per magnet mass with a smaller magnet height while maintaining better torque density than both the Camay and Prius motors.

This thesis has put forward a new method of achieving higher torque density from a conventional PM machine, and it has been illustrated that the proposed machine is better than the two commercially available IPM machines for EV applications. The STPM machine has overcome most of the challenges faced in EV motor design. There is no sign of cogging torque, either from calculations or in practice, and hence minimal torque ripple and audible noise. It achieves a high starting torque and has a high level of reliability. Although the STPM machine is a first design, and hence has the potential to be further improved, it has achieved the purpose of this thesis.

11.1. Future Work

A high torque density STPM machine was successfully designed and constructed during this research, and the design has successfully increased torque by increasing the rate of flux change with position, and hence a higher factor is achieved in the torque equation. An inner stator inclusion has resulted in 21% improvement in torque because of the better magnet utilisation achieved. In addition, the optimisation used allowed every vertex of the machine to be varied has resulted in the best possible combination of parameters for a fixed outer diameter. A new case design has been introduced which has shown good mechanical stability both theoretically and in practice.

Although, there were some differences in performance compared to expectations, they are generally validated. It has been shown that the machine is capable of operating at the optimised current density and achieving increased torque density.

The aim of this thesis was to find a way to improve the torque density of PM machines,

targeting the fast-growing field of EVs. The following, some recommendations for future work are;

1. Investigating different rotor topologies, such as introducing flux barriers and investigating their mechanical strength in order to either increase the field of the magnets or reduce their mass as can be seen in Figure 11.2.
2. Using the Inconel sleeve.
3. Using a forced cooling method.
4. Obtaining performance measurements at full speed and load.
5. Investigating the possibility of increasing the inductance of the windings.
6. Introducing windings to the inner stator to increase the electric loading of the machine
7. Reducing the torque to magnet mass achieved (reducing the magnet mass and hence the cost).
8. Enhancing the mechanical bearings chosen in order to reduce the associated losses generated in the machine such as (misalignment causing extra heat within the constructed STPM machine).
9. Reducing the cables used on the external power connectors to reduce the long cable losses.
10. Investigating an improved manufacturing technique in order to reduce the manufacturing costs.

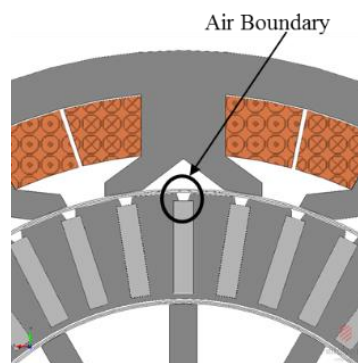


Figure 11.2. Introduction of Flux Barriers.

References

- [1] M. Benhaddadi and G. Olivier, "Barriers and incentives policies to high-efficiency motors and drives market penetration," in *Power Electronics, Electrical Drives, Automation and Motion*, 2008. *SPEEDAM 2008. International Symposium on*, 2008, pp. 1161-1164.
- [2] D. M. Ionel, "High-efficiency variable-speed electric motor drive technologies for energy savings in the US residential sector," in *Optimization of Electrical and Electronic Equipment (OPTIM)*, 2010 12th International Conference on, 2010, pp. 1403-1414.
- [3] M. Benhaddadi, G. Olivier, D. Labrosse, and P. Tetrault, "Premium efficiency motors and energy saving potential," in *Electric Machines and Drives Conference, 2009. IEMDC '09. IEEE International*, 2009, pp. 1463-1468.
- [4] M. Benhaddadi, G. Olivier, and J. Yelle, "Premium efficiency motors effectiveness," in *Power Electronics Electrical Drives Automation and Motion (SPEEDAM)*, 2010 International Symposium on, 2010, pp. 1607-1612.
- [5] R. Boteler and J. Malinowski, "Review of upcoming changes to global motor efficiency regulations," in *Pulp and Paper Industry Technical Conference, 2009. PPIC '09. Conference Record of 2009 Annual*, 2009, pp. 26-30.
- [6] A. T. De Almeida, F. J. T. E. Ferreira, J. A. C. Fong, and C. U. Brunner, "Electric motor standards, ecodesign and global market transformation," in *Industrial and Commercial Power Systems Technical Conference, 2008. ICPS 2008. IEEE/IAS*, 2008, pp. 1-9.
- [7] W. R. Finley, B. Veerkamp, D. Gehring, and P. Hanna, "Improving motor efficiency levels globally," *Industry Applications Magazine, IEEE*, vol. 15, pp. 39-49, 2009.
- [8] K. Singh Salana, T. Singh, and N. Singh, "Saving energy using energy efficient motors:A case study," in *Power Electronics, Machines and Drives (PEMD 2010)*, 5th IET International Conference on, 2010, pp. 1-4.
- [9] F. Demmelmayr, M. Troyer, and M. Schroedl, "Advantages of PM-machines compared to induction machines in terms of efficiency and sensorless control in traction applications," in *IECON 2011 - 37th Annual Conference on IEEE Industrial Electronics Society*, 2011, pp. 2762-2768.
- [10] W. R. Finley, B. Veerkamp, D. Gehring, and P. Hanna, "Advantages of using High Efficiency Motors Such as NEMA Premium® Around the World," in *Petroleum and Chemical Industry Technical Conference, 2007. PCIC '07. IEEE*, 2007, pp. 1-14.
- [11] P. Pillay, "Factors to consider in the application of energy efficient motors," in *Industrial Electronics, 1995. ISIE '95., Proceedings of the IEEE International Symposium on*, 1995, pp. 99-109 vol.1.

- [12] A. G. J. B.C.Mecrow, "Efficiency trends in electric machines and drives," 2008, pp. 4336-4341.
- [13] P. Lazari, J. Wang, and L. Chen, "A computationally efficient design technique for electric vehicle traction machines," in *Electrical Machines (ICEM), 2012 XXth International Conference on*, 2012, pp. 2596-2602.
- [14] F. Assadian, S. Fekri, and M. Hancock, "Hybrid electric vehicles challenges: Strategies for advanced engine speed control," in *Electric Vehicle Conference (IEVC), 2012 IEEE International*, 2012, pp. 1-8.
- [15] V. Gulhane, M. R. Tarambale, and Y. P. Nerkar, "A Scope for the Research and Development Activities on Electric Vehicle Technology in Pune City," in *Electric and Hybrid Vehicles, 2006. ICEHV '06. IEEE Conference on*, 2006, pp. 1-8.
- [16] K. W. E. CHENGL, "Recent Development on Electric Vehicles," presented at the 3rd International Conference on Power Electronics Systems and Applications, 2009.
- [17] M. Ehsani, K. M. Rahman, and H. A. Toliyat, "Propulsion system design of electric and hybrid vehicles," *Industrial Electronics, IEEE Transactions on*, vol. 44, pp. 19-27, 1997.
- [18] X. Wei, Z. Jianguo, G. Youguang, W. Shuhong, W. Yi, and S. Zhanghai, "Survey on electrical machines in electrical vehicles," in *Applied Superconductivity and Electromagnetic Devices, 2009. ASEMD 2009. International Conference on*, 2009, pp. 167-170.
- [19] D. Hermance and S. Sasaki, "Hybrid electric vehicles take to the streets," *Spectrum, IEEE*, vol. 35, pp. 48-52, 1998.
- [20] K. T. Chau and C. C. Chan, "Emerging Energy-Efficient Technologies for Hybrid Electric Vehicles," *Proceedings of the IEEE*, vol. 95, pp. 821-835, 2007.
- [21] A. Emadi, L. Young-Joo, and K. Rajashekara, "Power Electronics and Motor Drives in Electric, Hybrid Electric, and Plug-In Hybrid Electric Vehicles," *Industrial Electronics, IEEE Transactions on*, vol. 55, pp. 2237-2245, 2008.
- [22] S. S. Williamson, A. Emadi, and K. Rajashekara, "Comprehensive Efficiency Modeling of Electric Traction Motor Drives for Hybrid Electric Vehicle Propulsion Applications," *Vehicular Technology, IEEE Transactions on*, vol. 56, pp. 1561-1572, 2007.
- [23] T.M.Corporation, "Toyota Hybrid System THS II," presented at the Japan2003.
- [24] K. T. Chau, C. C. Chan, and L. Chunhua, "Overview of Permanent-Magnet Brushless Drives for Electric and Hybrid Electric Vehicles," *Industrial Electronics, IEEE Transactions on*, vol. 55, pp. 2246-2257, 2008.
- [25] S. Grammatico, A. Balluchi, and E. Cosoli, "A series-parallel hybrid electric

- powertrain for industrial vehicles," in *Vehicle Power and Propulsion Conference (VPPC), 2010 IEEE*, 2010, pp. 1-6.
- [26] G. Zorpette, "The smart hybrid," *Spectrum, IEEE*, vol. 41, pp. 44-51, 2004.
 - [27] C. C. Chan, "The state of the art of electric and hybrid vehicles," *Proceedings of the IEEE*, vol. 90, pp. 247-275, 2002.
 - [28] K. C. X. D. Xue, and N. C. Cheung, "Selection of Electric Motor Drives for Electric Vehicles," A. A. U. presented at the Power Engineering Conference, 2008., Ed., ed.
 - [29] M. C. Pera, D. Hissel, and J. M. Kauffmann, "Fuel cell systems for electrical vehicles," in *Vehicular Technology Conference, 2002. VTC Spring 2002. IEEE 55th*, 2002, pp. 2097-2102 vol.4.
 - [30] T. Katrasnik, F. Trenc, and S. R. Opresnik, "Analysis of Energy Conversion Efficiency in Parallel and Series Hybrid Powertrains," *Vehicular Technology, IEEE Transactions on*, vol. 56, pp. 3649-3659, 2007.
 - [31] S. S. Williamson, S. M. Lukic, and A. Emadi, "Comprehensive drive train efficiency analysis of hybrid electric and fuel cell vehicles based on motor-controller efficiency modeling," *Power Electronics, IEEE Transactions on*, vol. 21, pp. 730-740, 2006.
 - [32] C. Montero, A. Oliva, D. Marcos, E. Gonzalez, C. Bordons, M. A. Ridao, *et al.*, "Fuel cell and power control for a hybrid vehicle. Experimental results," in *IECON 2012 - 38th Annual Conference on IEEE Industrial Electronics Society*, 2012, pp. 4121-4126.
 - [33] M. Amrhein and P. T. Krein, "Dynamic simulation for analysis of hybrid electric vehicle system and subsystem interactions, including power electronics," *Vehicular Technology, IEEE Transactions on*, vol. 54, pp. 825-836, 2005.
 - [34] P. Bajec, D. Voncina, D. Miljavec, and J. Nastran, "Bi-directional power converter for wide speed range integrated starter-generator," in *Industrial Electronics, 2004 IEEE International Symposium on*, 2004, pp. 1117-1122 vol. 2.
 - [35] L. Chedot, G. Friedrich, M. Biedinger, and P. Macret, "Integrated Starter Generator: The Need for an Optimal Design and Control Approach. Application to a Permanent Magnet Machine," *Industry Applications, IEEE Transactions on*, vol. 43, pp. 551-559, 2007.
 - [36] A. K. Jain, S. Mathapati, V. T. Ranganathan, and V. Narayanan, "Integrated starter generator for 42-V powernet using induction machine and direct torque control technique," *Power Electronics, IEEE Transactions on*, vol. 21, pp. 701-710, 2006.
 - [37] *Tesla Motors* [Online]. Available: http://www.teslamotors.com/en_GB/models/design.

- [38] L. Zhengshuo, G. Qinglai, S. Hongbin, W. Yao, and X. Shujun, "Emission-Concerned Wind-EV Coordination on the Transmission Grid Side With Network Constraints: Concept and Case Study," *Smart Grid, IEEE Transactions on*, vol. 4, pp. 1692-1704, 2013.
- [39] G. H. Fox, "Getting ready for electric vehicle charging stations," in *Industry Applications Society Annual Meeting (IAS), 2011 IEEE*, 2011, pp. 1-7.
- [40] G. H. Fox, "Electric Vehicle Charging Stations: Are We Prepared?," *Industry Applications Magazine, IEEE*, vol. 19, pp. 32-38, 2013.
- [41] G. Khalil, "Challenges of hybrid electric vehicles for military applications," in *Vehicle Power and Propulsion Conference, 2009. VPPC '09. IEEE*, 2009, pp. 1-3.
- [42] S. Chakraborty, M. Lukasiewicz, C. Buckl, S. Fahmy, C. Naehyuck, P. Sangyoung, *et al.*, "Embedded systems and software challenges in electric vehicles," in *Design, Automation & Test in Europe Conference & Exhibition (DATE), 2012*, 2012, pp. 424-429.
- [43] J. M. Miller, "Energy storage system technology challenges facing strong hybrid, plug-in and battery electric vehicles," in *Vehicle Power and Propulsion Conference, 2009. VPPC '09. IEEE*, 2009, pp. 4-10.
- [44] M. Lukasiewicz, S. Steinhorst, S. Andalam, F. Sagstetter, P. Waszecki, C. Wanli, *et al.*, "System architecture and software design for Electric Vehicles," in *Design Automation Conference (DAC), 2013 50th ACM / EDAC / IEEE*, 2013, pp. 1-6.
- [45] I. A. D. Laboratories. *Apex PM Brushless Motors [Online]*. Available: <http://www.apexdrivelabs.com/brushless-DC-motor-technology.html>.
- [46] F. Caricchi, F. Crescimbini, F. Mezzetti, and E. Santini, "Multistage axial-flux PM machine for wheel direct drive," *Industry Applications, IEEE Transactions on*, vol. 32, pp. 882-888, 1996.
- [47] C. Feng, X. Jing, G. Bin, and C. Shukang, "Double-Stator Permanent Magnet Synchronous In-Wheel Motor For Hybrid Electric Drive System," in *Electromagnetic Launch Technology, 2008 14th Symposium on*, 2008, pp. 1-5.
- [48] S. P. Enstroj. *EMRAX Motors [Online]*. Available: <http://www.enstroj.si/Electric-products/emrax-motors.html>.
- [49] W. Jiabin, K. Atallah, Z. Q. Zhu, and D. Howe, "Modular Three-Phase Permanent-Magnet Brushless Machines for In-Wheel Applications," *Vehicular Technology, IEEE Transactions on*, vol. 57, pp. 2714-2720, 2008.
- [50] K. M. Rahman, N. R. Patel, T. G. Ward, J. M. Nagashima, F. Caricchi, and F. Crescimbini, "Application of Direct-Drive Wheel Motor for Fuel Cell Electric and Hybrid Electric Vehicle Propulsion System," *Industry Applications, IEEE Transactions on*, vol. 42, pp. 1185-1192, 2006.

- [51] Y. Yee-Pien, L. Jia-Yuan, and X. Xian-Yee, "Design and application of axial-flux permanent magnet wheel motors for an electric vehicle," in *AFRICON, 2009. AFRICON '09.*, 2009, pp. 1-5.
- [52] D. Luque, E. Ruppert, N. Bianchi, and M. Castiello, "Analysis of a three-phase in-wheel electric motor," in *Universities Power Engineering Conference (UPEC), 2009 Proceedings of the 44th International*, 2009, pp. 1-5.
- [53] C. J. Ifedi, B. C. Mecrow, J. D. Widmer, G. J. Atkinson, S. T. M. Brockway, and D. Kostic-Perovic, "A high torque density, direct drive in-wheel motor for electric vehicles," in *Power Electronics, Machines and Drives (PEMD 2012), 6th IET International Conference on*, 2012, pp. 1-6.
- [54] I. Husain and M. S. Islam, "Design, Modeling and Simulation of an Electric Vehicle System," presented at the SAE Technical Paper, pp. 1-9, 1999.
- [55] Z. Q. Zhu and D. Howe, "Electrical Machines and Drives for Electric, Hybrid, and Fuel Cell Vehicles," *Proceedings of the IEEE*, vol. 95, pp. 746-765, 2007.
- [56] R. Sadoun, N. Rizoug, P. Bartholomeus, B. Barbedette, and P. Le Moigne, "Influence of the drive cycles on the sizing of hybrid storage system battery-supercapacitor supplying an electric vehicle," in *IECON 2011 - 37th Annual Conference on IEEE Industrial Electronics Society*, 2011, pp. 4106-4112.
- [57] S. L. T J Barlow, I S McCrae, P G Boulter, "A Reference Book of Driving Cycles for use in the Measurement of Road Vehicle Emissions [online]. available: <https://www.gov.uk/government/uploads/system/...dat>," ed, 2009.
- [58] J. D. Widmer and B. C. Mecrow, "Optimised Segmental Rotor Switched Reluctance Machines with a greater number of rotor segments than stator slots," in *Electric Machines & Drives Conference (IEMDC), 2011 IEEE International*, 2011, pp. 1183-1188.
- [59] J. Herbst, J. Hahne, H. Jordan, H. Liu, A. Gattozzi, and W. Ben, "Challenges in the design of a 100 kw induction motor for a PHEV application," in *Vehicle Power and Propulsion Conference, 2009. VPPC '09. IEEE*, 2009, pp. 408-413.
- [60] W. Tiecheng, Z. Ping, Z. Qianfan, and C. Shukang, "Design characteristics of the induction motor used for hybrid electric vehicle," *Magnetics, IEEE Transactions on*, vol. 41, pp. 505-508, 2005.
- [61] W. C. Lo, C. C. Chan, Z. Q. Zhu, X. Lie, D. Howe, and K. T. Chau, "Acoustic noise radiated by PWM-controllel induction machine drives," *Industrial Electronics, IEEE Transactions on*, vol. 47, pp. 880-889, 2000.
- [62] S. Z. Jiang, K. T. Chau, and C. C. Chan, "Spectral analysis of a new six-phase pole-changing induction motor drive for electric vehicles," *Industrial Electronics, IEEE Transactions on*, vol. 50, pp. 123-131, 2003.
- [63] P. C. Desai, M. Krishnamurthy, N. Schofield, and A. Emadi, "Novel Switched Reluctance Machine Configuration With Higher Number of Rotor Poles Than

- Stator Poles: Concept to Implementation," *Industrial Electronics, IEEE Transactions on*, vol. 57, pp. 649-659, 2010.
- [64] Y. J. Zhan, C. C. Chan, and K. T. Chau, "A novel sliding-mode observer for indirect position sensing of switched reluctance motor drives," *Industrial Electronics, IEEE Transactions on*, vol. 46, pp. 390-397, 1999.
- [65] R. B. Inderka, M. Menne, and R. W. A. A. De Doncker, "Control of switched reluctance drives for electric vehicle applications," *Industrial Electronics, IEEE Transactions on*, vol. 49, pp. 48-53, 2002.
- [66] K. M. Rahman, B. Fahimi, G. Suresh, A. V. Rajarathnam, and M. Ehsani, "Advantages of switched reluctance motor applications to EV and HEV: design and control issues," *Industry Applications, IEEE Transactions on*, vol. 36, pp. 111-121, 2000.
- [67] S. A. Long, Z. Q. Zhu, and D. Howe, "Effectiveness of active noise and vibration cancellation for switched reluctance machines operating under alternative control strategies," *Energy Conversion, IEEE Transactions on*, vol. 20, pp. 792-801, 2005.
- [68] N. Schofield and S. A. Long, "Generator operation of a switched reluctance starter/generator at extended speeds," in *Vehicle Power and Propulsion, 2005 IEEE Conference*, 2005, p. 8 pp.
- [69] T. M. Jahns, "Torque Production in Permanent-Magnet Synchronous Motor Drives with Rectangular Current Excitation," *Industry Applications, IEEE Transactions on*, vol. IA-20, pp. 803-813, 1984.
- [70] D. Ishak, Z. Q. Zhu, and D. Howe, "Permanent-magnet brushless machines with unequal tooth widths and similar slot and pole numbers," *Industry Applications, IEEE Transactions on*, vol. 41, pp. 584-590, 2005.
- [71] K. I. Laskaris and A. G. Kladas, "Internal Permanent Magnet Motor Design for Electric Vehicle Drive," *Industrial Electronics, IEEE Transactions on*, vol. 57, pp. 138-145, 2010.
- [72] L. Yuefeng, F. Liang, and T. A. Lipo, "A novel permanent magnet motor with doubly salient structure," in *Industry Applications Society Annual Meeting, 1992., Conference Record of the 1992 IEEE*, 1992, pp. 308-314 vol.1.
- [73] C. Ming, K. T. Chau, and C. C. Chan, "Static characteristics of a new doubly salient permanent magnet motor," *Energy Conversion, IEEE Transactions on*, vol. 16, pp. 20-25, 2001.
- [74] R. P. Deodhar, S. Andersson, I. Boldea, and T. J. E. Miller, "The flux-reversal machine: a new brushless doubly-salient permanent-magnet machine," *Industry Applications, IEEE Transactions on*, vol. 33, pp. 925-934, 1997.
- [75] C. Wang, S. A. Nasar, and I. Boldea, "Three-phase flux reversal machine (FRM)," *Electric Power Applications, IEE Proceedings -*, vol. 146, pp. 139-146,

1999.

- [76] E. Hoang, M. Gabsi, M. Lecrivain, and B. Multon, "Influence of magnetic losses on maximum power limits of synchronous permanent magnet drives in flux-weakening mode," in *Industry Applications Conference, 2000. Conference Record of the 2000 IEEE*, 2000, pp. 299-303 vol.1.
- [77] A. Zulu, B. C. Mecrow, and M. Armstrong, "A Wound-Field Three-Phase Flux-Switching Synchronous Motor With All Excitation Sources on the Stator," *Industry Applications, IEEE Transactions on*, vol. 46, pp. 2363-2371, 2010.
- [78] W. Hua, Z. Q. Zhu, M. Cheng, Y. Pang, and D. Howe, "Comparison of flux-switching and doubly-salient permanent magnet brushless machines," in *Electrical Machines and Systems, 2005. ICEMS 2005. Proceedings of the Eighth International Conference on*, 2005, pp. 165-170 Vol. 1.
- [79] A. S. Thomas, Z. Q. Zhu, R. L. Owen, G. W. Jewell, and D. Howe, "Multiphase Flux-Switching Permanent-Magnet Brushless Machine for Aerospace Application," *Industry Applications, IEEE Transactions on*, vol. 45, pp. 1971-1981, 2009.
- [80] F. Profumo, Z. Zheng, and A. Tenconi, "Axial flux machines drives: a new viable solution for electric cars," in *Industrial Electronics, Control, and Instrumentation, 1996., Proceedings of the 1996 IEEE IECON 22nd International Conference on*, 1996, pp. 34-40 vol.1.
- [81] P. R. Upadhyay and K. R. Rajagopal, "Comparison of performance of the axial-field and radial-field permanent magnet brushless direct current motors using computer aided design and finite element methods," *Journal of Applied Physics*, vol. 97, pp. 10Q506-10Q506-3, 2005.
- [82] T. J. Woolmer and M. D. McCulloch, "Axial flux permanent magnet machines: A new topology for high performance applications," in *Hybrid Vehicle Conference (Conf. Pub. CP526), IET*, 2006, pp. 27-42.
- [83] T. J. Woolmer and M. D. McCulloch, "Analysis of the Yokeless And Segmented Armature Machine," in *Electric Machines & Drives Conference, 2007. IEMDC '07. IEEE International*, 2007, pp. 704-708.
- [84] S. L. Ho, N. Shuangxia, and W. N. Fu, "Design and Analysis of a Novel Axial-Flux Electric Machine," *Magnetics, IEEE Transactions on*, vol. 47, pp. 4368-4371, 2011.
- [85] C. C. Chan, K. T. Chau, J. Z. Jiang, W. Xia, M. Zhu, and R. Zhang, "Novel permanent magnet motor drives for electric vehicles," *Industrial Electronics, IEEE Transactions on*, vol. 43, pp. 331-339, 1996.
- [86] S. Baserrah, K. Rixen, and B. Orlik, "Transverse flux machines with distributed windings for in-wheel applications," in *Power Electronics and Drive Systems, 2009. PEDS 2009. International Conference on*, 2009, pp. 102-108.

- [87] G. Youguang, Z. Jian Guo, P. A. Watterson, and W. Wei, "Development of a PM transverse flux motor with soft magnetic composite core," *Energy Conversion, IEEE Transactions on*, vol. 21, pp. 426-434, 2006.
- [88] J. G. Washington, G. J. Atkinson, N. J. Baker, A. G. Jack, B. C. Mecrow, B. B. Jensen, *et al.*, "Three-Phase Modulated Pole Machine Topologies Utilizing Mutual Flux Paths," *Energy Conversion, IEEE Transactions on*, vol. 27, pp. 507-515, 2012.
- [89] Z. Q. Zhu, Y. Pang, D. Howe, S. Iwasaki, R. Deodhar, and A. Pride, "Analysis of electromagnetic performance of flux-switching permanent-magnet Machines by nonlinear adaptive lumped parameter magnetic circuit model," *Magnetics, IEEE Transactions on*, vol. 41, pp. 4277-4287, 2005.
- [90] M. R. Harris and B. C. Mecrow, "Variable reluctance permanent magnet motors for high specific output," in *Electrical Machines and Drives, 1993. Sixth International Conference on (Conf. Publ. No. 376)*, 1993, pp. 437-442.
- [91] M. R. Harris, G. H. Pajooman, and S. M. A. Sharkh, "Comparison of alternative topologies for VRPM (transverse-flux) electrical machines," in *New Topologies for Permanent Magnet Machines (Digest No: 1997/090), IEE Colloquium on*, 1997, pp. 2/1-2/7.
- [92] G. Henneberger and M. Bork, "Development of a new transverse flux motor," in *New Topologies for Permanent Magnet Machines (Digest No: 1997/090), IEE Colloquium on*, 1997, pp. 1/1-1/6.
- [93] M. R. Harris, G. H. Pajooman, and S. M. Abu Sharkh, "The problem of power factor in VRPM (transverse-flux) machines," in *Electrical Machines and Drives, 1997 Eighth International Conference on (Conf. Publ. No. 444)*, 1997, pp. 386-390.
- [94] Y. Zhao and J. Chai, "Power factor analysis of transverse flux permanent machines," in *Electrical Machines and Systems, 2005. ICEMS 2005. Proceedings of the Eighth International Conference on*, 2005, pp. 450-459 Vol. 1.
- [95] Z. Rahman, "Evaluating radial, axial and transverse flux topologies for 'in-wheel' motor," in *Power Electronics in Transportation, 2004*, 2004, pp. 75-81.
- [96] C. Anyuan, R. Nilssen, and A. Nysveen, "Performance Comparisons Among Radial-Flux, Multistage Axial-Flux, and Three-Phase Transverse-Flux PM Machines for Downhole Applications," *Industry Applications, IEEE Transactions on*, vol. 46, pp. 779-789, 2010.
- [97] K. Sitapati and R. Krishnan, "Performance comparisons of radial and axial field, permanent magnet, brushless machines," in *Industry Applications Conference, 2000. Conference Record of the 2000 IEEE*, 2000, pp. 228-234 vol.1.
- [98] N. Kim, A. Rousseau, and E. Rask, "Vehicle-Level Control Analysis of 2010 Toyota Prius Based on Test Data," *Journal Name: Proceedings of the Institution*

- of Mechanical Engineers, Part D: Journal of Automobile Engineering; Journal Volume: 226; Journal Issue: 11 ; Nov. 1, 2012, pp. Medium: X; Size: 1483-1494, 2012.*
- [99] T. A. Burrell, C. L. Coomer, S. L. Campbell, L. E. Seiber, L. D. Marlino, R. H. Staunton, *et al.*, "Evaluation of the 2007 Toyota Camry Hybrid Syneregy Drive System," ORNL/TM-2007/190, Revised United States10.2172/928684Thu Jun 05 09:21:36 EDT 2008ORNLEnglish, 2008.
 - [100] D. G. Dorrell, M. Popescu, L. Evans, D. A. Staton, and A. M. Knight, "Comparison of permanent magnet drive motor with a cage induction motor design for a hybrid electric vehicle," in *Power Electronics Conference (IPEC), 2010 International*, 2010, pp. 1807-1813.
 - [101] D. G. Dorrell, M. Popescu, L. Evans, D. A. Staton, and A. M. Knight, "Modern electrical machine analysis and design techniques applied to hybrid vehicle drive machines," in *Industrial Electronics (ISIE), 2010 IEEE International Symposium on*, 2010, pp. 3728-3733.
 - [102] D. G. Dorrell, A. M. Knight, M. Popescu, L. Evans, and D. A. Staton, "Comparison of different motor design drives for hybrid electric vehicles," in *Energy Conversion Congress and Exposition (ECCE), 2010 IEEE*, 2010, pp. 3352-3359.
 - [103] C. Sanabria-Walter, H. Polinder, J. A. Ferreira, P. Janker, and M. Hofmann, "Torque enhanced Flux-Switching PM machine for aerospace applications," in *Electrical Machines (ICEM), 2012 XXth International Conference on*, 2012, pp. 2585-2595.
 - [104] C. Sanabria-Walter, H. Polinder, and J. A. Ferreira, "High-Torque-Density High-Efficiency Flux-Switching PM Machine for Aerospace Applications," *Emerging and Selected Topics in Power Electronics, IEEE Journal of*, vol. 1, pp. 327-336, 2013.
 - [105] F. Caricchi, F. Crescimbeni, E. Santini, and L. Solero, "High-efficiency low-volume starter/alternator for automotive applications," in *Industry Applications Conference, 2000. Conference Record of the 2000 IEEE*, 2000, pp. 215-222 vol.1.
 - [106] Y. Ming, L. Gengyin, Z. Ming, and Z. Chengyong, "Modeling of the Wind Turbine with a Permanent Magnet Synchronous Generator for Integration," in *Power Engineering Society General Meeting, 2007. IEEE*, 2007, pp. 1-6.
 - [107] F. B. Chaaban, T. S. Birch, D. Howe, and P. H. Mellor, "Topologies for a permanent magnet generator/speed sensor for the ABS on railway freight vehicles," in *Electrical Machines and Drives, 1991. Fifth International Conference on (Conf. Publ. No. 341)*, 1991, pp. 31-35.
 - [108] Y. Honda, T. Higaki, S. Morimoto, and Y. Takeda, "Rotor design optimisation of a multi-layer interior permanent-magnet synchronous motor," *Electric Power Applications, IEE Proceedings -*, vol. 145, pp. 119-124, 1998.

- [109] F. Leonardi, T. Matsuo, Y. Li, T. A. Lipo, and P. McCleer, "Design considerations and test results for a doubly salient PM motor with flux control," in *Industry Applications Conference, 1996. Thirty-First IAS Annual Meeting, IAS '96., Conference Record of the 1996 IEEE*, 1996, pp. 458-463 vol.1.
- [110] J. Parrish, S. Moll, and R. C. Schaefer, "Plant efficiencies benefit by selection of synchronous motor," in *Pulp and Paper Industry Technical Conference, 2005. Conference Record of 2005 Annual*, 2005, pp. 71-80.
- [111] H. Hayashi, K. Nakamura, A. Chiba, T. Fukao, K. Tungpimolrut, and D. G. Dorrell, "Efficiency Improvements of Switched Reluctance Motors With High-Quality Iron Steel and Enhanced Conductor Slot Fill," *Energy Conversion, IEEE Transactions on*, vol. 24, pp. 819-825, 2009.
- [112] H. Hayashi, A. Chiba, and T. Fukao, "Efficiency Comparison of Switched Reluctance Motors with Low Loss Materials," in *Power Engineering Society General Meeting, 2007. IEEE*, 2007, pp. 1-6.
- [113] J. L. Kirtley, Jr., J. G. Cowie, E. F. Brush, D. T. Peters, and R. Kimmich, "Improving Induction Motor Efficiency with Die-cast Copper Rotor Cages," in *Power Engineering Society General Meeting, 2007. IEEE*, 2007, pp. 1-6.
- [114] K. Young-Gook, B. Chae-Bong, K. Jang-Mok, and K. Hyun-Cheol, "Efficiency improvement by changeover of phase windings of multiphase permanent magnet synchronous motor with outer-rotor type," in *Applied Power Electronics Conference and Exposition (APEC), 2010 Twenty-Fifth Annual IEEE*, 2010, pp. 112-119.
- [115] L. Dong-Yeup, J. Chun-Gil, Y. Kang-Jun, and K. Gyu-Tak, "A study on the efficiency optimum design of a permanent magnet type linear synchronous motor," *Magnetics, IEEE Transactions on*, vol. 41, pp. 1860-1863, 2005.
- [116] P. H. Mellor, R. Wrobel, N. McNeill, and D. Drury, "Impact of winding and rotor design on efficiency and torque ripple in brushless AC permanent magnet traction motors," in *Power Electronics, Machines and Drives, 2008. PEMD 2008. 4th IET Conference on*, 2008, pp. 240-244.
- [117] M. Sanada and S. Morimoto, "Efficiency Improvement in High Speed Operation using Slot-less Configuration for Permanent Magnet Synchronous Motor," in *Power Engineering Society General Meeting, 2007. IEEE*, 2007, pp. 1-7.
- [118] K. Atallah, S. Calverley, R. Clark, J. Rens, and D. Howe, "A new PM machine topology for low-speed, high-torque drives," in *Electrical Machines, 2008. ICEM 2008. 18th International Conference on*, 2008, pp. 1-4.
- [119] p. a. N. 9001604, "Doubly Excited Synchronous Electrical Machine Arrangments ".
- [120] H. Weh and H. May, "Achievable Force Densities for Permanent Magnet Excited Machines in New Configurations " presented at the ICEM 86, pp. 1107-1111.

- [121] H. Weh, H Hoffmann, and J. Landrath, "New Permanent Magnet Excited Synchronous Machine with High Efficiency at Low Speeds " presented at the ICEM 88, vol 3, pp.35-40.
- [122] M R Harris and T. J. E. Miller, "Comparison of Design and Performance Parameters in Switch Reluctance and Induction Motors " presented at the IEE fourth International Conference on Electrical Machines and Drives, 1989, pp 303-307. .
- [123] Y. D. Yao, D. R. Huang, S. M. Lin, and S. J. Wang, "Theoretical computations of the magnetic coupling between magnetic gears," *Magnetics, IEEE Transactions on*, vol. 32, pp. 710-713, 1996.
- [124] P. O. Rasmussen, T. O. Andersen, F. T. Joergensen, and O. Nielsen, "Development of a high performance magnetic gear," in *Industry Applications Conference, 2003. 38th IAS Annual Meeting. Conference Record of the*, 2003, pp. 1696-1702 vol.3.
- [125] C. Mu, K. T. Chau, L. Wenlong, L. Chunhua, and Q. Chun, "Design and Analysis of a New Magnetic Gear With Multiple Gear Ratios," *Applied Superconductivity, IEEE Transactions on*, vol. 24, pp. 1-4, 2014.
- [126] K. T. Chau, Z. Dong, J. Z. Jiang, L. Chunhua, and Z. Yuejin, "Design of a Magnetic-Geared Outer-Rotor Permanent-Magnet Brushless Motor for Electric Vehicles," *Magnetics, IEEE Transactions on*, vol. 43, pp. 2504-2506, 2007.
- [127] X. Li, K. T. Chau, M. Cheng, and W. Hua, "Comparison of magnetic-geared permanent-magnet machines," *Progr. Electromagn. Res.*, vol. 133, pp. 177–198, 2013.
- [128] A. Emadi, *Handbook of Automotive Power Electronics and Motor Drives*: Taylor & Francis, 2005.
- [129] L. Chunhua, K. T. Chau, and Z. Zhen, "Novel Design of Double-Stator Single-Rotor Magnetic-Geared Machines," *Magnetics, IEEE Transactions on*, vol. 48, pp. 4180-4183, 2012.
- [130] S. Niu, K. T. Chau, J. Z. Jiang, and L. Chunhua, "Design and Control of a New Double-Stator Cup-Rotor Permanent-Magnet Machine for Wind Power Generation," *Magnetics, IEEE Transactions on*, vol. 43, pp. 2501-2503, 2007.
- [131] S. Niu, K. T. Chau, and J. Z. Jiang, "A Permanent-magnet double-stator integrated-starter-generator for hybrid electric vehicles," in *Vehicle Power and Propulsion Conference, 2008. VPPC '08. IEEE*, 2008, pp. 1-6.
- [132] Z. Dong, S. Niu, K. T. Chau, J. Z. Jiang, and G. Yu, "Design and Analysis of a Double-Stator Cup-Rotor Directly Driven Permanent Magnet Wind Power Generator," in *Power Electronics and Motion Control Conference, 2006. IPEMC 2006. CES/IEEE 5th International*, 2006, pp. 1-5.

- [133] Z. Dong, K. T. Chau, S. Niu, and J. Z. Jiang, "Design and Analysis of a Double-Stator Cup-Rotor PM Integrated-Starter-Generator," in *Industry Applications Conference, 2006. 41st IAS Annual Meeting. Conference Record of the 2006 IEEE*, 2006, pp. 20-26.
- [134] N. Bianchi, S. Bolognani, and M. Dai Pre, "Magnetic loading of fractional-slot three phase PM motors with non-overlapped coils," in *Industry Applications Conference, 2006. 41st IAS Annual Meeting. Conference Record of the 2006 IEEE*, 2006, pp. 35-43.
- [135] N. Bianchi, Pre, x, M. D., G. Grezzani, and S. Bolognani, "Design considerations on fractional-slot fault-tolerant synchronous motors," in *Electric Machines and Drives, 2005 IEEE International Conference on*, 2005, pp. 902-909.
- [136] Z. Q. Zhu and D. Howe, "Influence of design parameters on cogging torque in permanent magnet machines," *Energy Conversion, IEEE Transactions on*, vol. 15, pp. 407-412, 2000.
- [137] J. S. Hsu, B. P. Scoggins, M. B. Scudiere, L. D. Marlino, D. J. Adams, and P. Pillay, "Nature and assessments of torque ripples of permanent-magnet adjustable-speed motors," in *Industry Applications Conference, 1995. Thirtieth IAS Annual Meeting, IAS '95., Conference Record of the 1995 IEEE*, 1995, pp. 2696-2702 vol.3.
- [138] F. Sahin, H. B. Ertan, and K. Leblebicioglu, "Optimum geometry for torque ripple minimization of switched reluctance motors," *Energy Conversion, IEEE Transactions on*, vol. 15, pp. 30-39, 2000.
- [139] J. Seok-Myeong, P. Hyung-Il, C. Jang-Young, K. Kyoung-Jin, and L. Sung-Ho, "Magnet Pole Shape Design of Permanent Magnet Machine for Minimization of Torque Ripple Based on Electromagnetic Field Theory," *Magnetics, IEEE Transactions on*, vol. 47, pp. 3586-3589, 2011.
- [140] A. M. T. N.-I.-B. M. C.-N. S. O. A. http://www.arnoldmagnetics.com/Neodymium_Literature.aspx. [Online].
- [141] W. Shihua, T. Likun, and C. Shumei, "A comparative study of the interior permanent magnet electrical machine's rotor configurations for a single shaft hybrid electric bus," in *Vehicle Power and Propulsion Conference, 2008. VPPC '08. IEEE*, 2008, pp. 1-4.
- [142] P. B. Reddy, T. M. Jahns, P. J. McCleer, and T. P. Bohn, "Design, analysis and fabrication of a high-performance fractional-slot concentrated winding surface PM machine," in *Energy Conversion Congress and Exposition (ECCE), 2010 IEEE*, 2010, pp. 1074-1081.
- [143] P. B. Reddy, A. M. El-Refaie, and H. Kum-Kang, "Effect of number of layers on performance of fractional-slot concentrated-windings interior permanent magnet machines," in *Power Electronics and ECCE Asia (ICPE & ECCE), 2011 IEEE 8th International Conference on*, 2011, pp. 1921-1928.

- [144] S. Tao, K. Ji-Min, L. Geun-Ho, H. Jung-Pyo, and C. Myung-Ryul, "Effect of Pole and Slot Combination on Noise and Vibration in Permanent Magnet Synchronous Motor," *Magnetics, IEEE Transactions on*, vol. 47, pp. 1038-1041, 2011.

Appendix A: Principles of PM Machine Design

A.1. Magnetic Loading

The magnetic loading can be expressed as the peak radial flux density in the air gap of a machine with a symbol (B_{gmax}).

Magnetic loading is proportional to the flux density of the air gap and magnet span; however it is limited by the saturation in stator teeth, and hence by the saturation flux density of the material used for the stator.

Magnet location can affect the amount of flux density in the air gap and table D1 shows the relation between magnet residual flux density (B_o) and air gap flux density (B_g) for different magnet locations.

Magnet location	Surface mounted magnets	Inset magnets	Buried magnets	Flux concentration Magnets
Air gap flux density	$B_g < B_o$	$B_g < B_o$	$B_g < B_o$	$B_g > B_o$

Table A2. Air Gap Flux Density at Different Magnet Locations.

Table D1 shows that the flux density in the air gap is smaller than the residual flux density of the magnets in all cases apart from the flux concentration topology.

A.2. Electrical Loading

The electric loading of a machine is the RMS current per unit length of periphery; the following equation can be used to calculate the electric loading of a machine.

$$A = \frac{2SNI}{\pi D} \quad 3.4$$

Where A is the electric loading, 2 is to represent the two sides of any coil, S is the number of slots, N is the number of turns, I is the RMS current applied to the machine and D is the diameter of the machine at the centre of the air gap.

In order to increase the electrical loading of a machine, more current should be applied. There are a few different ways to do this such as:

- Increasing the slot depth for the same current density. However, this will lead to

an increased outer diameter if the core back depth is kept constant, the leakage inductance will also be increased in the slot.

- Making the slot wider for the same current density, this will lead to a reduced magnetic loading as a result of making the tooth narrower.
- Increasing the current density, which will increase the I^2R losses this means an improved cooling method should be applied.

Increasing the current density has two negative effects, the end winding is going to have higher forces acting on it and the other is associated with increased stator leakage fields as a result of a higher stray losses. These effects can be of a great importance when it comes to the design of large machines and less important for designing small machines.

A.3. Magnet Operating Point

By finding the magnet operating point the magnet length and air gap length can be calculated for a specific machine size.

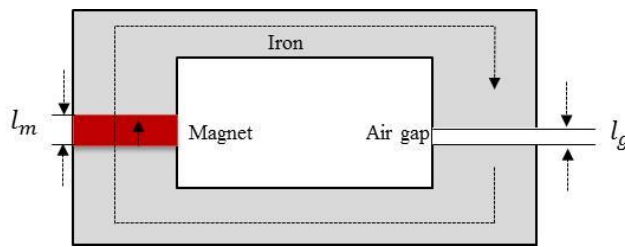


Figure A3. Iron Circuit with Magnet.

Figure A1 above shows an iron core with a magnet length of l_m , a cross sectional area of A_m and an air gap length of l_g with a cross sectional area of A_g . By assuming the iron is infinity permeable ($H=0$) and by performing a closed loop where ampere's circuital law is applied around the iron path ($\oint H_t dl = 0$), the following equation results:

$$H_m L_m + H_g L_g = 0 \quad A1$$

Where H_m , and H_g , are the iron and air magnetic field strength respectively, also H_g can be found as:

$$H_g = \frac{B_g}{\mu_o} \quad A2$$

By rearranging Equation A1 and A2 it's possible to find H_m as follows:

$$H_m = \frac{-l_g H_g}{l_m} = \frac{-l_g B_g}{l_m \mu_o} \quad A3$$

μ_o , is the permeability of free space and B_g is the air gap flux density (magnetic loading) in the air gap which is 70 % of the residual flux density of the magnet in most

cases. For simplicity by considering no leakage flux is present the following can be assumed:

$$B_m A_m + B_g A_g = 0 \quad \text{A4}$$

B_m , is the flux density of the magnet. And by taking A4 into account, Equation A3 can be rearranged as follows:

$$H_m = \left[\frac{-l_g}{l_m} \frac{A_m}{A_g} \frac{B_m}{\mu_o} \right] \quad \text{A5}$$

In order to find the operating point a plot of a load line on the B-H characteristic is drawn using Equation A5 along with a neodymium-iron boron magnet characteristic line as shown in Figure A2 below:

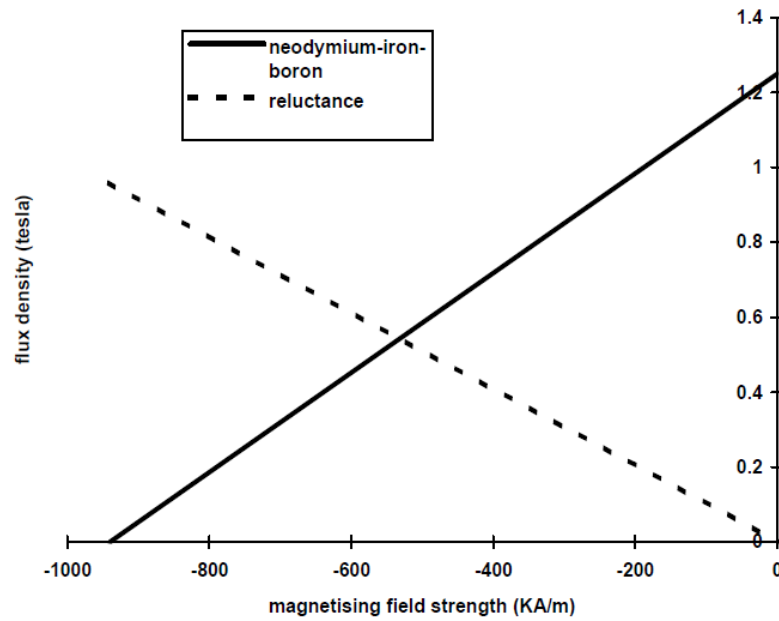


Figure A4. Magnet Operating Point.

From Figure A2 the operating point is the crossing point. By assuming the magnet and load lines are linear then the operating point can be calculated:

$$B_m = B_o + \mu_m H_m \quad \text{A6}$$

Then by substituting A5 into A6 the magnet operating point is calculated as followed

$$B_m = \frac{B_o}{1 + \frac{l_g A_m \mu_m}{l_m A_g \mu_o}} \quad \text{A7}$$

B_o , is the residual flux density of the magnets and μ_m is the permeability of the magnet.

A.4. Winding Arrangements

The arrangement of the winding in the machine plays a significant role when it comes to

the machine's performance, the magnetomotive force (MMF) and generated voltage's amplitude and waveform shape is determined by the arrangement of the windings. They can also have an impact on several factors such as the machine speed range by considering the limited supplied voltage from the inverter, the output torque as its proportional to the MMF that is applied to the windings, the weight of the machine, and the air gap harmonic distortion. Windings can be of two basic types, single tooth winding or distributed type where the former is increasingly used in permanent magnet machines for its short end windings and simplicity whilst the latter, used to obtain better reluctance torque and an induced voltage of near sinusoidal varying. However, distributed winding increases the machines' copper loss and weight [141]. The basic winding configurations can be also broken to different types as shown in the following [142-144]:

- Single layer winding where each slot contains one half of the coil.
- Double layer winding where each slot contains one half of two coils.
- Fractional slot winding where each slot contains any number of coils and different number of turns and the slot per pole per phase (SPP) is not an integer.
- Concentrated winding where each phase wound in a concentrated manner.

From above the double layer type is used in most machines over a few kilowatts (kW) and is the most common used type as it has a simple layout. When there are a few slots per pole a fractional slot winding is used while concentrated winding is used mostly in small machines and turbo generators' rotors. When considering winding arrangements it's very important to take into account the pitch factor of the specific arrangement, this is defined as the angle between two sides of a coil of a phase. When there are 180° electrical between two sides of a coil it is called a fully pitched winding. When the angle between the two sides is reduced to less than 180° electrical the coils are considered to be short pitched coil by a pitch angle (α). Figure A3 below shows α and the vector diagram when there is a short pitched coil. Where V_1 , V_2 is the voltages generated in each side of a coil and V_c is the coil resulted voltage.

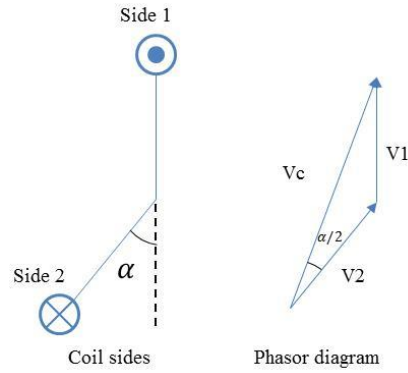


Figure A5. Pitch Angle (α) and Phasor Diagram of a Short Pitched Coil of Two Sides.

The above vector diagram illustrates that the resulted voltage in a short pitched coil is.

$$V_c = (V_1 + V_2) \times \cos\left(\frac{\alpha}{2}\right) \quad \text{A8}$$

Short pitched coils shorten the end windings and hence minimise its losses and also decrease the induced voltage harmonics.

While the distributed angle (β) can be shown in Figure A4, this is the angle between the coils that represent one phase.

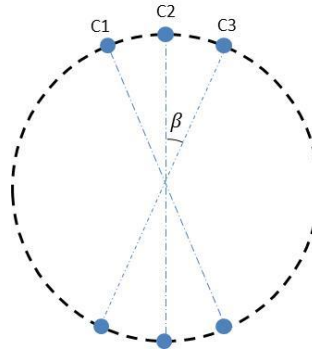


Figure A6. Distribution Angle (β) Between Two Coils of the Same Phase.

Figure A4 shows the distributed angle between coils C1 C2, C3 that make up one phase. The spatial harmonics in the air gap can be affected by the windings layout, dependent on the phase angle span between winding coils of one phase and their distribution. The following Equations A9, A10, A11 show the pitch factor, distribution factor and winding factor for m harmonic number respectively.

$$kP_m = \cos\left(\frac{m\alpha}{2}\right) \quad \text{A9}$$

$$kd_m = \frac{\sin\left(\frac{mn\beta}{2}\right)}{n \sin\left(\frac{mn\beta}{2}\right)} \quad \text{A10}$$

$$kw = kP_m \times kd_m \quad \text{A11}$$

k_p , is the pitch factor, kd is the distribution factor, kw is the winding factor, α is the

pitch angle, β is the distribution angle and n is the number of coils per phase.

A.5. Initial PM Machines Physical Dimension Calculation

A.5.1. Number of Poles

The number of poles and the electrical frequency of a machine are directly proportional while the number of poles is inversely proportional to the synchronous speed of the machine and the following highlights some of the advantages of a high pole number:

- Increasing the pole number will reduce the flux per pole, meaning a reduced size of stator and rotor core back is required.
- Reduced copper loss, as pole number is inversely proportional to the end-winding length; hence increasing the number of poles will reduce the amount of copper used.

There are also disadvantages of having a high pole number such as:

- A higher electrical frequency for a given speed results, which will require an increased switching speed from the inverter that will increase the switching losses and may require more expensive power electronics.
- Iron loss in the lamination is mainly caused by hysteresis and eddy currents. Both increase with frequency, hence increased iron loss results from a high pole number.

The equation to calculate the pole number is as shown in the following:

$$p = \frac{f}{N_s} \quad A12$$

p , is the number of pole pairs, f is the supply frequency in Hertz and N_s is the synchronous speed in rev/sec.

A.5.2. Number of Teeth and Slots

The number of slots has to be chosen in order to insure the correct electrical phase shift between phases, for example 120° electrical between phases in a three phase machine.

The following are the basic formulas to calculate the number of both slots and teeth;

$$SN = PN \times p \quad A13$$

$$TN = SN \quad A14$$

SN , is the number of slots, PN is the number of phases and TN is the number of teeth.

A.5.3. Permanent Magnet Depth and Span

The mass of permanent magnet used in the machine should be minimised in order to reduce cost their size also needs to be such that they aren't demagnetised by the armature reaction field. In order to calculate the magnet depth Equation A7 above can be rearranged to find l_m . The magnet span is usually chosen to be between 120° and 180° electrical, this choice reflects in the fundamental air gap flux density, which has a magnitude that can be found using the following equation, ignoring any effects by the leakage flux for simplicity:

$$B_{g \text{ fundamental}} = \frac{4}{\pi} B_g \sin(\alpha_m/2) \quad A15$$

$B_{g \text{ fundamental}}$, is the fundamental air gap flux density and α_m is the magnet span. From Equation A15 above it can be seen that any increase in the magnet span above the 120° electrical will only result in up to 15% increase in the $B_{g \text{ fundamental}}$. On the other hand increasing α will increase magnet volume and hence price. So careful consideration must be taken when choosing a magnet span (where a typical span of 140-160 is widely used depending on the application), it's also important to note that the magnetic loading is equal to the product of B_g and $\sin(\alpha_m/2)$.

A.5.4. Tooth and Slot Widths

The tooth width of any machine must not be highly saturated before its rated performance. This should be taken into account when a tooth width is to be chosen. The wider the slot width the more electric loading can be applied to that machine. However, a compromise between tooth and slot widths is essential in order to prevent saturation in the tooth whilst having the required electric loading applied. The following formula shows how to calculate the total pitch that a tooth and slot can fit into of a machine:

$$w_{\text{pitch}} = \frac{\pi(Dr + 2lg + 2lm)}{\text{number of slots}} \quad A16$$

w_{pitch} , is the total pitch that a tooth and slot can fit into, Dr is the outer diameter of the rotor. After finding w_{pitch} using Equation A16 and by assuming that the product of the iron width and the flux density of the iron are equal to the product of the slot width and the flux density in the air gap, the tooth width can be calculated as follows.

$$w_t = \frac{w_{\text{pitch}} \times B_g}{B_{\text{iron}}} \quad A17$$

w_t , is the tooth width and B_{iron} is the flux density in the stator iron. After finding w_t , the slot width, w_s , can be calculated by using:

$$w_s = w_{\text{spitch}} - w_t \quad A18$$

A.5.5. Slots Depth

The choice of the slot depth and the tooth depth for the machine take place by using a number of formulas as described in the following;

$$d_s = \frac{A_s}{w_s} \quad A19$$

d_s , is the slot depth and A_s is the slot area, which can be calculated as follows:

$$A_s = \frac{(\text{copper in slot})}{\text{ff}} \quad A20$$

ff, is the fill factor and the copper in the slot can be calculated as follows:

$$\left(\frac{\text{copper in slot}}{\text{slot}} \right) = A_{\text{conductor}} \times \left(\frac{\text{number of conductor for each slot}}{\text{each slot}} \right) \quad A21$$

$A_{\text{conductor}}$, is the area of each conductor and can be calculated as follows;

$$A_{\text{conductor}} = \frac{I_{\text{prms}}}{\text{current density}} \quad A22$$

I_{prms} is the RMS current per phase. Also the number of conductors in each slot can be calculated as follows;

$$\left(\frac{\text{number of conductors}}{\text{perslot}} \right) = \frac{\left(\frac{\text{number of phases}}{\text{phases}} \right) \times N \times \left(\frac{\text{number of coils}}{\text{perslot}} \right)}{\left(\frac{\text{number of slots}}{\text{slots}} \right)} \quad A23$$

A.5.6. Stator Core Back Depth

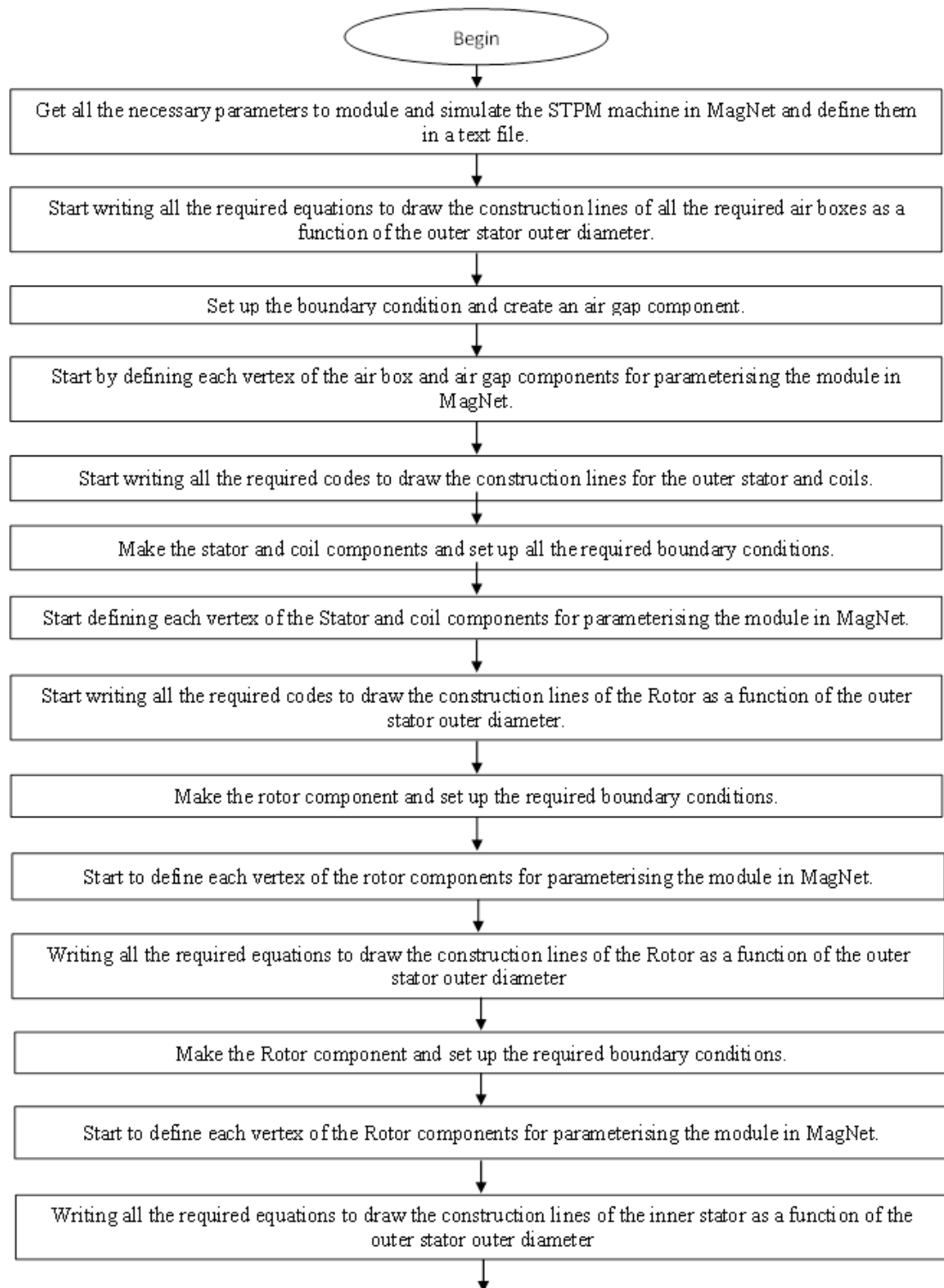
The core back of the stator will in most cases carry half of the flux that is generated in a single tooth; hence the core back depth can be calculated as:

$$d_{\text{scb}} = 0.5 w_t \quad A24$$

d_{scb} , is the core back depth of the stator.

Appendix B: Design Optimisation

The flow sequence in which the visual basic (VB) script was created in order to create and parameterise the STPM machine with concentrated magnets in MagNet software is in the diagram shown in Figure 5.4.



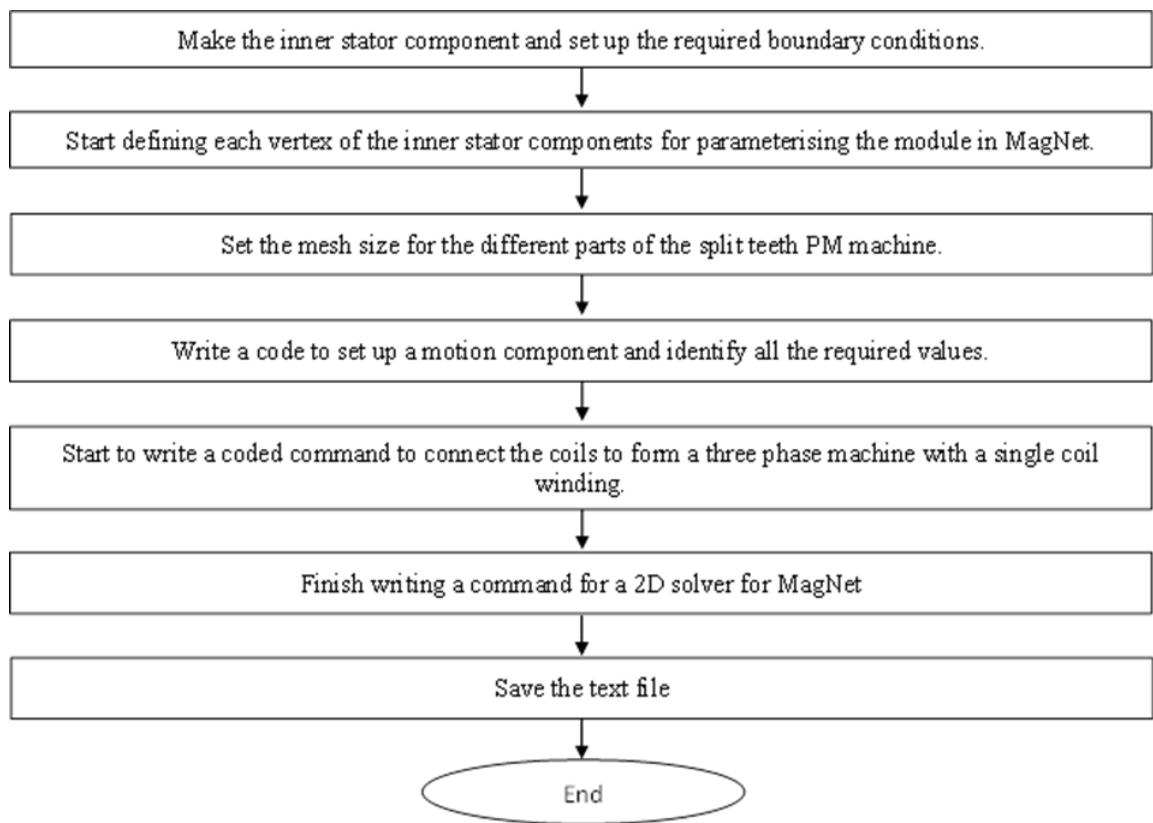


Figure A7. Flow Diagram Representation for the VB Script.

Appendix C: Investigative Design

The Torque Waveforms obtained at 15 A/mm², calculated mean torque and torque ripples, mass, torque density obtained through the 2D FE analyses during investigating the impact of different variable on torque density in Chapter 7 are shown here.

C.1 Outer Stator Impact on Torque Density

C.1.1. Tooth Body Width and Slot Depth

Table A3. Torque, Mass and Torque Density for Various Tooth Body Widths and Slot Depths at 15 A/mm²

Tooth Body Width			
Width (mm)/ Depth (mm)	Torque(Nm)	Mass (kg)	Torque Density (Nm/kg)
4	153.4	18.9	8.1
8	198.1	19.3	10.2
12	233.5	19.7	11.8
16	253.8	20.1	12.6
20	240.6	20.4	11.7
24	213.4	20.8	10.2
Slot Depth			
4	127.1	19.0	6.7
8	215.4	19.6	11.0
12	253.8	20.2	12.5
16	248.2	20.7	12.0
20	223.4	21.1	10.6

C.1.2. Coreback Depth

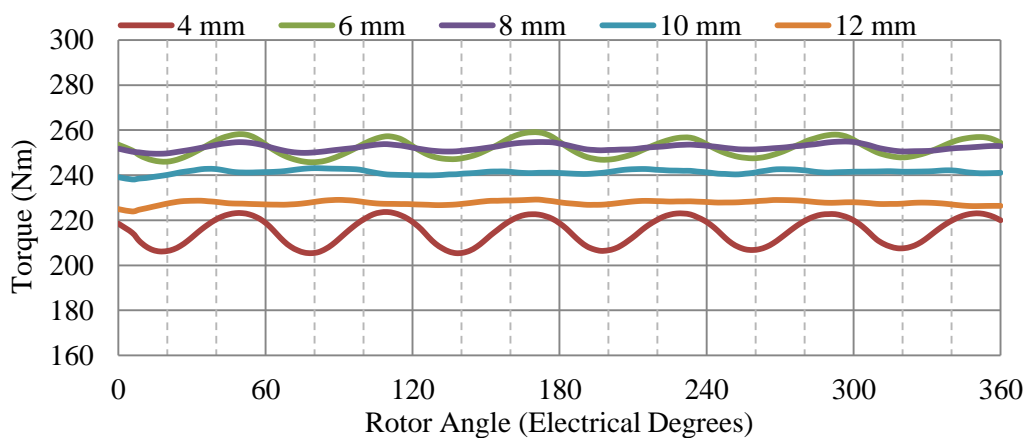


Figure A8. Torque Waveforms at 15 A/mm² Applied Current Density for Various Coreback Depths.

Table A4. Torque, Mass, Torque Density and Torque Ripple for Various Coreback Depths at 15 A/mm².

Coreback Depth (mm)	Torque (Nm)	Mass (kg)	Torque Density (Nm/kg)	Torque Ripple
4	142.4	18.5	7.7	8.2%
6	214.5	19.0	11.3	5.1%
8	245.8	19.8	12.4	2.1%
10	253.8	20.1	12.6	2.1%
12	240.6	20.5	11.8	2.3%

C.1.3. Slot Opening Width

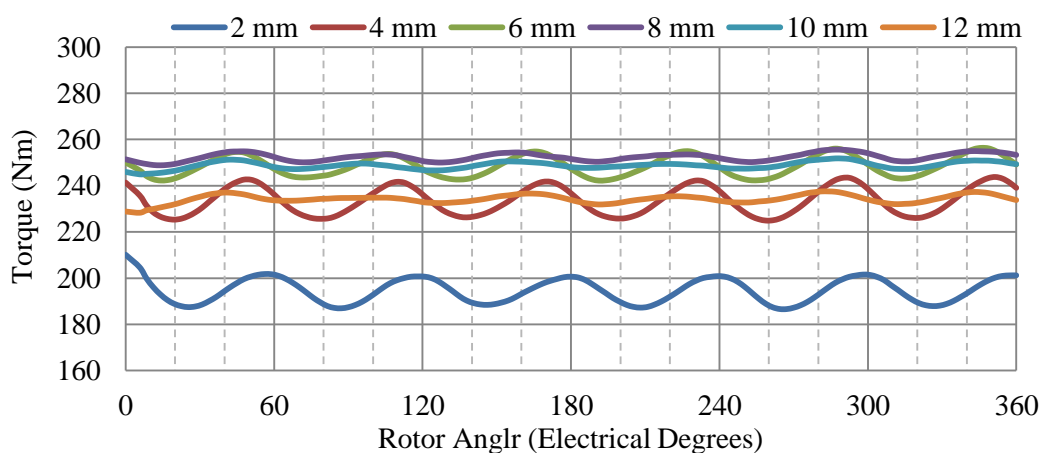


Figure A9. Torque Waveforms at 15 A/mm² Applied Current Density for Various Slot Opening Widths.

Table A5. Torque, Mass, Torque Density and Torque Ripple for Various Slot Opening Widths at 15 A/mm².

Slot Opening Widths (mm)	Slot Opening Span (Degrees)	Torque (Nm)	Mass (kg)	Torque Density (Nm/kg)	Torque Ripple
2	0.51	198.4	20.5	9.7	11%
4	2.07	234.4	20.4	11.5	8%
6	3.64	249.3	20.3	12.3	6%
8	5.23	253.8	20.1	12.6	3%
10	6.76	248.4	20.1	12.4	3%
12	8.33	232.9	20.0	11.7	4%

C.1.4. Tooth Split Width

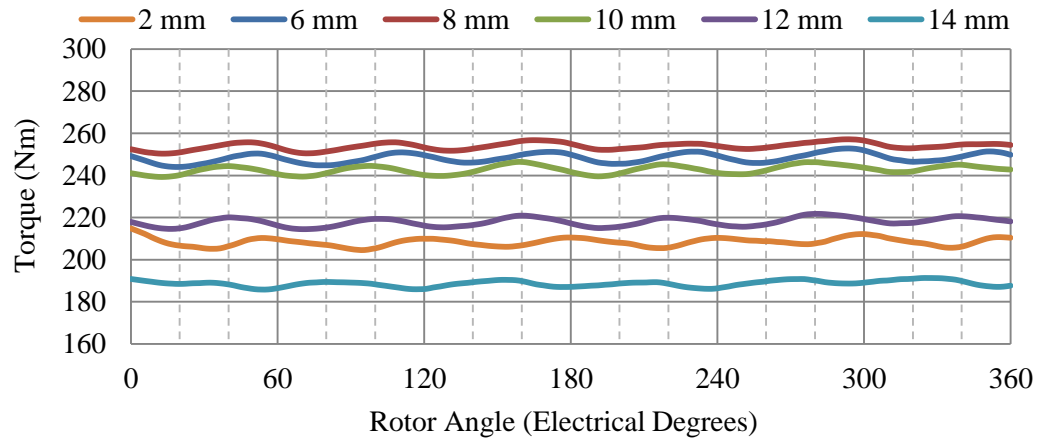


Figure A10. Torque Waveforms at 15 A/mm² Applied Current Density for Various Tooth Split Widths.

Table A6. Torque, Mass, Torque Density and Torque Ripple for Various Tooth Split Widths at 15 A/mm².

Tooth Split Width (mm)	Tooth Split Span(degrees)	Torque (Nm)	Mass (kg)	Torque Density (Nm/kg)	Torque ripple
2	3.13	216.9	20.6	10.5	4.8%
6	6.25	241.9	20.4	11.9	3.5%
8	9.38	253.8	20.1	12.6	2.6%
10	12.5	250.7	20.0	12.5	2.9%
12	15.64	245.0	19.8	12.4	3.3%
14	18.77	236.2	19.6	12.0	2.9%

C.1.5. Tooth Split Depth

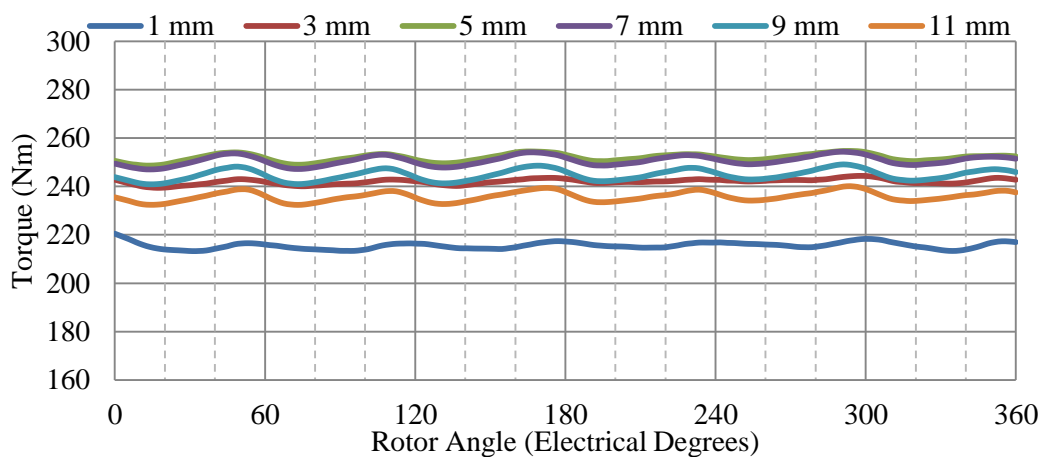
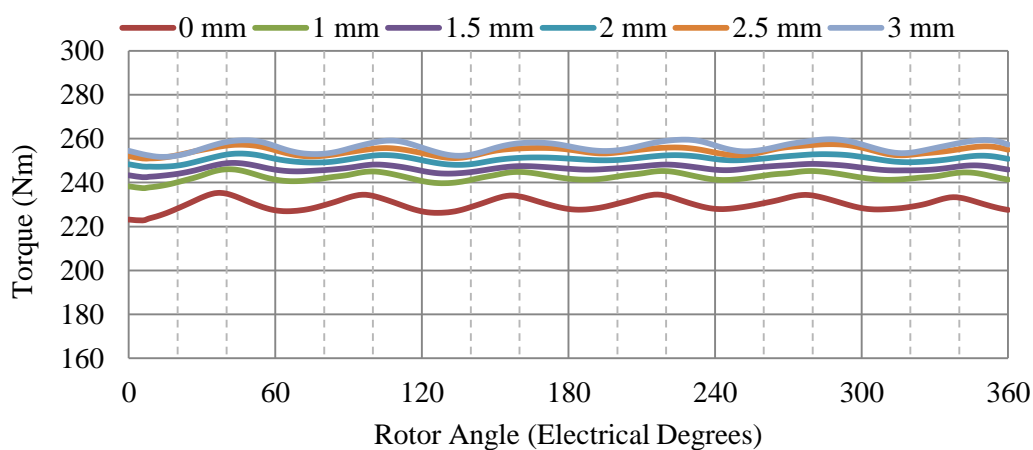


Figure A11. Torque Waveforms at 10 A/mm² Applied Current Density for Various Tooth Split Depths.

Table A7. Torque, Mass, Torque Density and Torque Ripple for Various Tooth Split Depths at 15 A/mm².

Tooth Split Depth (mm)	Torque (Nm)	Mass (kg)	Torque Density (Nm/kg)	Torque ripple
1	216.9	20.6	10.5	3.3%
3	241.9	20.4	11.9	2.0%
5	253.8	20.1	12.6	2.4%
7	250.7	20.0	12.5	2.9%
9	245.0	19.8	12.4	3.3%
11	236.2	19.6	12.0	3.2%

C.1.5. Tooth Tip Depth**Figure A12. Torque Ripple at 15 A/mm² Applied Current Density for Various Tooth Tip Depths.****Table A8. Torque, Mass, Torque Density and Torque Ripple for Various Tooth Tip Depths at 15 A/mm².**

Tooth Tip Depth (mm)	Torque (Nm)	Mass (kg)	Torque Density (Nm/kg)	Torque Ripple
0	229.0	19.9	11.5	5.1 %
1	241.8	20.0	12.1	3.6 %
1.5	245.7	20.0	12.3	3.3 %
2	250.2	20.1	12.5	3.6 %
2.5	253.8	20.1	12.6	3.8 %
3	254.5	20.2	12.6	4.2 %

C.2. Rotor Dimension Impact on Torque Density

C.2.1. Magnet Height

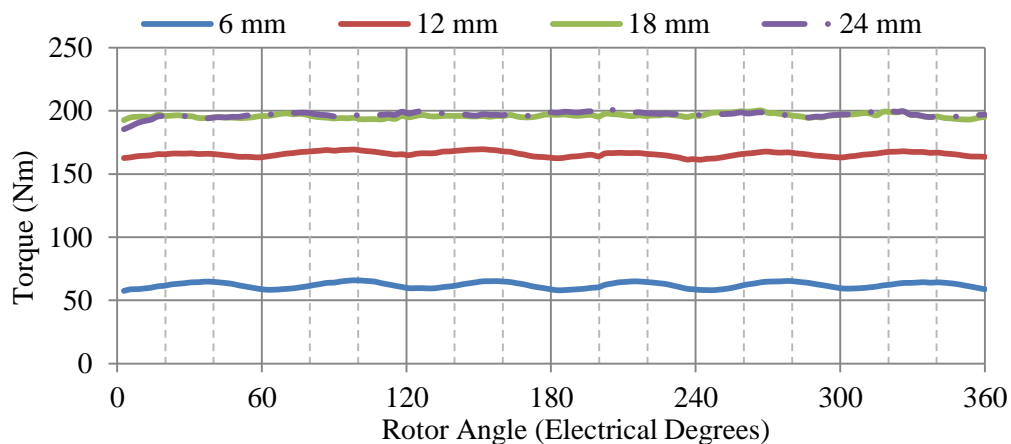


Figure A13. Torque Ripple at 10 A/mm² Applied Current Density for Various Magnet Height.

Table A9. Torque, Mass, Torque Density and Torque Ripple for Various Magnet Height at 15 A/mm².

Magnet Height (mm)	Torque (Nm)	Mass (kg)	Torque Density (Nm/kg)	Torque Ripple
6	88.4	16.4	5.4	7.9%
12	214.3	18.4	11.6	3.5%
18	253.8	20.1	12.6	2.6%
24	252.9	21.6	11.7	4.7%

C.2.2. Magnet Thickness

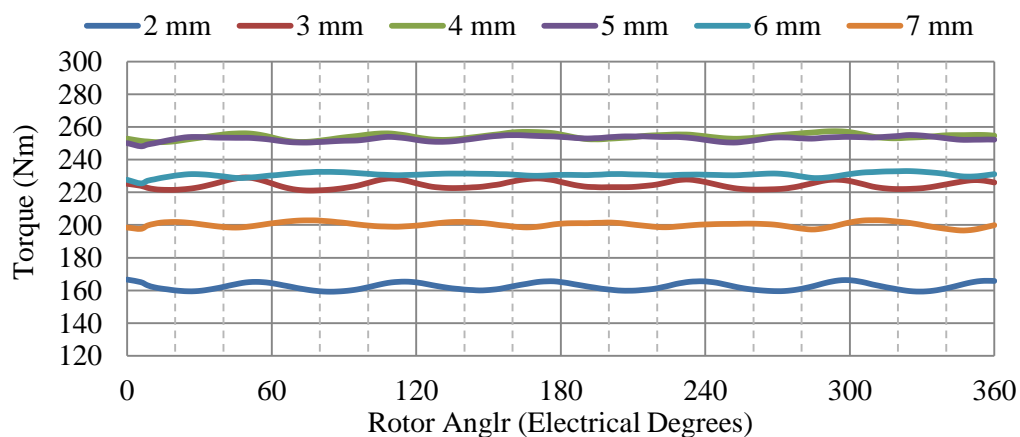


Figure A14. Torque Ripple at 15 A/mm² Applied Current Density for Various Magnet Thickness.

Table A10. Torque, Mass, Torque Density and Torque Ripple for Various Magnet Thicknesses.

Magnet Thickness (mm)	Torque (Nm)	Mass (kg)	Torque Density (Nm/kg)	Torque Ripple
2	163.0	20.2	8.1	4.4
3	225.1	20.2	11.2	3.4
4	253.8	20.1	12.6	2.6
5	251.6	20.1	12.5	2.7
6	229.2	20.1	11.4	3.2
7	199.8	20.1	9.9	3

C.3. Inner Stator Dimension Impact on Torque Density

C.3.1 Tooth Width

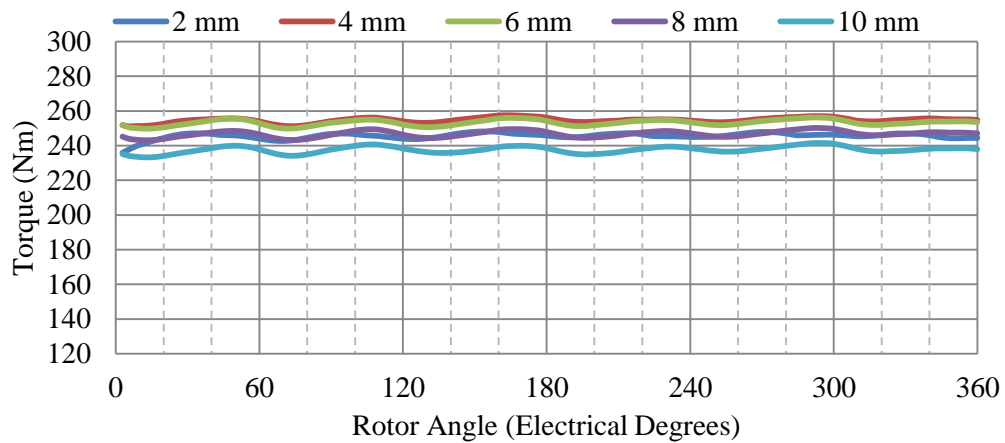


Figure A15. Torque Ripple at 15 A/mm² Applied Current Density for Various Inner Stator Tooth Widths.

Table A11. Torque, Mass, Torque Density and Torque Ripple for Various Inner Stator Tooth Widths.

Inner Stator Tooth Width (mm)	Peak Torque (Nm)	Mass (Kg)	Torque Density (Nm/kg)
2	242.1	19.68	12.3
4	250.1	19.8	12.5
6	253.8	20.1	12.6
8	246.7	20.5	12.0
10	237.4	20.8	11.4

C.3.2 Coreback Depth

Table A12. Torque, Mass, Torque Density and Torque Ripple for Various Coreback Depths.

Coreback Depth (mm)	Peak Torque (Nm)	Mass (Kg)	Torque Density (Nm/kg)
4	253.8	20.1	12.6
6	254	20.5	12.4
8	254.1	20.9	12.2
10	254.3	21.2	12.0
12	254.4	21.6	11.8

C.3.3 with and Without Inner Stator

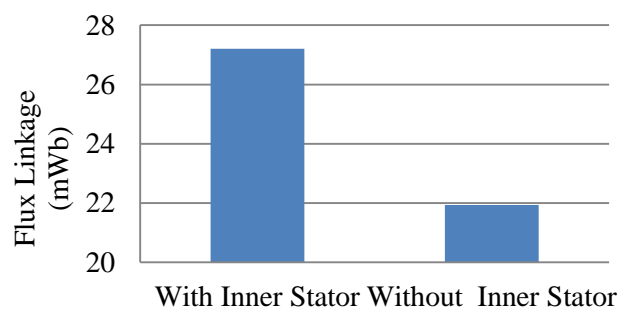


Figure A16. Flux Linkage Comparison Between the STPM Machine with Inner Stator and Without the Inner Stator.

Table A13. Torque, Mass, Torque Density Obtained with and without the Inner Stator.

	Peak Torque (Nm)	Mass (Kg)	Torque Density (Nm/kg)
Without Inner Stator	253.8	20.1	12.6
With Inner Stator	207.1	18.4	11.2

Appendix D: Design and Construction Drawings

